UNIVERSITY OF BIRMINGHAM

New Electrolyte Materials for Solid Oxide Fuel Cells

by

J. Felix SHIN

A thesis submitted to the University of Birmingham for
the degree of Doctor of Philosophy

Supervisor: Prof. Peter R. SLATER

School of Chemistry
College of Engineering and Physical Sciences
University of Birmingham
September 2012

Acknowledgements

I'd like to express thanks to;

Pete for his dedicated supervision,

The Malavasi and White groups for the collaborative works,

My colleagues in the Slater group and floor 5 Chemistry,

The University of Birmingham for the scholarship,

… and Sen, Rosie and Michael for their 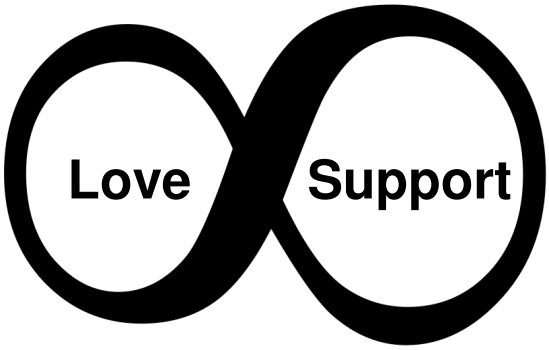

Abstract

Two general systems, brownmillerite-type $Ba_2In_2O_5$ and apatite-type silicates have been investigated for potential solid oxide fuel cell electrolyte applications. The combination of powder diffraction, NMR, TGA, Raman and AC impedance spectroscopy indicated the successful incorporation of phosphate, sulphate and silicate into the $Ba_2In_2O_5$ structure leading to a transition from an ordered brownmillerite-type structure to a disordered perovskite-type, which led to the conductivity enhancement below 800 °C, along with a significant protonic contribution in wet atmospheres. The CO_2 stability was also shown to be improved on doping. This oxyanion doping strategy has been extended to the analogous system, $Ba_2Sc_2O_5$, which resulted in samples with high conductivity and good stability towards CO_2.

Neutron diffraction studies on $La_{9.6}Si_6O_{26.4}$ indicated that the interstitial oxide ion is located near the channel centre. Further interstitial anions could be accommodated through hydration, which led to displacement of the interstitial site away from the channel centre, with an accompanying swelling of the channel. Although long term annealing of these apatite silicates showed no apparent significant structural change, a reduction in the bulk conductivity was observed, while the grain boundary conductivity was improved, thus resulting in a small enhancement in the total conductivity below 400 °C.

Contents

Chapter 1 Introduction

Fossil fuels including coal, oil and natural gas have been the main energy source for human activities since the industrial revolution. Their contribution to the advancement of the civilisation for the past 200 years is undoubted. However, the growing concerns over their limited reserves, consequent environmental pollution, unstable price and supply have resulted in a progressive swing to the development of alternative energy sources as well as more efficient energy conversion devices [1-5].

1.1 Fuel Cells

A fuel cell is an electrochemical energy conversion device that requires a constant feed of a fuel (e.g. hydrogen, hydrocarbons or alcohols) and an oxidant (e.g. air/oxygen) like a combustion engine, but the main reaction for the energy conversion is governed by an electrochemical reaction as in a battery, rather than combustion of a fuel. The efficiency of fuel cells is generally high, owing to the direct energy conversion of chemical energy to electrical energy. The products vary depending on the fuel, but in the case of hydrogen, the by-product is only water [6-9]. Fuel cell systems have much fewer moving parts compared to combustion engines which leads to quiet, reliable and long lasting systems. Thus, they are ideal for mobile power systems as well as combined heat and power systems (CHP) for a stationary application.

The fuel cell was identified in the nineteenth century as the reverse process of the electrolysis of water. Sir William Robert Grove converted hydrogen and oxygen into water using platinum electrodes in a sulphuric acid electrolyte [10], and the electrochemical reaction produced heat and electrical energy to an external circuit: the electrochemical reactions on each electrode for a hydrogen fuel cell are:

Anode	$H_2 \rightarrow 2H^+ + 2e^-$	
Cathode	$½O_2 + 2e^- + 2H^+ \rightarrow H_2O$	
Overall	$H_2 + ½O_2 \rightarrow H_2O$	(1.1.1)

1.1.1 Fuel Cell Efficiency

The maximum efficiency of conventional heat engines, having the maximum temperature of T_1 (in Kelvin), and the temperature of heat sink of T_2, is given by:

$$\text{Carnot limit} = \frac{T_1 - T_2}{T_1} \qquad (1.1.2)$$

This limit is due to the inevitable waste of heat energy proportional to T_2. The efficiency generally increases with the operating temperature of the heat engine (Fig. 1.1.1).

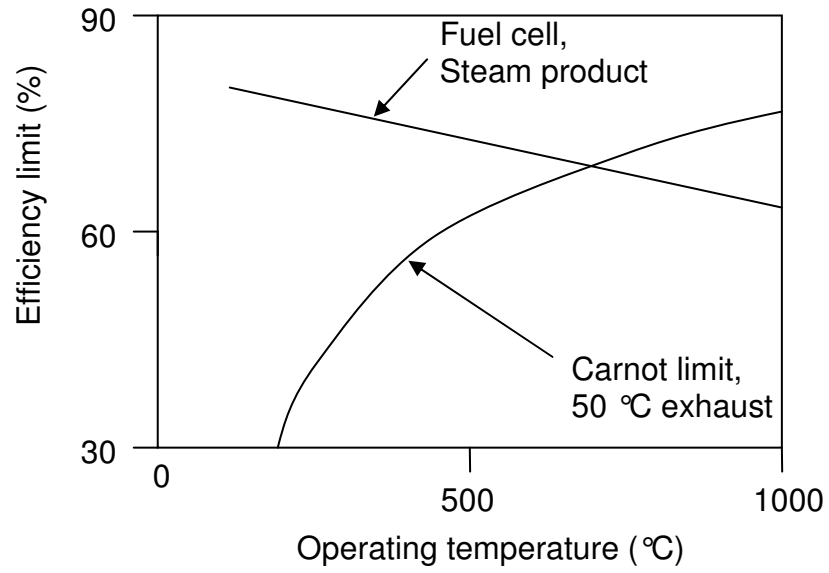

Fig. 1.1.1 Maximum efficiency of H_2 fuel cell at standard pressure with the steam product compared to the Carnot limit with a 50 ℃ exhaust temperature. Reproduced with permission from [11].

Because no heat energy is involved in the energy conversion process of an ideal fuel cell, they are not affected by the Carnot limit. Their efficiency is generally expressed with the thermodynamic efficiency, that is the comparison between the electrical energy converted per mole, $\Delta\overline{G}_f$, and enthalpy released per mole, $\Delta\overline{H}_f$, by the reaction: $\eta = \frac{\Delta\overline{G}_f}{\Delta\overline{H}_f}$. Thus, unlike heat engines, the efficiency of fuel cells, using H_2 as fuel, decreases with temperature as Gibbs free energy, $\Delta\overline{G}_f$ becomes less negative with temperature due to the greater contribution of entropy at higher temperatures (Fig. 1.1.1). However, other fuels, such as methane, have a different $\Delta\overline{G}_f$ change over the temperature, and thus fuel cells using different fuels show different maximum efficiencies at their operating temperatures.

Other than a fuel contribution, the activity of reactants (a_{H_2} and a_{O_2}) and products (a_{H_2O}) at the triple phase boundary (TPB - where reactant gas, electrolyte and current collector for electrons meet together) also contribute to the Gibbs free energy and this can be predicted by using the Nernst equation,

$$\Delta\overline{G}_f = \Delta\overline{G}_f^0 + RT \cdot \ln\left(\frac{a_{H_2O}}{a_{H_2} \cdot a_{O_2}^{\frac{1}{2}}}\right) \qquad (1.1.3)$$

where R is the gas constant (8.314 J K^{-1} mol^{-1}) and T is temperature in Kelvin. At high operating temperature, it can be assumed the gases behave ideally, and thus the activity of gases is identical to the partial pressure, $a_{H_2} \approx \frac{p_{H_2}}{p^0}$. Then, the efficiency can be rewritten:

$$\Delta\overline{G}_f = \Delta\overline{G}_f^0 + RT \cdot \ln\left(\frac{p_{H_2O}}{p_{H_2} \cdot p_{O_2}^{\frac{1}{2}}}\right) \qquad (1.1.4)$$

Thus the partial pressures of the gases involved in the reaction are factors that determine the efficiency of a fuel cell system.

1.1.2 Fuel Cell Voltage

Electrical work done (energy) is the product of charge and electric potential. The reaction for equation 1.1.1 involves two electrons, thus

Electrical energy converted = $-2FE$

where F is the Faraday constant ($F = eN_A$ = 96485 C mol^{-1}) and E is the electric potential. If the system is reversible, electrical energy = $\Delta\overline{G}_f = -2FE$, thus:

$$E = -\frac{\Delta\overline{G}_f}{2F} \qquad (1.1.5)$$

This is either called the open circuit voltage (OCV) or the electromotive force (EMF) for fuel cell operation.

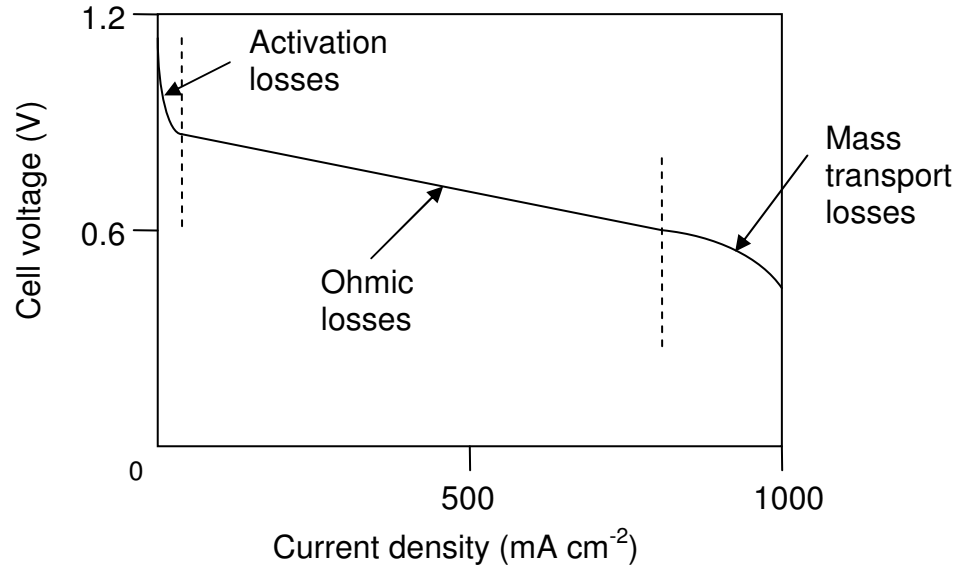

Fig. 1.1.2 Plot showing typical voltage losses for a low temperature fuel cell fed with hydrogen and air [11].

In practice, a lower value of voltage is obtained due to the various losses involved in the fuel cell operation,

$$V_{\text{cell}} = E_{\text{thermo}} - V_{\text{act}} - V_{\text{ohmic}} - V_{\text{conc}} \tag{1.1.6}$$

where, V_{cell} is the fuel cell voltage output under operating condition (i.e. with current drawn), V_{act} is the activation losses, V_{ohmic} is the ohmic losses, V_{conc} is the mass transport losses and E_{thermo} is the thermodynamically predicted potential for the reaction, which is analogous to equation 1.1.4,

$$E_{thermo} = E^0 - \frac{RT}{2F} \cdot \ln\left(\frac{p_{H_2O}}{p_{H_2} \cdot p_{O_2}^{\frac{1}{2}}} \right) \tag{1.1.7}$$

Activation losses are due to the kinetics of the electrode reaction taking place at the TPB, and this is generally analysed with a Tafel plot (Fig. 1.1.3) and given by the equation:

$$\Delta V_{act} = a \cdot \log\left(\frac{i}{i_0} \right) \tag{1.1.8}$$

where a is the slope of Tafel plot, i is the current and i_0 is the exchange current density and only when $i > i_0$, is the equation valid. For a two electron process, the slope is given by,

$$a = \frac{RT}{2\alpha F} \tag{1.1.9}$$

where α is the charge transfer coefficient and is proportional to the energy required for the reaction to proceed.

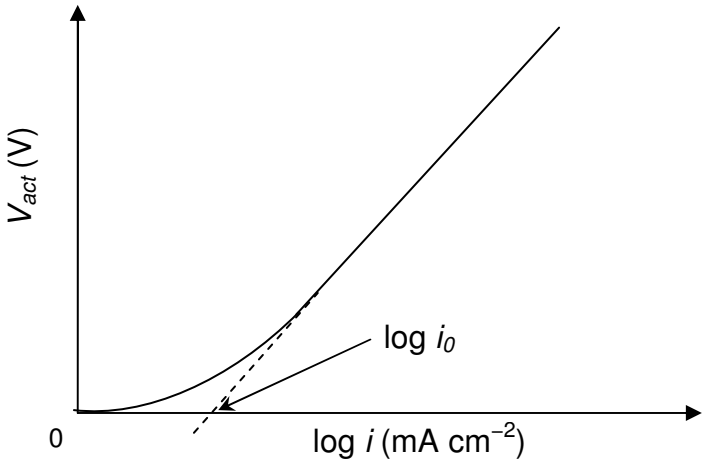

Fig. 1.1.3 A Tafel plot showing the variation of the quantities involved in the Tafel equation [11].

The term i_0 is one of the most important parameters for the fuel cell electrode. This is the current at open circuit, which is in equilibrium, such that the rate of both forward and reverse reaction is the same. Therefore, a high i_0 value means more active sites in the electrode, and most importantly, there are no activation losses below i_0. Generally i_0 for a cathode (oxygen reduction reaction) is several orders of magnitude lower than the anode (hydrogen oxidation reaction), and thus the i_0 of the anode is often excluded from calculations. As activation losses are related to the activation barrier for the reaction profile, it can be reduced with an increase in the operating temperature, by using a more effective catalyst, or an electrode design with a much greater TPB area.

Ohmic losses are the energy losses on the movement of charge carriers thorough the cell components, and the rate of the energy loss, P with current, I is given by:

$$P = I^2R \tag{1.1.10}$$

where R is the resistance of the component. The electrolyte is the most resistive component of the cell, and in order to reduce these losses, a thin electrolyte membrane (inter-electrode distance in case of aqueous or liquid electrolyte) is typically employed.

Mass transport losses are due to the limitation of supply of reactants to, and removal of products from the TPB. When a high current is drawn from a fuel cell system, a large continuous feed of fuel and oxidant are required to sustain the high rate of the reaction. Thus, high partial pressures of the gases, and a good electrode design, to enhance the efficiency of the diffusion process, are desired to reduce these mass transport losses.

1.1.3 Fuel Cell Types

A list of common fuel cell types and their characteristics and reactions are given in table 1.1.1 and Fig. 1.1.4. Each system has its own unique advantages and disadvantages, and thus different types of fuel cells are adopted for different applications.

For example, the PEMFC is ideal for mobile applications due to the use of a solid membrane electrolyte and its low operating temperature. The U.S. government has been investigating PEMFC heavily for the replacement of the ICE in the transportation sector [12]. However, the relatively high cost of the sulfonated tetrafluorethylene-based membrane, the tricky water management for the membrane, and low tolerance towards carbon monoxide are the main problems for commercialisation.

The alkaline fuel cell (AFC) can be constructed at lower cost than a PEMFC, because it has relatively faster kinetics for the oxygen reduction reaction, owing to the high pH of the electrolyte, and thus non-precious metal catalysts can be utilised. Furthermore, the electrolyte, aqueous KOH, is much cheaper compared to polymer membranes, and thus a low cost system is possible. However, carbon dioxide has to be removed when air is used as the oxidant, because of the resulting precipitation of potassium carbonate, lowering the conductivity of the electrolyte and blocking the active sites on the electrode.

Table 1.1.1 Fuel cell types and characteristics. Reprinted with permission from [11].

Fuel cell type	Operating temperature (°C)	Electrolyte	Catalyst	Fuel	Application
Proton exchange membrane (PEMFC)	30–100	Sulfonated PTFE membrane	Platinum	H_2, methanol (DMFC)	Transportation Portable power
Alkaline (AFC)	50–100	Potassium hydroxide	Platinum, nickel, silver	H_2	Speciality vehicles
Phosphoric acid (PAFC)	~200	Phosphoric acid	Platinum	H_2, CO	Large scale CHP
Molten carbonate (MCFC)	~650	Alkali metal carbonate	Nickel	H_2, CH_4, natural gas	Medium to large scale CHP
Solid oxide (SOFC)	500–1000	Ceramic	Mixed metal oxide, Ni	H_2, CH_4, natural gas	Small to large scale CHP

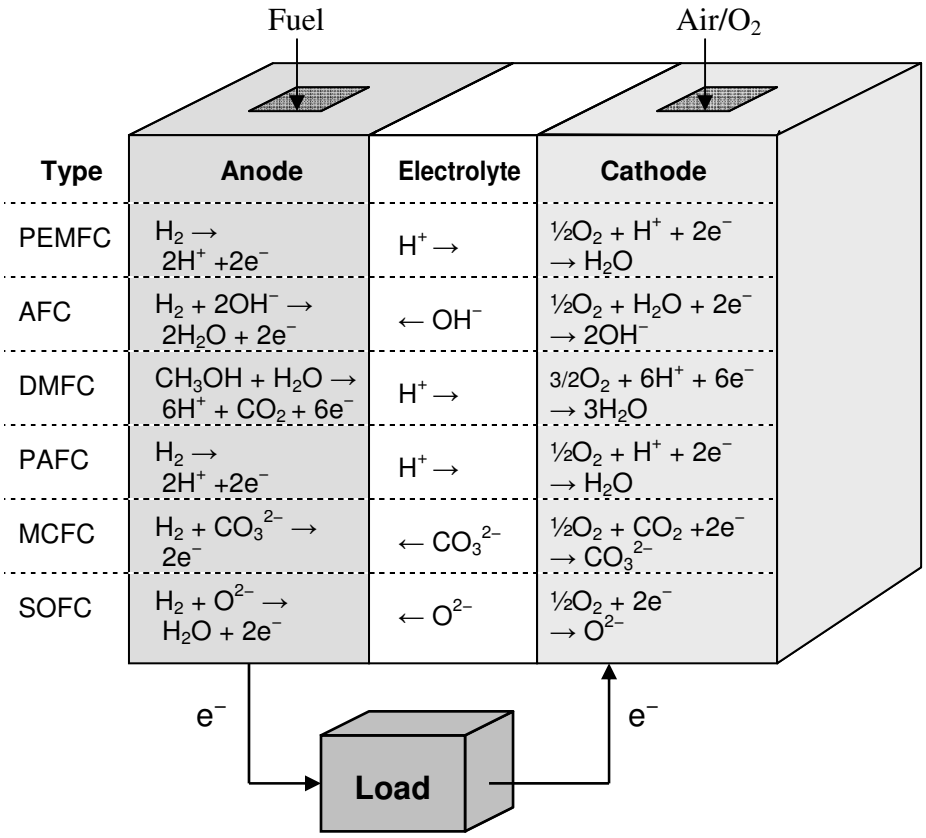

Fig. 1.1.4 Anode and cathode reactions with different types of Fuel cells.

The solid oxide fuel cell (SOFC) is also free from an expensive precious metal catalyst owing to its high operating temperature, and can operate with methane/natural gas (internal reforming), which makes it good for stationary power generating applications. Its overall efficiency can be further improved by the integration with classical thermodynamic technologies to utilise its waste heat (combined heat and power, CHP) [13]. However, its components/fabrications have to be stable at high operating temperatures.

The phosphoric acid fuel cell (PAFC) uses H_3PO_4 as an electrolyte, and has been utilised for a long time for stationary applications, and is commercially available. It is mostly suitable where uninterrupted power generation is required to avoid the mechanical stresses caused by repeated freezing and re-thawing due to the high freezing point of 42 °C for 100% H_3PO_4. Utilisation as a CHP unit is also common to increase the maximum efficiency [11].

The molten carbonate fuel cell (MCFC) uses a mixture of molten alkali metal carbonates (e.g. lithium and potassium carbonates) as the electrolyte, and unlike any other fuel cells, feeding of CO_2 is also required along with an oxidant to provide carbonate for the ionic conduction through the electrolyte. Due to the high operating temperature of 650 °C, natural gas can be fed as the fuel, and nickel and doped nickel oxide are adequate as anode and cathode respectively. The slow start-up time is required to prevent mechanical stresses during the melting of the metal carbonates, and this restricts the application of MCFC to an uninterrupted power generation [11].

1.1.4 Solid Oxide Fuel Cells

The thermodynamic efficiency calculation predicts that SOFCs are less efficient than lower temperature fuel cells. However, the low efficiency is easily compensated by much faster reaction kinetics, which means that while SOFCs have lower OCV, they exhibit much smaller

activation losses compared to lower temperature fuel cells. Furthermore, the lower efficiency can be overcome and total efficiency can be maximised by the integration with a heat engine (Fig. 1.1.1). Combining this with its fuel flexibility (internal reforming), the complete system is economically feasible. However, construction (material selection and sealing) and durability of the SOFC systems at the high operating temperature remain the key issues. Lowering the operating temperature would solve these issues, but new electrode and electrolyte materials that perform well at lower temperature are required (such as proton conducting solid state electrolytes).

An SOFC electrode requires electrocatalytic activity for hydrogen oxidation reaction for the anode, and the oxygen reduction reaction for the cathode, along with stability in harshly reducing/oxidising condition, while showing high electronic conductivity and compatibility with other components. For the anode, a nickel cermet is employed, which is a composite of nickel dispersed in the matrix of the electrolyte material. While nickel shows electrochemical activity for hydrogen oxidation and hydrocarbon reforming, it suffers from a low tolerance to sulphur, which is the significant impurity in natural gas [14-16]. For the cathode, doped perovskite manganate, cobaltate, or cobalt ferrates are commonly employed. The latter two tend to show good mixed conduction allowing an extension of the reactive area to the whole surface of the electrode [17]. However, Co containing materials tend to have high thermal expansion coefficients compared to electrolyte materials which can give rise to electrode delamination [18].

1.1.5 SOFC Electrolyte Materials

An SOFC electrolyte requires good sinterability and high ionic conductivity, while showing negligible electronic conductivity in a wide range of p_{O_2} to minimise losses due to

internal current across the electrolyte. In addition, it has to be stable at high operating temperature under reducing/oxidising atmospheres. Traditional SOFC electrolyte materials are fluorite- and perovskite-type oxide ion conductors (oxygen vacancy conduction) such as yttria stabilised zirconia (YSZ) and doped lanthanum gallate systems ($La_{1-x}Sr_xGa_yMg_{1-y}O_{3-\delta}$, LSGM).

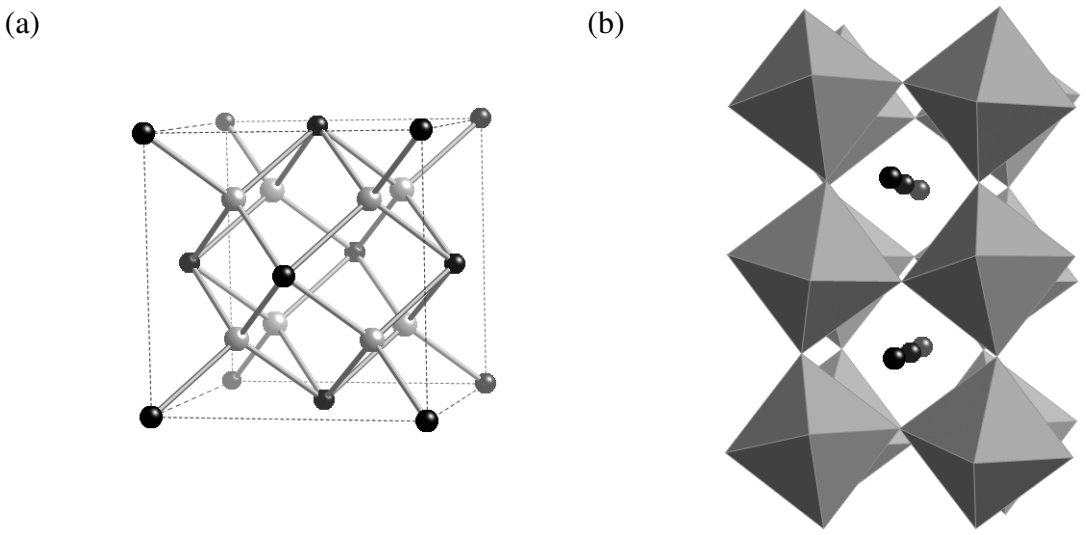

Fig. 1.1.5 (a) Fluorite structure of ZrO_2 and CeO_2 (black spheres for Zr/Ce and grey sphere for O). (b) Perovskite structure of $LaGaO_3$ (GaO_6 octahedra and Lanthanum black spheres).

Stabilised zirconia is the one of the first (reported in 1937 [19]) and widely used SOFC electrolyte materials [11]. 8 mol % yttria addition to zirconia incorporates oxide ion vacancies and stabilises the high symmetry cubic phase, showing excellent properties for a SOFC electrolyte [20, 21]. However, it does require a high operating temperature (800-1000°C) for sufficient oxide ion conductivity, which is the major drawback of the material due to cell degradation/sealing issues. To lower the operating temperature, the fabrication of very thin film YSZ using various methods [22-24] is being investigated.

Another fluorite type material, stabilised ceria, has a higher conductivity than YSZ, and thus lower operating temperature is possible [25-27]. 10 mol % gadolinium doped ceria shows very good properties for an operating temperature below 600 °C, although there are issues with high temperature, as partial reduction of Ce^{4+} to Ce^{3+} is evident leading to an electronic contribution to the conductivity [28].

Another issue with these fluorite-type SOFC electrolytes is that they are susceptible to problems due to silica impurities, which can form a siliceous intergranular phase and significantly reduce grain boundary conductivity. As silicon is a very common impurity in common reagents, the methods to trap these siliceous phases and overcome this conductivity reduction are being investigated [29].

Apart from fluorite materials, perovskite materials have attracted the most interest as alternative SOFC electrolyte, with the best example being Mg-doped $LaGaO_3$ (LSGM) which shows higher conductivity than YSZ [30, 31]. Furthermore, addition of Co has been shown to result in a further increase in the conductivity at lower temperature (e.g. 650°C) without increasing *p*-type conduction significantly [32, 33]. However, LSGM suffers from loss of Ga at high temperature under reducing condition and shows reactivity towards Ni, which is a problem at the anode/electrolyte interface [34].

1.1.5.1 Proton Conductors

Some oxide ion conductors also show proton conduction in wet atmosphere [35]. This arises as proton conducting species are created by the dissolution of gaseous water into the oxide ion vacancies present in the materials:

$$H_2O + V_O^{\bullet\bullet} + O_O^x \leftrightarrow 2OH_O^{\bullet} \qquad (1.1.11)$$

Analogous to a liquid phase solution, an oxide ion in the lattice behaves as a base to accommodate a proton dissociated from a water molecule, and a hydroxide ion from the same molecule fills an oxide ion vacancy. The charge transfer is not by the migration of the hydroxide ion itself but rather the transfer of a proton on the hydroxide ion to a neighbouring oxide ion (Grotthus mechanism) [36].

The most extensively studied materials for proton conduction are perovskite-type cerates and zirconates ($BaCeO_3$, $BaZrO_3$). In order to produce the oxide ion vacancies required to allow the incorporation of water, doping on the Zr/Ce site with a trivalent cation (e.g. Y, Yb, Sc) is required. Although the cerates ($BaCeO_3$ and $SrCeO_3$) have high proton conductivities, they suffer from the decomposition at operating temperature in the presence of CO_2, as well as the formation of alkaline earth metal hydroxides under high water activities [37-39]. Y-doped $BaZrO_3$ shows better CO_2 stability than the cerates, but generally suffers from poor grain boundary conductivity [40, 41]. In case of In doping, complete replacement of the Zr/Ce with In is possible, which gives the brownmillerite-type $BaInO_{2.5}$ ($Ba_2In_2O_5$).

1.2 $Ba_2In_2O_5$

Brownmillerite-type $Ba_2In_2O_5$ has attracted considerable interest for application as a SOFC electrolyte material since the first report of high oxide ion conductivity ($\approx 10^{-1}$ S cm^{-1}) above 930 °C in 1990 [42], followed by the discovery of proton conduction, due to the incorporation of water at lower temperature a few years later [43]. Since the investigation of novel doping strategies into $Ba_2In_2O_5$ forms a major part of the work in this thesis, the characteristics of this system will be dealt with in more detail.

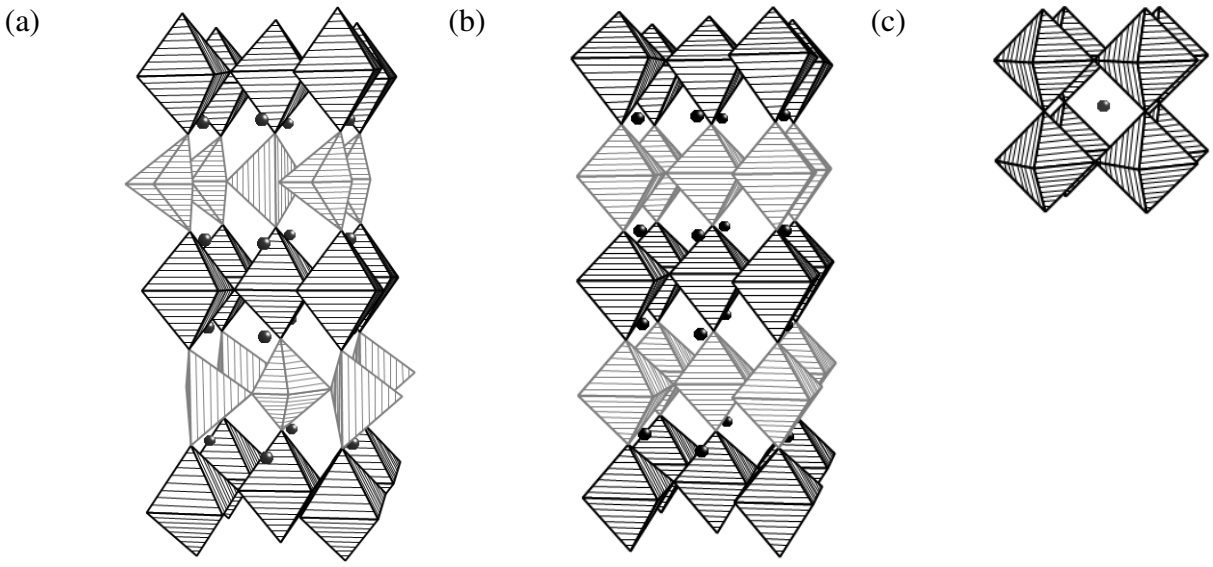

Fig. 1.2.1 Crystal structures adopted by $Ba_2In_2O_5$: (a) orthorhombic *Icmm* (b) tetragonal *I4cm* and (c) cubic $Pm\bar{3}m$ space groups. Black spheres are Ba^{2+} and polyhedra are centered around In^{3+}.

This material exhibits a range of structural transformations at different temperatures, as determined by a combination of techniques including powder diffraction, AC impedance spectroscopy, TGA/DSC, TEM/ED and ^{17}O NMR [44-48]. At room temperature, it adopts the brownmillerite-type orthorhombic structure (*Icmm*) consisting of alternating layers of corner-shared InO_6 octahedra and InO_4 tetrahedra (Fig. 1.2.1.a). Thus, oxygen vacancies are ordered

around the InO_4 tetrahedra, and this localised "trapping" of the oxide ion vacancies results in limited oxide ion conductivity. Above 925 °C, the phase transition to tetragonal (*I4cm*) symmetry is observed and the oxygen vacancies are starting to get disordered (Fig. 1.2.1.b). Above 1040 °C, it adopts an ideal cubic perovskite-type structure ($Pm\bar{3}m$) where 1/6 of the oxygen sites are empty (Fig. 1.2.1.c). The high concentration of charge carriers (oxygen vacancies) and their random distribution in the lattice allow high conductivity in phases with tetragonal/cubic symmetry. Hence, there is a characteristic 2-fold conductivity increase in the narrow temperature range from 900 to 1000 °C, as a result of the entropy driven oxygen vacancy order-disorder transition accompanying the phase change as illustrated in Fig. 1.2.2 and 1.2.3 [49]. Furthermore, in wet atmospheres at lower temperature, there is another phase change to tetragonal symmetry (*P4/mmm*) due to the uptake of the water, which facilitates protonic conduction [46].

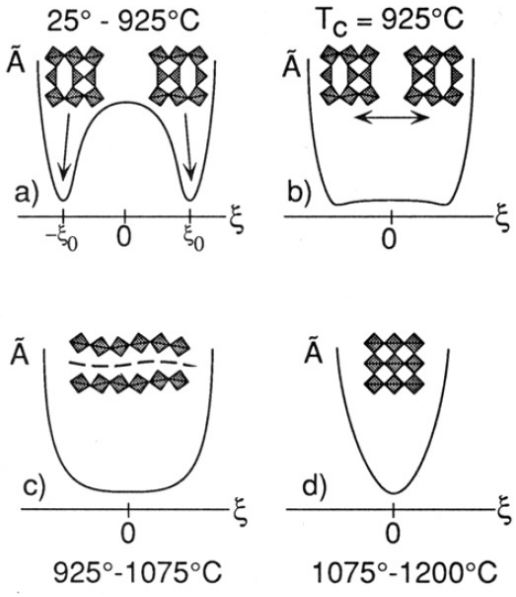

Fig. 1.2.2 $Ba_2In_2O_5$ structure and dynamics over the temperature range showing progressive changes from oxygen vacancy order to disorder (ξ denotes an order parameter). Reproduced with permission from [47].

While Bragg diffraction techniques suggest long range disorder of oxide ion vacancies, it has been suggested by thorough computational works that the local structure of $Ba_2In_2O_5$ as a function of temperature contains a range of In-O polyhedra [50]. Thus the structures determined by various techniques are the average of various local structures including InO_4 tetrahedra, InO_5 square pyramids and InO_6 octahedra.

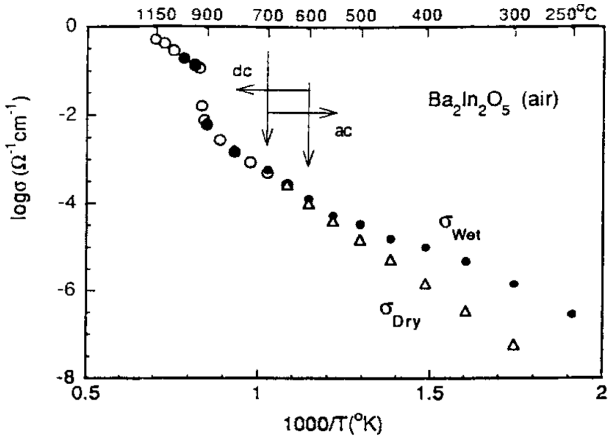

Fig. 1.2.3 Conductivity variation of $Ba_2In_2O_5$ corresponding to its phase change over the temperature and atmosphere (dry and wet air). Reproduced with permission from [43].

The solubility of water in the material is also very high: one mole of $Ba_2In_2O_5$ can accommodate one mole of water to form $Ba_2In_2O_4(OH)_2$ [46, 51]. The existence of the structure with a high concentration of oxygen vacancies coupled with the very high water solubility limit has made the material a promising candidate for oxide ion/proton conducting electrolytes for SOFCs. However, it is reported that the volume change due to hydration/dehydration destroys ceramic membranes on repeated thermal cycling [46, 52] and it is also expected that the basic nature of the material makes it prone to attack by acidic gases (e.g. CO_2) [37].

1.2.1 Doping Studies in $Ba_2In_2O_5$

The traditional doping strategy for perovskite-type structured ionic conductors has been to dope with aliovalent elements to introduce oxygen vacancies into the structure, while maintaining a high symmetry cubic structure. However, $Ba_2In_2O_5$ already has a very high number of oxygen vacancies, and thus the doping studies of this material have been concentrated on the stabilisation of the tetragonal/cubic phase to lower temperatures, so as to achieve high oxide ion/protonic conductivity at temperatures lower than 925 °C.

1.2.2 Isovalent Doping

In terms of isovalent doping, only Sr^{2+} has been tried on the Ba^{2+} site, and it was shown to increase the order-disorder transition temperature, T_d [53-55]. On the other hand, many trivalent ions (Al^{3+}, Ga^{3+}, Sm^{3+}, Gd^{3+}, Dy^{3+}, Yb^{3+}, Lu^{3+}, Sc^{3+} and Y^{3+}) have been doped onto the In^{3+} site and a trend has been established: T_d increases with the ionic radius of the dopant ion up to Y^{3+}, and decreases again thereafter (Fig.1.2.4) [56]. Only doping of Ga^{3+}, i.e. $Ba_2(In_{1-x}Ga_x)_2O_5$ for $x \geq 0.25$, has been reported to give cubic symmetry at room temperature, and the ionic conductivity of such samples was shown to decrease with doping level due to defect trapping [53, 57].

It was suggested that the local structural change due to the dopant ions (e.g. smaller ions induce a distortion in the orthorhombic symmetry due to the change in bond length to oxygen) influences T_d [57]. The unit cell free volume, which is a value obtained by the subtraction of the sum of the volumes occupied by component ions from the unit cell volume obtained experimentally, has also been used to rationalise the change in T_d and conductivity [58]: the more space for the transfer of oxide ions, the easier the oxide ion conduction.

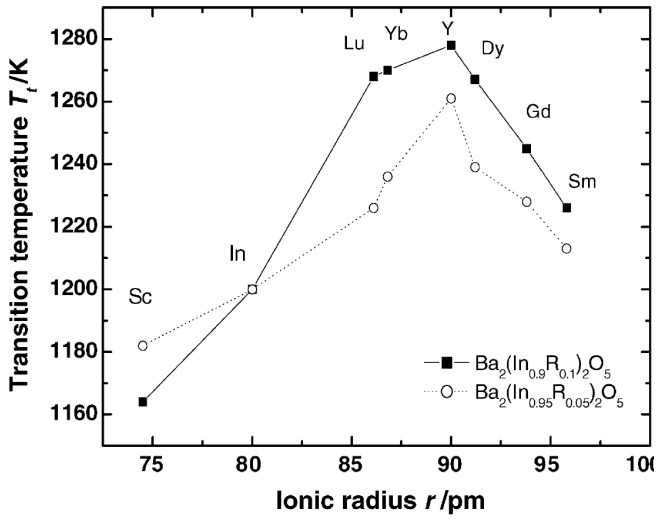

Fig.1.2.4 Order-disorder transition temperature change as a function of ionic radius of isovalent dopants. Reproduced with permission from [56].

1.2.3 Aliovalent Doping

In terms of aliovalent doping, only La^{3+} doping has been tried on the Ba^{2+} site, *i.e.* $(Ba_{1-x}La_x)_2In_2O_{5+x}$, and the order-disorder transition was reported to be suppressed for $x \geq 0.3$ [59-61] or $x \geq 0.5$ [62, 63]. The conductivity of the materials in the cubic phase increased with increasing doping level [61, 62]. Several transition metals have been doped on the In^{3+} site. V^{5+} doped phases $Ba_2In_{2-x}V_xO_{5+x}$, and Mo^{6+} doped phases $Ba_2In_{2-x}Mo_xO_{5+3x/2}$, were both shown to be cubic at room temperature for $x \geq 0.3$ [64]. The Ti^{4+} doped phases $Ba_2In_{2-x}Ti_xO_{5+x/2}$, were shown to be cubic for $x \geq 0.4$ [65]. The Zr^{4+} doped phases $Ba_2In_{2-x}Zr_xO_{5+x/2}$, were shown to be cubic for $x \geq 0.67$ [66]. The conductivity of the cubic phases of the above materials decreased with increasing doping level, most likely due to a reduction in the oxide ion vacancies [64-67]. The cobalt doped phases $BaIn_{1-x}Co_xO_{3-\delta}$, were also shown to be cubic for $x \geq 0.2$ and the conductivity in the cubic phase increased with doping level, which was due to the significant increase in electronic conduction [68]. W^{6+} doped phases $Ba_2In_{2-x}W_xO_{5+3x/2}$, were also shown to be cubic for $x \geq 0.3$ [64], and the conductivity of the materials in the cubic

phase increased with doping level [69]. $BaIn_{0.5}Sn_{0.5}O_{2.75}$ has also been synthesised and it was also shown to be cubic [70].

Apart from the size of the dopant ions, the introduction of additional oxide ions, to compensate the charge difference, was shown to be important for many cubic symmetry systems stabilised to room temperature. The conductivity increase on La^{3+} doping was rationalised by an increase in the unit cell free volume [62].

Although the average structures of these doped phases are cubic, as determined mostly by X-ray powder diffraction, there is evidence that the local structure might be orthorhombic as X-ray absorption spectroscopy studies of W^{6+} doped samples have shown [71]. It was suggested that local distortion away from cubic symmetry is inevitable due to the bond length difference between In-O and W-O.

1.2.4 Co-doping Strategies

Additional Sr, Zr, Ce, Mg, Ca, Y, Ga doping in La^{3+} doped $Ba_2In_2O_5$ have also been reported and their conductivity change with different ions were rationalised by the competition between the unit cell free volume and local distortion [72-74]. The best conductivity of 0.12 S cm^{-1} at 800 °C was observed for $(Ba_{0.2}Sr_{0.3}La_{0.5})_2In_2O_{5.5}$ [73].

1.2.5 Fluorination Studies

The incorporation of F into $Ba_2In_2O_5$ has also been investigated with a view to analysing its effect on the structure and conductivity. Fluorine doped $Ba_2In_2O_5$ has been reported in the form of $Ba_{2-0.5x}In_2O_{5-x}F_x$ which retained orthorhombic symmetry and showed an improvement in oxide ion and proton conductivity, as well as most likely fluoride ion conduction (best conductivity for $Ba_{1.95}In_2O_{4.9}F_{0.1}$) [75]. In terms of higher F levels, it has

been shown that the high temperature synthesis of $BaScO_2F$ is possible using BaF_2, but this can not be applied to the synthesis of $BaInO_2F$ owing to the higher thermodynamic stability of the alternative products BaF_2 and $BaIn_2O_4$, compared to $BaInO_2F$ [76].

1.2.6 Hydration Behaviour

The solubility of water in doped $Ba_2In_2O_5$, and the thermal stability of the hydrated phases (i.e. dehydration temperature) are important factors for proton conduction. Proton conductivity increases with the solubility of water, and the temperature range exhibiting proton conductivity is closely linked to the dehydration temperature [61, 67, 70, 77, 78]. The solubility of water and dehydration temperature decreased with the doping of less basic ions (e.g. La^{3+} and Ti^{4+}) [61, 67, 77-80], while the doping of more basic ions than In^{3+} (e.g. Sc^{3+} and Y^{3+}) increased the dehydration temperature while keeping the maximum solubility of water (i.e. 1 mole of water per mole sample) [79-81]. Hence, the basicity of a system is an important feature for water incorporation and proton conductivity. However, the volume change due to the repeated hydration/dehydration process have been shown to weaken the material's mechanical integrity especially for the systems with high solubility of water [46, 52, 81]. In addition, the Sn doped system, $BaIn_{0.5}Sn_{0.5}O_{2.75}$, were reported to show relatively high grain boundary impedance [70], which might be due to the separation of the grains as the result of this process.

Recently, even more significant proton conductivity (0.3 S cm^{-1} at 450 °C) for undoped $Ba_2In_2O_5$ in a H_2 atmosphere has been reported [82, 83]. Interestingly, the authors reported that La and Ce doped samples did not show such low temperature proton conductivity [83].

1.2.7 Fuel Cell Tests with $Ba_2In_2O_5$ Based Electrolytes

A range of doped $Ba_2In_2O_5$ samples have been examined as electrolyte materials in actual SOFC tests. A $Ba_{0.6}Sr_{0.4}LaIn_2O_{5.5}$ electrolyte with a Pt cathode and Ni anode, using moistened 1% H_2-argon mixture as fuel, resulted in a maximum power density of 510 mW cm^{-2} at 800 °C [84]. A single chamber SOFC test using $BaLaIn_2O_{5.5}$ as the electrolyte with a Ni-$(La_{0.75}Sr_{0.25})_{0.9}Cr_{0.5}Mn_{0.5}O_3$ cermet anode and $Sm_{0.5}Sr_{0.5}CoO_3$ cathode, using a methane-air mixture, resulted in a maximum power density of 64.7 mW cm^{-2} at 800 °C [85]. A $BaIn_{0.3}Ti_{0.7}O_{2.85}$ electrolyte with Ni- $BaIn_{0.3}Ti_{0.7}O_{2.85}$ cermet anode and $La_{0.58}Sr_{0.4}Co_{0.2}Fe_{0.8}O_{3-\delta}$ cathode, using humidified H_2 and air, resulted in a maximum power density of 336 mW cm^{-2} at 800 °C [86].

1.2.8 $Ba_2Sc_2O_5$

Although the Y analogue system of $Ba_2In_2O_5$, $Ba_2Y_2O_5$ has never been reported as a single phase [87], the Sc analogue system, $Ba_2Sc_2O_5$ has been synthesised (tetragonal symmetry with a = 4.148 Å, c = 3.994 Å) but it was shown to be unstable above 1000 °C [87]. However, subsequent studies showed that a stoichiometric (Ba:Sc, 1:1) mixture resulted in the formation of significant $Ba_3Sc_4O_9$ impurities [88] while utilising a Ba excess (Ba:Sc, 1.3:1) showed mainly the $Ba_2Sc_2O_5$ phase with no sign of $Ba_3Sc_4O_9$ [89] (Fig 1.2.5). All these facts emphasise the difficulty in the preparation of this phase. Nonetheless, $Ba_2Sc_2O_5$ showed oxide ion and proton conduction and preparation of Ba_2ScInO_5 also has been reported [88]. The cubic phase of $Ba_2Sc_2O_5$ was reported to be stabilised by synthesis following a precursor ($Ba_3Sc_2(OH)_{12}$) route, which resulted in a slight reduction in the lattice parameter [89]. In terms of fluorination of this phase, the single phase oxide fluoride, $BaScO_2F$ has been reported, and it adopts ideal cubic perovskite structure with a slight increase in the lattice

parameter (a_0 = 4.171) owing to the filling of the oxygen vacancies with fluoride ions [76].

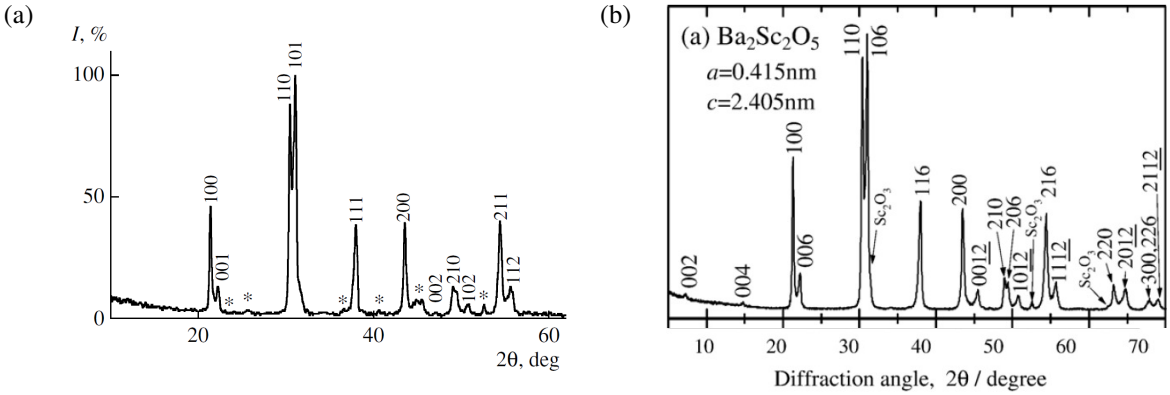

Fig. 1.2.5 $Ba_2Sc_2O_5$ synthesised with Ba:Sc ratio of (a) 1:1 (reproduced with permission from [88]) and (b) 1.3:1 (reproduced with permission from [89]) showing the impurities: $Ba_3Sc_4O_9$ (asterisked) in (a) and Sc_2O_3 (arrowed) in (b).

1.3 Oxyanions in Perovskites

Perovskites have general formula ABO_3 where A is a large cation (e.g. rare earth, alkaline earth) and B is a smaller cation (e.g. transition metals, Ga, Al). Somewhat surprisingly, it has been shown that oxyanions (such as carbonate, sulphate, phosphate) can be accommodated in some perovskite systems, as exemplified by the studies of cuprate systems: driven by the large interest in the study of perovskite related cuprate following the discovery of superconductivity by Bednorz and Müller in $La_{2-x}Sr_xCuO_4$ [90].

1.3.1 Oxyanions in Perovskite Related Cuprates

The studies of oxyanions in perovskite related materials were triggered by the discovery of the carbonate containing cuprate, $Sr_2CuO_2CO_3$ [91], followed by the determination of the structure which contains alternating layers of carbonate and CuO_2 [92]. Although this material is not superconducting due to the oxidation state of copper being 2+, the boron doped phase, $Sr_2CuO_2(CO_3)_{1-x}(BO_3)_x$ is superconducting due to the introduction of holes into the CuO_2 layers [93-95].

Following on from this work, further studies showed the widespread accommodation of carbonate in perovskite cuprate systems. The non-stoichiometric carbonate containing phase, $Ba_4YCu_{2+x}O_{6+y}(CO_3)_z$ was reported. This is a common impurity phase during the preparation of superconducting phase $YBa_2Cu_3O_{7-x}$. The structure shows Y, Cu, CO_3^{2-} ordering leading to an expanded perovskite cell (Fig 1.3.1) [96]. Further work involving varying the size of the rare earth cations indicated that oxide ion vacancies and the carbonate groups are only located neighbouring the Cu, suggesting that it is the Cu that is vital for the accommodation of the carbonate in the structure [96]. Further studies examined doping of carbonate into $YBa_2Cu_3O_{7-x}$ itself. Interestingly, the Sr analogue of this system, $YSr_2Cu_3O_{7-x}$, which was

only possible to prepare via a high pressure synthesis route, was able to be synthesised at ambient pressure by carbonate incorporation. It was believed that the introduction of carbonate could help to relieve local strain due to the smaller size of Sr [97].

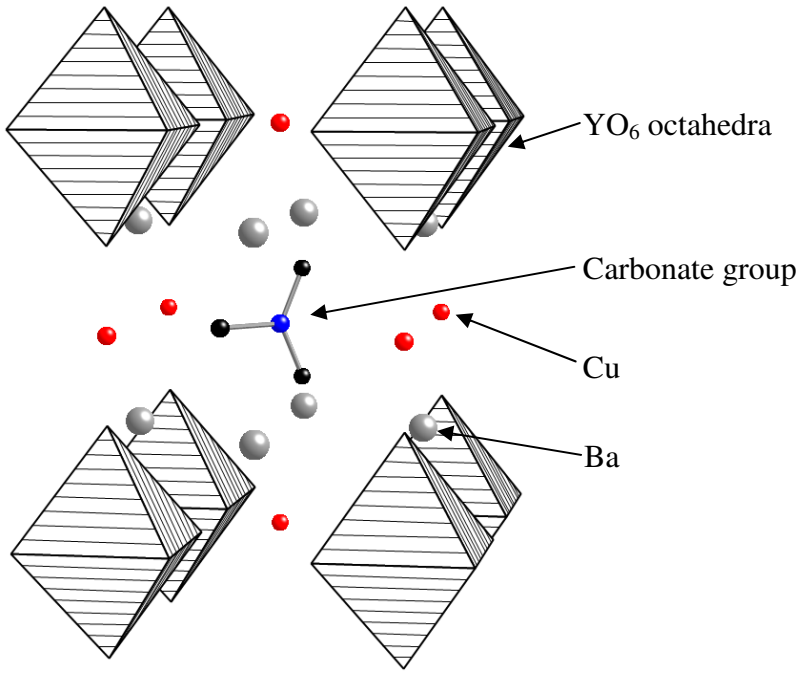

Fig. 1.3.1 Structure of $Ba_4YCu_{2+x}O_{6+y}(CO_3)_z$ [96].

However, these carbonate containing systems suffer from relatively low thermal stability, resulting in difficulty in controlling the carbonate content. Thus, many syntheses of these phases utilise sealed tubes to avoid the loss of carbonate as CO_2 [98]. To overcome this issue, the incorporation of more thermally stable oxyanions such as borate, phosphate and sulphate has been examined in such systems. The incorporation of borate, having identical geometry as carbonate was successful for most of systems shown to accommodate carbonate. Tetrahedrally coordinated phosphate and sulphate were also shown to be accommodated in $YBa_2Cu_3O_{7-x}$ giving $YBa_2Cu_{2.97}(PO_4)_{0.03}O_{7-\delta}$ exhibiting T_c's up to 97 K [99] and $Ba_4YCu_{3-x}O_{6+y}(CO_3)_x$ giving $Ba_4YCu_{2.37}O_{7.85}(SO_4)_{0.5}$ [100]. Furthermore, these oxyanions

also could stabilise Sr analogues of $YBa_2Cu_3O_{7-x}$, resulting in compositions such as $YSr_2Cu_{2.79}(PO_4)_{0.21}O_y$. The phase co-doped with Ca, $Y_{0.7}Ca_{0.3}Sr_2Cu_{2.8}(PO_4)_{0.2}O_y$ showed superconductivity at 37 K and the sulphate equivalent showing superconductivity within the range of 45-60 K [101-105]. In addition, another oxyanion, nitrate, can also take the place of carbonate in these stabilised systems leading to systems showing superconductivity [103, 106].

1.3.2 Oxyanions in Other Perovskite Related Materials

Following the work involving superconducting cuprates, oxyanion incorporation in other systems has been examined. Manganese containing systems have been shown to accommodate carbonate and borate, resulting in the perovskite phases $Sr_5Mn_4CO_3O_{10}$ and $Sr_4Mn_{3+x}B_{1-x}O_{10}$ respectively [107, 108]. The rigidity of triangular CO_3/BO_3 groups is compensated by the flexible apical Mn-O distance in the MnO_6 octahedra and MnO_5 pyramids, due to Mn^{III} being a Jahn-Teller effect ion, which was also the case for Cu in the cuprate systems [107, 108]. The carbonate doped Ruddlesden Popper phase, $Sr_4Fe_{3-x}(CO_3)_xO_{10-4x}$ has been reported [109-111] and showed some interesting structural features. Carbonate is accommodated in the middle perovskite layer replacing FeO_6 octahedra, and it can have either the same (flag) or have different orientation between the layers (hang coat) (Fig 1.3.2) [110]. This was attributed to the ability of iron to exhibit variable coordination: distorted octahedra in flag version and distorted FeO_6 octahedra alternating with FeO_5 pyramids in hang coat version.

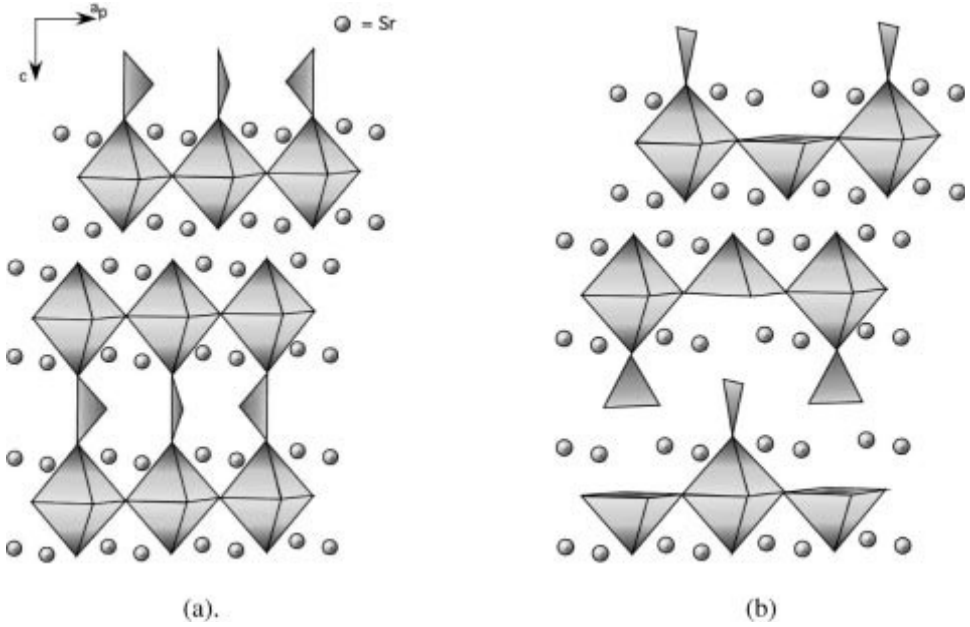

Fig 1.3.2 Structure of the oxycarbonate $Sr_4Fe_2CO_3O_6$ showing the two configurations of the carbonate groups within the "$Sr_3Fe_2O_5$ CO_3" layers, flag (a) and hang coat (b). Reprinted with permission from [110].

Overall, a large number of perovskite systems have been shown to accommodate a significant level of oxyanions, such as carbonate, borate, sulphate, phosphate and such incorporation has led to the stabilisation of some phases, which could not be prepared without the presence of the oxyanion. Despite these successes, oxyanion doping has received comparatively little attention. In this work, we aim to examine the potential of oxyanion doping to be used in other technologically important systems (e.g. fuel cell materials), especially the introduction of phosphate and sulphate due to their relatively high thermal stability. In addition, the extension to other groups, e.g. silicate, has been examined.

1.4 Apatite-type Materials

Apatite-type oxides have attracted a considerable interest for application as SOFC electrolyte materials, since the first report of high oxide ion conductivity for $(Nd/La)_{10}Si_6O_{27}$ in 1995 [112], followed by the report of similarly excellent oxide ion conductivity for germanium containing analogues [113]. The ideal apatite oxide stoichiometry can be written $A_{10}(MO_4)_6O_2$, (A = alkaline earth or rare earth metals and M = Si, Ge, P, V), and their structure can be viewed as consisting of an $A_4(MO_4)_6$ framework (Fig. 1.4.1.a), with the remaining A_6O_2 units filling the channels within the framework (Fig. 1.4.1.b) [114].

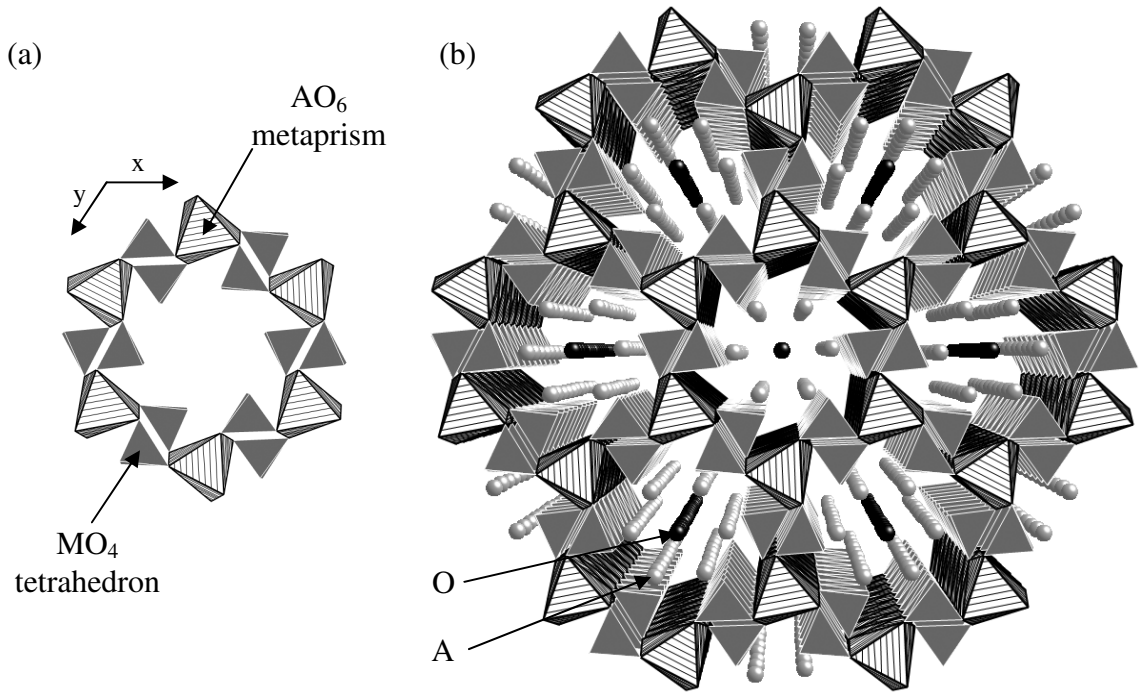

Fig. 1.4.1 The apatite structure showing (a) the $A_4(MO_4)_6$ framework (AO_6 trigonal metaprisms linked to MO_4 tetrahedra) (b) the full structure, with the A_6O_2 units filling the channels within the framework.

1.4.1 Conductivity Optimisation

Among the various rare-earth apatite systems synthesised, the lanthanum silicates and germanates have shown the highest conductivities [112, 115-117], and these apatite systems can accommodate a wide range of dopant species (e.g. B, Ga, Mg, Ca, Sr and Ba) [112, 115, 116, 118, 119]. Generally, silicate apatites show lower activation energy compared to germanate apatites resulting in higher conductivity at lower temperature (Fig. 1.4.2). Combined with the low cost of raw materials, the silicates have gained more attention for the application as SOFC electrolytes.

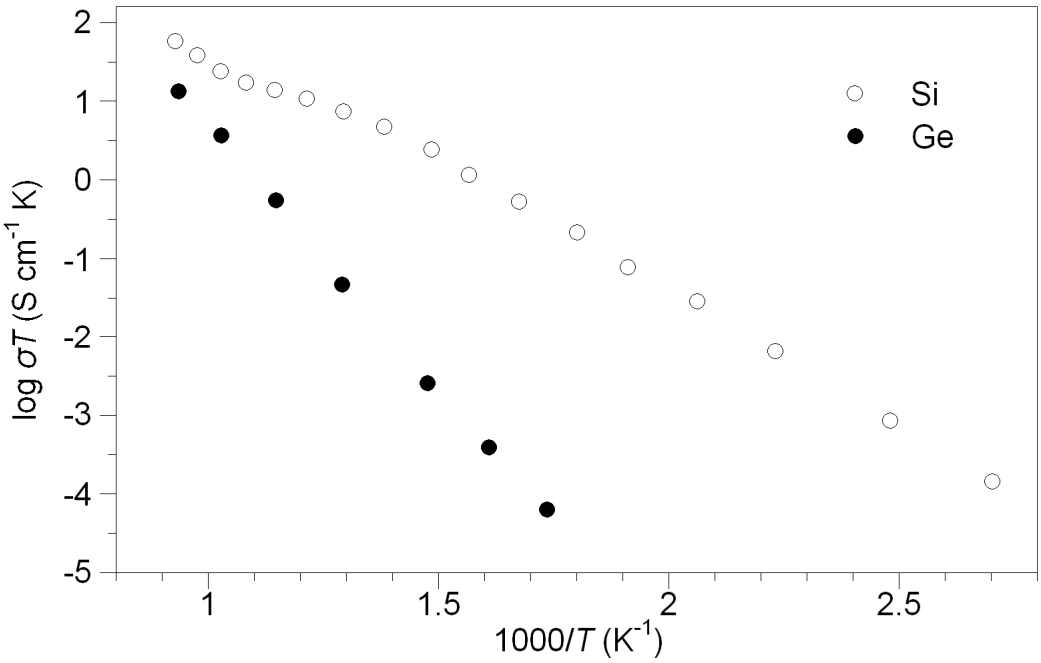

Fig. 1.4.2 Bulk conductivity plots for $La_{10}Si_5GaO_{26.5}$ and $La_{10}Ge_5GaO_{26.5}$ samples. Both phases have similar conductivity at elevated temperatures, but the latter has higher activation energy leading to much lower conductivity at lower temperatures, showing the activation energy difference of the two apatite-type materials. The data are collected by the procedure described in [120].

Table 1.4.1 Selected conductivity data for apatite-type silicates. Data set (d) are from single crystals. Reproduced with permission from [120].

	Composition	σ (S cm^{-1}) at 500 °C	Ea (eV) (Low temp/ High temp)	Reference
(a)	$La_{9.33}Si_6O_{26}$	$1.1x10^{-4}$	0.74	121
	$Pr_{9.33}Si_6O_{26}$	$8.1x10^{-5}$	0.75	120
	$Nd_{9.33}Si_6O_{26}$	$1.0x10^{-4}$	0.72	120
	$Sm_{9.33}Si_6O_{26}$	$2.2x10^{-5}$	0.83/0.71	120
	$Gd_{9.33}Si_6O_{26}$	$1.5x10^{-6}$	0.95	120
(b)	$La_{9.67}Si_6O_{26.5}$	$1.3x10^{-3}$	0.62	121
	$Nd_{9.67}Si_6O_{26.5}$	$1.6x10^{-3}$	0.66/0.49	120
	$Sm_{9.67}Si_6O_{26.5}$	$3.4x10^{-4}$	0.66	120
(c)	$La_{8.67}BaSi_6O_{26}$	$1.4x10^{-4}$	0.67	122
	$La_8Ba_2Si_6O_{26}$	$5.4x10^{-4}$ (800°C)	1.21	122
	$La_{8.67}SrSi_6O_{26}$	$8.3x10^{-5}$	0.87	122
	$La_8Sr_2Si_6O_{26}$	$5.6x10^{-4}$ (800°C)	1.14	122
	$La_{9.5}Si_{5.5}Ga_{0.5}O_{26}$	$4.6x10^{-4}$	0.67	122
	$La_{10}Si_4Ga_2O_{26}$	$4.1x10^{-6}$	0.72	122
	$La_{9.5}Si_{5.5}B_{0.5}O_{26}$	$4.1x10^{-4}$	0.69	122
	$La_{10}Si_4B_2O_{26}$	$5.5x10^{-7}$	0.98	122
(d)	$Pr_{9.33}Si_6O_{26}$ ∥ c-axis	$1.3x10^{-2}$	0.68/0.33	123
	$Pr_{9.33}Si_6O_{26}$ ⊥ c-axis	$1.2x10^{-3}$	0.62/0.48	123
	$Nd_{9.33}Si_6O_{26}$ ∥ c-axis	$6.4x10^{-2}$	0.62/0.31	124
	$Nd_{9.33}Si_6O_{26}$ ⊥ c-axis	$1.3x10^{-3}$	0.61/0.50	124
	$Sm_{9.33}Si_6O_{26}$ ∥ c-axis	$1.2x10^{-2}$	0.77/0.45	123
	$Sm_{9.33}Si_6O_{26}$ ⊥ c-axis	$2.6x10^{-3}$	0.69/0.49	124

Selected conductivity data are reported in table 1.4.1 and these data show much higher conductivity in oxygen excess samples compared to oxygen stoichiometric samples, with very poor conductivity values for the fully stoichiometric samples (i.e. both cation and oxygen stoichiometries). These findings suggested the major role of interstitial oxide ions in the conduction mechanism. These interstitial oxide ions can be accommodated in the structure

either by oxygen non-stoichiometry or by Frenkel defect formation, which early work suggested was favoured by the presence of cation vacancies (as neutron diffraction studies of cation deficient samples showed a significant displacement of some channel oxide ions away from the ideal site [120]).

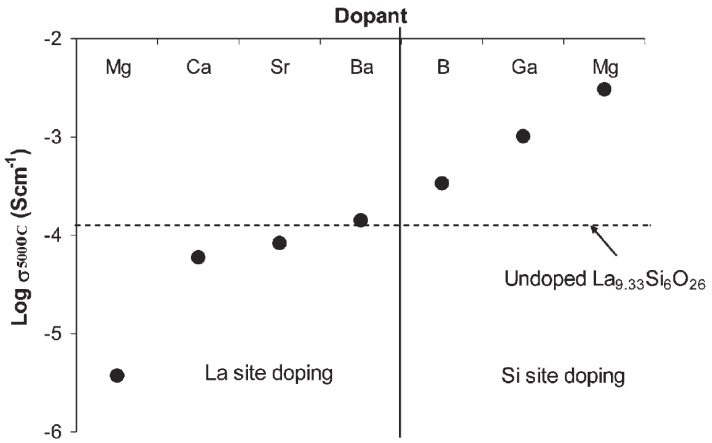

Fig. 1.4.3 Conductivity comparison of oxygen stoichiometric samples with the same A cation content, doped with lower valent dopants showing the beneficial effect on Si site and detrimental effect on La site. (Compositions = $La_{9.67}Si_5MO_{26}$ (M = B, Ga), $La_{9.67}Si_{5.5}Mg_{0.5}O_{26}$, $La_{8.67}MSi_6O_{26}$ (M = Mg, Ca, Sr, Ba)). Reproduced with permission from [125].

Another interesting point has been made from doping studies of lower valent dopants on both La and Si sites in oxygen stoichiometric samples containing cation vacancies: this study showed that the conductivity decreased on La site doping but increased on Si site doping (Fig. 1.4.3) [125]. In particular, further detailed modelling work suggested that a coordination environment change of La from 9 to 6 by the substitution with small lower valent cations (e.g. Mg) on the La site induced a change in the channel structure, which may inhibit the interstitial oxide ion movement, while the presence of lower valent ions on the Si sites promoted local

cooperative relaxation of silicate framework, which resulted in aiding the interstitial oxide ion movement [126].

In addition, conductivity data for single crystals showed (table 1.4.1.d) that the conductivity parallel to the c-axis is much higher compared to that perpendicular to the c-axis, which shows that these systems exhibit anisotropic conduction. However, somewhat surprisingly, the activation energy for both conduction directions were quite similar, an observation that has not yet been fully explained.

1.4.2 Conduction Mechanism in Apatite Germanates

Unlike apatite-type silicates (discussed in the next section), there is general consensus for apatite-type germanates regarding the location of the interstitial site and the conduction mechanism [114, 127-129]. A combination of atomic simulation and neutron diffraction studies for high oxygen excess compounds, $La_8Y_2Ge_6O_{27}$ and $La_{10}Ge_6O_{27}$, has indicated the location of interstitial oxide ions as being associated with the GeO_4 tetrahedra leading to 5 coordinated Ge [114, 129]. From computer modelling studies, the conduction mechanism was proposed with the following key points [129]:

i. The channel oxide ion act as a "reservoir" to supply interstitial oxide ions;
ii. the interstitial oxide ion forms a GeO_5 unit with a nearby GeO_4 unit;
iii. by the rotation of GeO_5 unit, it forms Ge_2O_9 unit with a neighbouring GeO_4 unit;
iv. the Ge_2O_9 unit is broken into GeO_5 and GeO_4 units, and consequently, the interstitial oxide ion is moved into the neighbouring position resulting in a "fan-like" trajectory.

The interaction with the GeO_4 tetrahedra also allows for conduction perpendicular to c-axis, and modelling studies predict that the oxide ion conduction is more isotropic than for the apatite silicates. Measurements on single crystals are, however, required to confirm this. In

addition to the above interstitial mechanism, modelling studies also suggested a contribution from channel oxide ion migration through a vacancy mechanism (E_a = 1.05 eV). However, for oxygen excess compositions having high interstitial oxide ion content, the cooperative conduction through GeO_4 tetrahedra (E_a = 0.79 eV) is predicted to dominate due to a lack of channel vacancies [129].

1.4.3 Conduction Mechanism in Apatite Silicates

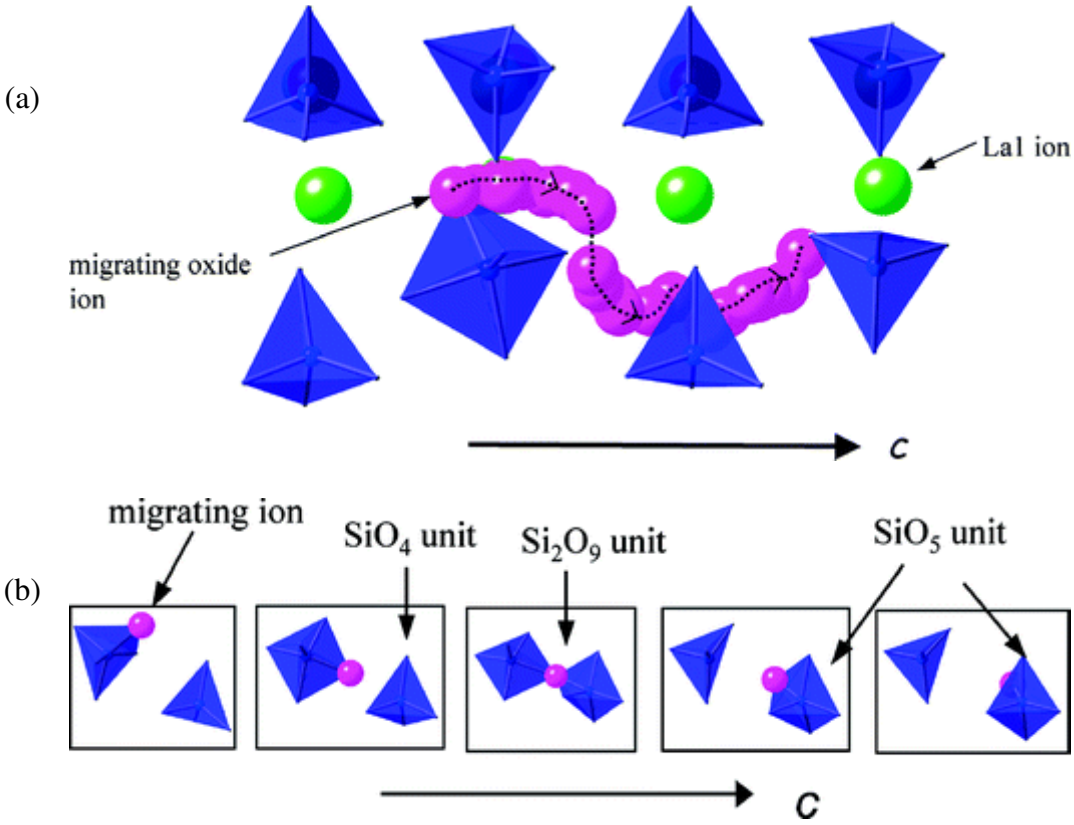

Fig. 1.4.4 (a) Interstitial oxide-ion migration pathway along the channel in $La_{9.67}Si_6O_{26.5}$ obtained from atomistic simulation studies and possible mechanism responsible for such sinusoidal pathway, (b) expanded viewpoint showing the relaxation and rotation of Si polyhedra. Reproduced with permission from [130].

Unlike apatite-type germanates, there have been many theories suggested for the conduction pathway of the interstitial oxide ion for apatite-type silicates, and there is no universal agreement on the matter currently.

Kendrick et al., through a combination of powder diffraction techniques, ^{29}Si NMR and computational modelling of $La_{9.33}Si_6O_{26}$, suggested that the position of the interstitial oxide ion is at the channel periphery, and that the migration of the interstitial oxide ion is facilitated by the cooperative displacements of the silicate substructure, thus resulting in a complex sinusoidal pathway along the c-axis (Fig. 1.4.4) [131]. Furthermore, the conduction perpendicular to c-axis (inter-channel conduction) was also suggested as being due to a series of two cooperative S_N2 (bimolecular nucleophilic substitution) type processes involving accompanying rotation of the tetrahedra.

In other studies, Masubuchi *et al*. proposed the channel oxide ion migration along the c-axis through an investigation of structural studies comparing oxygen stoichiometric samples with and without cation vacancies [132]. They proposed a cooperative migration of channel oxide ions, because of the observation of the greater anisotropic displacement of the channel oxide ions along the c-axis for a sample with cation vacancies. They suggested that a slight silicate rotation induced by the cation vacancy encourages the cooperative migration of the channel oxygen [132].

Ali et al. suggested that channel oxide ion conduction occurred along the c-axis by a vacancy mechanism and a non-linear migration pathway, through a silicate oxide ion near the channel – interstitial oxide ion – channel oxide ion – interstitial oxide ion – silicate oxide ion pathway. However, the authors stated that this non-linear migration was not continuous through all the unit cells [133].

More recently, Béchade et al. proposed another non-linear cooperative migration of the

interstitial oxide ion, with their work suggesting an interstitial oxide ion position near the channel centre [134]. In this mechanism, which requires a local structural relaxation to be facilitated, the interstitial oxide ion pushes the neighbouring channel oxide ion to the next interstitial position and takes its place instead (Fig. 1.4.5). The displaced oxide ion from channel centre (which is now in an interstitial site) again pushes the next channel oxide ion to an interstitial position to form a defect complex, which can be written in Kroger-Vink notation,

$$2O_O^x \rightarrow V_O^{\bullet\bullet} + (2O_i'' + V_O^{\bullet\bullet})$$

This defect complex ($2O_i'' + V_O^{\bullet\bullet}$) is involved in the push-pull mechanism of oxide ion migration along the c-axis [134].

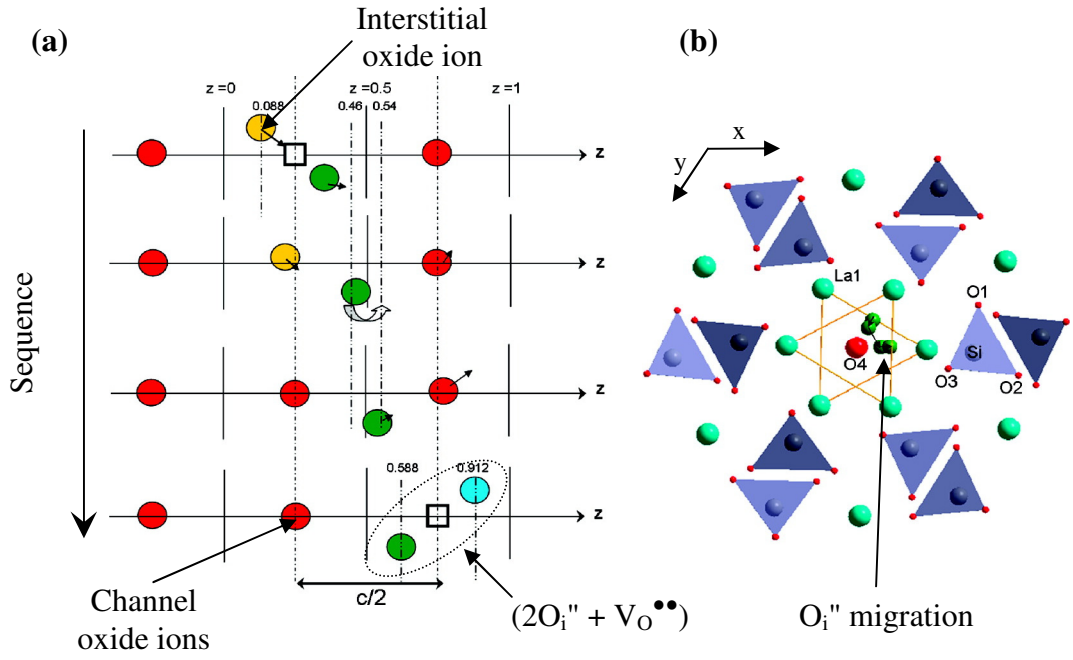

Fig. 1.4.5 (a) Schematic sequence of the formation and migration of the ($2O_i'' + V_O^{\bullet\bullet}$) defect complex achieved by push-pull mechanism along the c-axis and (b) resulting nonlinear O_i'' migration on ab plane (top view). Reprinted with permission from [134].

While there have been a range of theories for the oxide ion conduction in these apatite silicates, all theories described above indicate the crucial role of the interstitial oxide ion and its position in the structure. However, unlike apatite-type germanates which have general consensus regarding the location of the interstitial site and the conduction mechanism, there still is controversy regarding the location of interstitial site as described above: the problems with accurately locating this interstitial position can be attributed to the low interstitial site occupancy (maximum limit close to 0.5 O per formula unit [130]) and large displacement exhibited by both interstitial and channel oxide ions.

1.4.4 AO_6 Metaprism Twist Angle in Apatite-type Materials

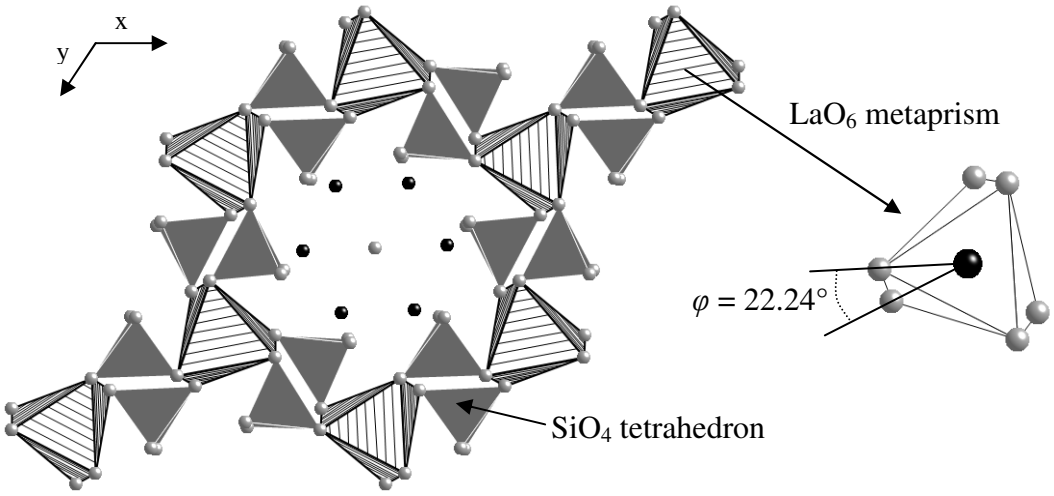

Fig. 1.4.6 Polyhedral representation of $La_{9.6}Si_6O_{26.4}$ showing the LaO_6 metaprism twist angle of 22.24°.

Along with the bond lengths and angles calculated from the atomic positions obtained from powder diffraction data, the metaprism twist angle, φ can provide further structural information for apatite-type materials. As described earlier, the apatite structure can be viewed as consisting of an $A_4(MO_4)_6$ framework (AO_6 metaprism linked to MO_4 tetrahedra), with the remaining A_6O_2 units (or A_6X_2 for halide containing apatites) filling the channels

within the framework. Through the structural studies of a wide range of apatite-type materials, White *et al.* suggested high sensitivity of the twist angles of the AO_6 metaprism to crystallochemical variation (i.e. substitution/insertion on A, M and X sites) [135]:

- for systems substituted with larger divalent A cations, the twist angle change takes a parabolic form as a function of doping level due to the preference for the accommodation of larger cations in the channel A site first [136];
- for systems substituted with halides, the twist angle decreases with an increase in the average ionic radius of the formula unit (unless there is high degree of the deviation from $P6_3/m$ symmetry or cation ordering) [135].

The channel size is also related to the metaprism twist angle as illustrated in Fig. 1.4.7: systems with a small twist angle provide more space in the channel, and for systems with large twist angle, the oxide ions from the tetrahedra are closer to the channel centre reducing the available free space [135]. Moreover, the dynamic change of the metaprism twist angle may be involved in the movement of interstitial oxide ion along the c direction as required in many proposed conduction mechanisms in apatite type silicates/germanates.

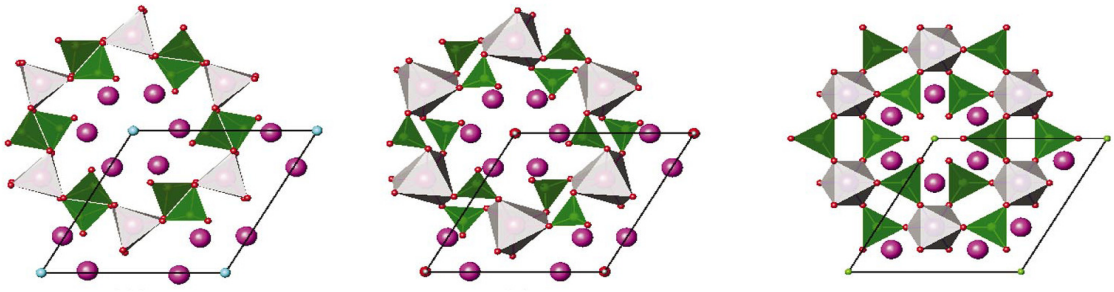

Fig. 1.4.7 Three apatites with various metaprism twist angles indicating the decrease in the channel space with increasing metaprism twist angles (from left, $Ca_4Pb_6(AsO_4)Cl_2$, $Pd_{10}(PO_4)_6(OH)_2$ and a model structure with $\varphi = 60°$). Reprinted with permission from [135].

1.4.5 Fuel Cell Tests Using Apatite Electrolytes

There have been numerous reports of fuel cell tests utilising apatite-type silicates as electrolyte materials, although at present maximum power densities have tended to be low. Plasma-sprayed $La_{9.71}Si_{5.72}Mg_{0.28}O_{26.29}$ on a Ni-$La_{9.71}Si_{5.72}Mg_{0.28}O_{26.29}$ anode support, using a $La_{0.6}Sr_{0.4}Co_{0.2}Fe_{0.8}O_{3-\delta}$ cathode, resulted in maximum power densities of 79.9 mW cm^{-2} at 800 °C and 45.4 mW cm^{-2} at 700 °C [137]. A fuel cell using a $La_{9.8}Si_{5.7}Mg_{0.3}O_{26.4}$ electrolyte with a Ni-$Sm_{0.2}Ce_{0.8}O_{1.9}$ cermet anode and $La_{0.9}Sr_{0.1}CoO_{3-\delta}$ cathode resulted in maximum power densities of 120 mW cm^{-2} at 800 °C and 35 mW cm^{-2} at 700 °C [138]. Use of a $La_{9.4}Ba_{0.6}Si_6O_{26.7}$ electrolyte with a Ni-$Sm_{0.2}Ce_{0.8}O_{1.9}$ cermet anode and $La_{0.9}Sr_{0.1}CoO_{3-\delta}$ cathode gave a lower maximum power density of 65 mW cm^{-2} at 800 °C [139]. The highest power density has been observed for a $La_{9.62}Si_{5.79}Al_{0.21}O_{26.33}$ electrolyte, with a Ni-$Ce_{0.9}Gd_{0.1}O_{1.95-\delta}$ cermet anode and $La_{0.6}Sr_{0.4}Co_{0.2}Fe_{0.8}O_{3-\delta}$ cathode resulting in a maximum power density of 250 mW cm^{-2} at 800 °C [140]. Other work on an Al doped apatite electrolyte, $La_{10}Si_{5.5}Al_{0.5}O_{26.75}$, prepared by a freeze-dried precursor method also gave respectable power densities of 195 mW cm^{-2} at 850 °C and 65 mW cm^{-2} at 700 °C. This cell used a Ni-$Ce_{0.8}Gd_{0.2}O_{1.9}$ cermet anode and $La_{0.6}Sr_{0.4}Co_{0.8}Fe_{0.2}O_{3-\delta}$ cathode [141].

1.5 Aims of the Project

In this project, new materials for SOFCs electrolyte application have been studied. Two general systems, perovskite related $Ba_2(In/Sc)_2O_5$ and apatite-type silicates, owing to their high ionic conductivity, were subject to investigation to improve the properties and to optimise them for this application.

1.5.1 Oxyanion Doping in $Ba_2In_2O_5$ and $Ba_2Sc_2O_5$

In this project, a doping strategy involving the incorporation of oxyanions, such as phosphate, sulfate and silicate into $Ba_2In_2O_5$ has been examined. The aim was to make use of the much smaller oxyanion tetrahedra coupled with the introduction of extra oxide ions, due to the charge compensation, to induce a phase change to a high symmetry with low level of dopants. The stabilisation of the high symmetry phase at lower temperature would be expected to result in an increase in the conductivity, especially at lower temperature, which is beneficial for applications for intermediate temperature SOFC. In addition, the more acidic nature of the oxyanions would be expected to reduce the basicity of the system and so might prevent or reduce the degree of the attack of acidic gas present such as CO_2 in the fuel cell operation, resulting in a more chemically stable electrolyte material. Finally, the greater local distortion due to the much smaller size of oxyanions and preference for tetrahedral coordination for the dopant will decrease the solubility of water which may increase mechanical stability under operating conditions, while maintaining high proton conductivity. The aim therefore was to investigate this alternative doping strategy to improve the properties of $Ba_2In_2O_5$ for intermediate temperature proton conducting SOFC electrolyte application.

As the preliminary results showed that this strategy was successful for $Ba_2In_2O_5$, the use of this doping strategy has been extended to the Sc analogue, $Ba_2Sc_2O_5$. As the difficulty of the

preparation of $Ba_2Sc_2O_5$ has been discussed earlier, the focus was on the stabilisation of $Ba_2Sc_2O_5$ phases through oxyanion doping, along with the implication on properties such as conductivity and CO_2 stability.

1.5.2 Long Term Stability of Apatite-type Silicates

Apatite-type silicates have been studied as alternative SOFC electrolyte materials to the conventionally used fluorite-type materials. There have been a number of fuel cell tests performed as discussed in the earlier section. However, some of the properties of these apatite materials, such as long term stability of the material for SOFC electrolyte applications, have not been studied in detail. Thus in addition to the work on oxyanion doping, research in this project has also targeted the study of the effect of long term heating at fuel cell operating temperatures on these apatite-type silicates. In particular, samples with cation vacancies were examined to see whether long term annealing may lead to a local change in cation ordering and hence change in performance. The preliminary results indicated a slight reduction in the bulk conductivity, hence more systematic studies involving conductivity measurements on single crystals and polycrystalline samples have been conducted followed by structural studies involving powder neutron diffraction. The latter is important as the structure of the materials especially the position of interstitial oxide ion is crucial for the conduction mechanism. The aim was to expand the understanding of the apatite-type silicates with regard to the location of the interstitial position, and to design the optimal material for use as a SOFC electrolyte.

1.5.3 Application of Apatite Silicates in Fuel Cells

While there have been a number of fuel cell tests performed with apatite electrolytes, there have been limited systematic studies aimed at the optimisation of the electrode materials. To

rectify this, a range of studies have been performed on composite cathodes on apatite-type silicates as a part of a cathode optimisation study.

1.6 References

[1] Chau, J.; Sowlati, T.; Sokhansanj, S.; Preto, F. *Appl. Energ.* **2009,** *86*, 616.
[2] Mohammadi, H. *Energ. Econ.* **2009,** *31*, 503.
[3] Schilling, M. A.; Esmundo, M. *Energ. Policy* **2009,** *37*, 1767.
[4] Jegatheesan, V.; Liow, J. L.; Shu, L.; Kim, S. H.; Visvanathan, C. *J. Clean. Prod.* **2009,** *17*, 637.
[5] Franzese, P. P.; Rydberg, T. r.; Russo, G. F. *Ecol. Indic.* **2009,** *9*, 959.
[6] Gulzow, E. *J. Power Sources* **1996,** *61*, 99.
[7] Neburchilov, V.; Martin, J.; Wang, H.; Zhang, J. *J. Power Sources* **2007,** *169*, 221.
[8] Prater, K. B. *J. Power Sources* **1994,** *51*, 129.
[9] Lin, B. Y. S.; Kirk, D. W.; Thorpe, S. J. *J. Power Sources* **2006,** *161*.
[10] Grove, W. R.; *Philos. Mag.*, **1839**, *14*, 127.
[11] Larminie, J.; Dicks, A. *Fuel Cell Systems Explained*, 2nd Edition, John Wiley & Sons, **2003**.
[12] Marcinkoski, J.; Kopasz, J. P.; Benjamin, T. G. *Int. J. Hydrogen Energ.* **2008,** *33*, 3894.
[13] Zhang, X.; Chan, S. H.; Li, G.; Ho, H. K.; Li, J.; Feng, Z. *J. Power Sources* **2010,** *195*, 685.
[14] Setoguchi, T.; Okamoto, K.; Eguchi, K.; Arai, H. *J. Electrochem. Soc.* **1992**, *139*, 2875.
[15] Gorte, R. J.; Park, S.; Vohs, J. M.; Wang, C. *Adv. Mater.* **2000**, *12*, 1465.
[16] Rostrup-Nielsen, J. R.; Sehested, J.; Nørskov, J. K. *Adv. Catal.* **2002**, *47*, 65.
[17] Yamamoto, O.; Takeda, Y.; Kanno, R.; Noda, M. *Solid State Ionics* **1987**, *22*, 241.
[18] Skinner, S. J. *Int. J. Inorg. Mater.* **2001**, *3*, 113.
[19] Baur, E.; Preis, H. *Z. Elktrochem.* **1937**, 43, 727.
[20] Gorelov, V. P.; Palguev, S. F. *Doklady Akademii Nauk Sssr* **1979**, 248, 1356.
[21] Kharton, V. V.; Naumovich, E. N.; Vecher, A. A. *J. Solid State Electrochem.* **1999**, 3,61.
[22] Oh, E. O.; Whang, C. M.; Lee, Y. R.; Lee, J. H.; Yoon, K. J.; Kim, B. K.; Son, J. W.; Lee, H. W. *J. Eur. Ceram. Soc.* **2012**, *32*, 1733.
[23] Nedelec, R.; Uhlenbruck, S.; Sebold, D.; Haanappel, V. A. C.; Buchkremer, H. P.; Stover, D. *J. Power Sources* **2012**, *205*, 157.
[24] Schlupp, M. V. F.; Prestat, M.; Martynczuk, J.; Rupp, J. L. M.; Bieberle-Hutter, A.; Gauckler, L. J. *J. Power Sources* **2012**, *202*, 47.
[25] Tuller, H. L.; Nowick, A. S. *J. Electrochem. Soc.* **1975**, 122, 255.
[26] Doshi, R.; Richards, V. L.; Carter, J. D.; Wang, X. P.; Krumpelt, M. *J. Electrochem. Soc.***1999**, 146,1273.
[27] Inoue, T.; Setoguchi, T.; Eguchi, K.; Arai, H. *Solid State Ionics* **1989**, 35, 285.
[28] Kharton, V. V.; Figueiredo, F. M.; Navarro, L.; Naumovich, E. N.; Kovalevsky, A. V.; Yaremchenko, A. A.; Viskup, A. P.; Carneiro, A.; Marques, F. M. B.; Frade, J. R. *J. Mater. Sci.* **2001**, 36, 1105.
[29] Lee, J. H. *Mon. Chem.* **2009**, *140*, 1081.
[30] Feng, M.; Goodenough, J. B. *Eur. J. Solid State Inorg. Chem.* **1994**, 31, 663
[31] Ishihara, T.; Matsuda, H.; Takita, Y. *J. Am. Chem. Soc.* **1994**, 116

[32] Ishihara, T.; Furutani, H.; Honda, M.; Yamada, T.; Shibayama, T.; Akbay, T.; Sakai, N.; Yokokawa, H.; Takita, Y. *Chem. Mater.* **1999**, 11, 2081.
[33] Trofimenko, N.; Ullmann, H. *Solid State Ionics* **1999**, 118, 215.
[34] Kawahara, K.; Suda, S.; Suzuki, M.; Kawano, M.; Yoshida, H.; Inagaki, T. *Solid Oxide Fuel Cells 10*; Eguchi, K., Singhai, S. C., Yokokawa, H., Mizusaki, H., Eds.; Electrochemical Society Inc: Pennington, 2007; Vol. 7, p 1381.
[35] Norby, T.; Larring, Y. *Curr. Opin. Solid St. M.* **1997,** *2*, 593.
[36] Munch, W.; Seifert, G.; Kreuer, K. D.; Maier, J. *Solid State Ionics* **1996,** *86,* 647.
[37] Scholten, M. J.; Schoonman, J.; vanMiltenburg, J. C.; Cordfunke, E. H. P. *Thermochim. Acta* **1995,** *268,* 161.
[38] Tanner, C. W.; Virkar, A. V. *J. Electrochem. Soc.* **1996,** *143*, 1386.
[39] Scholten, M. J.; Schoonman J.; van Miltenburg J. C.; Oonk H. A. J. *Proceedings of Electrochemical Society* **1993**. *93*, 146.
[40] Kreuer, K. D.; Munch, W.; Traub, U.; Maier, J. *Berichte der Bunsen-Gesellschaft-Physical Chemistry Chemical Physics* **1998,** *102*, 552.
[41] Kreuer, K. D. *Annu. Rev. Mater. Res.* **2003,** *33,* 333.
[42] Goodenough, J. B.; Ruizdiaz, J. E.; Zhen, Y. S. *Solid State Ionics* **1990,** *44*, 21.
[43] Zhang, G. B.; Smyth, D. M. *Solid State Ionics* **1995,** *82*, 153.
[44] Speakman, S. A.; Richardson, J. W.; Mitchell, B. J.; Misture, S. T. *Solid State Ionics* **2002,** *149*, 247.
[45] Adler, S. B.; Reimer, J. A.; Baltisberger, J.; Werner, U. *J. Am. Chem. Soc.* **1994,** *116*, 675.
[46] Schober, T.; Friedrich, J.; Krug, F. *Solid State Ionics* **1997,** *99*, 9.
[47] Fischer, W.; Reck, G.; Schober, T. *Solid State Ionics* **1999,** *116*, 211.
[48] Mitome, M.; Okamoto, M.; Bando, Y.; Yamamura, H. *J. Vac. Sci. Technol. B* **2001,** *19*, 2284.
[49] Allan, N. L.; Stolen, S.; Mohn, C. E. *J. Mater. Chem.* **2008,** *18*, 4124.
[50] Mohn, C. E.; Allan, N. L.; Freeman, C. L.; Ravindran, P.; Stolen, S. *J. Solid State Chem.* **2005**, *178*, 346.
[51] Hashimoto, T.; Inagaki, Y.; Kishi, A.; Dokiya, M. *Solid State Ionics* **2000,** *128*, 227.
[52] Manthiram, A.; Kuo, J. F.; Goodenough, J. B. *Solid State Ionics* **1993,** *62*, 225.
[53] Yamamura, H.; Yamada, Y.; Mori, T.; Atake, T. *Solid State Ionics* **1998,** *108*, 377.
[54] Hashimoto, T.; Yoshinaga, M.; Ueda, Y.; Komazaki, K.; Asaoka, K.; Wang, S. *J. Therm. Anal. Calorim.* **2002,** *69*, 909.
[55] Yoshinaga, M.; Yamaguchi, M.; Furuya, T.; Wang, S. R.; Hashimoto, T. *Solid State Ionics* **2004,** *169*, 9.
[56] Ta, T. Q.; Tsuji, T.; Yamamura, Y. *J. Alloy. Compd.* **2006,** *408,* 253.
[57] Yao, T.; Uchimoto, Y.; Kinuhata, M.; Inagaki, T.; Yoshida, H. *Solid State Ionics* **2000,** *132*, 189.
[58] Fisher, C.A.J.; Derby B.; Brook R. J. *British Ceramic Proceedings* **1996**, *56,* 25.
[59] Tenailleau, C.; Pring, A.; Moussa, S. M.; Liu, Y.; Withers, R. L.; Tarantino, S.; Zhang, M.; Carpenter, M. A. *J. Solid State Chem.* **2005,** *178*, 882.
[60] Liu, Y.; Withers, R. L.; Fitz Gerald, J. D. *J. Solid State Chem.* **2003,** *170*, 247.
[61] Noirault, S.; Celerier, S.; Joubert, O.; Caldes, M. T.; Piffard, Y. *Solid State Ionics* **2007,** *178*, 1353.

[62] Kakinuma, K.; Yamamura, H.; Haneda, H.; Atake, T. *Solid State Ionics* **2001,** *140*, 301.
[63] Li, X. G.; Jacob, K. T.; Kale, G. M. *J. Electrochem. Soc.* **2010**, *157*, J285.
[64] Rolle, A.; Vannier, R. N.; Giridharan, N. V.; Abraham, F. *Solid State Ionics* **2005,** *176*, 2095.
[65] Animitsa, I. E.; Dogodaeva, E. N.; Nokhrin, S. S.; Kosareva, O. A.; Neiman, A. Y. *Russ. J. Electrochem.* **2010**, *46*, 734.
[66] Jayaraman, V.; Magrez, A.; Caldes, M.; Joubert, O.; Ganne, M.; Piffard, Y.; Brohan, L. *Solid State Ionics* **2004,** *170*, 17.
[67] Quarez, E.; Noirault, S.; Caldes, M. T.; Joubert, O. *J. Power Sources* **2010,** *195*, 1136.
[68] Kobayashi, T.; Senoo, Y.; Hibino, M.; Yao, T. *Solid State Ionics* **2006,** *177*, 1743.
[69] Shimura, T.; Yogo, T. *Solid State Ionics* **2004,** *175*, 345
[70] Schober, T. *Solid State Ionics* **1998,** *109*, 1.
[71] Daviero-Minaud, S.; Rolle, A.; Kongmark, C.; Vannier, R. N. *J. Solid State Chem.* **2009,** *182*, 289.
[72] Kakinuma, K.; Yamamura, H.; Haneda, H.; Atake, T. *Solid State Ionics* **2002,** *154,* 571.
[73] Kakinuma, K.; Yamamura, H.; Atake, T. *J. Therm. Anal. Calorim.* **2002,** *69*, 897.
[74] Kakinuma, K.; Takahashi, N.; Yamamura, H.; Nomura, K.; Atake, T. *Solid State Ionics* **2004,** *168*, 69.
[75] Animitsa, I.; Tarasova, N.; Filinkova, Y. *Solid State Ionics* **2012**, *207*, 29.
[76] Needs, R. L.; Weller, M. T. *J. Solid State Chem.* **1998**, *139*, 422.
[77] Kakinuma, K.; Tomita, A.; Yamamura, H.; Atake, T. *J. Mater. Sci.* **2006,** *41*, 6435.
[78] Jayaraman, V.; Magrez, A.; Caldes, M.; Joubert, O.; Taulelle, F.; Rodriguez-Carvajal, J.; Piffard, Y.; Brohan, L. *Solid State Ionics* **2004,** *170*, 25.
[79] Omata, T.; Kita, M.; Goto, Y.; Okura, T.; Otsuka-Yao-Matsuo, S. *J. Electrochem. Soc.* **2005,** *152*, A1068.
[80] Spesivtseva, I. V.; Kochetova, N. A.; Gorbunova, E. M.; Animitsa, I. E. *Russ. J. Phys. Chem. A* **2011**, *85*, 1689.
[81] Noirault, S.; Quarez, E.; Piffard, Y.; Joubert, O. *Solid State Ionics* **2009,** *180*, 1157.
[82] Jankovic, J.; Wilkinson, D. P.; Hui, R. *J. Electrochem. Soc.* **2011**, *158*, B61.
[83] Jankovic, J.; Wilkinson, D. P.; Hui, R. *J. Power Sources* **2012**, *201*, 49.
[84] Kakinuma, K.; Arisaka, T.; Yamamura, H.; Atake, T. *Solid State Ionics* **2004**, *175*, 139.
[85] Asahara, S.; Michiba, D.; Hibino, M.; Yao, T. *Electrochem. Solid State Lett.* **2005**, *8*, A449.
[86] Letilly, M.; Joubert, O.; La Salle, A. L. *J. Power Sources* **2012**, *206*, 210.
[87] Kwestroo, W.; Vanhal, H. A. M.; Langerei.C *Mater. Res. Bull.* **1974**, *9*, 1623.
[88] Animitsa, I. E.; Kochetova, N. A.; Shailkhlislamova, A. R. *Russ. J. Electrochem.* **2007**, *43*, 708.
[89] Omata, T.; Fuke, T.; Otsuka-Yao-Matsuo, S. *Solid State Ionics* **2006**, *177*, 2447.
[90] Bednorz, J. G.; Muller, K. A. *Z. Phys. B-Condens. Mat.* **1986**, *64*, 189.
[91] Vonschnering, H. G.; Walz, L.; Schwarz, M.; Becker, W.; Hartweg, M.; Popp, T.; Hettich, B.; Muller, P.; Kampf, G. *Angew. Chem.-Int. Edit. Engl.* **1988**, *27*, 574.
[92] Babu, T. G. N.; Fish, D. J.; Greaves, C. *J. Mater. Chem.* **1991**, *1*, 677.

[93] Francesconi, M. G.; Greaves, C. *Supercon. Sci. Tech.* **1997**, *10*, A29.
[94] Uehara, M.; Nakata, H.; Akimitsu, J. *Physica C* **1993**, *216*, 453.
[95] Nakata, H.; Akimitsu, J.; Katano, S.; Minami, T.; Ogita, N.; Udagawa, M. *Physica C* **1995**, *255*, 157.
[96] Slater, P. R.; Gover, R. K. B. *Mater. Res. Bull.* **2002**, *37*, 485.
[97] Slater, P. R.; Greaves, C.; Slaski, M.; Muirhead, C. M. *Physica C* **1993**, *208*, 193.
[98] Rao, C. N. R.; Nagarajan, R.; Vijayaraghavan, R. *Supercon. Sci. Tech.* **1993**, *6*, 1.
[99] Sarmiento, M. P. R.; Laverde, M. A. U.; Lopez, E. V.; Tellez, D. A. L.; Roa-Rojas, J. *Phys. B-Condens. Mat.* **2007**, *398*, 360.
[100] Slater, P. R.; Greaves, C. *Physica C* **1994**, *223*, 37.
[101] Nagarajan, R.; Ayyappan, S.; Rao, C. N. R. *Physica C* **1994**, *220*, 373.
[102] Uehara, M.; Uoshima, M.; Ishiyama, S.; Nakata, H.; Akimitsu, J.; Matsui, Y.; Arima, T.; Tokura, Y.; Mori, N. *Physica C* **1994**, *229*, 310.
[103] Dominguez, A. B.; Scorzelli, R. B.; Saitovitch, E. B. *Hyperfine Interactions* **1997**, *110*, 17.
[104] Slater, P. R.; Greaves, C.; Slaski, M.; Muirhead, C. M. *Physica C* **1993**, *213*, 14.
[105] Slater, P. R.; Greaves, C.; Slaski, M.; Muirhead, C. M. *Physica C* **1993**, *208*, 193.
[106] Chapman, J. P.; Zhou, W. Z.; Attfield, J. P. *J. Alloy. Compd.* **1997**, *261*, 187.
[107] Caignaert, V.; Domenges, B.; Raveau, B. *J. Solid State Chem.* **1995**, *120*, 279.
[108] Pelloquin, D.; Hervieu, M.; Michel, C.; Nguyen, N.; Raveau, B. *J. Solid State Chem.* **1997**, *134*, 395.
[109] Breard, Y.; Michel, C.; Hervieu, M.; Nguyen, N.; Ducouret, A.; Hardy, V.; Maignan, A.; Raveau, B.; Bouree, F.; Andre, G. *Chem. Mater.* **2004**, *16*, 2895.
[110] Raveau, B.; Hervieu, M.; Pelloquin, D.; Michel, C.; Retoux, R. *Zeitschrift Fur Anorganische Und Allgemeine Chemie* **2005**, *631*, 1831.
[111] Breard, Y.; Michel, C.; Hervieu, M.; Raveau, B. *J. Mater. Chem.* **2000**, *10*, 1043.
[112] Nakayama, S.; Aono, H.; Sadaoka, Y. *Chem. Lett.* **1995**, *24*, 431.
[113] Arikawa, H.; Nishiguchi, H.; Ishihara, T.; Takita, Y. *Solid State Ionics* **2000**, *136–137*, 31.
[114] Pramana, S. S.; Klooster, W. T.; White, T. J. *Acta Crystallogr. B* **2007**, *63*, 597.
[115] Nakayama, S.; Kageyama, T.; Aono, H.; Sadaoka, Y. *J. Mater. Chem.* **1995**, *5*, 1801.
[116] Nakayama, S.; Higuchi, Y.; Kondo, Y.; Sakamoto, M. *Solid State Ionics* **2004**, *170*, 219.
[117] Tao, S.; Irvine, J. T. S. *Mater. Res. Bull.* **2001**, *36*, 1245.
[118] Kharton, V. V.; Shaula, A. L.; Patrakeev, M. V.; Waerenborgh, J. C.; Rojas, D. P.; Vyshatko, N. P.; Tsipis, E. V.; Yaremchenko, A. A.; Marques, F. M. B. *J. Electrochem. Soc.* **2004**, *151*, A1236.
[119] Shaula, A. L.; Kharton, V. V.; Marques, F. M. B. *J. Solid State Chem.* **2005**, *178*, 2050.
[120] Slater, P. R.; Sansom, J. E. H.; Tolchard, J. R. *Chem. Rec.* **2004**, *4*, 373.
[121] Slater, P. R.; Sansam, J. E. H. *Solid State Chemistry V*; Sajgalik, P., Drabik, M., Varga, S., Eds. **2003**, *90-91*, 195.
[122] Sansom, J. E. H.; Kendrick, E.; Tolchard, J. R.; Islam, M. S.; Slater, P. R. *J. Solid State Electr.* **2006**, *10*, 562.

[123] Nakayama, S.; Highchi, M. *J. Mater. Sci. Lett.* **2001**, *20*, 913.
[124] Nakayama, S.; Sakamoto, M.; Highchi, M.; Kodaira, K. *J. Mater. Sci. Lett.* **2000**, *19*, 91.
[125] Sansom, J. E. H.; Kendrick, E.; Tolchard, J. R.; Islam, M. S.; Slater, P. R. *J. Solid State Electr.* **2006**, *10*, 562.
[126] Najib, A.; Sansom, J. E. H.; Tolchard, J. R.; Slater, P. R.; Islam, M. S. *Dalton T.* **2004**, 3106.
[127] Pramana, S. S.; Klooster, W. T.; White, T. J. *J. Solid State Chem.* **2008**, *181*, 1717
[128] Kendrick, E.; Islam, M. S.; Slater, P. R. *Chem. Comm.* **2008**, 715.
[129] Kendrick, E.; Orera, A.; Slater, P. R. *J. Mater. Chem.* **2009**, *19*, 7955.
[130] Jones, A.; Slater, P. R.; Islam, M. S. *Chem. Mater.* **2008**, *20*, 5055.
[131] Kendrick, E.; Islam, M. S.; Slater, P. R. *J. Mater. Chem.* **2007**, *17*, 3104.
[132] Masubuchi, Y.; Higuchi, M; Takeda, T.; Kikkawa, S. *Solid State Ionics* **2006**, *177*, 263.
[133] Ali, R.; Yashima, M.; Matsushita, Y.; Yoshioka, H.; Okoyama, K.; Izumi, F. *Chem. Mater.***2008**, *20*, 5203.
[134] Bechade, E.; Masson, O.; Iwata, T.; Julien, I.; Fukuda, K.; Thomas, P.; Champion, E. *Chem. Mater.* **2009**, *21*, 2508.
[135] White, T. J.; Dong, Z. L. *Acta Crystallogr. Sect. B-Struct. Sci.* **2003**, *59*, 1.
[136] Lim, S. C.; Baikie, T.; Pramana, S. S.; Smith, R.; White, T. J. *J. Solid State Chem.* **2011**, *184*, 2978.
[137] Yoshioka, H.; Mitsui, T.; Mineshige, A.; Yazawa, T. *Solid State Ionics* **2010**, *181*, 1707.
[138] Yoshioka, H.; Nojiri, Y.; Tanase, S. *Solid State Ionics* **2008**, *179*, 2165.
[139] Nojiri, Y.; Tanase, S.; Iwasa, M.; Yoshioka, H.; Matsumura, Y.; Sakai, T. *J. Power Sources* **2010**, *195*, 4059.
[140] Mineshige, A.; Nakao, T.; Ohnishi, Y.; Sakamoto, R.; Daiko, Y.; Kobune, M.; Yazawa, T.; Yoshioka, H.; Fukutsuka, T.; Uchimoto, Y. *J. Electrochem. Soc.* **2010**, *157*, B1465.
[141] Marrero-Lopez, D.; Martin-Sedeno, M. C.; Pena-Martinez, J.; Ruiz-Morales, J. C.; Nunez, P.; Aranda, M. A. G.; Ramos-Barrado, J. R. *J. Power Sources* **2010**, *195*, 2496.

1.7 Bibliography

[1] O'Haure, R. P.; Cha, S.; Colella, W.; Prinz, F. B. *Fuel Cell Fundamentals*, Wiley, New York, **2006**

[2] Larminie, J.; Dicks, A. *Fuel Cell Systems Explained*, 2nd Edition, John Wiley & Sons, **2003**.

Chapter 2 Experimental Techniques

2.1 Solid State Reaction

Solid state reaction involves a direct reaction between two or more solids, generally at high temperature, for an extended period of time (typically above 800 °C and several days). It is one of the most widely used methods to prepare inorganic solid products due to its relatively simple procedure. Equation 2.1.1 shows an example of a solid state reaction for the preparation $Ba_2In_2O_5$.

$$2BaCO_3 + In_2O_3 \xrightarrow{1000\text{–}1400°C,72hrs} Ba_2In_2O_5 + 2CO_2 \uparrow \qquad (2.1.1)$$

One of the disadvantages of the method is that purification of the product is almost impossible, and thus the purity of the reactants and accurate weighing are crucial. It is easy to obtain high purity chemicals from suppliers nowadays but care must be taken to select the reactants to keep the stoichiometry right. Hygroscopic and air sensitive chemicals should be avoided or processed in a controlled atmosphere, as otherwise this can trigger an inaccurate ratio of reactants.

The formation of the products only occurs at the interface, the contact between the reactants. After the initial formation of the product, the reactants have to pass through the initial product, which becomes a barrier for the contact between reactants. The diffusion of the reactants involves hopping of a reactive species through the interfacial region. The point defects (vacancy and interstitial) in the product phase help this hopping process. However, as the product layer grows, the length of the diffusion path increases and this reduces the rate of diffusion and subsequently the rate of reaction. This is one of the reasons for the requirement of a high reaction temperature, in order to increase the diffusion rate so as to promote the reaction. The particle size of the reactant is also important as diffusion through smaller size particles is easier and their high surface area to volume ratio makes them more reactive.

Intermediate grinding is usually applied to break up the product interface phase and to introduce fresh reaction sites. Pressing a sample into a pellet is another way to increase the contact between the reactants.

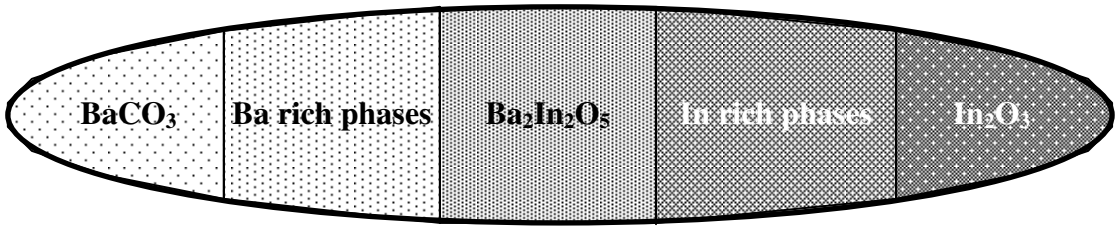

Fig. 2.1.1 The formation of a mixture of products during the initial stage of a solid state reaction between $BaCO_3$ and In_2O_3.

Even after the repeated intermediate grinding between the heating stages, it is common that the product is actually the mixture of two or more phases, if reaction is slow. In the case of alkaline earth containing systems, it is common to start with the carbonate rather than the oxide. These carbonates are more stable at room temperature compared to their hygroscopic or CO_2 sensitive oxide analogues. The decomposition of these carbonates produces an atomic scale reactant with high mobility and reactivity to overcome the build up of side products. Hence $BaCO_3$ is used for the synthesis of $Ba_2In_2O_5$ rather than BaO as shown in equation 2.1.1.

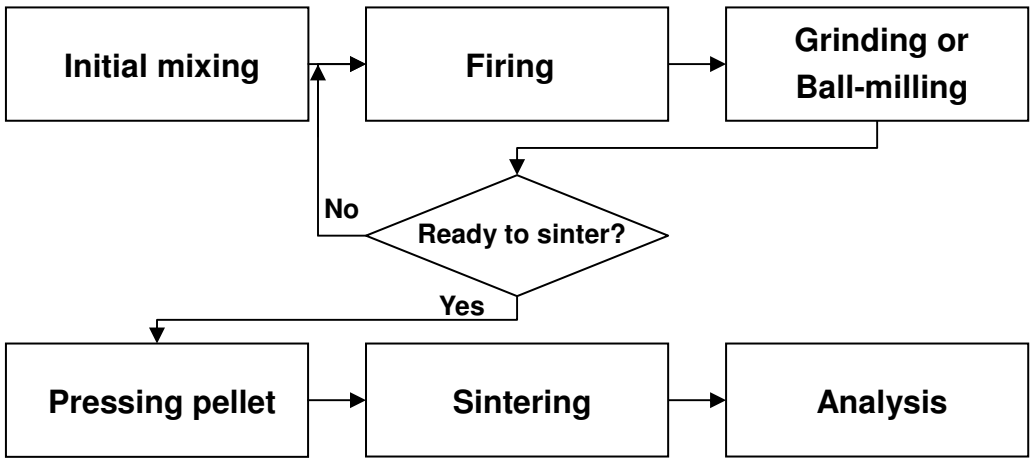

Fig. 2.1.2 Schematic of synthesis procedure.

Although the condition for the complete reaction may be met, high reaction temperatures may promote evaporation of reactants such as Ba. This is a common obstacle for the preparation of a product containing volatile elements through high temperature synthesis. The use of a sealed vessel may be beneficial to avoid evaporation of a volatile substance but this is not always possible owing to the high reaction temperature. Pressing a sample into a pellet may limit the evaporation by sacrificing the surface layer which forms a protective layer, hence preventing the diffusion of volatile substance into the atmosphere. The use of excess reactant is another common practice to balance the reaction stoichiometry. For the synthesis of $Ba_2In_2O_5$, 3% excess Ba is employed to overcome Ba loss and the sample fired at 1000 °C was pelletised and covered with sacrificial powder, and then placed in an alumina crucible, which was covered with a lid. Even after all these procedures, the surface of the pellet contained a Ba deficient phase which was removed by using sand paper.

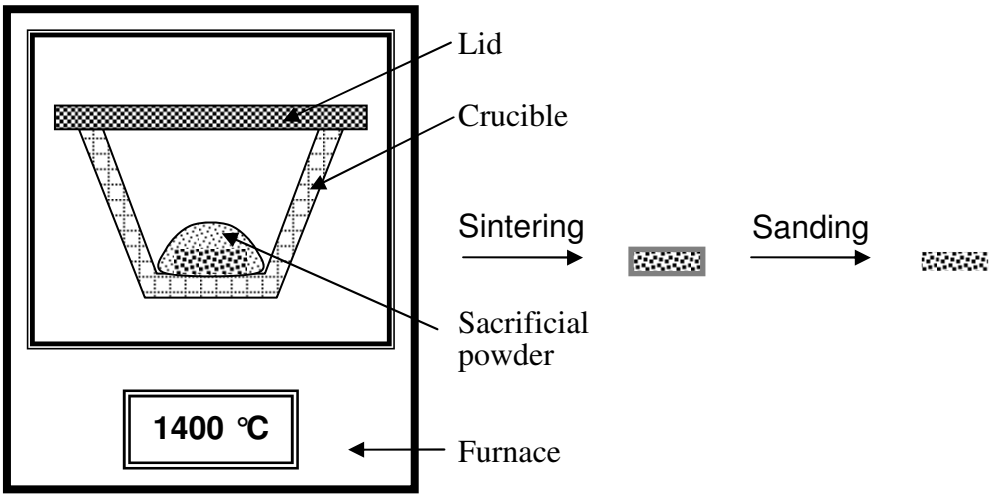

Fig. 2.1.2 The procedure employed to prevent Ba loss.

2.1.1 Fluorination Using Polytetrafluoroethylene

The vast majority of literature studies in the solid state chemistry area have focussed on oxide systems. However, the discovery of the superconducting oxide fluoride, $Sr_2CuO_2F_{2+\delta}$ triggered many studies on the fluorination of perovskite-type oxides such as $La_{2-x}A_xCuO_4$ (A: alkaline earth), Sr_2TiO_4, $BaFeO_{3-x}$, etc. [1]. Such compounds are prepared by low temperature (< 400 °C) fluorination of an oxide precursor: e.g. Sr_2CuO_3 in F_2 gas to give $Sr_2CuO_2F_{2+\delta}$ [1]. This low temperature route is required due to the high thermodynamic stability of the simple fluorides such as SrF_2. Thus heat treatment of $Sr_2CuO_2F_{2+\delta}$ above 400 °C leads to decomposition to SrF_2 and $SrCuO_2$ [1]. In these low temperature fluorination studies, a wide range of fluorinating reagents have been utilised, but each exhibited various problems as listed in Table 2.1.1 [2, 3]. As an alternative method, an organic fluorine containing compound, polyvinylidene fluoride (PVDF) or polytetrafluoroethylene (PTFE) have been tested and shown to result in high quality samples without impurities for many perovskite-related systems [2].

In prior studies, it has been shown that the high temperature synthesis of $BaScO_2F$ is possible using BaF_2, but this can not be applied to the synthesis of $BaInO_2F$ owing to the higher thermodynamic stability of the alternative products BaF_2 and $BaIn_2O_4$, compared to $BaInO_2F$ [4]. Thus, in this project, a low temperature route utilising PTFE was employed to investigate whether $BaInO_2F$ could indeed be prepared. PTFE is mixed with the oxides and heated to 350 °C for 12 h, and then ground and reheated to 350 °C for 12 h. This fluorination strategy was also examined for oxyanion doped phases to determine whether it was possible to increase the coordination number of the central atom of the oxyanion.

Table 2.1.1 Characteristics and problems of various low-temperature fluorinating agents for inorganic oxide systems. Reprinted with permission from [2].

Fluorinating agent	Characteristics	Problems
F_2 gas [1, 5-8]	Highly oxidising: helps favour fluorine insertion giving very high oxidation states	Toxicity, handling problems of F_2 gas: difficult to control fluorination level
NH_4F [3, 6, 9-11]	Substitution (two fluorine for one oxygen), so oxidation state maintained: can potentially give reduced oxidation state (e.g. $Nd_2CuO_{4-x}F_x$)	Tendency to give AF_2, LnOF (A: alkaline earth, Ln: rare earth) impurities
XeF_2 [12, 13]	Can give both fluorine substitution and insertion	Need to employ in sealed tubes and will tend to give similar impurities as for NH_4F
CaF_2, ZnF_2 [10, 14, 15]	Can give both fluorine substitution and insertion	Negligible AF_2, LnOF impurities formed, but CuO and ZnO from the fluorinating agent left in the sample

2.2 Powder Diffraction

Powder diffraction techniques using X-ray, neutron and electron are some of the fundamental characterisation methods to study the crystal structure of materials. They are non-destructive and provide information such as phase identity, lattice parameters, and structural solution, *etc.*

2.2.1 Scattering

Scattering is an interaction between a wave and an object that accompanies the change in propagation direction (elastic scattering) and/or energy (inelastic scattering) of the wave. Thus, reflections in diffraction experiments can be treated as a special case of scattering. Generally, when a wave is scattered by a point object, it propagates radially and when there are more than two such objects stationed at regular interval with comparable separation to the wavelength of the incident wave, diffraction occurs (e.g. double slit interference and diffraction grating). The diffracted waves propagate and interfere with each other to make a characteristic pattern on a screen in the form of the combination of maxima (where the intensity is the greatest) and minima (where the intensity is the lowest or zero).

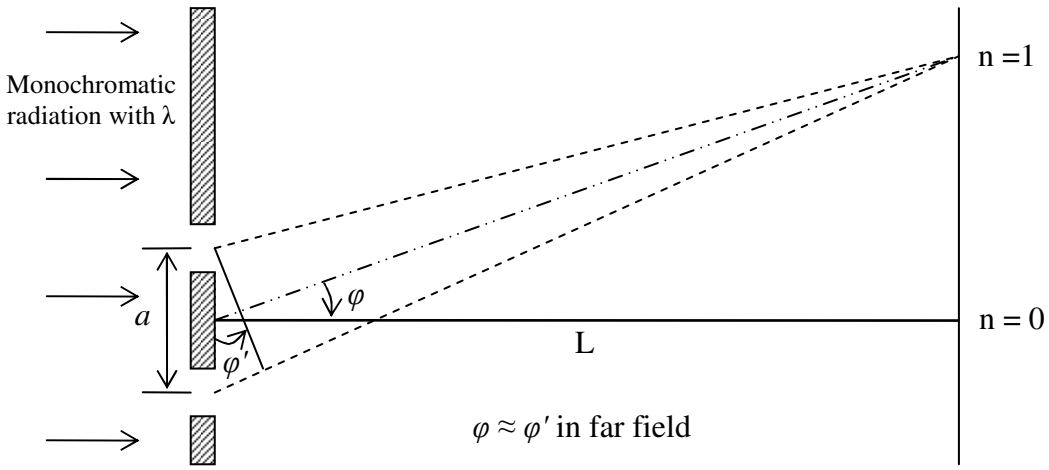

Fig. 2.2.1 Double slit experiment under the Fraunhofer approximation

The Fraunhofer approximation states that two diffracted waves arriving at the same point on the screen can be treated as parallel to each other when the screen is far enough from the diffraction source (far field, the quantities involved are in shown in Fig. 2.2.1) [16]:

$$\frac{a^2}{L\lambda} << 1 \qquad (2.2.1)$$

Under the approximation, the prediction of maxima is much simplified that only consideration of the length of the path difference is required. To make the constructive interference of two diffracted waves, they have to be in phase which means the path difference has to be the integer multiple of wavelength,

$$a \sin \varphi = n\lambda \qquad (2.2.2)$$

The Bragg equation is a simplified form of three dimensional theory of diffraction (Laue equations) that considers the diffracted radiation as reflection by sets of parallel planes of atoms [17, 18].

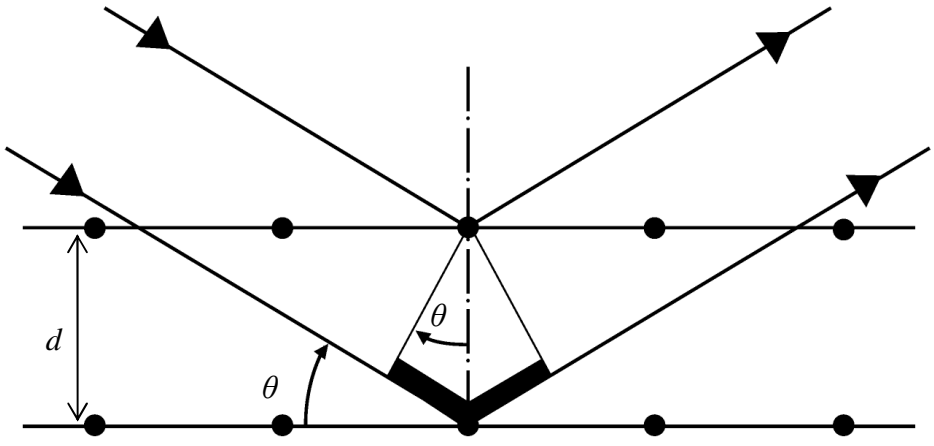

Fig. 2.2.2 Bragg reflection by the consecutive parallel planes

As shown for the Fraunhofer diffraction, the path difference is an integer multiple of wavelength to form a maxima (Bragg reflection),

$$2d \sin \theta = n\lambda \qquad (2.2.3)$$

The parallel planes of atoms in a unit cell are described using Miller indices (*hkl*) which is the notation of the reciprocal lattice vector (Fig.2.2.3) and the spacing between the planes can be worked out using the *hkl* values and the lattice parameters (*a,b* and *c*) [19]:

$$d_{hkl} = \left[\frac{h^2}{a^2} + \frac{k^2}{b^2} + \frac{l^2}{c^2} \right]^{-\frac{1}{2}} \quad \text{for an orthorhombic cell,}$$

$$d_{hkl} = \left[\frac{4}{3a^2} \left(\frac{h^2 + hk + k^2}{a^2} \right) + \frac{l^2}{c^2} \right]^{-\frac{1}{2}} \quad \text{for an hexagonal cell.}$$

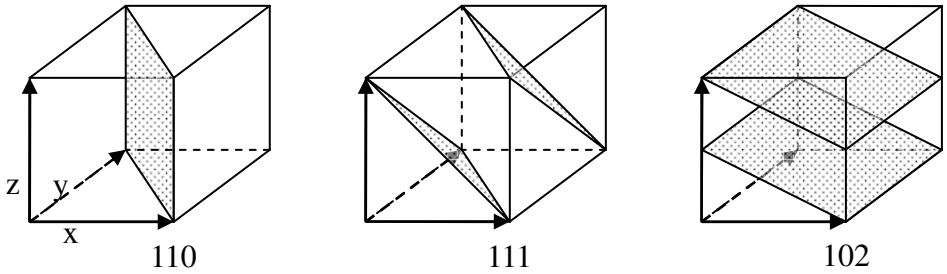

Fig. 2.2.3 Examples of lattice planes with the corresponding Miller indices.

For a powder sample, a great number of crystallites are distributed in a random fashion. Thus, high energy radiation penetrating deep inside the sample encounters a large number of crystallites oriented in every possible way to produce the diffraction from all the sets of planes simultaneously: this only leaves sharp diffraction peaks. However, the interaction between the radiation and crystallites are complex and complicated. Hence, it is also assumed that the radiation entering a crystal is only scattered once and leaves the crystal, and thus the scattered radiation does not interact again with other crystallites. This is called Kinematic diffraction and it is simple, accurate and adequate for general use [20].

Diffraction only occurs when the wavelength and the separation are of the same order of magnitude. As the inter-atomic distance in solids is usually in the range of 0.5-2.5 Å, the X-

ray region of electromagnetic radiation and neutrons and electrons with suitable velocities can be used for the radiation. X-rays are scattered by electrons, hence not by atomic centre (nuclei) but by electron density distributed in the crystal structure. On the other hand, neutrons are scattered by the nuclei. Thus, in the ideal case, the diffraction of a sample using X-rays and neutrons having identical wavelength will produce the same pattern with the only difference in the intensities of the peaks.

The scattering of X-rays by an electron is in all directions but because of the presence of an electric field due to the motion of the electron, the intensity is angle dependent and it is given by the Thomson equation [21],

$$I = I_0 \frac{K}{r^2}\left(\frac{1+\cos^2 2\theta}{2}\right) \qquad (2.2.4)$$

where I_0 is the absolute intensity of the incident radiation, K is a constant ($K = (e^4)/m^2c^2$ = 7.94 x 10^{-30} m^2), r is the distance between the electron and the detector and θ is the Bragg angle. The scattering power of an atom is the product of the number of electrons in the atom and the intensity of scattering of an electron. Thus the intensity of the diffraction peaks is dominated by the atoms with greater number of electrons.

Unlike X-rays, neutrons are scattered by the nuclei, which are much smaller than atoms. Thus the scattering intensity is angle and atomic number independent and varies with each isotope. In addition, because a neutron has a spin, it interacts with the magnetic moment of the atom. Thus neutron diffraction can be used to study magnetic ordering.

In the constant wavelength method, neutrons with desired wavelength (energy) are selected and used for the diffraction study. On the other hand, in the time of flight (TOF) method which can be used with spallation sources, the wavelength of the neutrons is calculated from the de Broglie relation [22]:

$$\lambda = \frac{h}{p} = \frac{h(t+t_0)}{m_n(L+L_0)} \qquad (2.2.5)$$

where, h is the Plank constant, p is the momentum of a neutron, t is the time taken to travel from the target to the detector, m_n is the mass of a neutron, L is the path length and t_0 and L_0 are experimentally determined offsets. The TOF method maximises the use of the available neutron flux.

2.2.2 Structure Solution

Crystal structure determination from powder diffraction data is complicated because the pattern is only a one-dimensional projection of three-dimensional reciprocal space. The first step is indexing the Bragg peaks, which has intrinsic difficulties due to:

- inaccurate peak position (zero-point error, low resolution, sample misplacement, poor crystallinity);
- presence of impurities (presence of additional peaks);
- the case of dominant zone (when b is much smaller than a,c the early peaks are dominated by h0l peaks).

The indexing of the peaks is usually aided by software such as *WinPLOTR* integrated - *TREOR, DICVOL* or *Macllile* [23]. These programmes suggest the possible symmetry, lattice parameters and space group with FoMs (figure-of-merit) and the user has to make a decision from his/her understanding of the sample.

The next step is the structure refinement which determines fractional atomic coordinates, occupancies and atomic displacement parameters. In classical methods, the intensities of Bragg peaks are converted into the observed structure factor amplitudes (F^o_{hkl}), which are related to the electron densities (ρ) (for X-ray diffraction) distributed in the unit cell,

$$\rho_{xyz} = \frac{1}{V}\sum_{h=-\infty}^{h=+\infty}\sum_{k=-\infty}^{k=+\infty}\sum_{l=-\infty}^{l=+\infty}\left|F^o_{hkl}\right|\cos\left[2\pi(hx+ky+lz)-\alpha_{hkl}\right] \qquad (2.2.6)$$

where V is the unit cell volume and α is the phase angle of the diffraction reflection (hkl). The quality of the fitting using non-linear least-square techniques is monitored by the weighted R-factor,

$$\sum_{hkl} w_{hkl} \left(\left| F^{o}_{hkl} \right| - k \left| F^{c}_{hkl} \right| \right)^2 \qquad (2.2.7)$$

where the weight of the reflection, $w_{hkl} = 1/\sigma_{hkl}^2(F^o_{hkl})$ ($\sigma_{hkl}^2(F^o_{hkl})$ is the square of the statistical spread of F^o_{hkl}), F^c_{hkl} is the calculated structure factor and k is a scale factor. However, powder diffraction data does not have a three-dimensional set of peaks (like diffraction data from a single crystal) but rather a one-dimensional pattern, which inevitably contains many overlapping diffraction peaks. Thus, the accurate determination of the structure factor is difficult in many cases.

To overcome these issues, the Rietveld method is used. This method uses the individual data points in a powder diffraction pattern as least-square quantities and the intensity of the overlapping peaks are partitioned according to the intensities calculated by a starting structural model [24]. Obviously, the intensity of a point in the powder diffraction data is much easier to measure than the structure factor amplitude. However, many parameters such as absorption, preferred orientation, multiplicity and profile shape function influence the intensity, and many of them are correlated to each other. Nevertheless, this method can accommodate a reasonable amount of non-idealities frequently encountered in real data collection in a physically meaningful way [25].

The quality of the fitting requires various considerations including statistical, graphical and chemical. There are several statistical quantities starting from the unweighted profile R-factor,

$$R_p = \frac{\sum_i \left| y_{oi} - y_{ci} \right|}{\sum_i y_{oi}} \qquad (2.2.8)$$

where y_{oi} is the observed intensity of the point and y_{ci} is the calculated intensity using the

model. The weighted profile R-factor takes the consideration of the spread of the observed point as weight of the point, $w_i = 1/\sigma^2(y_{oi})$,

$$R_{wp} = \left[\frac{\sum_i w_i (y_{oi} - y_{ci})^2}{\sum_i w_i y_{oi}^2} \right]^{\frac{1}{2}} \qquad (2.2.9)$$

The best possible R_{wp} can be obtained when the mean value of $(y_{oi}-y_{ci})^2$ is $\sigma^2(y_{oi})$. This is called the expected R-factor and with N number of data points and P number of least-square variables (parameters),

$$R_{\exp} = \left[\frac{N-P}{\sum_i w_i y_{oi}^2} \right]^{\frac{1}{2}} \qquad (2.2.10)$$

Then the goodness of fit is given by:

$$\chi^2 = \frac{1}{N-P} \sum_i \frac{(y_{oi} - y_{ci})^2}{\sigma^2(y_{oi})} = \left(\frac{R_{wp}}{R_{\exp}} \right)^2 \qquad (2.2.11)$$

This is large at the beginning of the refinement and reduced to closer 1 at convergence. However, care must be taken in using the goodness of fit parameter, since if the errors of measurement are too great (low quality diffraction data), the $\sigma^2(y_{oi})$ term would be too big, thus χ^2 can be close to 1 even for a relatively poor refinement, due to the dominant effect of errors on the statistical quantity. Therefore, it is important to consider not only such statistical data but also graphical representations such as observed, calculated and difference plots to see the quality of the refinement.

Another quantity that can be derived from the refined data and used to validate the crystal structure is the bond valence calculation. The bond valence, s between the atoms i and j with the bond length of r_{ij} is given by:

$$s_{ij} = \exp\left[\frac{\left(r_0 - r_{ij}\right)}{B}\right] \qquad (2.2.12)$$

where r_0 and B are empirically determined parameters, which can be obtained from various publications [26]. Thus the sum of all the bond valences of an atom i indicate the overall valence state of the atom and this can be compared with that expected.

The limitation of such structure refinement is the fact that the diffraction data is fitted to a model, and thus the fitting is only good if the model is appropriate and data are of high quality. Because the model is generally assumed to be crystalline with long-range atomic ordering, the presence of stacking faults, defects or local structural deviations are excluded. This is a problem for the characterisation of amorphous materials or nanomaterials, where the local structure dominates. Diffraction will still occur in such samples, but they produce broad diffraction features which lack sharp Bragg peaks. The analysis of such data is still possible utilising total scattering analysis techniques based on the pair distribution function, which takes into consideration all points of the powder diffraction pattern as a continuous diffraction pattern instead of the discreet Bragg peaks [27]. In such studies, the emphasis is on the distribution of interatomic vectors. Thus, this is a complementary technique to the powder diffraction pattern analysis based on discrete Bragg peaks and can provide information such as local distortions in the structure. However, data quality is even more important in such studies, as every single data point is used and also both random and systematic errors can be significant.

2.2.3 Instrumentation

Two Brüker D8 Advance diffractometers with Cu $K_{\alpha 1}$ radiation (1.5406 Å) were utilised in experiments. For the general X-ray diffraction data collection, the instrument with transmission geometry, equipped with an autosampler was used, and for the high temperature

X-ray diffraction data collection, the instrument with reflection geometry equipped with a heating stage, which surrounds the sample holder, was used.

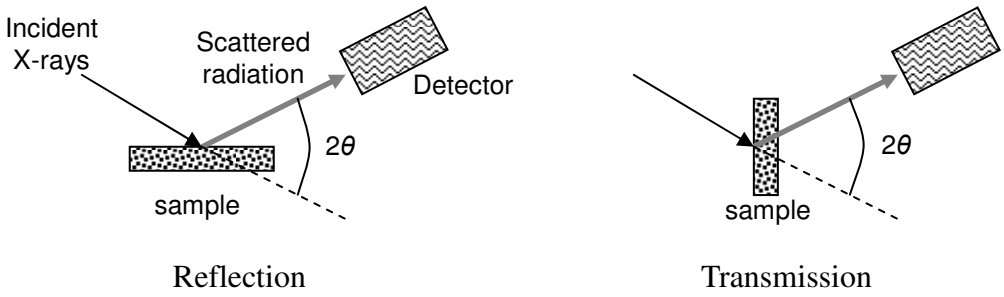

Fig. 2.2.4 Two different geometries for the data collection .

Two instruments were used to collect neutron diffraction data: diffractometer HRPD (High resolution powder diffraction) at the ISIS facility, Rutherford Appleton Laboratory, with data analysed using the time of flight method [28] and diffractometer HRPT (High resolution powder diffractometer for thermal neutrons) at the SINQ, Paul Scherrer Institut using neutrons with constant wavelength of 1.1551 Å [29].

All structural refinements employed the GSAS (General structure analysis system) suite of Rietveld refinement software, which contains a set of programmes for the processing and analysis of X-ray and neutron diffraction data [30].

2.3 Raman Spectroscopy

Raman spectroscopy is a technique used to study the vibrational modes in a sample, and thus the chemical nature of a sample, such as type and strength of bonding.

2.3.1 Raman Scattering

A stretching of a diatomic molecule can be easily viewed as an oscillating spring. Thus a vibration of a bond in a molecule can be modelled as a spring. In classical physics, a spring behaves as a simple harmonic oscillator and it obeys Hooke's law,

$$F = -kx \tag{2.3.1}$$

where F is the restoring force, x is the displacement and k is the spring constant. The angular frequency of the oscillation, ω is defined as:

$$\omega = \left(\frac{k}{\mu_{eff}} \right)^{\frac{1}{2}} \tag{2.3.2}$$

where μ_{eff} is effective mass of the system. For a diatomic system with masses m_A and m_B:

$$\mu_{eff} = \frac{m_A m_B}{m_A + m_B} \tag{2.3.3}$$

Quantum mechanics states that a motion of a molecule has a discrete energy level and the solution of the quantum harmonic oscillator (the analogue to simple harmonic oscillator) gives the energy of the motion at an energy level of n,

$$E_n = \left(n + \frac{1}{2} \right) \hbar \omega \tag{2.3.4}$$

where $\hbar$ is the reduced Plank constant ($h/2\pi$). Therefore, the vibrational energies are greater with stiff bonds (large k) and systems having low effective masses. The energies are usually expressed in terms of wavenumber,

$$\bar{\nu} = \frac{1}{\lambda} = \frac{\nu}{c} = \frac{\omega}{2\pi c} \tag{2.3.5}$$

where λ is a wavelength and c is the speed of light in vacuum.

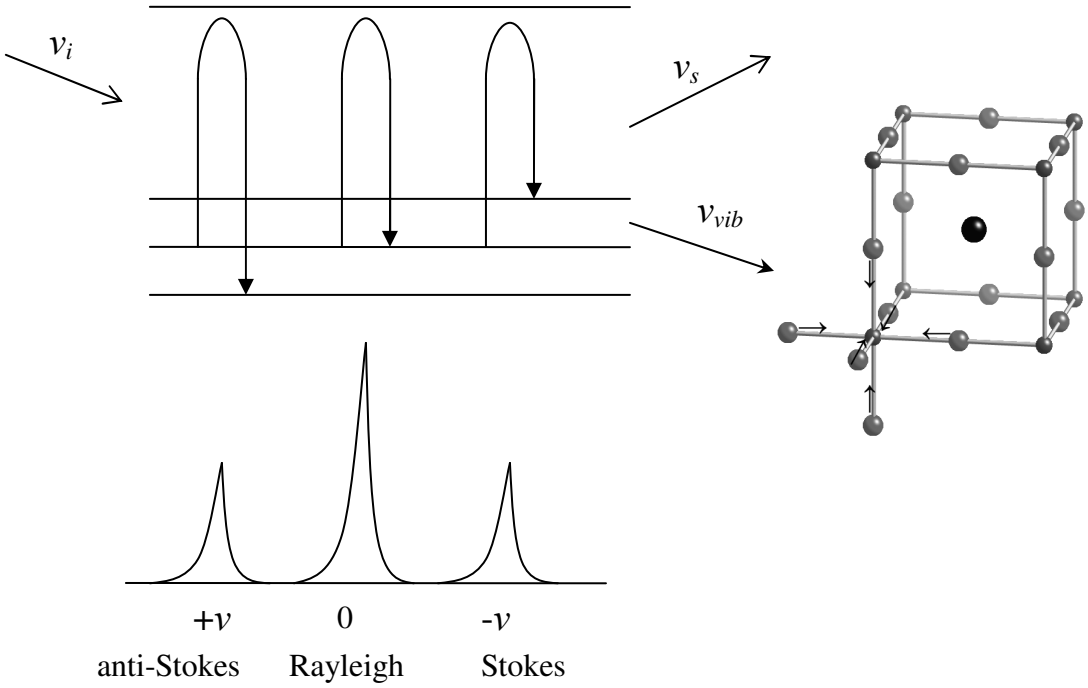

Fig. 2.3.1 Phonon energy level transitions and corresponding scattering frequency changes.

Photons are not only absorbed or emitted but can also be scattered by matter and the intensity, I of such scattering by a molecule is given by:

$$I = I_0 \frac{8\pi^4 N\alpha^2}{\lambda^4 R^2}(1+\cos^2\theta) \qquad (2.3.6)$$

I_0 is the incident intensity, N is the number of scatterers, R is the distance between scatterer and observer and α is the polarizability [31]. Polarizability is a tendency of a molecule to have a dipole moment, μ in an applied field, E and for an oscillating field: E can be expressed with a cosine function:

$$\mu = \alpha E = \alpha E_0 \cos(2\pi\nu t) \qquad (2.3.7)$$

For the stretching of the bond in a diatomic molecule, assuming simple harmonic motion, the inter-atomic distance q_{vib} is

$$q_{vib} = q_0 cos(2\pi\nu_{vib} t) \qquad (2.3.8)$$

The polarizability during the vibration can be expressed using a Taylor series in terms of the coordination change due to the vibration:

$$\alpha = \alpha_0 + \left(\frac{d\alpha}{dq}\right)_0 q_{vib} + ...$$

$$\approx \alpha_0 + \left(\frac{d\alpha}{dq}\right)_0 q_0 \cos(2\pi\nu_{vib}t) \qquad (2.3.9)$$

Combining equation 2.3.7 and equation 2.3.9 gives:

$$\mu = E_0\alpha_0 \cos(2\pi\nu_0 t) + E_0\left(\frac{d\alpha}{dq}\right)_0 q_0 \cos(2\pi\nu_0 t)\cos(2\pi\nu_{vib}t) \qquad (2.3.10)$$

$$= E_0\alpha_0 \cos(2\pi\nu_0 t) + E_0\left(\frac{d\alpha}{dq}\right)_0 q_0 \frac{1}{2}\{\cos[2\pi(\nu_0 - \nu_{vib})t)] + \cos[2\pi(\nu_0 + \nu_{vib})t)]\}$$

The first term describes Rayleigh scattering where the scattered photons have identical energy to the incident photons. The second term is Raman scattering and here there is an energy change either $\nu_0 - \nu_{vib}$ (Stokes) or $\nu_0 + \nu_{vib}$ (anti-Stokes). (Fig. 2.3.1) Most importantly, the second term also contain the gross selection rule for Raman scattering, the change in polarizability, $\left(\frac{d\alpha}{dq}\right)_0 \neq 0$. Hence, only vibrational modes with a change in polarizability are Raman active. For a simple molecule such as CO_2, the prediction of a Raman active mode can be achieved using the irreducible representation in the character table of its point group.

The vibrational modes in the lattice are also quantised and are called phonons. There are two type of phonons, acoustic and optical. Atoms in the lattice vibrate in phase for acoustic vibration and out of phase in optical vibration. The quantum mechanical solution for their phonon energies as a function of wave vector, k, is presented in Fig. 2.3.2.

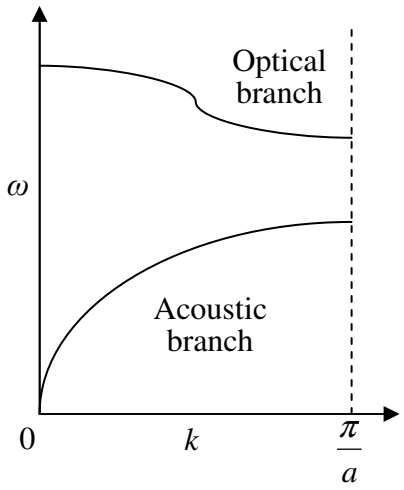

Fig. 2.3.2 Angular frequency corresponding to phonons in first Brillouin zone [32].

As Raman scattering follows the rules of conservation of momentum and energy, and because photons of visible light have wavenumber of ≈ 10^5 cm^{-1}, only phonons with similar scale can be involved in Raman scattering. This leaves the optical phonons at Brillouin zone centre (typical cubic cell wavenumber from centre to boundary is $\pi/a \approx 10^7$ cm^{-1}), because acoustic phonons near the Brillouin zone centre have nearly zero energy (Fig. 2.3.2). Therefore, only optical phonons are involved in the first order (involving single phonon) Raman scattering, and activities for normal modes can be predicted by using only the point group of the space group and the Wyckoff position of atoms. For example, nuclear site group analysis predicts that the orthorhombic and tetragonal $Ba_2In_2O_5$ should show 30 and 36 Raman active normal modes respectively (Table 2.3.1 and 2) while cubic $Ba_2In_2O_5$ should show none [33]. Hence, there should not be any Raman activity for any samples isostructural to cubic $Ba_2In_2O_5$ with the exception of weak second order Raman effect (two phonon processes) [34, 35].

Table 2.3.1 The Raman mode symmetry in orthorhombic (*Icmm* (74) space group) $Ba_2In_2O_5$ as determined from nuclear site group analysis [33]

Atom	Wyckoff position	Raman mode symmetry
Ba	8h	$2A_g + B_{1g} + B_{2g} + 2B_{3g}$
In(1)	4a	not Raman active
In(2)	8i	$2A_g + B_{1g} + 2B_{2g} + B_{3g}$
O(1)	8g	$A_g + 2B_{1g} + B_{2g} + 2B_{3g}$
O(2)	8h	$2A_g + B_{1g} + B_{2g} + 2B_{3g}$
O(3)	8i	$2A_g + B_{1g} + 2B_{2g} + B_{3g}$

Table 2.3.2 The Raman mode symmetry in tetragonal (*I4cm* (108) space group) $Ba_2In_2O_5$ as determined from nuclear site group analysis [33]

Atom	Wyckoff position	Raman mode symmetry
Ba(1)	4b	$A_1 + B_2 + 2E$
Ba(2)	4b	$A_1 + B_2 + 2E$
In(1)	4a	$A_1 + 2E$
In(2)	4a	$A_1 + 2E$
O(1)	8c	$2A_1 + B_1 + 2B_2 + 3E$
O(2a)	4a	$A_1 + 2E$
O(2b)	4a	$A_1 + 2E$
O(3)	8c	$2A_1 + B_1 + 2B_2 + 3E$

2.3.2 Instrumentation

The instrument used in this study was a Renishaw inVia Raman microscope with excitation using a Cobolt Samba CW 532 nm DPSS Laser, and its schematic is given in Fig. 2.3.3. Powder samples are placed on a glass plate. The samples were exposed to monochromatic electromagnetic radiation with wave length of 532 nm and intensities of back-scattered waves are detected with CCD. A notch filter is used to remove the intensity arising from elastic scattering. The technique was mostly employed to confirm the presence of oxyanion groups (phosphate, silicate, carbonate, *etc*) in the structures.

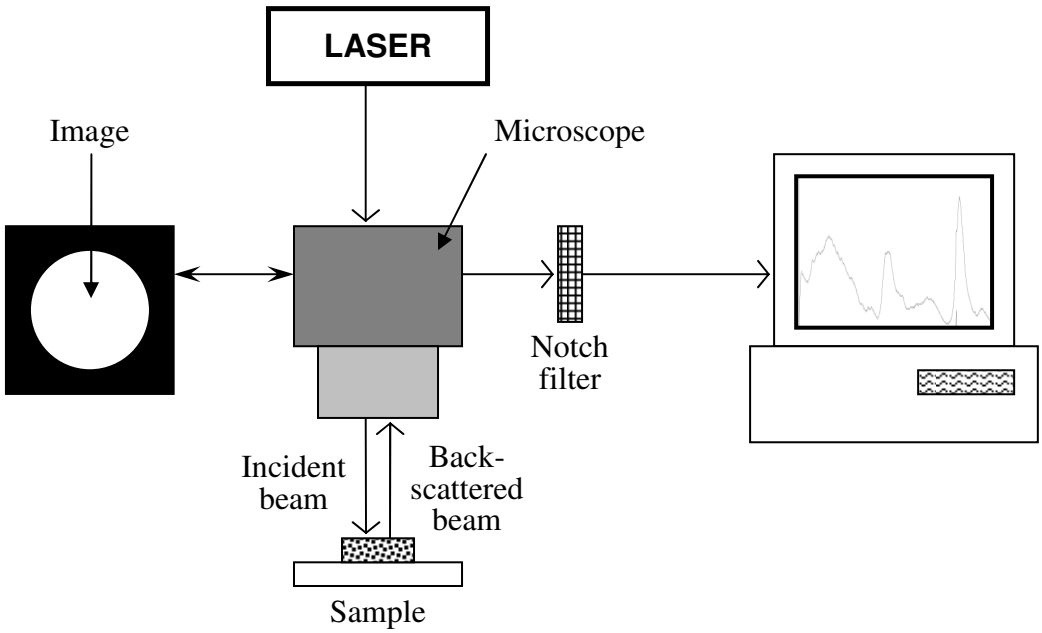

Fig. 2.3.3 Schematic diagram of a Raman microscope.

2.4 Solid State NMR Spectroscopy

Solid state NMR spectroscopy is a technique for the characterisation of solid materials, especially the local chemical environments.

2.4.1 Net Magnetisation

The magnetic moment, μ_i of a nucleus of an atom is given by:

$$\mu_i = \gamma J_i \tag{2.4.1}$$

where γ is the gyromagnetic ratio, which is a constant for a specific nucleus and J_i is its angular momentum. The net magnetisation, M, by the same type of nuclei is the sum of all of the magnetic moments of individual nuclei (vectorial sum):

$$\mathrm{M} = \sum_i \mu_i = \gamma J \tag{2.4.2}$$

where J is the total angular momentum. Torque is a rate of change in angular momentum, and for the nuclei placed in a uniform external magnetic field, B, it is given by:

$$T = \frac{d}{dt} J = \mathrm{B} \times \mathrm{M} \tag{2.4.3}$$

Combining equation 2.4.2 and 2.4.3 gives:

$$\frac{d}{dt}\mathrm{M} = \gamma \frac{d}{dt} J = \gamma \mathrm{B} \times \mathrm{M} \tag{2.4.4}$$

This relationship predicts that M precesses about a fixed field B, at a constant angular frequency, $\omega = \gamma \mathrm{B}$. Therefore, in an NMR experiment, the magnetisation precesses about the applied magnetic field B_0 (usually along z axis) with tilting in the Larmor frequency, ω_0:

$$\omega_0 = \gamma \mathrm{B}_0 \tag{2.4.5}$$

The z component of the angular momentum of a nucleus is quantised and its values are given by:

$$J_z = m_s \frac{h}{2\pi} = m_s \hbar \tag{2.4.6}$$

where m_s is the magnetic quantum number and has values of -I, -I+1,...0..I-1, I, where I is the spin quantum number. The potential energy of the two states is given by:

$$E_{pot} = \mu_z \mathrm{B} = \gamma \hbar \mathrm{B} \tag{2.4.7}$$

The energy difference between two quantised states of nucleus having spin number 1/2 is:

$$\Delta E_{pot} = \mu_z \mathrm{B} = \gamma \left[\frac{1}{2_s} \hbar - \left(-\frac{1}{2_s} \hbar \right) \right] \mathrm{B} = \gamma \hbar \mathrm{B} \tag{2.4.8}$$

2.4.2 Resonance

In the case of a sample with only identical nuclei, all the nuclei precess about the z-axis under the applied field B_0 in a random distribution, and thus the net magnetic moment is along the z axis. When electromagnetic radiation, B_1 (generally in the region of radio frequency, hence called rf pulse) is applied along the x-axis, there is a change in the external magnetic field. However, when the ω of the rf pulse is identical to the Larmor frequency, ω_0, the energy is transferred to induce a flip in the energy state of some nuclei (from ground state to exited state) and the individual magnetisation vector becomes coherent (Fig. 2.4.1.b). When the rf pulse is turned off, the magnetisation vector goes back to the state as described in Fig. 2.4.1.a and this relaxation of the magnetisation vector follows the trajectory in Fig. 2.4.1.c. The electromagnetic induction caused by this movement of the magnetisation vector is recorded to a receiver and analysed (Fig. 2.4.1.d).

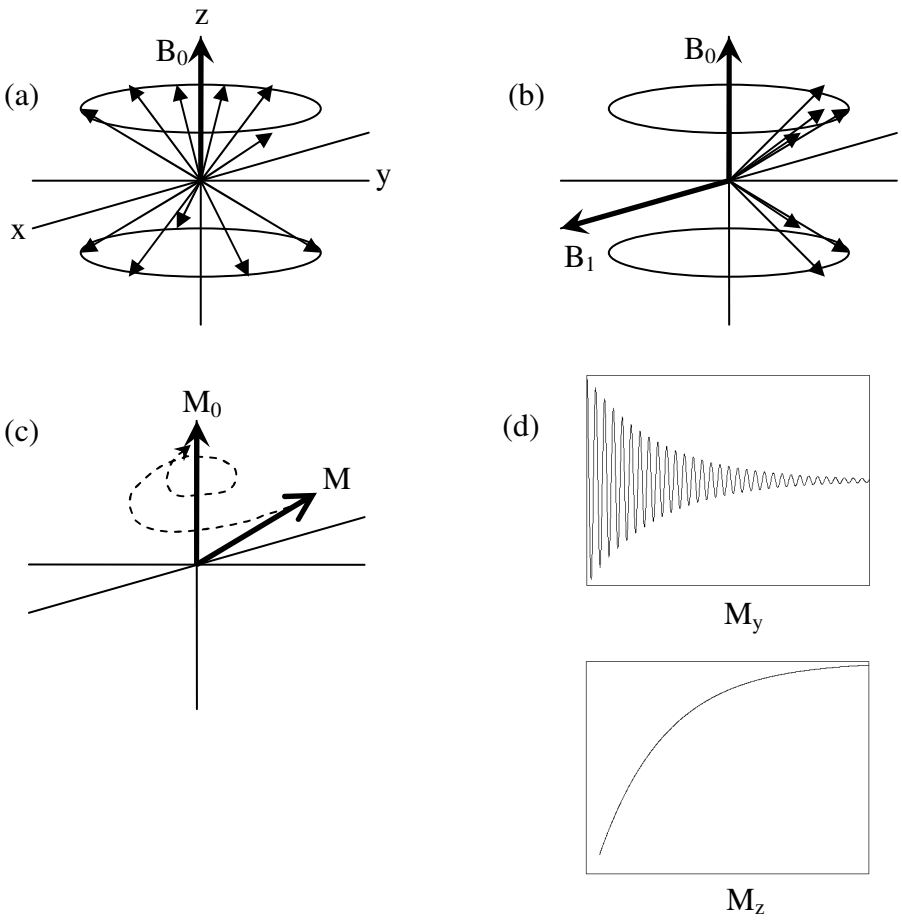

Fig. 2.4.1 Individual magnetic moments (a) under B_0 (b) with addition of B_1. (c) The relaxation of magnetisation vector and (d) corresponding electromagnetic signals along y and z axes [36].

However, in a real sample, B_0 experienced by a nucleus is altered by the electronic environment around it. This is called diamagnetic shielding and its strength, σ influences the effective magnetic field, B_{eff}:

$$B_{eff} = (1-\sigma)B_0 \qquad (2.4.9)$$

Thus, identical nuclei with different chemical environments have different ω_0. Consequently, to induce the magnetic resonance for all the nuclei, rf pulses covering a wide range of ω are applied in a very short time interval. The relaxation of all the magnetisation vectors for the

nuclei with different environments precess at different frequencies, and thus the electromagnetic signal recorded to the receiver is the sum of all the signals produced by the nuclei. This complex time domain signal can be simplified to frequency domain data through a Fourier transformation (Fig. 2.4.2).

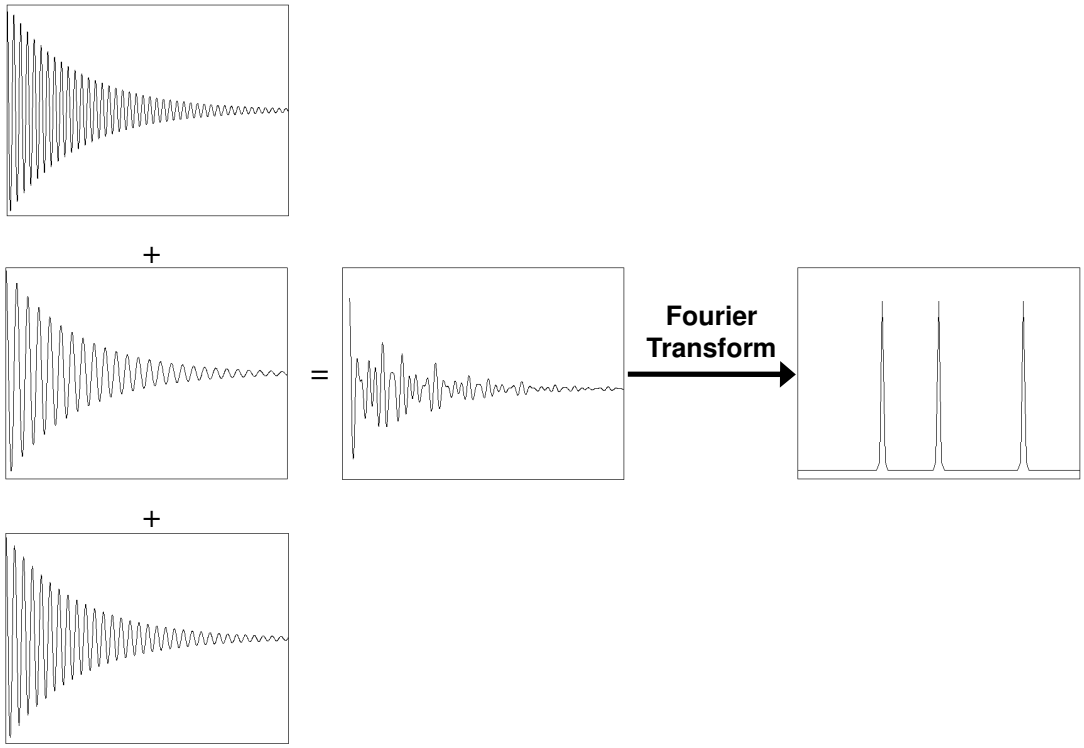

Fig. 2.4.2 Superposition of time domain signals from three nuclei with different ω_0 and the frequency domain signal obtained by Fourier transform [36].

2.4.3 Solid State NMR

Conventional NMR data collected from crystalline solids produces excessively broad lines due to the lack of random orientation of nuclei. The broad lines are caused by chemical shift anisotropy and asymmetry, which give a variation in signals rather than a single sharp line. In addition, dipolar coupling, which averages to zero in solution, results in line splitting in crystalline solid samples.

Spinning of the sample at a angle of 54.74°, so called magic angle spinning (MAS) eliminates this broadening as both features contains the term ($3\cos^2\theta$-1), which becomes zero when θ is 54.74° related to B_0. However, in order to remove this peak broadening, the spin rate has to be equal to or greater than the dipolar linewidth.

2.4.4 Instrumentation

All the measurements were performed by the Solid state NMR service at Durham University utilising a Varian VNMRS system operating at 161.87 MHz for ^{31}P and at 79.44 MHz for ^{29}Si. The spectra were obtained using direct excitation and spectral referencing was with respect to 85% H_3PO_4 and tetramethylsilane for ^{31}P and ^{29}Si respectively.

2.5 AC Impedance Spectroscopy

AC (alternating current) Impedance Spectroscopy (also known as Electrochemical Impedance Spectroscopy or Impedance Spectroscopy) is a technique used to characterise the electrochemical behaviour of a system of interest by studying the response (current or voltage) from a stimulus (a certain voltage or current). The process involves relatively simple electrical measurement, which can be easily automated. Many intrinsic properties of a material and electrode-materials interface can be studied (Table 2.5.1) and they can be correlated with many complex materials variables, such as corrosion, dielectric properties, mass transport and rate of reaction.

Table 2.5.1 Properties that can be studied using AC impedance spectroscopy [37]

Intrinsic property	Electrode-material interface
Conductivity	Adsorption-reaction rate constants
Dielectric constant	Capacitance of the interface region
Mobilities of charge carrier	
Equilibrium constant of charged species	

2.5.1 Electrical Impedance

Current is a rate of flow of charge and two types of current can arise from a ceramic material by the interaction with an electric field. Displacement current is caused by the dielectric mechanism, such as a reorientation of defects having electric dipole moments:

$$I = \frac{dD}{dt} \tag{2.5.1}$$

where D is the electric displacement:

$$D = \varepsilon_0 E + P \tag{2.5.2}$$

where E is the electric field, ε_0 is the permittivity of free space and P is the polarization of dielectric material. The second type is caused by the translational motion of charge carriers such as ion vacancies and interstitial species, which leads to a DC (direct current)

conductivity σ, and current is given by:

$$I = \sigma E \tag{2.5.3}$$

Electrical impedance, Z is a measure of the ability of a circuit to resist AC and it can be calculated from Ohm's law, which states the relationship between the applied voltage, V and responding current, I,

$$I = \frac{V}{Z} \tag{2.5.4}$$

When a signal, $V(t)$ with a frequency, $\nu = \omega/2\pi$ and amplitude, V_0,

$$V(t) = V_0 \sin(\omega \cdot t) \tag{2.5.5}$$

is applied to a cell, a resulting current, I_0,

$$I(t) = I_0 \sin(\omega \cdot t + \theta) \tag{2.5.6}$$

is observed with phase difference between $V(t)$ and $I(t)$, θ. Impedance is given as:

$$Z(t) = \frac{V(t)}{I(t)} = \frac{V_0 \sin(\omega \cdot t)}{I_0 \sin(\omega \cdot t + \theta)} = Z_0 \frac{\sin(\omega \cdot t)}{\sin(\omega \cdot t + \theta)} \tag{2.5.7}$$

This time domain impedance function is very complex due to the presence of capacitive and inductive behaviour of elements in the cell,

$$I(t) = \frac{dV(t)}{dt} C \tag{2.5.8}$$

$$V(t) = \frac{dI(t)}{dt} L \tag{2.5.9}$$

where C is the capacitance and L is the inductance.

The mathematical treatment (Fourier transform to the time domain function) greatly simplifies this to the frequency domain function, and this can be represented in a complex plane with the Euler relationship,

$$Z(\omega) = |Z| \exp(j\theta) = |Z|(\cos\theta + j \sin\theta) = Z' + jZ'' \tag{2.5.10}$$

where j is an imaginary number ($j^2 = -1$) and θ is the phase difference, which is represented in the complex plane as the angle between the vectorial sum of Z' and Z'' and Z' axis,

$$\theta = \tan^{-1}\left(\frac{Z''}{Z'}\right) \tag{2.5.11}$$

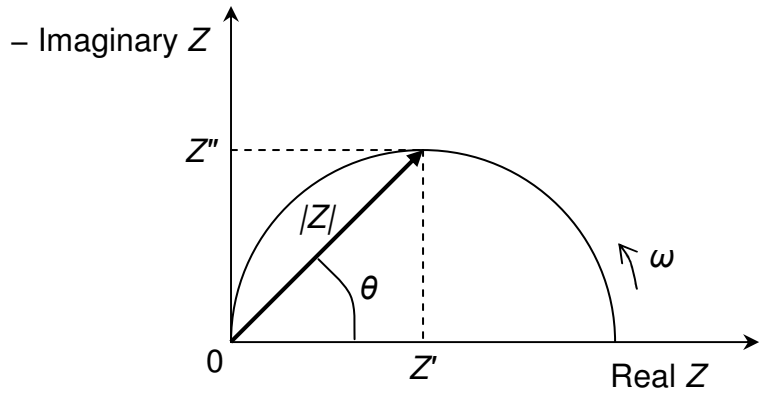

Fig. 2.5.1 A complex impedance plane plot representing each quantity involved

$|Z|$ is the magnitude of the vectorial sum of Z' and Z'',

$$|Z| = \left[(Z')^2 + (Z'')^2\right]^{\frac{1}{2}} \tag{2.5.12}$$

Z' is the real component of Z and is also called the resistance, R. Z'' is the imaginary component of Z and also called the reactance, X:

$$Z = Z' + jZ'' \equiv R + jX \tag{2.5.13}$$

where X is the sum of inductive reactance, X_L and capacitive reactance, X_C:

$$X = X_L + X_C = \omega \cdot L - \frac{1}{\omega \cdot C} \tag{2.5.14}$$

Hence, the reactance of an ideal resistor is zero and a circuit element showing predominant capacitive behaviour has negative values of Z'' and inductive behaviour has positive values of Z''. However, this impedance relationship can only be retained in the linear responsive region, and thus a small perturbation (low voltages and currents) has to be applied.

2.5.2 Analysis of impedance data

A detailed physicoelectrical model containing every single process in a system would be

too complicated for the analysis. Thus a much simplified mathematical model based on a plausible physical theory is used instead. A model usually consists of ideal and non-ideal elements.

2.5.2.1 Equivalent circuit elements

A simple RC circuit (the combination of a resistor and a capacitor in parallel) is often used to describe the electrochemical behaviour of an ionic conductor (Fig. 2.5.2) and its characteristic relaxation time, τ is the product of the resistance and the capacitance of the elements.

$$\tau = \mathrm{RC} = \frac{1}{\omega_{\max}} \tag{2.5.15}$$

Thus, both quantities, R and C can be obtained from the complex impedance plot. For a parallel plate capacitor with area A, separation l between two plates and a medium of permittivity ε', the capacitance is equal to the following:

$$\mathrm{C} = \varepsilon' \varepsilon_0 \frac{A}{l} \tag{2.5.16}$$

Hence, the capacitance value of a RC circuit is indicative of a region of origin of a response from the material (Table 2.5.1).

Table 2.5.1 Typical capacitance values for corresponding phenomena. Reproduced with permission from [38].

Capacitance (F)	Phenomenon Responsible
10^{-12}	Bulk
10^{-11}	Minor, second phase
$10^{-11} – 10^{-8}$	Grain boundary
$10^{-10} – 10^{-9}$	Bulk ferroelectric
$10^{-9} – 10^{-7}$	Surface layer
$10^{-7} – 10^{-5}$	Sample-electrode interface
10^{-4}	Electrochemical reactions

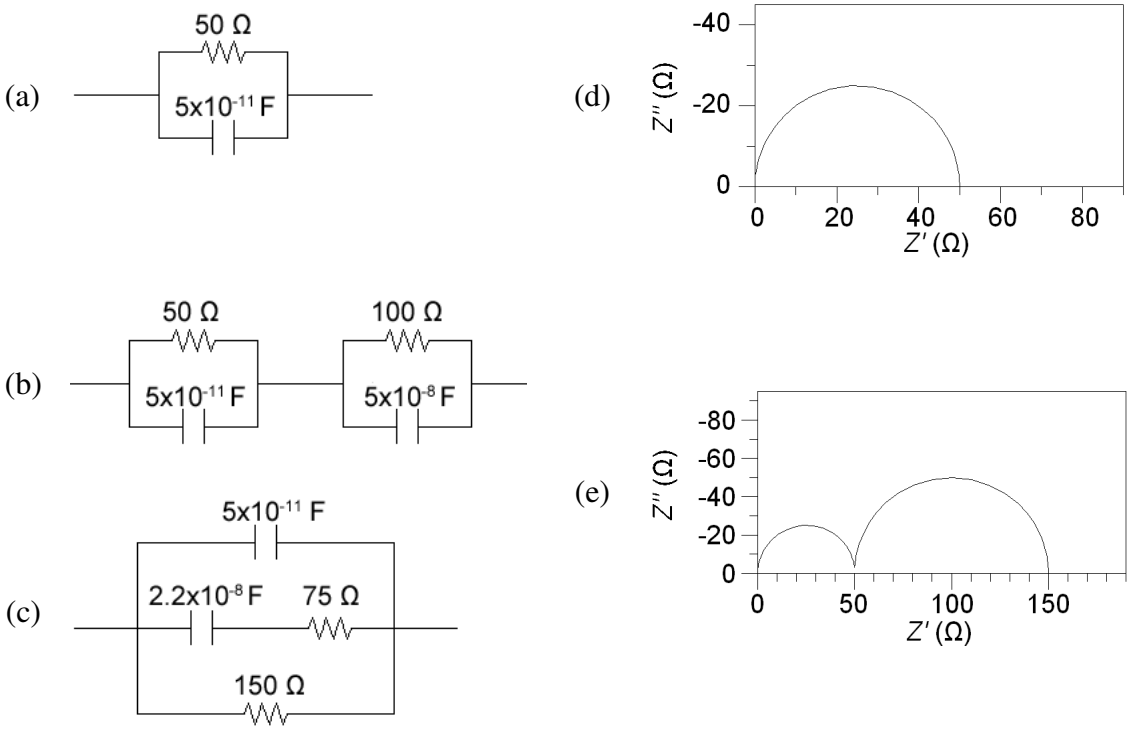

Fig. 2.5.2 Simple RC circuits and the simulated impedance plots. (a) gives plot (d) and both (b) and (c) give (e).

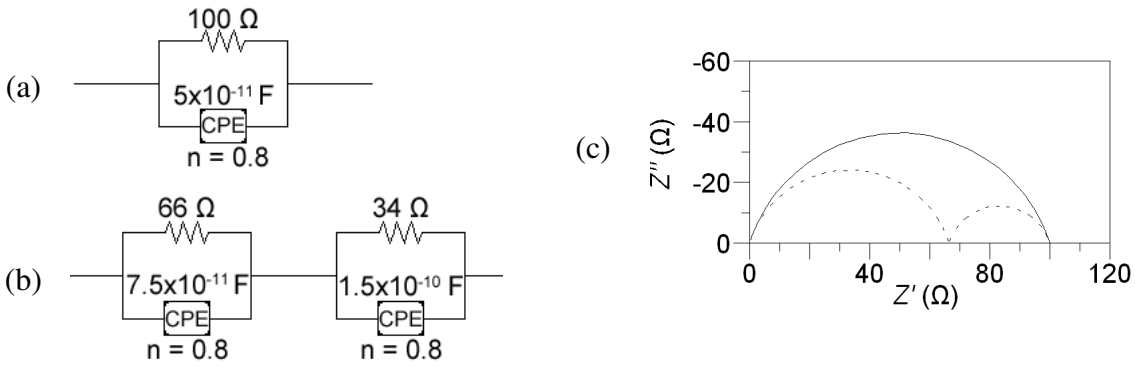

Fig. 2.5.3 Distorted arc and two equivalent models that can produce the same arc.

A good understanding of the physical characteristics of the material is essential for the analysis, as a measurement can be perfectly fitted to a different equivalent circuit as shown in Fig. 2.5.2.b and c. Both models result (Fig. 2.5.2.e) in exactly the same impedance data. In addition, a distorted arc is frequently encountered instead of perfect semicircle (Fig. 2.5.3.c). This could be caused by either the non-ideality of a material or the overlapping of arcs.

In practice, a manufactured resistor, which is originally designed to show only ideal resistive behaviour always exhibits some degree of capacitance and inductance, because it occupies finite space and its elements are distributed over the space. Since it is not a point element, assumed in a mathematical model, it only shows limited ideality over a limited frequency range. For a non-homogenous system, the non-regular distribution of elements results in a distributed relaxation time and resistance. Furthermore, in the case of an ionic conductor which conducts via an ion-hopping model, the different local surroundings of such charge carriers results in a distribution of hopping energies.

A constant phase element (CPE) is a circuit element taking account of such a distribution of relaxation times, which is related to a depressed angle of the distorted arc.

$$Z_{CPE} = \frac{1}{Q_0 (j\omega)^n} \qquad (2.5.17)$$

where $Q_0 = 1/|Z|$ at ω is 1. Thus, when n = 1, it is an ideal capacitor and when n = 0, it is an ideal resistor. This introduction of non-ideality can improve the fitting data using equivalent circuit elements. However, the same impedance data can also be obtained from the presence of two arcs (Fig. 2.5.3). From a close inspection of the values used for the simulation, it can be seen that the capacitance values of the two CPEs are not very different. Thus the system can be understood as a distribution of elements. This ambiguity again emphasises the importance of an understanding of the physical model, and it shows the possibility that an equivalent circuit can be simplified further for the system.

2.5.2.2 Equivalent circuit model for an electrolyte

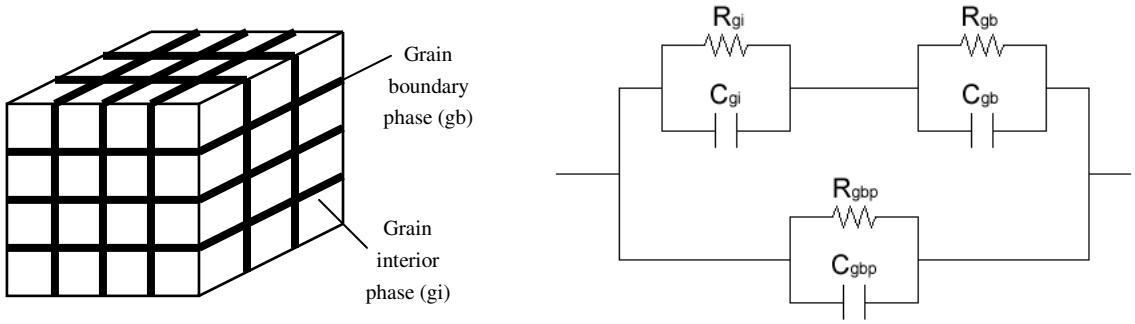

Fig. 2.5.4 Brick layer model and the corresponding equivalent circuit consisting of the components originated from grain interior phase (gi), grain boundary phase (gb) and grain boundary phase pathway (gbp) [37].

Polycrystalline materials can be described with the brick layer model, which consists of regular size cubic grains and secondary phases between them (Fig.2.5.4). Thus, there are two conduction pathways present: through the grains and grain boundary bridges, or just through the grain boundary phase if it is the favourable pathway: the equivalent circuit is given in Fig. 2.5.4. The easy path model introduces a shortcut for the grain boundary bridge between grains (Fig. 2.5.5). This concept can be broadened further to the various degrees of contact between grains, which can be represented with many different easy paths presented in equivalent circuit. However, this model can be simplified with the use of a CPE, as it accommodates various similar relaxation processes into one component. The possible origins of the grain boundary phase include:

- space charge effect – different defect (charge carrier) concentration in the core and towards the exterior of the grains;
- inhibition of anisotropic conduction by the random orientation of grains (e.g. apatite-type silicates);
- presence of other phases, such as SiO_2 agglomeration in YSZ;
- and combinations of the above mentioned.

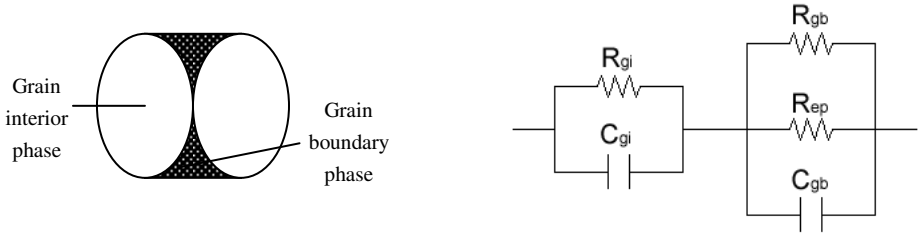

Fig. 2.5.5 Easy path (ep) model and the corresponding equivalent circuit [37].

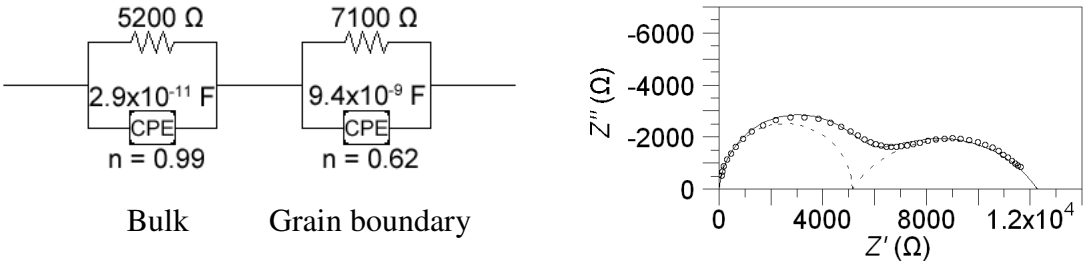

Fig. 2.5.6 The impedance plot of $Ba_2In_{1.7}P_{0.3}O_{5.3}$ sample measured at 195 °C in wet N_2 and the equivalent model for the fitting.

Nevertheless, all the descriptions mentioned above emphasize the complexity present in modelling the grain boundary conduction. However, generally the model with two series R-CPE with a R_{series} is adequate, as most of the grain boundary conduction processes have similar capacitance values, as shown in the fitting of the impedance data of $Ba_2In_{1.7}P_{0.3}O_{5.3}$ sample at 195 °C in wet N_2 (Fig. 2.5.6). The fitted model has ideal RC component for grain interior (bulk) and n = 0.62 for CPE of grain boundary component which emphasises the non-ideality of the component.

2.5.2.3 The model for a composite electrode

Fig. 2.5.7 The physical model for a composite electrode [37]

A composite electrode is used to enhance the conduction between electrode and electrolyte by increasing the number of triple phase boundary (TPB), where cathodic or anodic processes are taking place (Fig. 2.5.7). The electrical components of the conduction processes happening in the TPB of a cathode consist of (descending order of frequency):

- one or two arcs of conductivity relaxation, which is related to the microstructure of the composite, and these are independent of P_{O2},
- the cathodic process involving adsorption, dissociation of O_2 on the surface of a TPB, which is P_{O2} dependent and has typical values of E_a of 2.0 eV and capacitance of 10^{-4} to 10^{-1} F cm^{-2};
- Gas diffusion impedance.

Thus the equivalent circuit for the system includes 2 to 4 elements excluding the response from the electrolyte. For example, the complex impedance plot of $La_{0.6}Sr_{0.4}Fe_{0.8}Co_{0.2}O_{3-\delta}$-$La_{10}Si_5GaO_{26.5}$ 1:1 composite on a $La_{10}Si_5GaO_{26.5}$ electrolyte is fitted with only two arcs which are attributed to the conduction related to the electrode-electrolyte interface and gas-electrode catalytic process (Fig. 2.5.8).

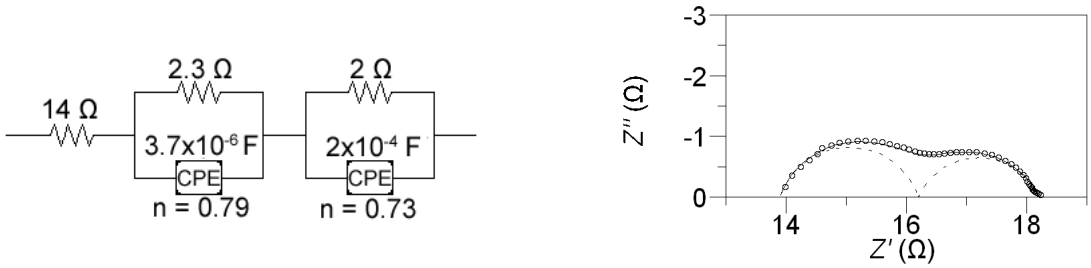

Fig. 2.5.8 The impedance plot of $La_{0.6}Sr_{0.4}Fe_{0.8}Co_{0.2}O_{3-\delta}$-$La_{10}Si_5GaO_{26.5}$ 1:1 composite on $La_{10}Si_5GaO_{26.5}$ electrolyte having area of 0.44 cm^2 measured at 700 ℃ in air, and the equivalent model for the fitting.

2.5.3 Instrumentation

Two sets of measurement rig-impedance analyser combinations were used for the experiments. The schematic representation of measurement setup A is given in Fig. 2.5.9.a. Platinum strips were attached on the surface of a sample which was coated with a platinum paste, and then heated to 800 °C for 1 hour to ensure bonding. The platinum strip was wrapped around platinum wire in the measurement rig to make an electrical connection to a Hewlett Packard 4182A impedance analyser. For samples which required a controlled atmosphere (e.g. N_2 to remove any contribution of *p*-type conduction for $Ba_2In_2O_5$ related systems) rather than just air, the required gas was bubbled through concentrated sulphuric acid or liquid paraffin or water. A schematic representation of measurement setup B is given in Fig. 2.5.9.b. Samples were coated with a platinum paste, and then heated to 800 °C for 1 hour to ensure bonding. Silver wires, pushed by springs, made contact with the sample and made an electrical connection to a Solartron SI 1260 impedance/gain-phase analyser. Voltage perturbation (100 mV) methods were used for both instruments. Induction correction was applied to the impedance data obtained from the measurement setup B [37]. All impedance data were analysed using *ZView* software, which estimates the resistance and capacitance values associated with equivalent circuits through complex nonlinear least squares fitting [39].

(a) Measurement setup A

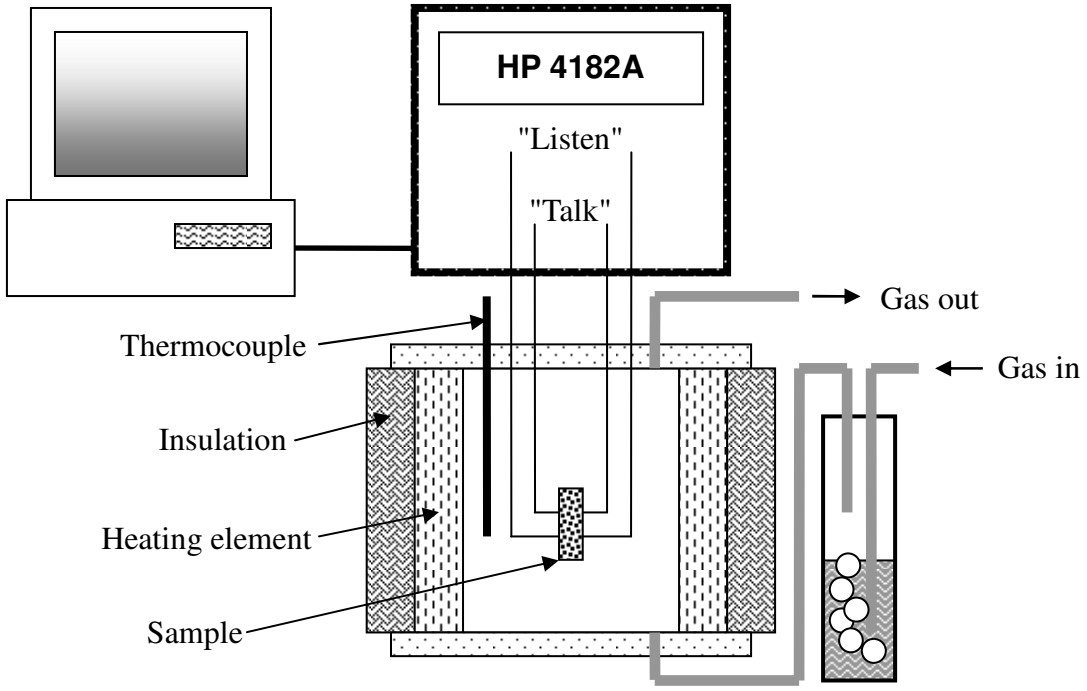

(b) Measurement setup B

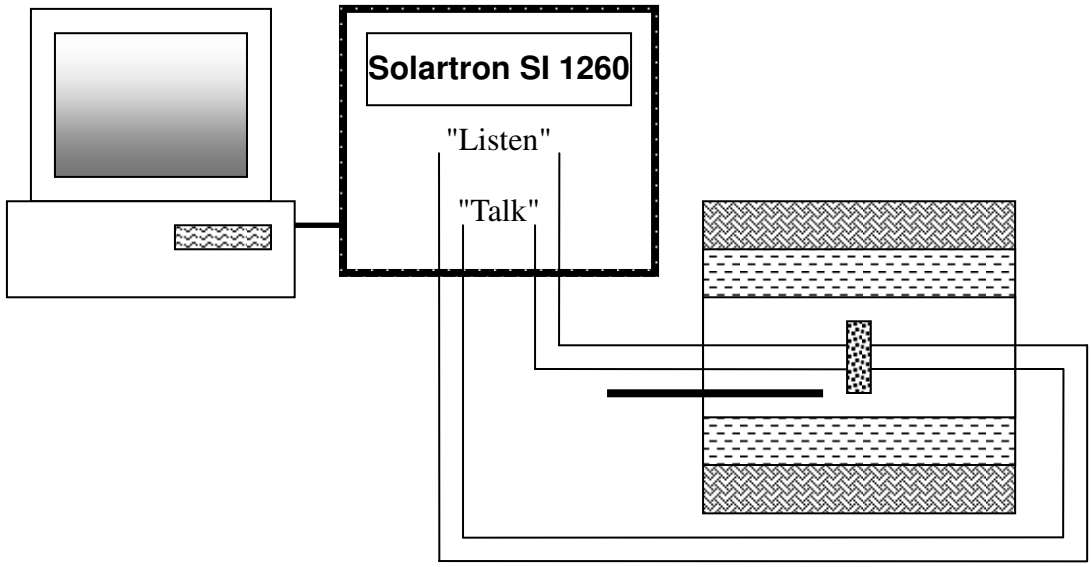

Fig. 2.5.9 Schematic diagrams of two impedance analyser-measurement rig configurations. All electric wires are earth shielded.

2.6 Thermal Analysis

Thermal analysis is the study of the physical and chemical changes occurring in a substance as a function of temperature and many branched techniques have been established for quantitative and/or qualitative analysis (Table 2.6.1).

Table 2.6.1 List of thermal analysis techniques [40]

Thermal analysis techniques	Measurement
Thermogravimetry (TG)	Mass change
Differential thermal analysis (DTA)	Temperature difference between sample and reference
Differential scanning calorimetry (DSC)	Energy required to reach zero temperature difference between sample and reference
Evolved gas analysis (EGA)	Identification and/or quantification of gaseous species evolved
Thermomechanical analysis (TMA)	Deformation of a material under a constant load
Dynamic mechanical analysis (DMA)	A strain is measured while a sinusoidal stress is applied
Dilatometry	Thermal expansion

2.6.1 Thermogravimetry

Thermogravimetry (TG) measures the mass change of a substance heated isothermally or dynamically. It utilises a microbalance, while the sample is surrounded by a furnace. It is mostly suitable for the studies of thermal stability and loss of components in a specific atmosphere. TG can be coupled with mass spectrometry to identify and/or quantify any gases evolved. Fig. 2.6.1 shows a typical TG profile of the dehydration reaction described in equation 2.6.1, and it clearly indicates the species responsible for the mass loss is H_2O by

accompanying mass-spec data.

$$Ba_2In_{1.7}P_{0.3}O_{5.3}.xH_2O \rightarrow Ba_2In_{1.7}P_{0.3}O_{5.3} + xH_2O(g) \qquad (2.6.1)$$

However, due to the dynamic nature of the measurement (10 °C min^{-1} in this experiment), it is difficult to determine an accurate temperature at which dehydration begins. The dehydration may have occurred in a wide range of temperature or occurred at the beginning of the mass change temperature but requiring more time to finish. Thus, care must be taken in the determination of the reaction temperature: slow heating rate near the reaction temperature is beneficial to gain a more accurate temperature value.

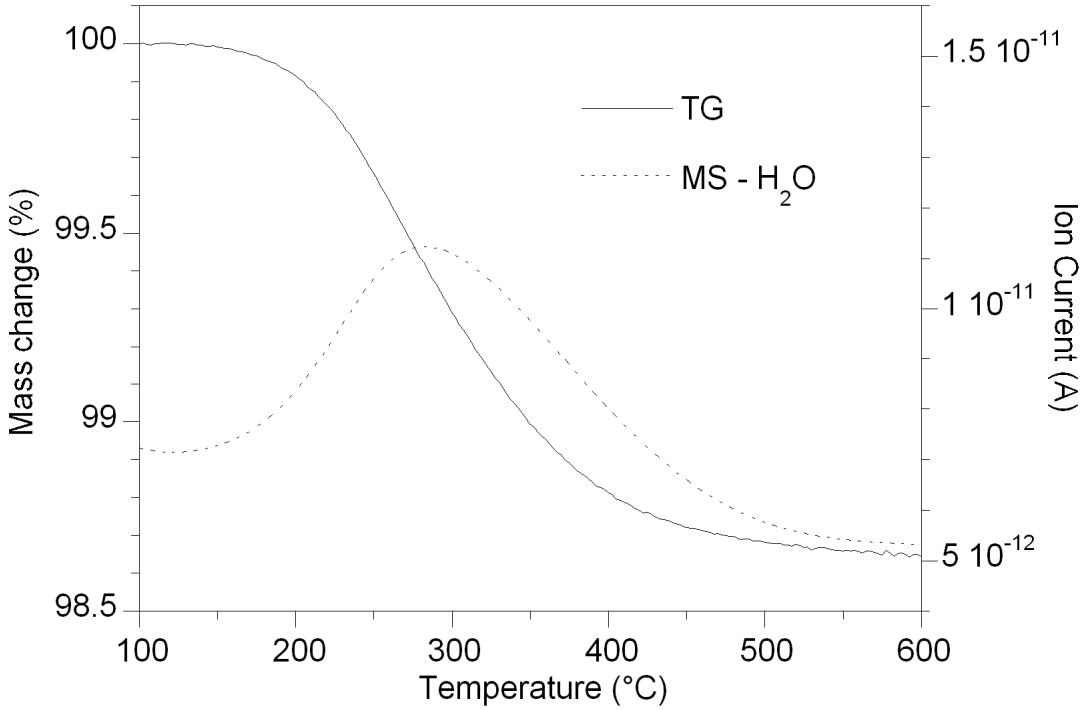

Fig. 2.6.1 TG profile for the dehydration process of hydrated $Ba_2In_{1.7}P_{0.3}O_{5.3,}$ along with Mass-spec data for water evolved.

2.6.2 Instrumentation

The instrument used in this study was a Netzsch STA 449 F1 Jupiter Thermal Analyser coupled with a Netzsch MS 403C Aëolos Mass Spectrometer, and its schematic is shown in

Fig. 2.6.2. In an experiment, a sample is placed on a thermobalance along with a reference crucible (which is required for DTA/DSC measurements), and surrounded by heating elements. A mixture of protective gas (N_2) and another desired gas such as CO_2 was passed through the instrument from below. The sample heating rate is controlled by a heating programme, and its mass change is recorded while outlet gases are fed to the mass spectrometer for analysis.

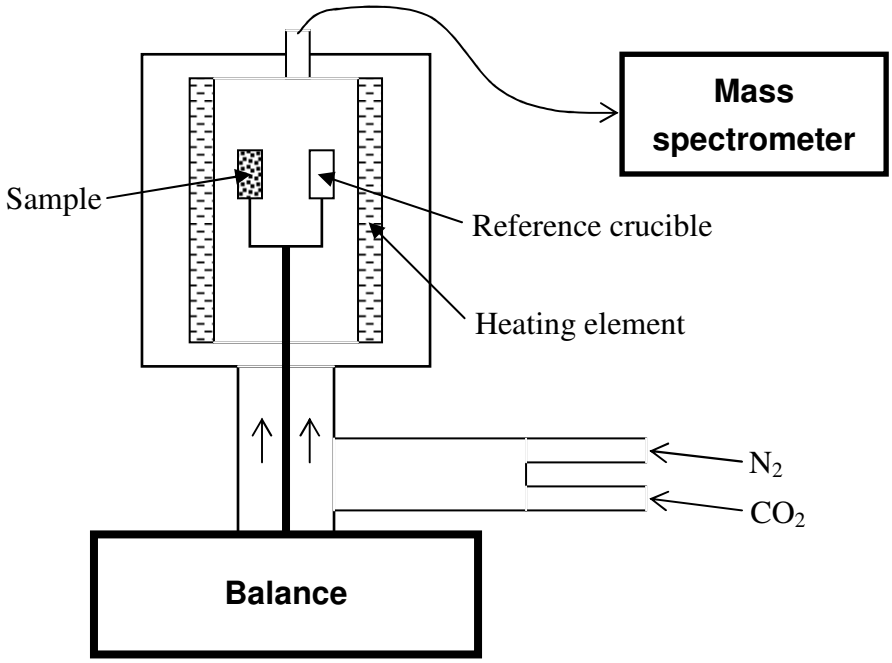

Fig. 2.6.2 Schematic diagram of the instrument.

2.7 References

[1] Al-Mamouri, M.; Edwards, P. P.; Greaves, C.; Slaski, M. *Nature* **1994**, *369*, 382.
[2] Slater, P. R. *J. Fluorine Chem.* **2002**, *117*, 43.
[3] Slater, P. R.; Edwards, P. P.; Greaves, C.; Gameson, I.; Francesconi, M. G.; Hodges, J. P.; Al-Mamouri, M.; Slaski, M. *Physica C* **1995**, *241*, 151.
[4] Needs, R. L.; Weller, M. T. *J. Solid State Chem.* **1998**, *139*, 422.
[5] Peacock, G. B.; Gameson, I.; Slaski, M.; Capponi, J. J.; Edwards, P. P. *Physica C* **1997**, *289*, 153.
[6] Greaves, C.; Kissick, J. L.; Francesconi, M. G.; Aikens, L. D.; Gillie, L. J. *J. Mater. Chem.* **1999**, *9*, 111.
[7] Case, G. S.; Hector, A. L.; Levason, W.; Needs, R. L.; Thomas, M. F.; Weller, M. T. *J. Mater. Chem.* **1999**, *9*, 2821.
[8] Al-Mamouri, M.; Edwards, P. P.; Greaves, C.; Slater, P. R.; Slaski, M. *J. Mater. Chem.* **1995**, *5*, 913.
[9] Yang, J.; Zuo, Y.; Liu, H.; Su, W. *J. Mater. Sci. Lett.* **1996**, *15*, 1891.
[10] Slater, P. R.; Hodges, J. P.; Francesconi, M. G.; Greaves, C.; Slaski, M. *J. Mater. Chem.* **1997**, *7*, 2077.
[11] Slater, P. R.; Gover, K. B. *J. Mater. Chem.* **2001**, *11*, 2035.
[12] Antipov, E. V.; Putilin, S. N.; Shpanchenko, R. V.; Alyoshin, V. A.; Rozova, M. G.; Abakumov, A. M.; Mikhailova, D. A.; Balagurov, A. M.; Lebedev, O.; Van Tendeloo, G. *Physica C* **1997**, *282–287, Part 1*, 61.
[13] Abakumov, A. M.; Hadermann, J.; Van Tendeloo, G.; Shpanchenko, R. V.; Oleinikov, P. N.; Antipov, E. V. *J. Solid State Chem.* **1999**, *142*, 440.
[14] Lightfoot, P.; Pei, S.; Jorgensen, J. D.; Tang, X. X.; Manthiram, A.; Goodenough, J. B. *Physica C* **1990**, *169*, 15.
[15] Slater, P. R.; Gover, R. K. B. *J. Mater. Chem.* **2002**, *12*, 291.
[16] Jenkins, F. A.; White, H. E. *Fundamentals of Optics*, 3rd Edition, McGraw Hill, **1957**
[17] Laue, M. *Ann. Phys.***1912**, 41, 989.
[18] Bragg, W. H.; Bragg, W. L. *Proc. R. Soc. Lond. Ser. A-Contain. Pap. Math. Phys. Character* **1913**, *88*, 428.
[19] Miller, W. H. A *Treatise on Crystallography* **1839**
[20] Ekstein, H. *Phys. Rev.* **1942**, *62*, 255.
[21] Hutchinson, I. H. *Prinsples of Plasma Diagnostics*, Cambridge University Press, **1987**
[22] de Broglie, L. *Ann. Phys. (Paris)* **1925**, 3, 22.
[23] Roisnel, T.; Rodriguez-Carvajal, J. *Proceedings of the Seventh European Powder Diffraction Conference (EPDIC 7)*, **2000**, 118
[24] Rietveld, H. M. *J. Appl. Crystallogr.* **1969**, *2*, 65.
[25] Kaduk, J. A. *Principles and Applications of Powder Diffraction*, John Wiley & Sons, **2009**. p310.
[26] Brown, I. D.; Altermatt, D. *Acta Crystallogr. Sect. B-Struct. Commun.* **1985**, *41*, 244.
[27] Enderby, J. E.; North, D. M.; Egelstaff, P. A. *Philosophical Magazine* **1966**, *14*, 961.
[28] http://www.isis.stfc.ac.uk/instruments/hrpd/ (02.06.2012)

[29] http://sinq.web.psi.ch/sinq/instr/hrpt/index.html (02.06.2012)
[30] Larson, A. C.; Von Dreele, R. B. *Los Alamos National Laboratory Report LAUR* **1994**, 86-748.
[31] Kerker. M. *The Scattering of Light and Other Electromagnetic Radiation*. Academic, **1969**.
[32] Brian, A.; Donovan, J. F. *Lattice Vibrations*, Chapman and Hall, **1971**
[33] Rousseau, D. L.; Bauman, R. P.; Porto, S. P. S. *J. Raman Spectrosc.* **1981**, *10*, 253.
[34] Schaufele, R. F.; Weber, M. J. *J. Chem. Phys.* **1967**, *46*, 2859.
[35] Ranson, P.; Ouillon, R.; Pinan-Lucarre, J. P.; Pruzan, P.; Mishra, S. K.; Ranjan, R.; Pandey, D. *J. Raman Spectrosc.* **2005**, *36*, 898.
[36] Melinda, J. M. *Solid-State NMR Spectroscopy Principles and Applications*, Wiley and Sons, Blackwell, **2002.**
[37] Macdonald, J. R. *Impedance Spectroscopy*, 2nd Edition, John Wiley & Sons, **2005.**
[38] Irvine, J. T. S.; Sinclair, D. C.; West, A. R. *Advanced Materials* **1990**, *2*, 132.
[39] Johnson, D. *ZView: a Software Program for IES Analysis, Version 3.1c*, Scribner Associates Inc., **2007**.
[40] Haines, P. J. *Principles of Thermal Analysis and Calorimetry*, Royal Society of Chemistry, Cambridge, **2002**.

2.8 Bibliography

[1] Aktins, P. W.; Shriver, D. F. *Inorganic Chemistry*, 5th Edition, Oxford, **2010**

[2] Kaduk, J. A. *Principles and Applications of Powder Diffraction*, John Wiley & Sons, Blackwell, **2009**.

[3] Sivia, D. S. *Elementary Scattering Theory: for X-ray and Neutron Users*; Oxford University Press, New York, **2011**.

[4] Kerker, M. *The Scattering of Light and Other Electromagnetic Radiation*. Academic, New York, **1969**.

[5] Maher, S. A. *Raman Spectroscopy for Soft Matter Application*, Wiley and Sons, New York, **2008**

[6] Mackenzie, K. J. D.; Smith, M. E. *Multinuclear Solid State NMR of Inorganic Materials*, Pergamon Materials Series, Permagon, Oxford, **2002**

[7] Melinda, J. M. *Solid-State NMR Spectroscopy Principles and Applications*, Wiley and Sons, Blackwell, **2002**

[8] Macdonald, J. R. *Impedance Spectroscopy*, 2nd Edition, John Wiley & Sons, **2005**

[9] Haines, P. J. *Principles of Thermal Analysis and Calorimetry*, Royal Society of Chemistry, Cambridge, **2002**.

Chapter 3 Oxyanion Doping in $Ba_2In_2O_5$

3.1 Introduction

$Ba_2In_2O_5$ has been the subject of extensive doping studies due to the high oxide ion conductivity achieved in the high symmetry cubic phase [1]. However, there is limited evidence and doubts about the long term stability of such doped systems towards CO_2 containing atmosphere. Hence, we have proposed an alternative doping strategy involving the use of acidic (oxyanion) dopants, with the aim to achieve high conductivity as well as improve the CO_2 stability. Previously, the successful incorporation of significant level of oxyanions (carbonate, nitrate, sulphate, phosphate) has been demonstrated in the studies of perovskite-type cuprate superconductors [2-7]. Interestingly, stabilisation of phases, which cannot be formed without doping (e.g. the Sr analogue of the high temperature superconductor, $YBa_2Cu_3O_{7-x}$), has been also achieved [4]. Hence, this doping strategy has been extended here to the $Ba_2In_2O_5$ system and incorporation of phosphate, sulphate and silicate anions on the In site has been investigated. In this chapter, the solid solution levels and the positive influence on the conductivity and CO_2 stability are reported. In particular, the effect of silicate doping on the conductivity is interesting as there are many publications that have argued the detrimental effect of silica addition to SOFC electrolytes such as yttria stabilised zirconia. In addition, the effect of co-doping of La and Zr on Ba and In sites on the CO_2 stability and conductivity is studied. Finally, the structural implication of fluorination by low temperature route on undoped and doped $Ba_2In_2O_5$ systems is also examined.

3.2 Experimental

High purity $BaCO_3$, In_2O_3, $NH_4H_2PO_4$, $(NH_4)_2SO_4$, SiO_2, La_2O_3 and ZrO_2 were used to prepare $Ba_2In_{2-x}P_xO_{5+x}$ (x = 0, 0.1, 0.2, 0.3), $Ba_2In_{2-x}S_xO_{5+3x/2}$ (x = 0.1, 0.2, 0.3), Ba_2In_{2-}

$_xSi_xO_{5+x/2}$ (x = 0.1, 0.2), $Ba_2In_{1.7-x}P_{0.3}Zr_xO_{5.3+x/2}$ (x = 0.1, 0.2), $Ba_{2-x}La_xIn_{1.7}P_{0.3}O_{5.3+x/2}$ (x = 0.1, 0.2, 0.3, 0.4), $Ba_2In_{1.8-x}Si_{0.2}Zr_xO_{5.1+x/2}$ (x = 0.1, 0.2) and $Ba_{2-x}La_xIn_{1.8}Si_{0.2}O_{5.1+x/2}$ (x = 0.1, 0.2, 0.3, 0.4) samples. In order to overcome Ba loss at elevated temperatures, a 3% excess of $BaCO_3$ was employed. Without this small Ba excess, low levels of Ba deficient impurity phases, such as $BaIn_2O_4$ and $Ba_4In_6O_{13}$, were observed after sintering, as has been seen in other studies synthesising similar Ba containing phases [8, 9]. The powders were intimately ground and heated initially to 1000 °C for 12h. They were then ball-milled (350 rpm for 1 hour, Fritsch Pulverisette 7 Planetary Mill) and reheated to 1000 °C for a further 50h. The resulting samples were then pressed as pellets (1.3 cm diameter) and sintered at 1400 °C for 10h. The pellets were covered in sample powder and the crucible was covered with a lid to limit the amount of Ba loss during the sintering process. For the fluorination, the samples were mixed with a calculated amount of polytetrafluoroethene (PTFE) to result in the fully stoichiometric samples (one O^{2-} exchanged by two F^-) and heated to 350 °C for 12h, and then reground and reheated to 350 °C for 12h.

Powder X-ray diffraction (Bruker D8 diffractometer with Cu $K_{\alpha 1}$ radiation = 1.5406 Å) was used to demonstrate phase purity. For the detailed information of the structural changes for $Ba_2In_{1.7}P_{0.3}O_{5.3}$, time of flight neutron diffraction data were recorded on diffractometer HRPD at the ISIS facility, Rutherford Appleton Laboratory. All structural refinements employed the GSAS suite of Rietveld refinement software [10].

Pair distribution function (PDF) analysis of X-ray diffraction data collected using synchrotron X-rays and a two-dimensional detector were carried out by the research group of Dr. L. Malavasi at University of Pavia in Italy (detailed experimental procedure is given in Mancini *et al.* [11]).

In order to provide further evidence for the successful incorporation of phosphate, sulphate and silicate, Raman spectroscopy measurements were made using a Renishaw inVia Raman

microscope with excitation using a Cobolt Samba CW 532 nm DPSS Laser. In addition, ^{31}P and ^{29}Si NMR data were collected to gain further information about the P and Si environment. These spectra were obtained using a Varian Unity Inova operating at 121.37 MHz for ^{31}P and at 59.56 MHz for ^{29}Si. Spectral referencing was with respect to 85% H_3PO_4 and tetramethylsilane respectively. The data were collected by the EPSRC Solid state NMR service at Durham University.

The water contents for the hydrated samples were determined from thermogravimetric analysis (Netzsch STA 449 F1 Jupiter Thermal Analyser). Samples were heated at 10 °C min^{-1} to 1000 °C in N_2, and the water content was determined from the observed mass loss.

In order to determine the CO_2 stability of samples, two sets of experiments were performed. In the first set of experiments, samples were heated at temperatures between 600 and 800 °C under CO_2, and the samples were analysed for decomposition by X-ray diffraction. In the second experiment, samples were analysed using thermogravimetric analysis. Samples were heated at 10 °C min^{-1} to 1000 °C in 1:1 CO_2 and N_2 mixture to determine at what temperature CO_2 pick up occurred.

An important aspect of the work was the investigation of the effect this doping strategy has on the conductivity. The sintered pellets (> 84% theoretical density) were coated with Pt paste, and then heated to 800 °C for 1 hour to ensure bonding to the pellet. Conductivities were then measured by AC impedance measurements (Hewlett Packard 4182A impedance analyser) in the range from 0.1 to 10^3 kHz. Since $Ba_2In_2O_5$ displays a small but significant p-type contribution to the conductivity in oxidising conditions, measurements were made in dry N_2 to eliminate this contribution. In addition, measurements were made in wet N_2 (in which the gas was bubbled at room temperature through water) to identify any protonic contribution to the conductivity.

The impedance data showed generally a single broad semicircle in dry atmospheres. The

capacitance of the broad semicircle was typical of a bulk response, suggesting that in dry atmospheres, the resistance of the grain boundary is small compared to that of the bulk. In wet atmospheres, instead of the single broad semicircle, there were now two partially resolved semicircles, whose capacitances were consistent with the bulk and grain boundary respectively (Appendix 3.1). In the text, bulk conductivities are reported.

3.3 Phosphate doped systems: $Ba_2In_{2-x}P_xO_{5+x}$ (x = 0, 0.1, 0.2, 0.3)

3.3.1 Structural study

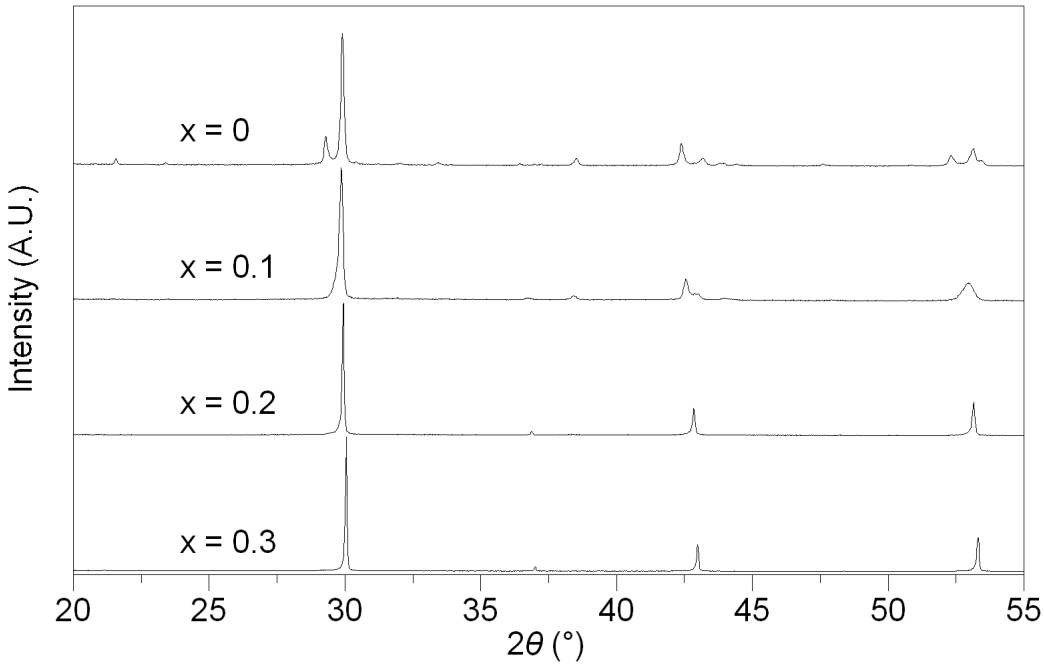

Fig. 3.1 X-ray diffraction patterns for $Ba_2In_{2-x}P_xO_{5+x}$

The X-ray powder diffraction analysis confirmed the successful synthesis of single phase samples of $Ba_2In_{2-x}P_xO_{5+x}$ in the range $0 \leq x \leq 0.3$ (Fig. 3.1). Undoped $Ba_2In_2O_5$ was orthorhombic as previously reported and there was a change in symmetry to cubic on incorporation of phosphate. Calculated cell parameters are given in table 3.1 and plotted in Fig. 3.2. These show a gradual decrease in cell volume with increase in phosphate level as a result of substitution of smaller size of P^{5+} in place of bigger In^{3+}. Cell size expansion due to

the additional oxygen content introduced by charge compensation (P^{5+} versus In^{3+}) is hence outweighed by the influence of this size difference. The extra oxygen can be accommodated within the vacant interstitial sites in the tetrahedral layer of the brownmillerite structure: in terms of a defect equation, it can be written as:

$$2NH_4H_2PO_4 + 2In_{In}^{x} \leftrightarrow 2P_{In}^{\bullet\bullet} + 2O_i'' + In_2O_3 + 2NH_3\uparrow + 3H_2O\uparrow \qquad (3.1)$$

Structure refinement has been performed using the X-ray (Fig. 3.3 and table 3.2) and neutron diffraction data (Fig. 3.4 and table 3.3) for the highest phosphate content sample, $Ba_2In_{1.7}P_{0.3}O_{5.3.}$ The structure refinement showed B site occupancies of 1.68(1) In and 0.32(1) P from X-ray diffraction data and 1.70(1) In and 0.30(1) P from neutron diffraction data, consistent with that expected for the nominal starting composition. However, a lower oxygen occupancy than expected was obtained. This can most likely be explained by the severe local distortion caused by the presence of the phosphate group. This feature coupled with the likely disorder in the orientation of the phosphate group makes the accurate location of the phosphate oxygens difficult, and thus explains the lower than expected refined oxygen content.

Table 3.1 Cell parameter data for $Ba_2In_{2-x}P_xO_{5+x}$

Sample (nominal composition)	Unit cell parameters (Å)			Unit cell volume (Å^3)
	a	b	c	
$Ba_2In_2O_5$	6.089(2)	16.736(8)	5.963(2)	607.6(2)
$Ba_2In_{1.9}P_{0.1}O_{5.1}$	6.055(6)	16.774(5)	5.957(7)	605.1(4)
$Ba_2In_{1.8}P_{0.2}O_{5.2}$	4.217(1)	-	-	75.0(1)
$Ba_2In_{1.7}P_{0.3}O_{5.3}$	4.208(1)	-	-	74.5(1)

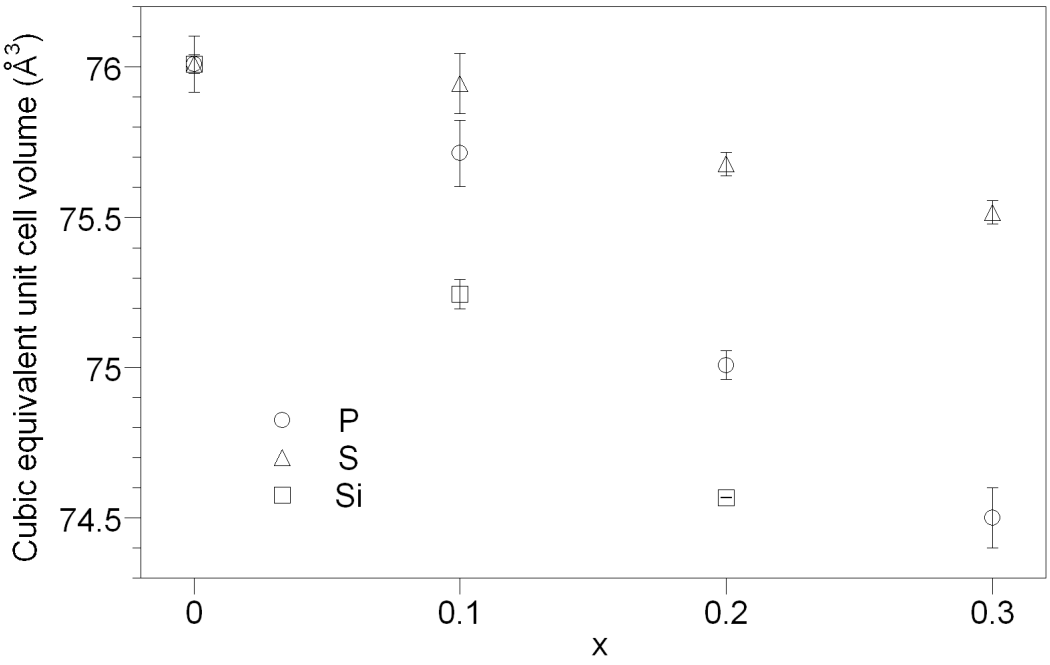

Fig. 3.2 Variation of cubic equivalent unit cell volume with phosphate, sulphate and silicate doped series.

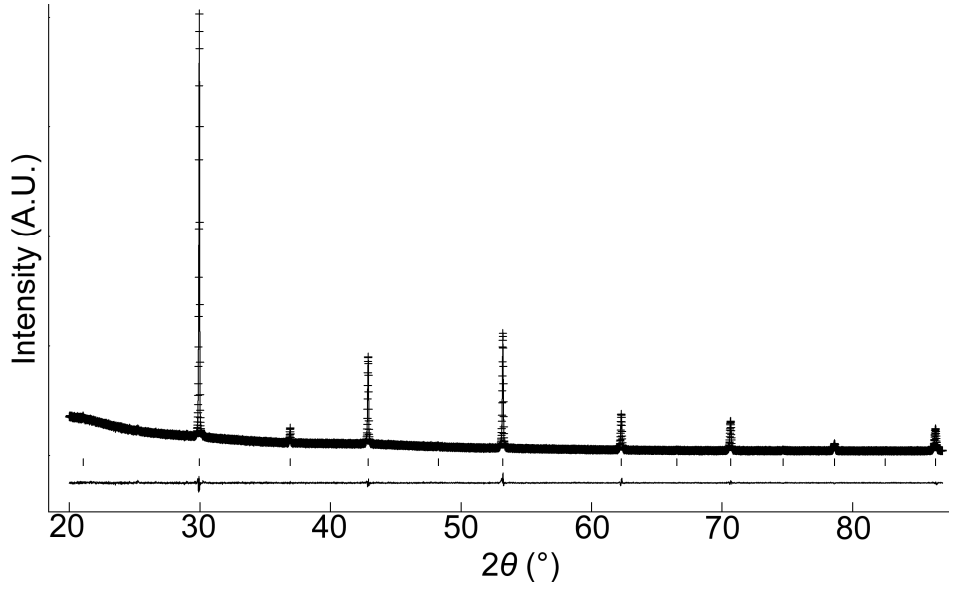

Fig. 3.3 Observed (cross), calculated (line), and difference plots of $Ba_2In_{1.7}P_{0.3}O_{5.3}$ from the Rietveld refinement for room temperature X-ray diffraction data.

Table 3.2 Refined structural parameters for $Ba_2In_{1.7}P_{0.3}O_{5.3}$ with cubic $Pm\bar{3}m$ (221) space group, from room temperature X-ray diffraction data

		a (Å)		R_{wp}	R_p	χ^2
		4.2116(1)		2.98	2.09	1.34
		x	y	z	Fractional occupancy	U_{iso} (Å^2 x 100)
Ba	1b	½	½	½	1.000	1.36(2)
In	1a	0	0	0	0.842(3)	1.79(5)
P	1a	0	0	0	0.156(3)	1.79(5)
O	3d	0	0	½	0.862(8)	4.30(20)

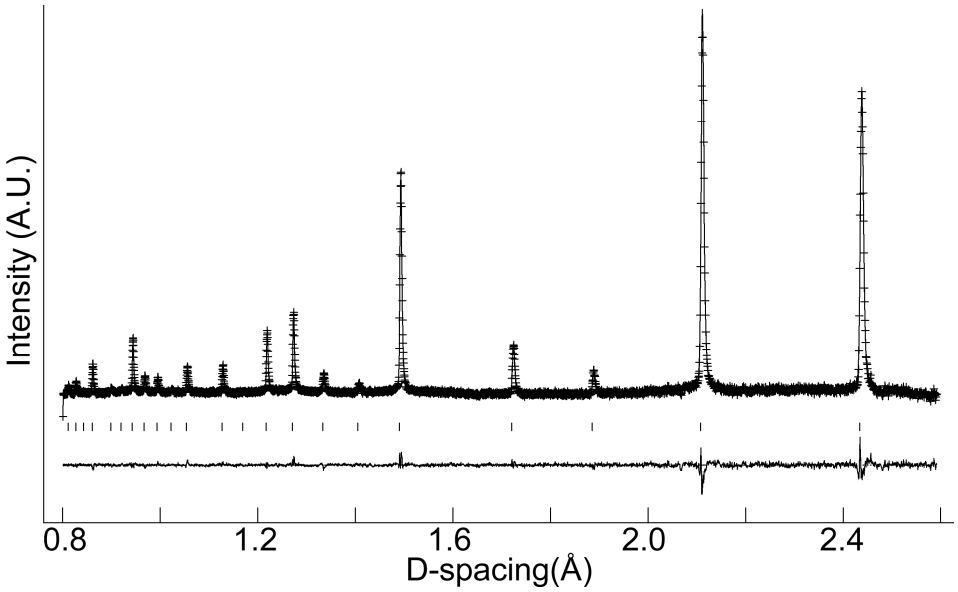

Fig. 3.4 Observed (cross), calculated (line), and difference plots of $Ba_2In_{1.7}P_{0.3}O_{5.3}$ from the Rietveld refinement for room temperature neutron diffraction data

Table 3.3 Refined structural parameters for $Ba_2In_{1.7}P_{0.3}O_{5.3}$ with cubic $Pm\bar{3}m$ (221) space group, from room temperature neutron diffraction data

		a (Å)		R_{wp}	R_p	χ^2
		4.2075(1)		4.02	4.22	1.54
		x	y	z	Fractional occupancy	U_{iso} (Å^2 x 100)
Ba	1b	½	½	½	1.000	1.53(2)
In	1a	0	0	0	0.850(10)	1.61(3)
P	1a	0	0	0	0.150(10)	1.61(3)
O	3d	0	0	½	0.766(1)	3.37(2)

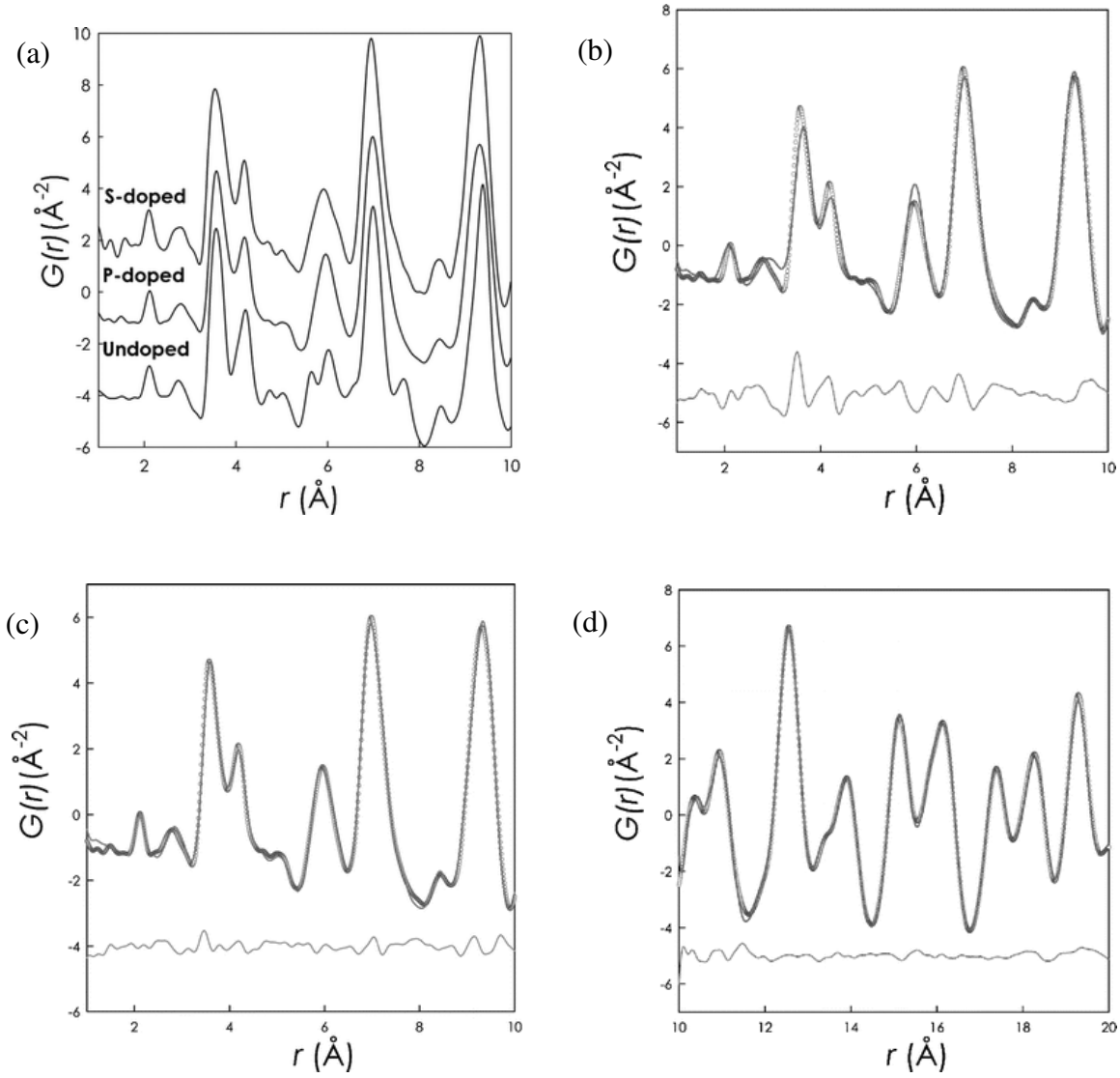

Fig. 3.5 (a) X-ray PDFs up to 10 Å for $Ba_2In_2O_5$, $Ba_2In_{1.7}P_{0.3}O_{5.3}P$ and $Ba_2In_{1.7}P_{0.3}O_{5.3}$. PDF fit of $Ba_2In_{1.7}P_{0.3}O_{5.3}$ up to 10 Å with (b) $Pm\bar{3}m$ and (c) *Icmm* space groups. Experimental, calculated and difference plots showing an improved fit for the latter orthorhombic space group. (d) PDF fit of $Ba_2In_{1.7}P_{0.3}O_{5.3}$ from 10 to 20 Å with $Pm\bar{3}m$ space group showing a good agreement. Reproduced with permission from [11].

X-ray total scattering and pair distribution function (PDF) analysis enlightened the complexity of the structure further. At first glance, X-ray PDFs up to 10 Å for undoped $Ba_2In_2O_5$ and $Ba_2In_{1.7}P_{0.3}O_{5.3}$ did not show any large differences (Fig. 3.5). Thus the PDF fitting of $Ba_2In_{1.7}P_{0.3}O_{5.3}$ up to 10 Å with *Icmm* space group, as for undoped $Ba_2In_2O_5$ yielded much better agreement factor than that of with $Pm\bar{3}m$ space group (R_w of 7.2% against 15.8%), while PDF fitting of $Ba_2In_{1.7}P_{0.3}O_{5.3}$ from 10 to 20 Å with $Pm\bar{3}m$ space group resulted in a good agreement (R_w of 7.2%). The good agreement was retained for further r-ranges, and thus the results indicated that for r-values closer to the unit cell size, the local structure is distorted away from the cubic symmetry [11, 12].

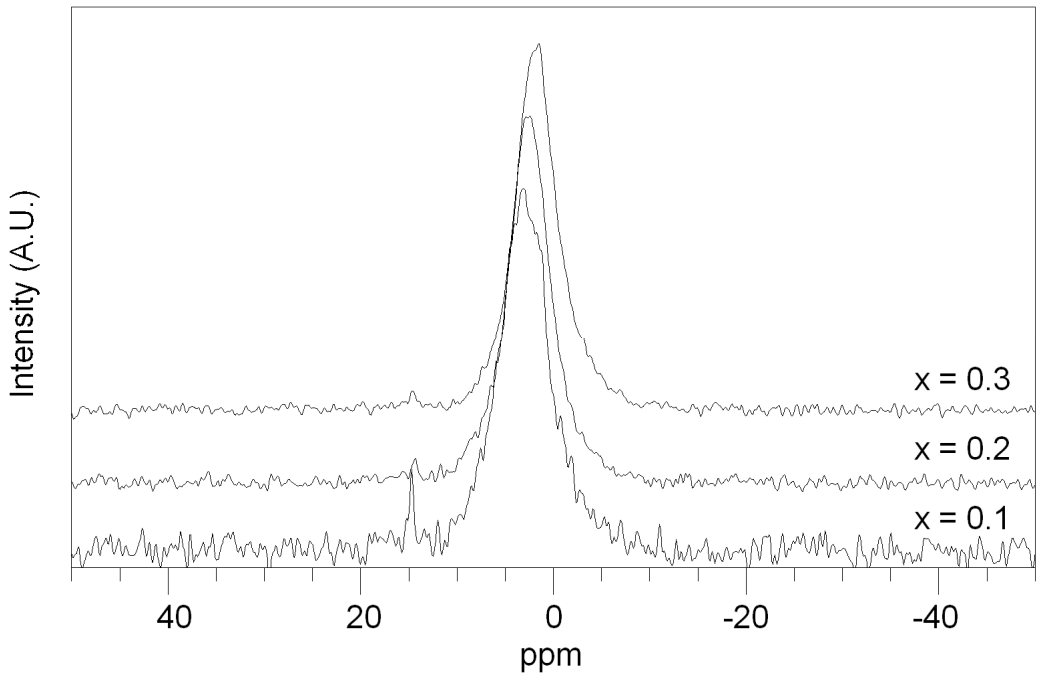

Fig. 3.6 ^{31}P NMR data for dry $Ba_2In_{2-x}P_xO_{5+x}$ (note: the small sharp peak at ≈ 15 ppm is an artefact of the instrument).

The ^{31}P NMR data for the x = 0.1, 0.2, 0.3 samples are given in Fig. 3.6. All the samples showed a single broad line with slight chemical shift difference from each other. The chemical shifts are ranged from 1.4 to 3.0 ppm, which are in the typical region for an alkaline earth

phosphate [13]. Thus, the phosphate groups are strongly linked with Ba. The ^{31}P NMR data for hydrated samples showed no significant difference to those of the dry samples. This suggests that the oxygens on In are the preferred location for the protons, which was not unexpected as these sites have higher basicity.

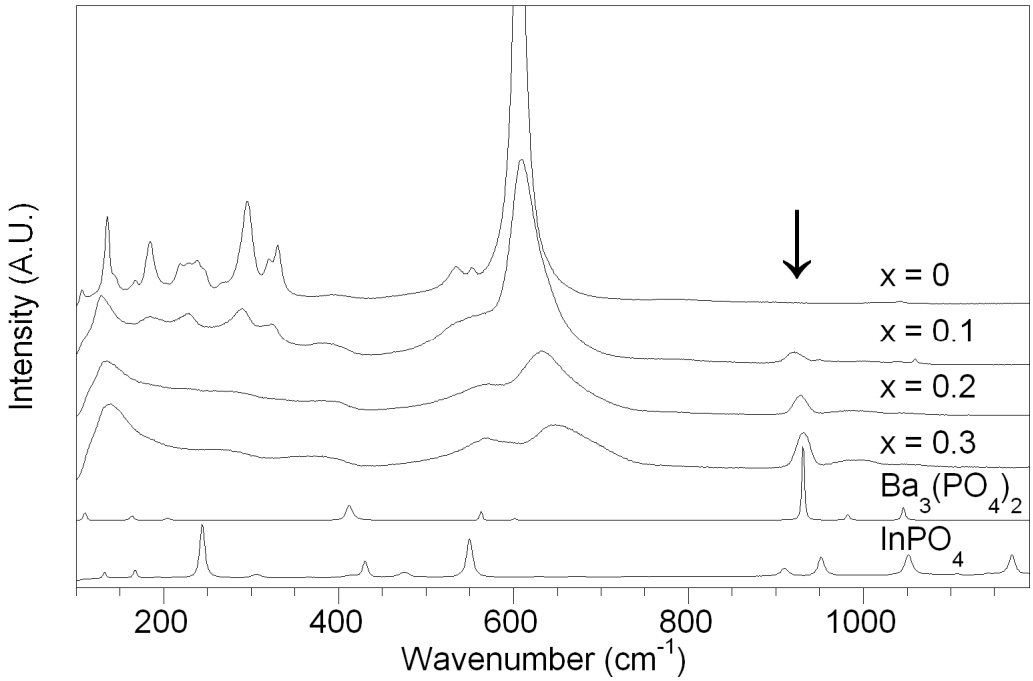

Fig. 3.7 Raman spectra of $Ba_2In_{2-x}P_xO_{5+x}$ showing the emergence of bands due to the presence of phosphate (most intense band highlighted). For comparison, Raman spectra for $Ba_3(PO_4)_2$ and $InPO_4$ are included.

The Raman spectra for the x = 0, 0.1, 0.2, 0.3 samples are given in Fig. 3.7. On incorporation of phosphate, there is the appearance of bands at ≈ 930 cm^{-1} and the reduction of the In-O bands, mostly notable for the band at 600 cm^{-1}. The position of the newly emerged bands at 930 cm^{-1} is similar to the bands observed for $Ba_3(PO_4)_2$, which again emphasize the close relationship of the phosphate group with Ba, as also evidenced by the NMR studies. This is not unexpected, as the shorter P-O bond when P is placed on the perovskite B cation site, will trigger a significant In-O bond length increase to an adjacent In site. Thus the

strongest linkage will be to Ba. In addition, there was a small peak shift to higher wavenumber with the increase in phosphate doping level, which is in agreement with chemical shift change in the ^{31}P NMR data. The In-O bands reduction was previously reported in other doping studies [14], which is a result of an introduction of disorder on the oxygen sublattice. However, here it should be noted that a perfect cubic perovskite should not be Raman active according to the selection rules, with the exception of possible second-order effects [15, 16]. Thus, the presence of some bands indicates that while the average structure determined in diffraction studies is cubic, there are considerable local distortions away from cubic symmetry as was shown by the PDF study.

3.3.2 Conductivity measurements

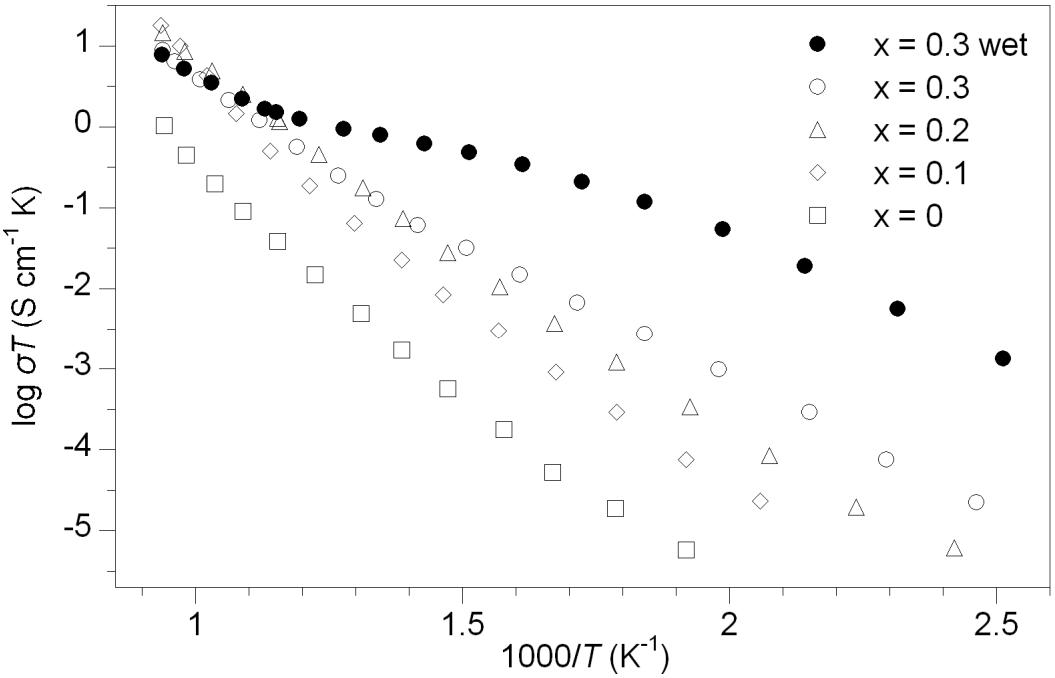

Fig. 3.8 Conductivity data in dry and wet N_2 for $Ba_2In_{2-x}P_xO_{5+x}$

Following on from the above structural studies, the effect of the phosphate doping on the conductivity was examined (Fig. 3.8) and the results showed that there is a general enhancement in conductivity. At low temperature, the conductivity is significantly enhanced with higher phosphate level, which can be associated with the oxygen sublattice disorder shown in X-ray powder diffraction and Raman spectroscopy studies. However, at higher temperature (greater than 700 °C), the x = 0.1 sample showed the highest conductivity and there is a slight reduction in conductivity with further doping (Fig. 3.9 and table 3.4). This high conductivity at elevated temperature even for the lowest P doped sample can be correlated with the presence of significant disorder in the oxygen sublattice in the phosphate doped samples at this elevated temperature, which was confirmed by variable temperature X-ray powder diffraction studies: e.g. the x = 0.1 sample showed the phase transition to higher symmetry above 625 °C indicating an increase of oxygen disorder (Fig. 3.10), and the temperature is also related to the steep increase in the conductivity for this sample (Fig. 3.8). Thus, the small decrease in the high temperature conductivity for higher doping levels is most likely related to the presence of a small degree of oxygen vacancy trapping on phosphate doping.

Table 3.4 Conductivity data for $Ba_2In_{2-x}P_xO_{5+x}$

Sample (nominal composition)	Conductivity (S cm^{-1})		
	400 °C		790 °C
	Wet	Dry	
$Ba_2In_2O_5$	1.6×10^{-5}	7.6×10^{-7}	9.7×10^{-4}
$Ba_2In_{1.9}P_{0.1}O_{5.1}$	1.8×10^{-4}	1.1×10^{-5}	1.6×10^{-2}
$Ba_2In_{1.8}P_{0.2}O_{5.2}$	8.8×10^{-4}	3.9×10^{-5}	1.4×10^{-2}
$Ba_2In_{1.7}P_{0.3}O_{5.3}$	7.8×10^{-4}	5.7×10^{-5}	8.4×10^{-3}

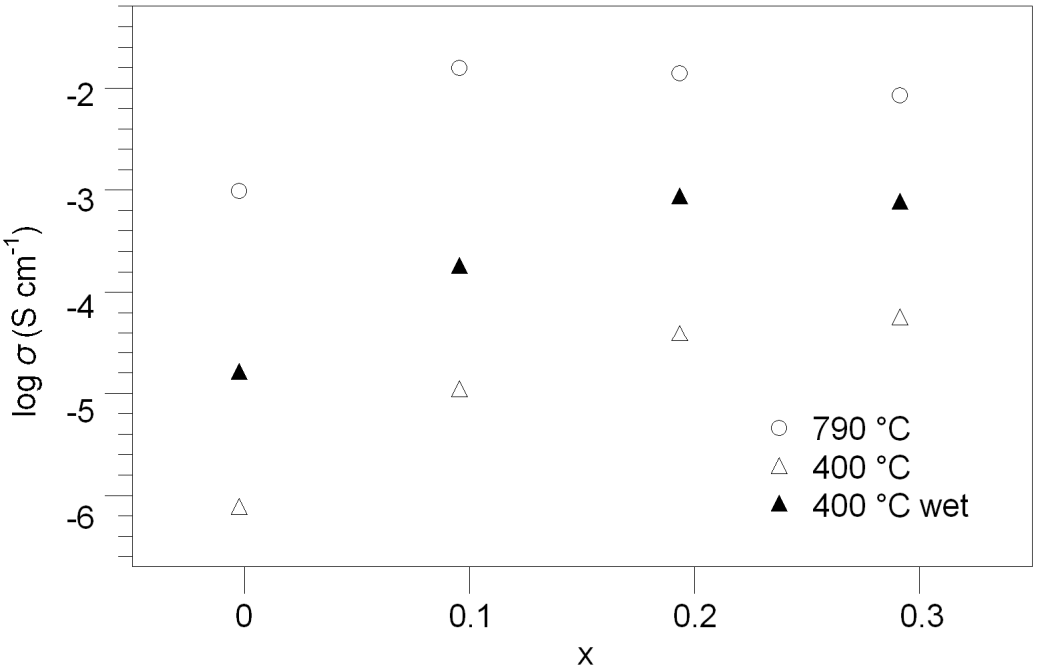

Fig. 3.9 Variation in $\sigma_{790°C}$ in dry N_2 and $\sigma_{400°C}$ in dry and wet N_2 for $Ba_2In_{2-x}P_xO_{5+x}$.

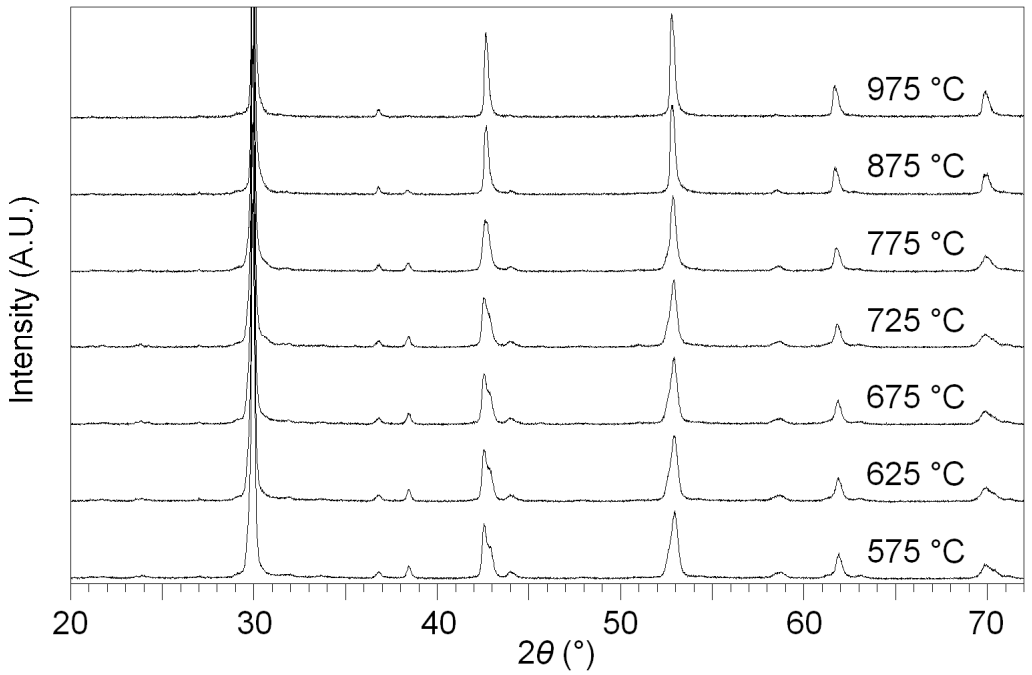

Fig. 3.10 Variable temperature XRD patterns for $Ba_2In_{1.9}P_{0.1}O_{5.1}$ showing a gradual reduction in orthorhombic splitting above 625°C.

A further enhancement in the conductivity was observed by changing the atmosphere to wet N_2, which is caused by water incorporation, as shown in the defect equation 3.2, similar to that of undoped $Ba_2In_2O_5$ [17, 18].

$$H_2O + 2O_O^x \leftrightarrow 2OH_O^\bullet + O_i'' \qquad (3.2)$$

This is an exothermic process in nature, and thus the introduction of water, and hence protons is most significant at lower temperatures. Therefore, an order of magnitude increase in conductivity in wet N_2 at temperatures below ≈ 350 °C was observed for all the samples, indicative of a significant protonic contribution. This proton conductivity then becomes less significant as the temperature increases, due to a reduction in the level of water incorporation. Thus the conductivities in dry and wet atmospheres do not show much difference above ≈ 650 °C.

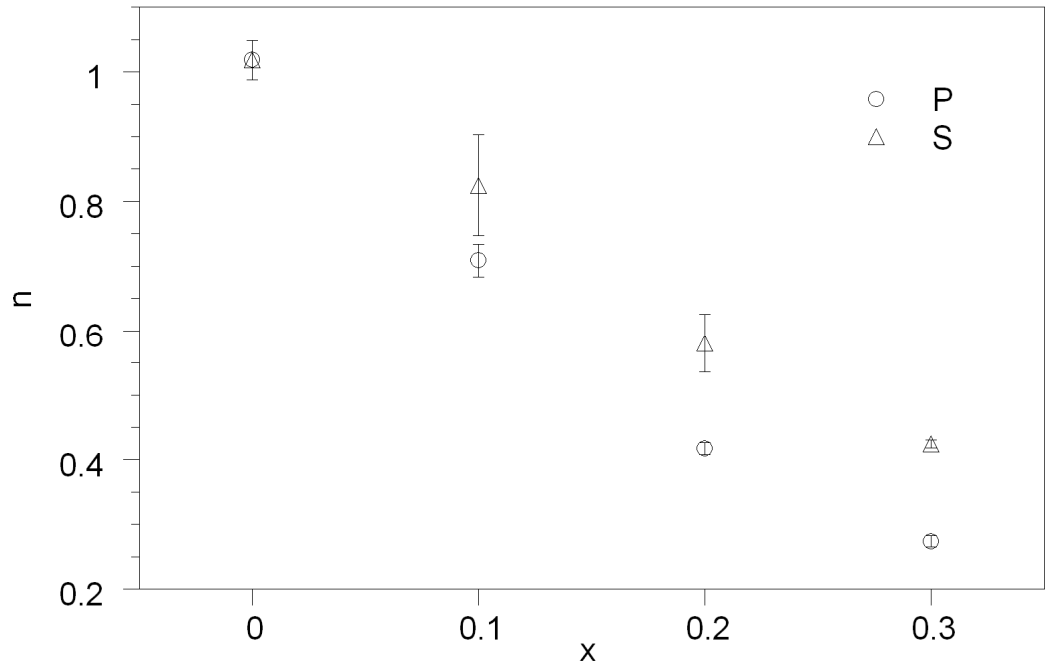

Fig. 3.11 Water contents (n) for $Ba_2In_{2-x}P_xO_{5+x}.nH_2O$ and $Ba_2In_{2-x}S_xO_{5+3x/2}.nH_2O$ determined from TGA data.

For the determination of the level of water incorporated, the samples were heated under wet N_2 to 800 °C, before slow cooling (0.4 °C min^{-1}) to room temperature. The water content was then determined by TGA measurements. The hydration and subsequent TGA measurements were performed in duplicate and the results showed a reduction in water content with increasing phosphate content (Fig. 3.11). This can be correlated with the increased oxygen content on phosphate incorporation which subsequently reduces the available sites for water incorporation. However, the reduction in water content did not have a simple linear correlation with the phosphate doping level but showed a much greater decrease. This can be explained by the tetrahedral geometry of P in the phosphate ion. Thus the vacant sites around the perovskite B site coordination sphere become inaccessible to the incoming water molecule, and thus the level of water incorporated is much lower than for dopants that have comparable size to In.

3.3.3 CO_2 stability results

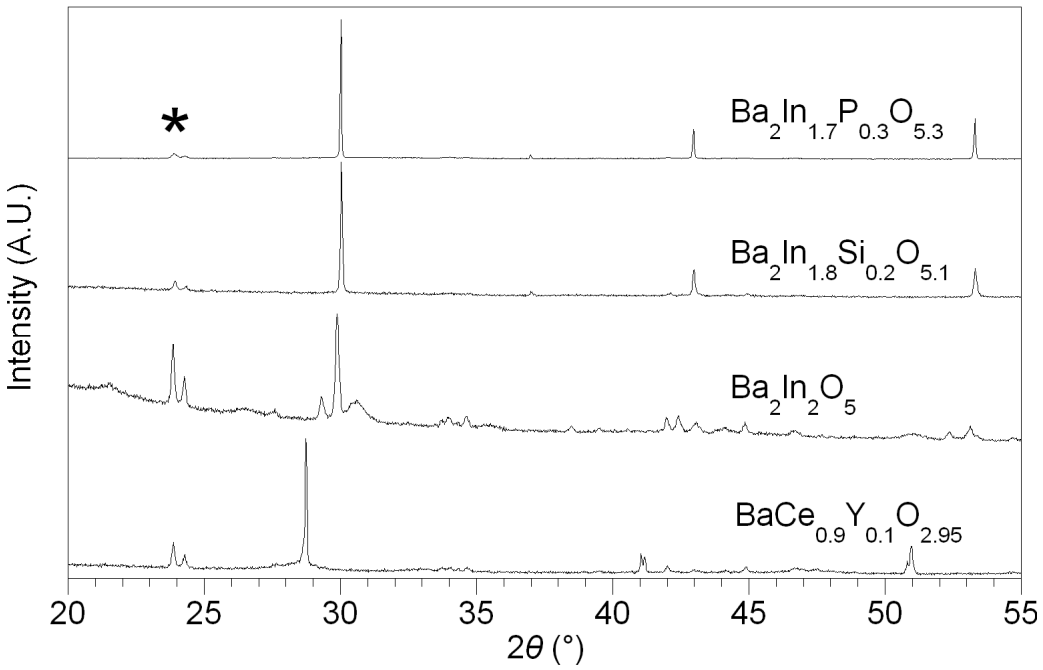

Fig. 3.12 XRD patterns for $Ba_2In_{1.8}Si_{0.2}O_{5.1}$, $Ba_2In_{1.7}P_{0.3}O_{5.3}$, $Ba_2In_2O_5$ and $Ba_2Ce_{0.9}Y_{0.1}O_{2.95}$ heating in CO_2 at 600°C for 12h.

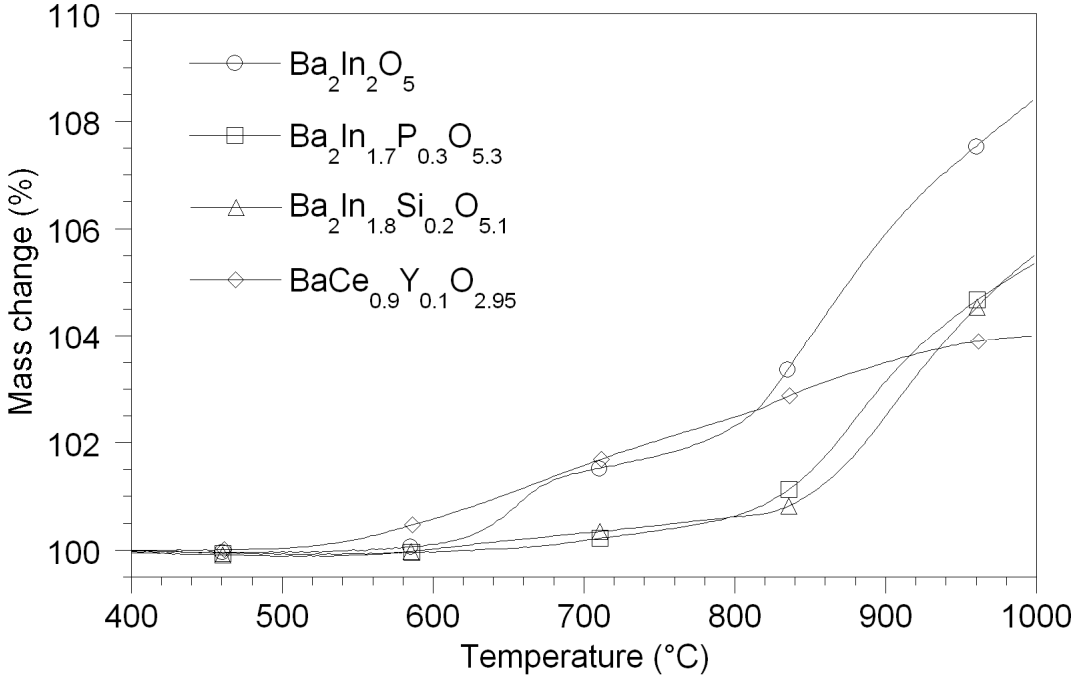

Fig. 3.13 TG profiles of $Ba_2In_2O_5$, $Ba_2Ce_{0.9}Y_{0.1}O_{2.95}$, $Ba_2In_{1.7}P_{0.3}O_{5.3}$ and $Ba_2In_{1.8}Si_{0.2}O_{5.1}$

One of the concerns of proton conducting perovskites for fuel cell applications is their stability towards CO_2. For example, although doped $BaCeO_3$ shows excellent proton conductivity, it is unstable towards CO_2 at fuel cell operating temperatures of 500-700 °C, leading to $BaCO_3$ formation [19, 20]. Thus, the effect of the phosphate doping on CO_2 stability was tested. X-ray diffraction data for the undoped $Ba_2In_2O_5$ and the x = 0.3 sample heated to 600 °C in CO_2 are given in Fig. 3.12. The data showed that the samples underwent CO_2 induced decomposition to varying degrees. In particular, the $BaCO_3$ impurities for the x = 0.3 sample were less significant than for undoped $Ba_2In_2O_5$ and also compared to other proton conducting perovskites such as Y doped $BaCeO_3$. The TGA results are shown in Fig. 3.13, and they provide further enlightenment on the relative stability towards CO_2. Undoped $Ba_2In_2O_5$ showed a clear mass increase ($BaCO_3$ formation by CO_2 pick up) at 600 °C, while the mass increase for $BaCe_{0.9}Y_{0.1}O_{2.95}$ was observed above 500 °C. However, phosphate doped $Ba_2In_2O_5$ showed generally flatter TG profile, with a significant mass change observed

only above 800 °C. Thus these results indicated that phosphate incorporation significantly enhanced the stability towards CO_2 of $Ba_2In_2O_5$, although at higher temperature, there was still some instability.

3.4 Sulphate doped systems: $Ba_2In_{2-x}S_xO_{5+3x/2}$ (x = 0, 0.1, 0.2, 0.3)

3.4.1 Structural study

The X-ray powder diffraction data of sulphate doped samples showed the transition from orthorhombic to cubic as shown earlier with phosphate doping (Fig. 3.14). Calculated cell parameters are given in table 3.5. Sulphate doping resulted in a smaller decrease in cell volume compared to phosphate doped samples, even though S^{6+} is smaller than P^{5+} (Fig. 3.2). In this case, the greater oxygen content resulting from incorporation of the higher charge species, S^{6+} in place of In^{3+} partially counterbalanced the effect of this size difference. The incorporation process can be represented using the relevant defect equation, as for phosphate doping, as shown below:

$$2(NH_4)_2SO_4 + 2In_{In}^{x} \leftrightarrow 2S_{In}^{\bullet\bullet\bullet} + 3O_i'' + In_2O_3 + 4NH_3\uparrow + 2H_2O\uparrow \qquad (3.3)$$

Table 3.5 Cell parameter data for $Ba_2In_{2-x}S_xO_{5+3x/2}$.

Sample (nominal composition)	Unit cell parameters (Å)			Unit cell volume (Å^3)
	a	b	c	
$Ba_2In_{1.9}S_{0.1}O_{5.15}$	6.007(2)	16.810(4)	6.011(5)	607.0(4)
$Ba_2In_{1.8}S_{0.2}O_{5.3}$	5.979(2)	16.843(3)	6.009(2)	605.2(2)
$Ba_2In_{1.7}S_{0.3}O_{5.45}$	4.227(1)	-	-	75.5(1)

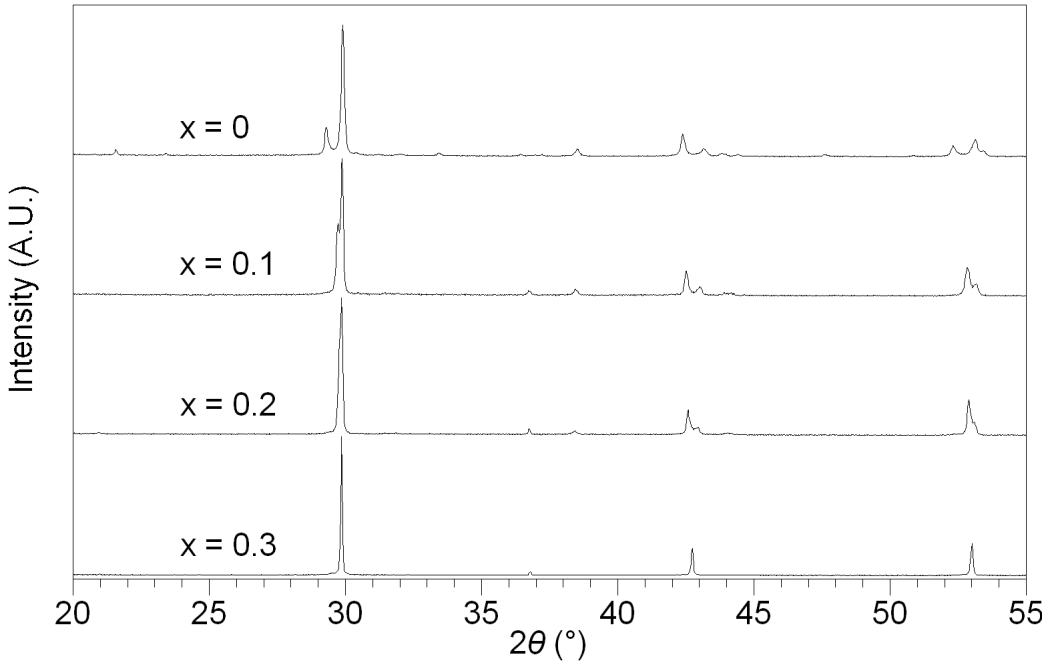

Fig. 3.14 X-ray diffraction patterns for $Ba_2In_{2-x}S_xO_{5+3x/2}$.

Structure refinement for the x = 0.3 sample, $Ba_2In_{1.7}S_{0.3}O_{5.45}$ from X-ray diffraction data suggested B site occupancies of 1.70(1) and 0.30(1) for In and S respectively, consistent with those expected (Fig. 3.15 and table 3.6). PDF fitting of $Ba_2In_{1.7}S_{0.3}O_{5.45}$ up to 10 Å with *Icmm* space group resulted in a better agreement factor than that with $Pm\bar{3}m$ space group (R_w of 8.2% against 24.1%) while PDF fitting from 10 to 20 Å with $Pm\bar{3}m$ space group resulted in a good agreement (R_w of 12.1%). Thus $Ba_2In_{1.7}S_{0.3}O_{5.45}$ also showed the local distortion from cubic symmetry as evidenced in $Ba_2In_{1.7}P_{0.3}O_{5.3}$.

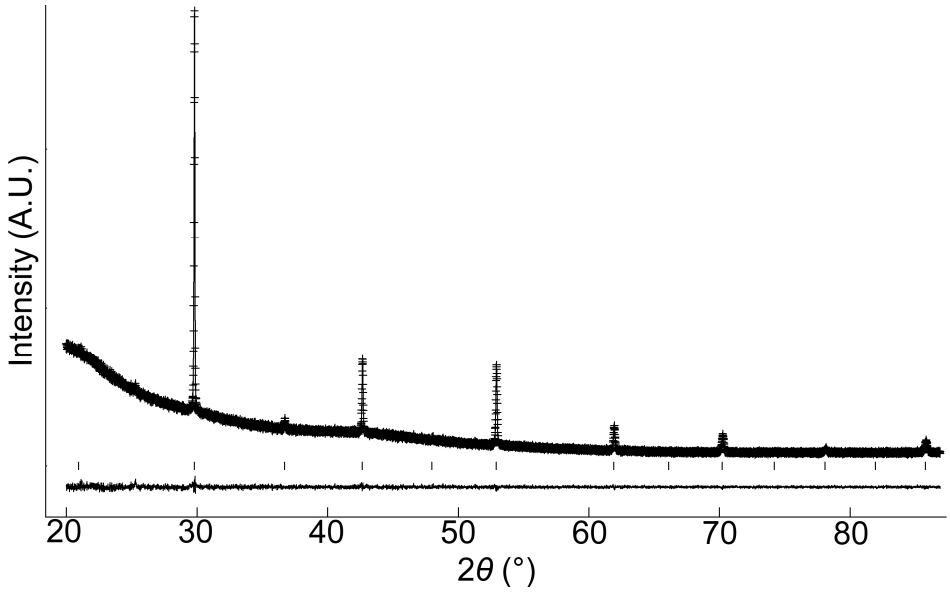

Fig. 3.15 Observed (cross), calculated (line), and difference plots (observed – calculated) of $Ba_2In_{1.7}S_{0.3}O_{5.45}$ from the Rietveld refinement for room temperature X-ray diffraction data.

Table 3.6 Refined structural parameters for $Ba_2In_{1.7}S_{0.3}O_{5.45}$ using cubic $Pm\bar{3}m$ (221) space group from room temperature X-ray diffraction data.

		a (Å)			R_{wp}	R_p	χ^2
		4.2352(1)			2.69	1.94	1.093
		x	y	z		Fractional occupancy	U_{iso} (Å^2 x 100)
Ba	1b	½	½	½		1.000	0.85(5)
In	1a	0	0	0		0.868(9)	2.17(16)
S	1a	0	0	0		0.133(9)	2.17(16)
O	3d	0	0	½		0.908(17)	8.42(48)

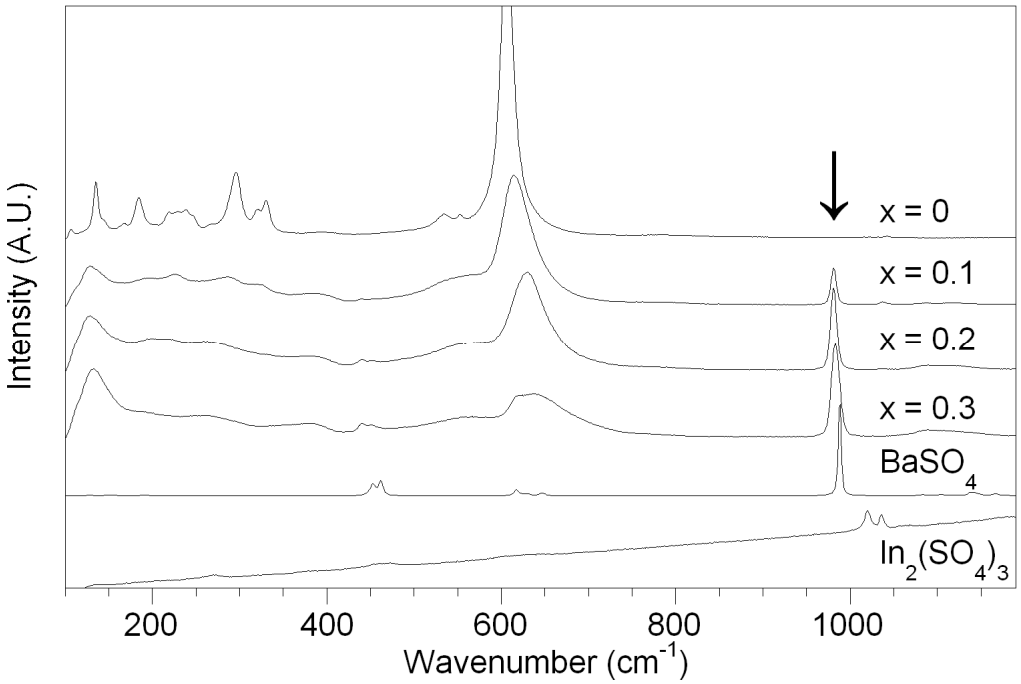

Fig. 3.16 Raman spectra of $Ba_2In_{2-x}S_xO_{5+3x/2}$ showing the emergence of bands due to the presence of sulphate (most intense band highlighted). For comparison, Raman spectra for $BaSO_4$ and $In_2(SO_4)_3$ are included.

The Raman spectra showed a similar trend to those for phosphate doping, with a decrease in the In-O band intensity with higher sulphate level, along with the appearance of new bands at ≈ 985cm^{-1}, which were assigned to sulphate groups in the structure (Fig. 3.16). As for phosphate doping, the sulphate groups incorporated showed greater association with the Ba cations compared to the In cations as the position of the new bands were in a similar position to the bands observed for $BaSO_4$. As outlined before, there should be no Raman active modes in a perfect cubic perovskite and the presence of these bands indicates that while the average structure determined in diffraction studies is cubic, there are considerable local distortions away from cubic symmetry, as also evidenced in the PDF studies [11].

3.4.2 Conductivity measurements

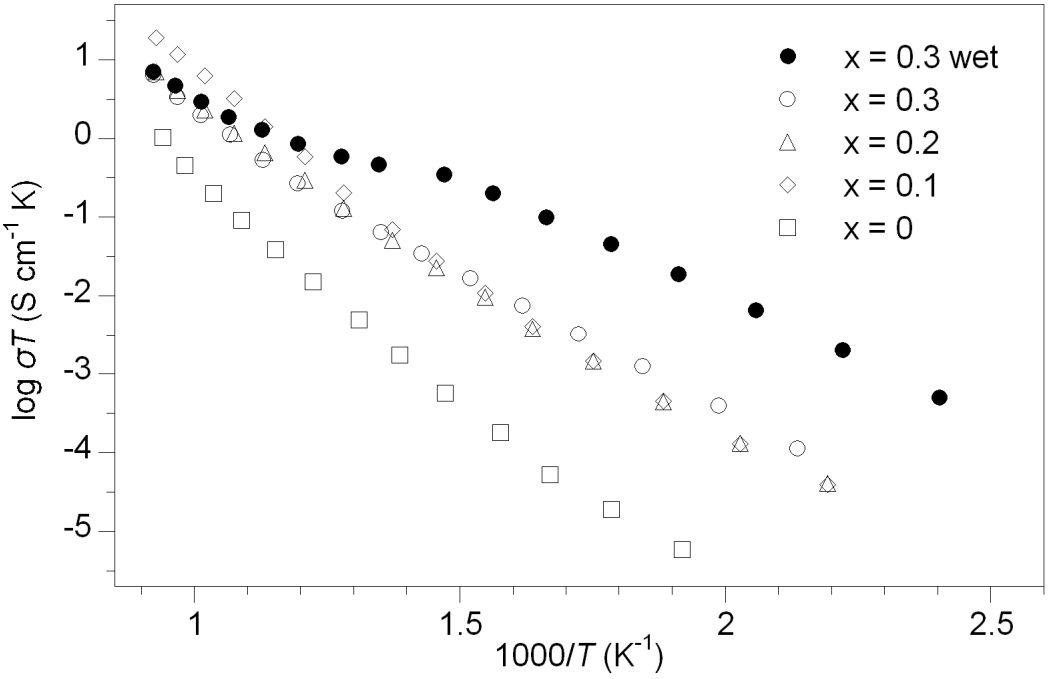

Fig. 3.17 Conductivity data in dry and wet N_2 for $Ba_2In_{2-x}S_xO_{5+3x/2}$

As for phosphate doping, there is an enhancement in the conductivity in dry N_2 on sulphate doping as a result of the increase in disorder on the oxygen sublattice (Fig. 3.17, 3.18 and table 3.7). However, while all sulphate doped samples showed higher conductivities than undoped $Ba_2In_2O_5$, there was not much difference at low temperature between the samples with various sulphate levels. At high temperature (greater than 650 °C), the x = 0.1 sample showed the best conductivity similar to the situation for phosphate doping. In general, the conductivities for the samples with the same level of doping were slightly lower compared to those of the phosphate doped samples, which can be correlated either with the lower number of oxide ion vacancies for the sulphate doped samples or with a stronger defect trapping effect by the sulphate groups. The conductivity in wet atmosphere was also enhanced in agreement with a contribution from protonic conduction. The water contents were determined by TGA analysis and showed slightly lower values than those for equivalent doping level phosphate

doped samples, in agreement with the higher starting oxygen content of the sulphate doped samples (Fig. 3.11). This correlation with the starting oxygen contents can be further emphasised by the plot of water content with the starting oxygen content for both phosphate and sulphate samples (Fig. 3.19).

Table 3.7 Conductivity data for $Ba_2In_{2-x}S_xO_{5+3x/2}$

Sample (nominal composition)	Conductivity (S cm^{-1})		
	400 °C		790 °C
	Wet	Dry	
$Ba_2In_{1.9}S_{0.1}O_{5.15}$	3.6×10^{-4}	3.2×10^{-5}	1.5×10^{-2}
$Ba_2In_{1.8}S_{0.2}O_{5.3}$	4.0×10^{-4}	2.6×10^{-5}	5.5×10^{-3}
$Ba_2In_{1.7}S_{0.3}O_{5.45}$	5.1×10^{-4}	3.3×10^{-5}	4.6×10^{-3}

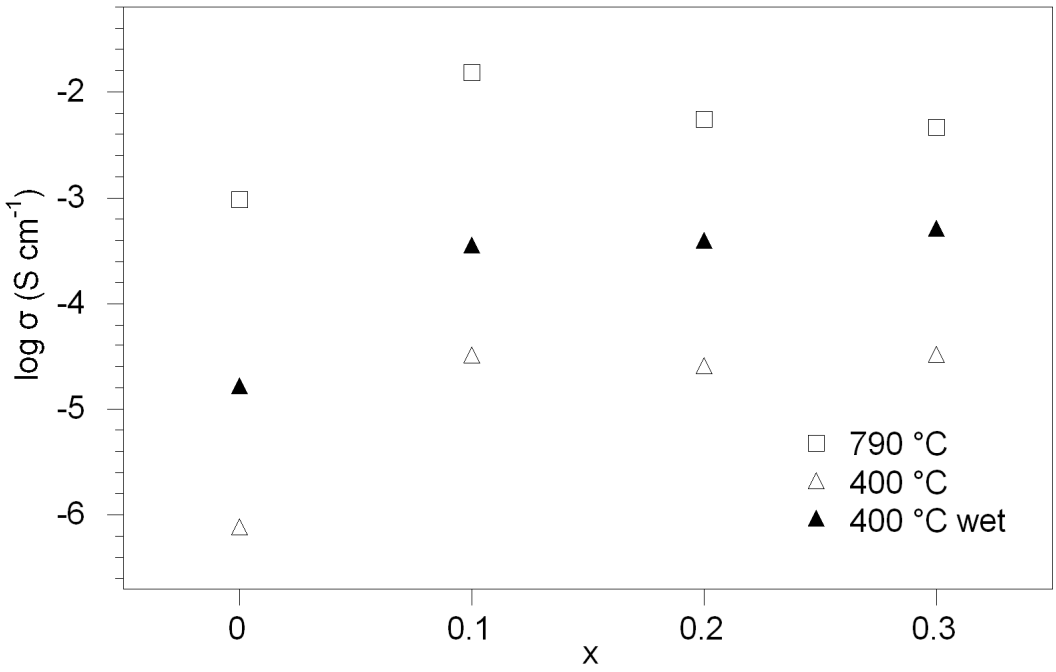

Fig. 3.18 Variation in $\sigma_{790\,°C}$ in dry N_2 and $\sigma_{400\,°C}$ in dry and wet N_2 for $Ba_2In_{2-x}S_xO_{5+3x/2}$

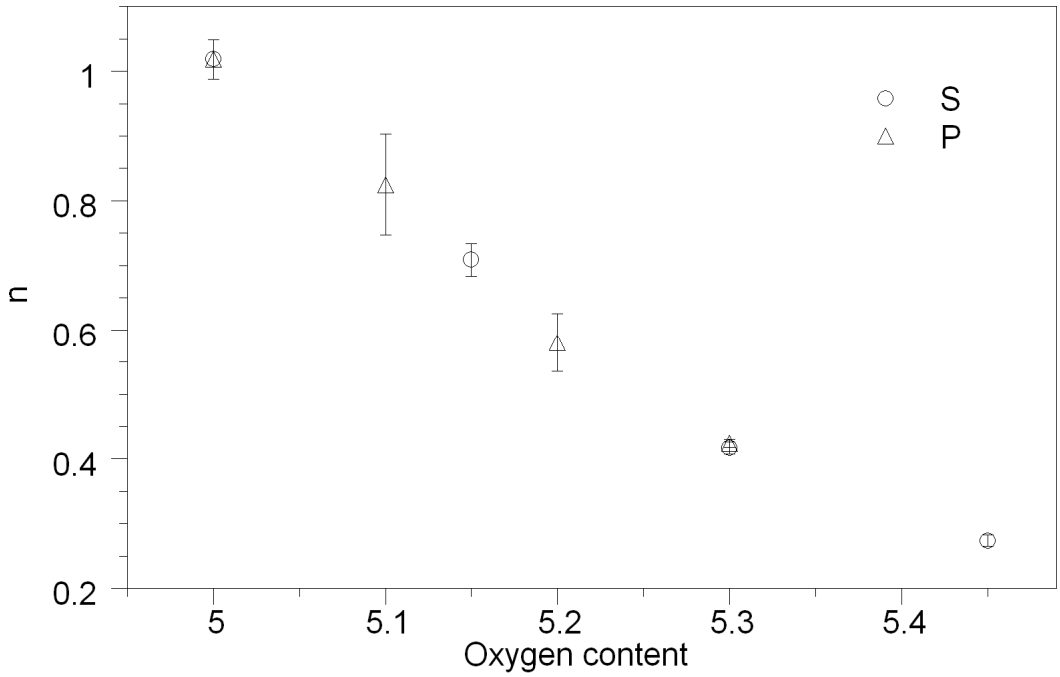

Fig. 3.19 Water contents (n) for $Ba_2In_{2-x}P_xO_{5+x}.nH_2O$ and $Ba_2In_{2-x}S_xO_{5+3x/2}.nH_2O$ as a function of oxygen content.

3.5 Silicate doped systems: $Ba_2In_{2-x}Si_xO_{5+x/2}$ (x = 0.1, 0.2)

3.5.2 Structural study

The X-ray powder diffraction data for the silicate doped samples showed the same transition from orthorhombic to cubic symmetry as shown by phosphate and sulphate doping (Fig. 3.20). For higher Si levels, small Ba_2SiO_4 impurities were observed, indicating a solubility limit of ≈ 10%. Calculated cell parameters are given in table 3.8, and silicate doping resulted in a greater decrease in cell volume compared to the phosphate doped samples, although Si^{4+} is larger in size than P^{5+} (Fig. 3.2). This can be explained by the fact that the lower oxygen level introduced by incorporation of the lower charged Si species outweighing this effect of size difference. The incorporation process can be represented using the defect equation below:

$$2SiO_2 + 2In_{In}^{x} \leftrightarrow 2Si_{In}^{\bullet} + O_i'' + In_2O_3 \qquad (3.4)$$

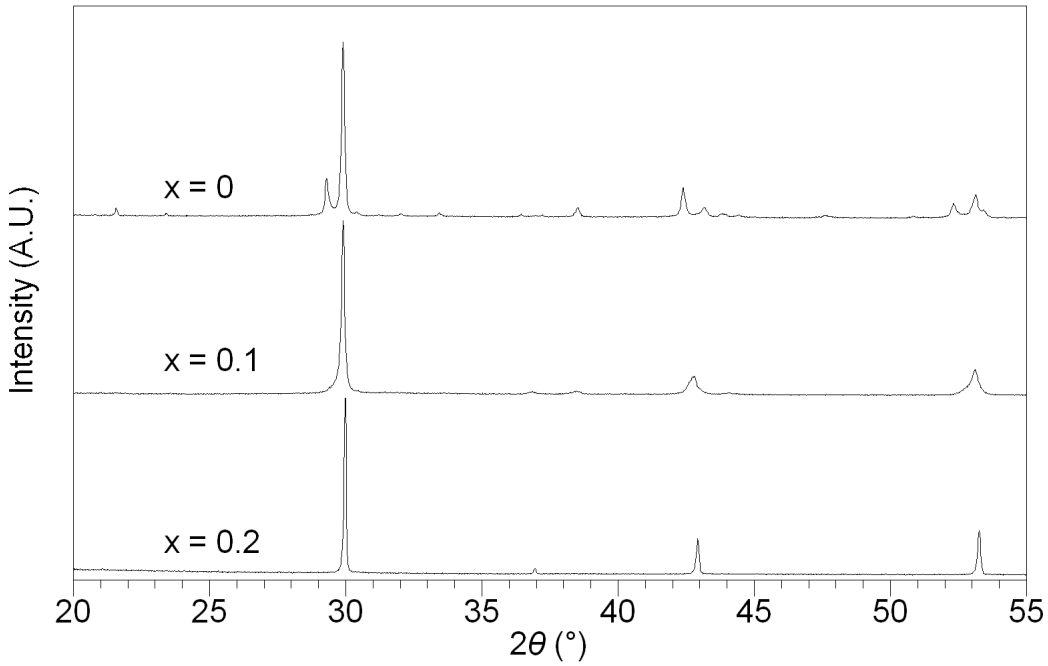

Fig. 3.20 X-ray diffraction patterns for $Ba_2In_{2-x}Si_xO_{5+x/2}$

Table 3.8 Cell parameter data for $Ba_2In_{2-x}Si_xO_{5+x/2}$

Sample (nominal composition)	Unit cell parameters (Å)			Unit cell volume (Å^3)
	a	b	c	
$Ba_2In_2O_5$	6.089(2)	16.736(8)	5.963(2)	607.6(2)
$Ba_2In_{1.9}Si_{0.1}O_{5.05}$	6.012(5)	16.794(5)	5.962(6)	602.0(4)
$Ba_2In_{1.8}Si_{0.2}O_{5.1}$	4.209(1)	-	-	74.6(1)

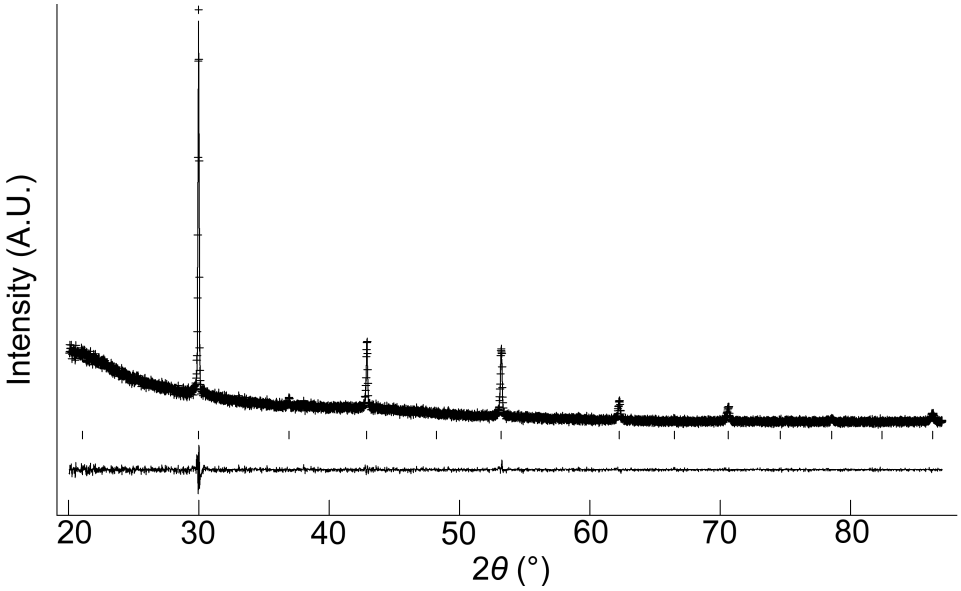

Fig. 3.21 Observed (cross), calculated (line), and difference plots (observed – calculated) of $Ba_2In_{1.8}Si_{0.2}O_{5.1}$ from the Rietveld refinement for room temperature X-ray diffraction data.

Table 3.9 Refined structural parameters for $Ba_2In_{1.8}Si_{0.2}O_{5.1}$ with cubic $Pm\bar{3}m$ (221) space group, from room temperature Neutron diffraction data

		a (Å)		R_{wp}	R_p	χ^2
		4.2094(1)		7.02	5.35	1.14
		x	y	z	Fractional occupancy	U_{iso} (Å^2 x 100)
Ba	1b	½	½	½	1.000	4.79(4)
In	1a	0	0	0	0.890(4)	3.91(4)
Si	1a	0	0	0	0.110(4)	3.91(4)
O	3d	0	0	½	0.856(18)	8.85(11)

Structure refinement for the x = 0.2 sample, $Ba_2In_{1.8}S_{0.2}O_{5.1}$ from X-ray diffraction data suggested B site occupancies of 1.80(1) and 0.20(1) for In and Si respectively, consistent with that expected (Fig. 3.21 and table 3.9).

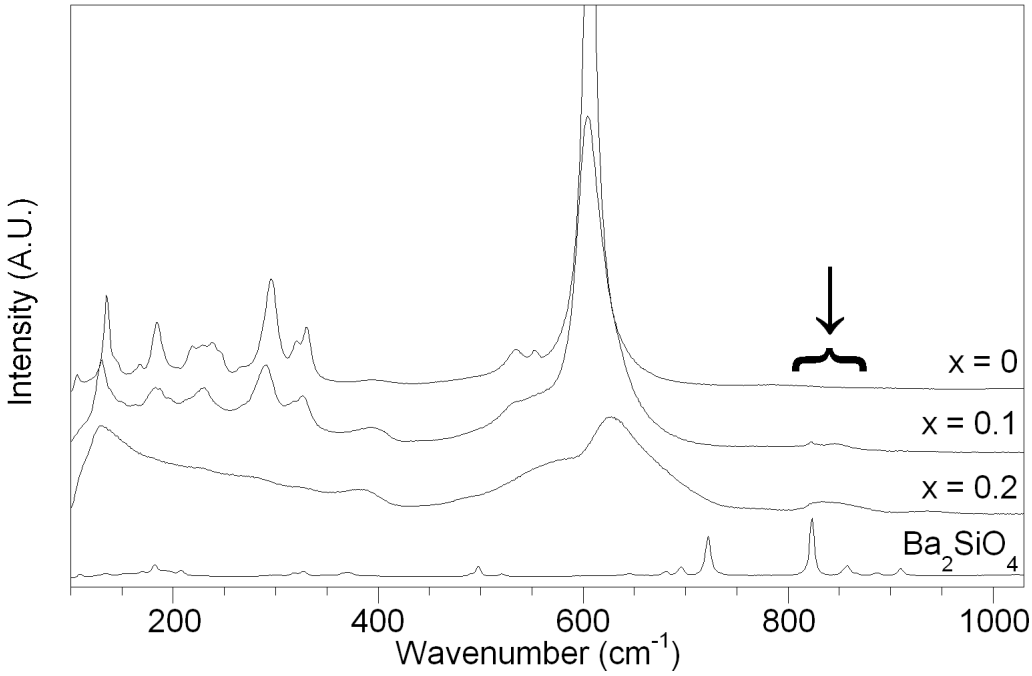

Fig. 3.22 Raman spectra for $Ba_2In_{2-x}Si_xO_{5+x/2}$ showing the emergence of bands due to the presence of silicate (most intense bands highlighted). For comparison, the Raman spectrum for Ba_2SiO_4 is included.

The Raman spectra showed a similar trend to those for phosphate and sulphate doping, with a decrease in the In-O band intensity with higher silicate level, along with the appearance of new bands at 800-900 cm^{-1}, similar to those of observed for Ba_2SiO_4, and consistent with tetrahedrally coordinated Si (Fig. 3.22). As outlined before, there should be no Raman active modes in a perfect cubic perovskite. The presence of these bands therefore indicates that while the average structure determined in diffraction studies is cubic, there are considerable local distortions away from cubic symmetry as illustrated in the PDF studies of phosphate and sulphate doped systems.

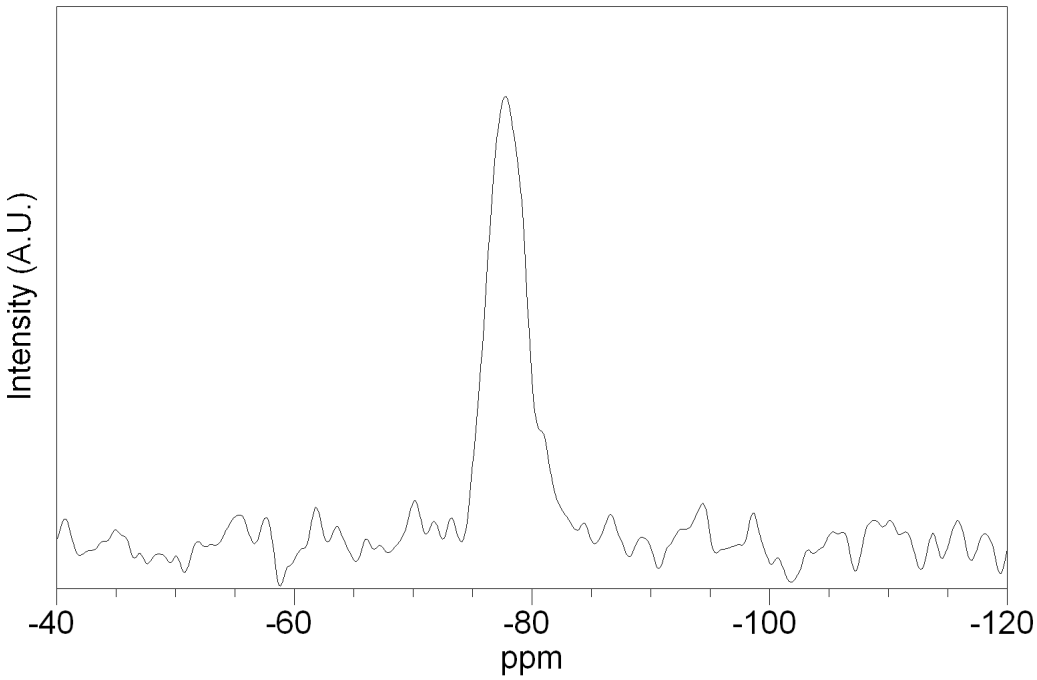

Fig. 3.23 ^{29}Si NMR spectrum for $Ba_2In_{1.8}Si_{0.2}O_{5.1}$

The ^{29}Si NMR spectrum for $Ba_2In_{1.8}Si_{0.2}O_{5.1}$ is given in Fig. 3.23 and it showed a single peak at a chemical shift of -77.8 ppm, which corresponds to tetrahedral Si (Q^0), consistent with the Raman spectra analysis. The chemical shift is observed at higher field than that of Ba_2SiO_4 (-70.3 ppm) [21], which suggests that there are interactions with both Ba and In in the present samples.

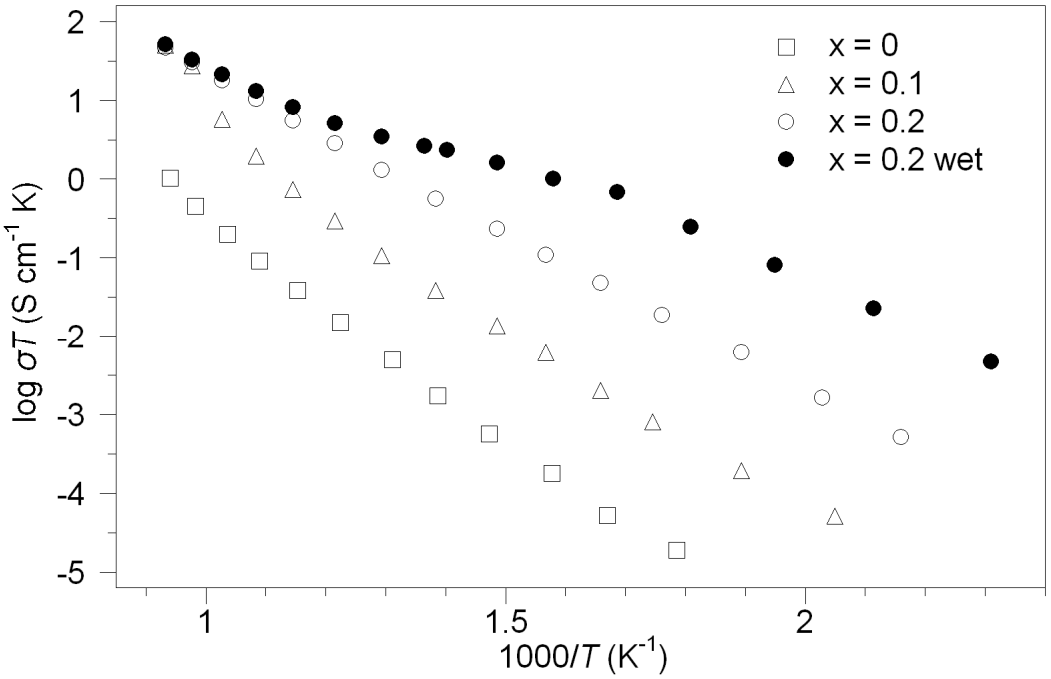

Fig. 3.24 Conductivity data in dry and wet N_2 for $Ba_2In_{2-x}Si_xO_{5+x/2}$

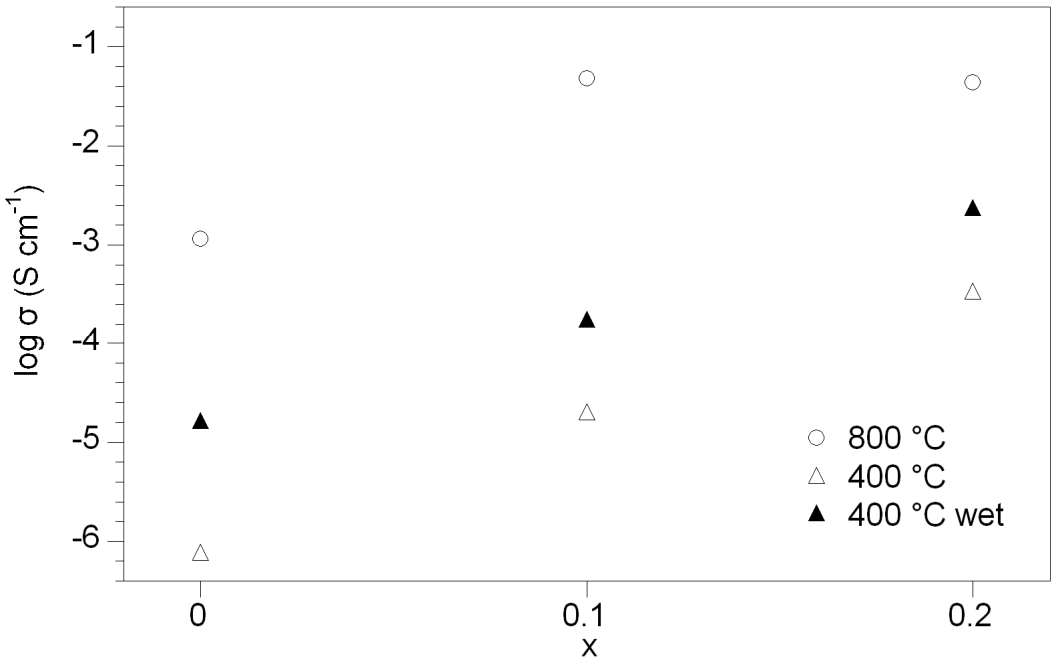

Fig. 3.25 Variation in $\sigma_{800\,°C}$ in dry N_2 and $\sigma_{400\,°C}$ in dry and wet N_2 for $Ba_2In_{2-x}Si_xO_{5+x/2}$

3.5.2 Conductivity measurements

It was particularly important to examine the effect of Si incorporation on conductivity as there are numerous reports that have argued the detrimental effect of silica addition to SOFC electrolytes such as yttria stabilised zirconia [22-24]. As for phosphate and sulphate doping, there is an enhancement in the conductivity in dry N_2 on silicate doping as a result of the increase in disorder on the oxygen sublattice (Fig. 3.24 and 3.25). At low temperature, the enhancement is substantial, as for the x = 0.2 sample a conductivity increase by nearly three orders of magnitude was observed (table 3.10), while at higher temperature the highest conductivity was observed for the x = 0.1 sample. The variable temperature X-ray powder diffraction studies for the x = 0.1 sample showed a phase transition to higher symmetry above 700 °C indicating the increase of oxygen disorder (Fig. 3.26), and this temperature is also related to the steep increase in the conductivity for this sample (Fig. 3.24). Thus, the possible presence of a small degree of vacancy defect trapping on silicate doping is most likely responsible for the lower conductivity of the x = 0.2 sample compared to the x = 0.1 sample in the higher temperature region, as already shown for phosphate and sulphate doping. The conductivity in a wet N_2 atmosphere was also significantly enhanced through a contribution from protonic conduction and the x = 0.2 sample showed a conductivity of 2.4 x 10^{-3} S cm^{-1} at 400 °C in wet N_2 which is comparable to that of the best proton conducting perovskites, $Ba(Zr/Ce)_{1-x}Y_xO_{3-x/2}$ [25], emphasizing the strong beneficial effect of Si doping in $Ba_2In_2O_5$. Thus the results from these studies are contrary to prior studies of fluorite electrolytes of the effect of SiO_2 incorporation, with a large improvement in the conductivity being observed. This can be related to the fact that in the present case the Si enters the structure, rather than collecting at the grain boundaries.

Table 3.10 Conductivity data for $Ba_2In_{2-x}Si_xO_{5+x/2}$

Sample (nominal composition)	Conductivity (S cm^{-1})		
	400 °C		800 °C
	Wet	Dry	
$Ba_2In_2O_5$	1.6×10^{-5}	7.6×10^{-7}	1.2×10^{-3}
$Ba_2In_{1.9}Si_{0.1}O_{5.05}$	1.8×10^{-4}	2.0×10^{-5}	4.7×10^{-2}
$Ba_2In_{1.8}Si_{0.2}O_{5.1}$	2.4×10^{-3}	3.4×10^{-4}	4.3×10^{-2}

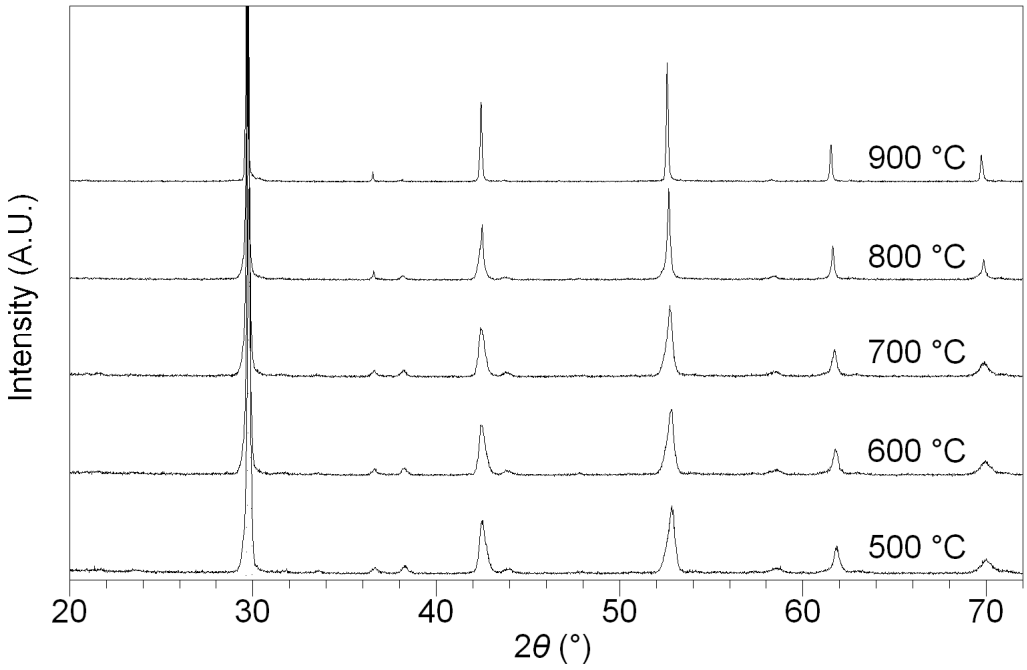

Fig. 3.26 Variable temperature XRD patterns for $Ba_2In_{1.9}Si_{0.1}O_{5.05}$ showing a gradual reduction in orthorhombic splitting above 700 °C.

3.5.3 CO_2 stability results

X-ray diffraction studies for the x = 0.2 sample heated to 600 °C in CO_2 showed an enhancement in the stability towards CO_2 through silicate doping, which was also confirmed by TGA studies (Fig. 3.12 and 3.13). As for the phosphate doping, $BaCO_3$ impurities were less significant than undoped $Ba_2In_2O_5$ and the TG profile was generally flatter with a significant mass change observed only above 800 °C.

3.6 Oxyanion doped $Ba_2In_2O_5$ systems co-doped with La, Zr

3.6.1 Structural study

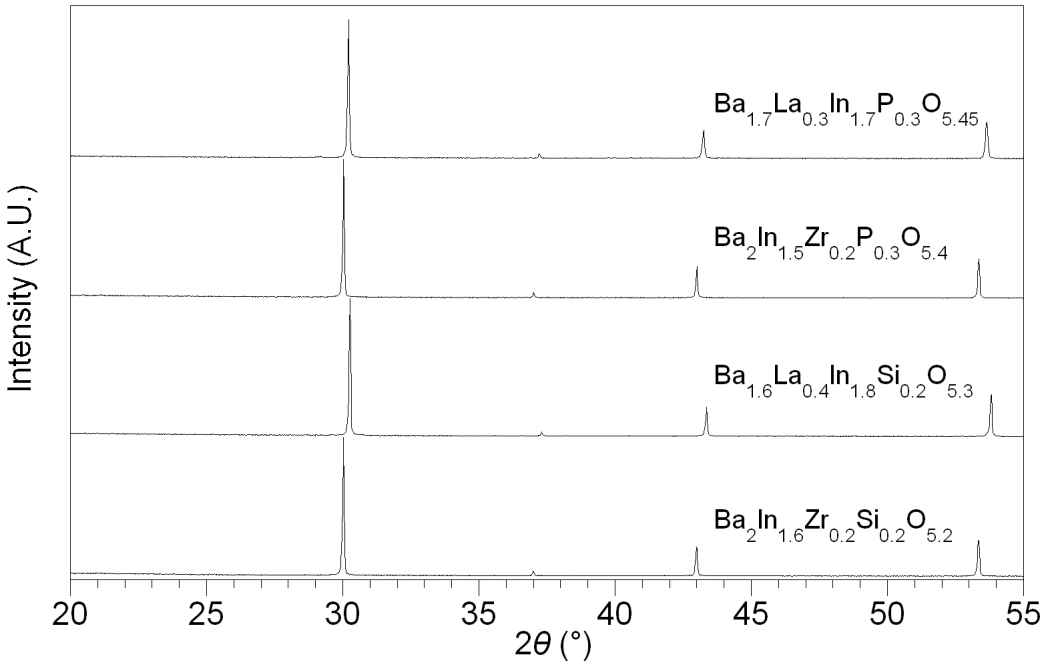

Fig. 3.27 XRD patterns for $Ba_{1.7}La_{0.3}In_{1.7}P_{0.3}O_{5.45}$, $Ba_2In_{1.5}Zr_{0.2}P_{0.3}O_{5.4}$, $Ba_{1.6}La_{0.4}In_{1.8}Si_{0.2}O_{5.3}$ and $Ba_2In_{1.6}Zr_{0.2}Si_{0.2}O_{5.2}$.

Although phosphate and silicate incorporation enhanced the stability towards CO_2 of $Ba_2In_2O_5$, the samples still showed some instability at higher temperature. Therefore, in order to try to enhance the CO_2 stability further, co-doping with La, Zr was investigated and its effect on conductivity and CO_2 stability examined. Single phase $Ba_{2-x}La_xIn_{1.7}P_{0.3}O_{5.3+x/2}$, $Ba_{2-x}La_xIn_{1.8}Si_{0.2}O_{5.1+x/2}$ ($0 \leq x \leq 0.4$) and $Ba_2In_{1.7-x}Zr_xP_{0.3}O_{5.3+x/2}$, $Ba_2In_{1.8-x}Zr_xSi_{0.2}O_{5.1+x/2}$ ($0 \leq x \leq 0.4$) were prepared and the CO_2 stability and conductivities were studied. The preliminary results revealed that higher level of La and Zr inhibited the reaction with CO_2 at higher temperature, although this beneficial effect was to the detriment of the conductivity. The compositions $Ba_{1.7}La_{0.3}In_{1.7}P_{0.3}O_{5.45}$, $Ba_2In_{1.5}Zr_{0.2}P_{0.3}O_{5.4}$, $Ba_{1.6}La_{0.4}In_{1.8}Si_{0.2}O_{5.3}$ and $Ba_2In_{1.6}Zr_{0.2}Si_{0.2}O_{5.2}$ were identified as the most promising for the promotion of CO_2 stability while retaining high conductivity. Thus these compositions were subjected to the more

detailed analysis. X-ray diffraction data for these samples are given in Fig. 3.27 and calculated cell parameters are shown in table 3.11 along with values for undoped $Ba_2In_2O_5$ and P/Si singly doped samples. On the incorporation of La and Zr, there is a reduction in the cell parameters reflecting the smaller size of La^{3+} and Zr^{4+} compared to Ba^{2+} and In^{3+} respectively. The cell volume change on La doping was greater due to the greater size difference between Ba^{2+} and La^{3+}.

Table 3.11.a Cell parameter data for P and La or Zr co-doped $Ba_2In_2O_5$

Sample (nominal composition)	Unit cell parameters (Å)			Unit cell volume (Å^3)
	a	b	c	
$Ba_2In_2O_5$	6.089(2)	16.736(8)	5.963(2)	607.6(2)
$Ba_2In_{1.7}P_{0.3}O_{5.3}$	4.208(1)	-	-	74.5(1)
$Ba_{1.7}La_{0.3}In_{1.7}P_{0.3}O_{5.45}$	4.183(1)	-	-	73.2(1)
$Ba_2In_{1.5}Zr_{0.2}P_{0.3}O_{5.4}$	4.199(1)	-	-	74.0(1)

Table 3.11.b Cell parameter data for Si and La or Zr co-doped $Ba_2In_2O_5$

Sample (nominal composition)	Unit cell parameters (Å)			Unit cell volume (Å^3)
	a	b	c	
$Ba_2In_2O_5$	6.089(2)	16.736(8)	5.963(2)	607.6(2)
$Ba_2In_{1.8}Si_{0.2}O_{5.1}$	4.209(1)			74.6(1)
$Ba_{1.6}La_{0.4}In_{1.8}Si_{0.2}O_{5.3}$	4.167(1)			72.4(1)
$Ba_2In_{1.6}Zr_{0.2}Si_{0.2}O_{5.2}$	4.200(1)			74.1(1)

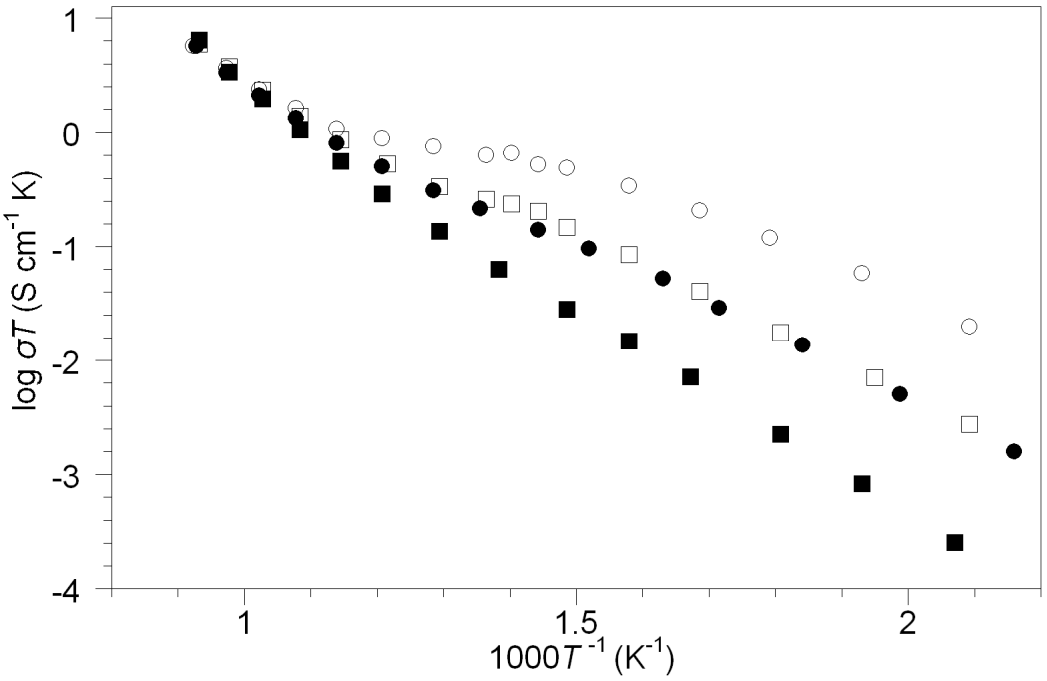

Fig. 3.28.a Conductivity data for $Ba_{1.7}La_{0.3}In_{1.7}P_{0.3}O_{5.45}$ (square) and $Ba_2In_{1.5}Zr_{0.2}P_{0.3}O_{5.4}$ (circle) in dry N_2 (filled) and wet N_2 (open).

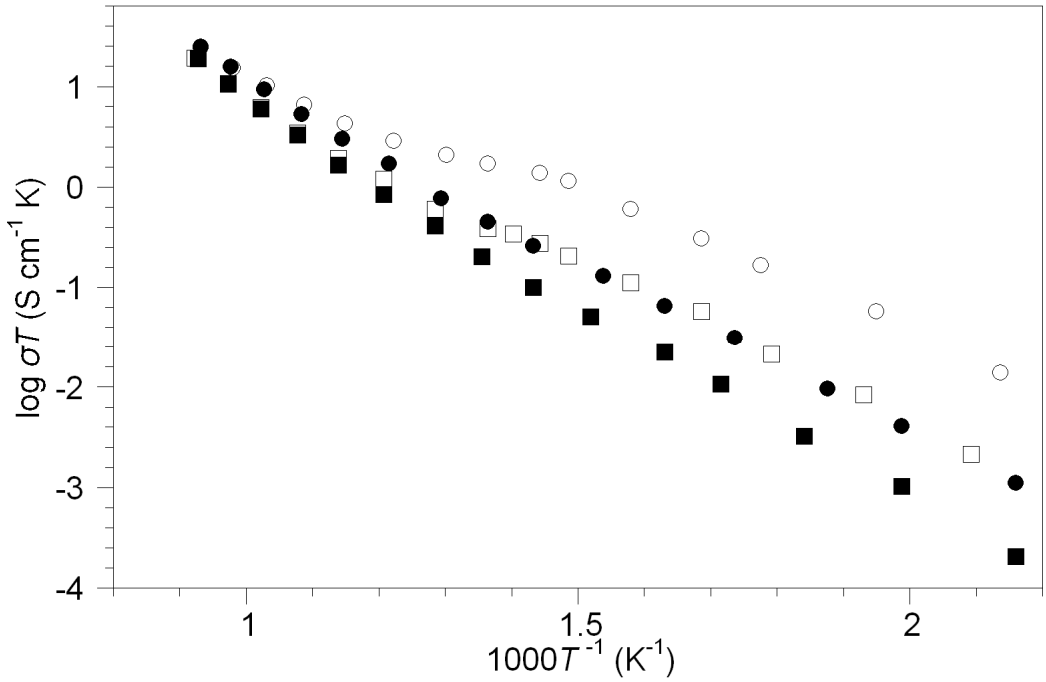

Fig. 3.28.b Conductivity data for $Ba_{1.6}La_{0.4}In_{1.8}Si_{0.2}O_{5.3}$ (square) and $Ba_2In_{1.6}Zr_{0.2}Si_{0.2}O_{5.2}$ (circle) in dry N_2 (filled) and wet N_2 (open).

3.6.2 Conductivity measurements

The conductivities of these samples and the P/Si singly doped samples are compared in Fig. 3.28 and table 3.12. As mentioned earlier, both La and Zr co-doping decreased conductivity compared to the P/Si singly doped phases. However, the decrease for the Zr co-doped samples was lower compared to those of La co-doped samples, while the Si based co-doped samples showed the highest conductivity. The difference in the decrease may be originating from the lower cell volume reduction of the Zr co-doped samples. Overall, all samples showed high conductivity with a further enhancement in wet atmospheres at low temperature (less than 650 °C) through a protonic contribution. In particular, $Ba_2In_{1.6}Zr_{0.2}Si_{0.2}O_{5.2}$ showed a high conductivity of 2.7 x 10^{-3} S cm^{-1} at 500 °C, which represents a promising value for technological applications.

Table 3.12.a Conductivity data for P and La or Zr co-doped series.

Sample (nominal composition)	Conductivity (S cm^{-1})		
	500 °C		800 °C
	Wet	Dry	
$Ba_2In_{1.7}P_{0.3}O_{5.3}$	1.9 x 10^{-3}	5.0 x 10^{-4}	1.2 x 10^{-2}
$Ba_{1.7}La_{0.3}In_{1.7}P_{0.3}O_{5.45}$	4.4 x 10^{-4}	1.8 x 10^{-4}	6.0 x 10^{-3}
$Ba_2In_{1.5}Zr_{0.2}P_{0.3}O_{5.4}$	9.7 x 10^{-4}	4.0 x 10^{-4}	5.3 x 10^{-3}

Table 3.12.b Conductivity data for Si and La or Zr co-doped series.

Sample (nominal composition)	Conductivity (S cm^{-1})		
	500 °C		800 °C
	Wet	Dry	
$Ba_2In_{1.8}Si_{0.2}O_{5.1}$	4.5 x 10^{-3}	1.7 x 10^{-3}	4.3 x 10^{-2}
$Ba_{1.6}La_{0.4}In_{1.8}Si_{0.2}O_{5.3}$	7.7 x 10^{-4}	5.3 x 10^{-4}	1.8 x 10^{-2}
$Ba_2In_{1.6}Zr_{0.2}Si_{0.2}O_{5.2}$	2.7 x 10^{-3}	9.9 x 10^{-4}	2.3 x 10^{-2}

3.6.3 CO_2 Stability results

X-ray diffraction data for these co-doped samples heated to 600 °C in CO_2 showed no evidence of $BaCO_3$ formation, which indicates an enhancement in the CO_2 stability by addition of La and Zr to singly Si, P doped phases. The heating temperature was increased to 800 °C and only the X-ray diffraction data for the P based co-doped samples showed the presence of small $BaCO_3$, which indicates the excellent CO_2 stability for the Si based co-doped samples (Fig. 3.29). The TG profiles of these latter samples are given in Fig. 3.30 and they showed no significant increase in mass up to 1000 °C, although there is a small mass increase for the P containing co-doped samples above 600 °C, which again emphasizes the excellent CO_2 stability of the Si based co-doped samples.

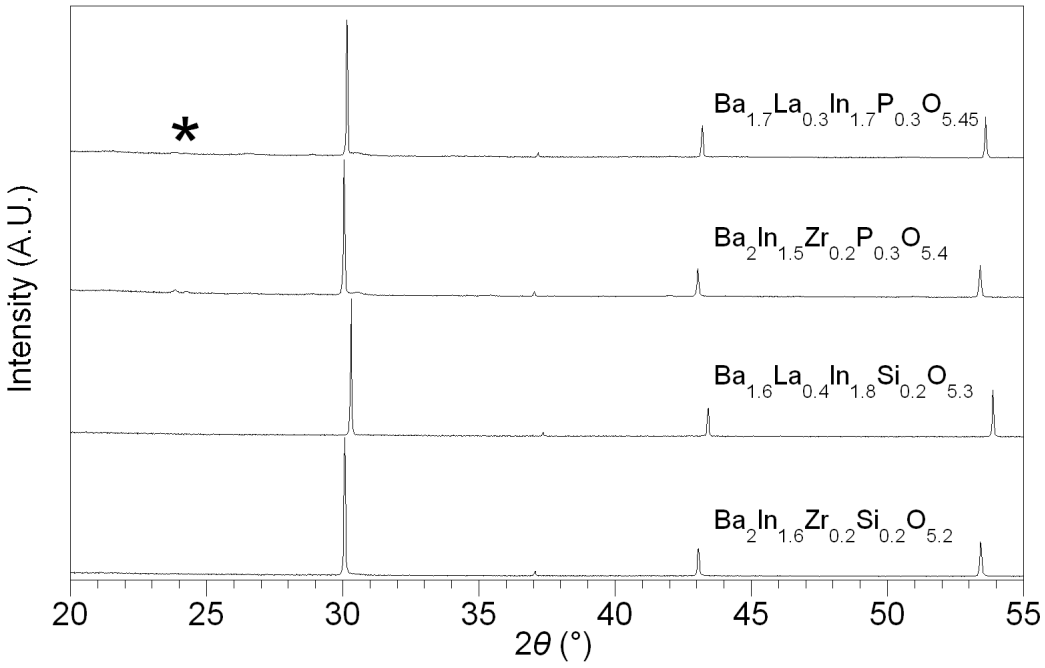

Fig. 3.29 XRD patterns for $Ba_{1.7}La_{0.3}In_{1.7}P_{0.3}O_{5.45}$, $Ba_2In_{1.5}Zr_{0.2}P_{0.3}O_{5.4}$, $Ba_{1.6}La_{0.4}In_{1.8}Si_{0.2}O_{5.3}$ and $Ba_2In_{1.6}Zr_{0.2}Si_{0.2}O_{5.2}$ heating in CO_2 at 800°C 12h

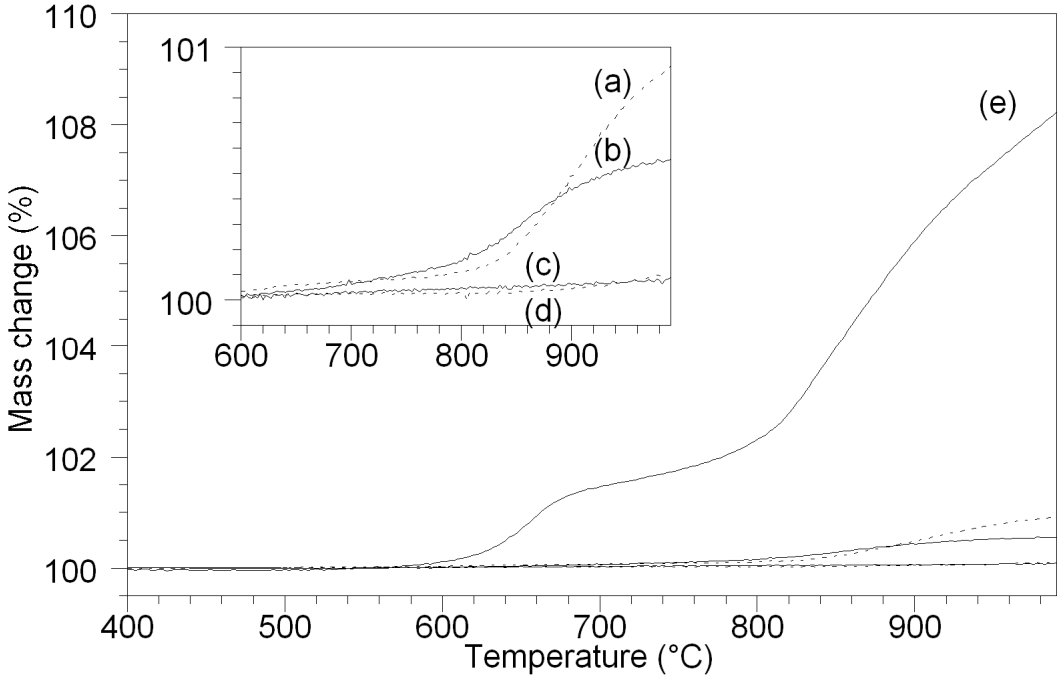

Fig. 3.30 TG profiles of (a) $Ba_{1.7}La_{0.3}In_{1.7}P_{0.3}O_{5.45,}$ (b) $Ba_2In_{1.5}Zr_{0.2}P_{0.3}O_{5.4}$, (c) $Ba_2In_{1.6}Zr_{0.2}Si_{0.2}O_{5.2}$ (d) $Ba_{1.6}La_{0.4}In_{1.8}Si_{0.2}O_{5.3}$ and (e) $Ba_2In_2O_5$.

The enhancement in CO_2 stability can be explained by two factors, as discussed by Yi et al. in their work on the stability of Ba(Fe,Co, Nb)O_{3-x} perovskite cathode materials [26]: namely the reduced oxygen vacancy levels and the increased acidity of the perovskite. In the present study, the incorporation of all the dopants, lanthanum, phosphate, silicate and zirconium will increase the oxygen content by charge compensation, which is also partly responsible for the decrease in the conductivity. Again, all the dopants are expected to decrease the basicity of the system. In this case, phosphate doping is expected to show a greater enhancement in CO_2 stability owing to its higher acidity and higher charge, which leads to higher oxygen contents for the doped phase compared to silicate doped phase. On the contrary, the result showed the opposite, the Si doped systems are the most stable towards CO_2, and this fact requires further investigation.

3.7 Fluorination of oxyanion doped $Ba_2In_2O_5$

Fluorination of undoped and oxyanion doped $Ba_2In_2O_5$ was investigated by low temperature reaction with PTFE. The X-ray powder diffraction data and the calculated cell parameters for the fluorinated $Ba_2In_2O_5$, $Ba_2In_{1.7}P_{0.3}O_{5.3}$ and $Ba_2In_{1.8}Si_{0.2}O_{5.1}$ (the amount of PTFE employed was sufficient to give complete filling of the anion sites) are given in Fig. 3.31 and table 3.14. There is an increase in the cell parameters on fluorination consistent with that observed for fluorinated $Ba_2Sc_2O_5$ due to filling of the oxygen vacancies [27]. Most importantly, the fluorination of $Ba_2In_2O_5$ resulted in the phase change to cubic symmetry and the structure refinement using X-ray diffraction data (fluoride ions are assigned as oxide due to the similar electron density) indicated the fully stoichiometric $Ba_2In_2O_4F_2$ (Fig. 3.32 and table 3.13), which was previously reported as unsuccessful through the solid state reaction between BaF_2 and In_2O_3 [24]. However, accurate determination of the anion contents would require neutron diffraction studies.

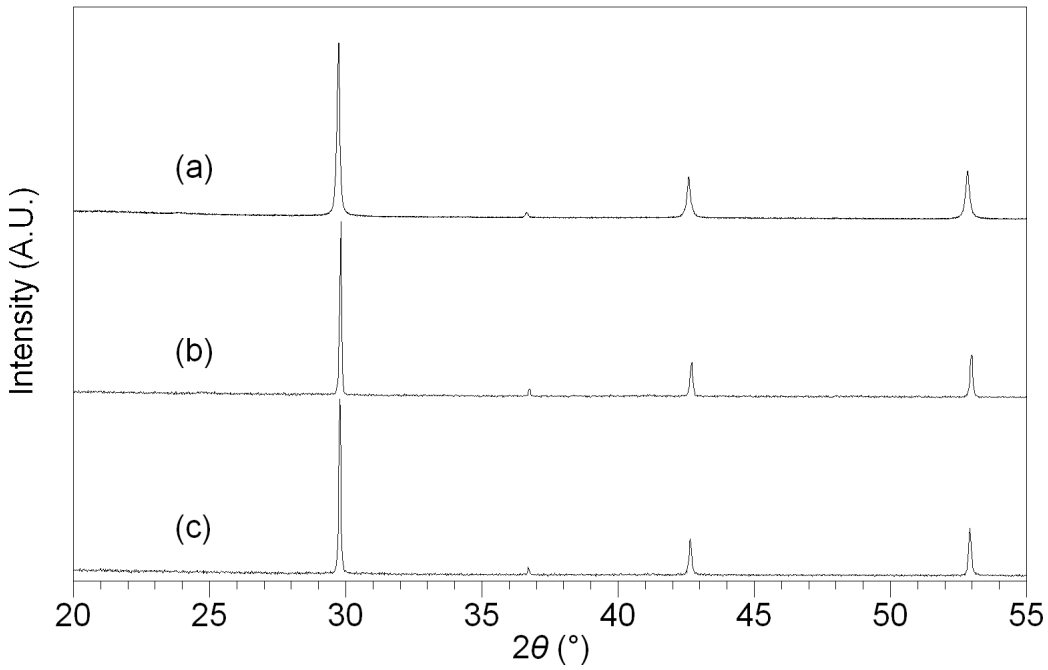

Fig. 3.31 XRD patterns for fluorinated (a) $Ba_2In_2O_5$, (b)$Ba_2In_{1.7}P_{0.3}O_{5.3}$ and (c) $Ba_2In_{1.8}Si_{0.2}O_{5.1}$.

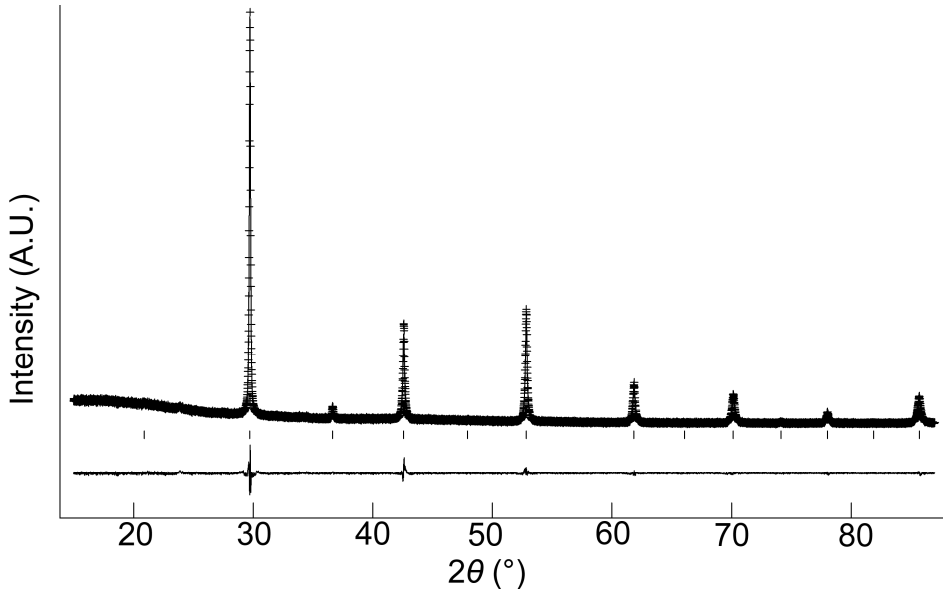

Fig. 3.32 Observed (cross), calculated (line), and difference plots (observed – calculated) of $Ba_2In_2O_{5-y/2}F_y$ from the Rietveld refinement for room temperature X-ray diffraction data.

Table 3.13 Refined structural parameters for $Ba_2In_2O_{5-y/2}F_y$ with cubic $Pm\bar{3}m$ (221) space group, from room temperature neutron diffraction data

		a (Å)		R_{wp}	R_p	χ^2
		4.2350(1)		6.13	4.69	1.40
		x	y	z	Fractional occupancy	U_{iso} (Å^2 x 100)
Ba	1b	½	½	½	1.000	0.85(6)
In	1a	0	0	0	0.997(2)	1.33(7)
O	3d	0	0	½	1.001(9)	1.45(2)

Table 3.14 Cell parameter data for fluorinated samples.

Sample	Unit cell parameters (Å)	Unit cell volume (Å^3)
	a_0	
$Ba_2In_2O_{5-y/2}F_y$	4.235(1)	76.0(1)
$Ba_2In_{1.7}P_{0.3}O_{5.3-y/2}F_y$	4.226(1)	75.5(1)
$Ba_2In_{1.8}Si_{0.2}O_{5.1-y/2}F_y$	4.230(1)	75.7(1)

Raman spectra of the fluorinated samples are given in Fig. 3.33. For all the samples, In-O bands around 600 cm^{-1} are not significant and the bands due to phosphate and silicate are consistent with those of reference materials shown in earlier sections, and thus indicating no significant change in the coordination numbers for the P and Si. This is consistent with the prior H_2O incorporation results, which suggested that the additional oxide ion vacancies around the oxyanion groups could not be filled.

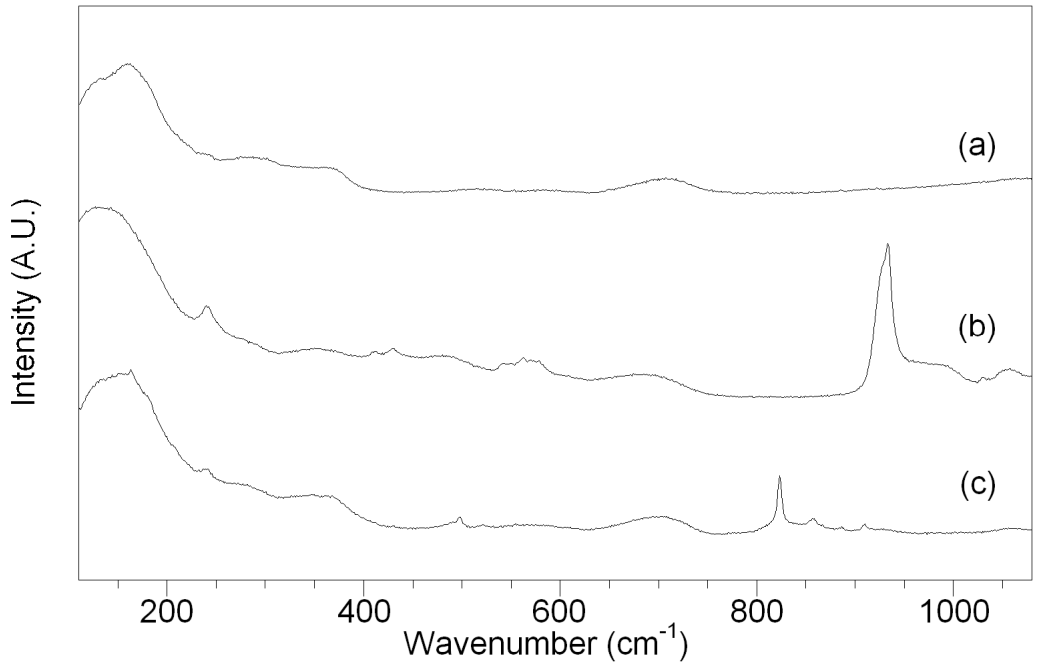

Fig. 3.33 Raman spectra for fluorinated (a) $Ba_2In_2O_5$, (b)$Ba_2In_{1.7}P_{0.3}O_{5.3}$ and (c) $Ba_2In_{1.8}Si_{0.2}O_{5.1}$.

3.8 Conclusions

In summary, it has been demonstrated that phosphate, sulphate and silicate groups can be incorporated onto the B cation site in $Ba_2In_2O_5$ resulting in a transition from low to high symmetry phases (from an orthorhombic to a cubic cell). The increased oxygen sublattice disorder causes an enhancement in the oxide ion conductivity at low temperature along with significant proton conductivity in wet atmospheres. Particularly promising results were observed for the silicate doped samples. These results are in contrast to prior reports of a negative effect on the conductivity of fluorite based oxide ion conductors by the addition of silica. This may be related to the incorporation of Si into the structure in the systems studied here, whereas for the fluorite systems it has been reported to collect at the grain boundaries. In addition to the improved conductivity, the stability towards CO_2 was also improved and further enhancements in the CO_2 stability were shown by co-doping with La/Zr on the Ba/In sites. In particular, the composition $Ba_2In_{1.6}Zr_{0.2}Si_{0.2}O_{5.2}$ exhibited promising results, with high conductivity and high CO_2 stability. A novel oxide fluoride, $BaInO_2F$ was also successfully prepared by the fluorination of $Ba_2In_2O_5$ with PTFE. The same method were also successfully applied to phosphate and silicate doped systems although Raman studies suggested no change in the P/Si coordination, indicating that complete filling of all the anion sites is not possible in such samples. This can be explained by the unwillingness of the phosphate and silicate groups to increase their coordination number.

3.9 Appendices

Appendix 3.1 Impedance spectra for $Ba_2In_{1.7}P_{0.3}O_{5.4}$ at 270 °C in (a) dry N_2 showing a bulk semicircle and (b) wet N_2 showing both bulk and grain boundary semicircles.

(a)

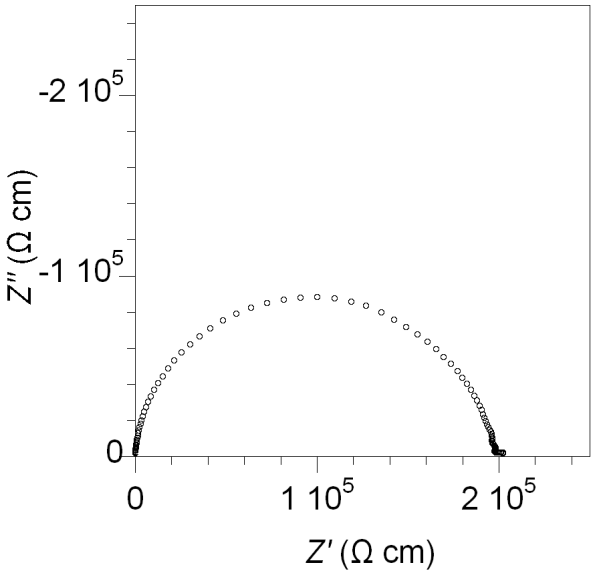

(b)

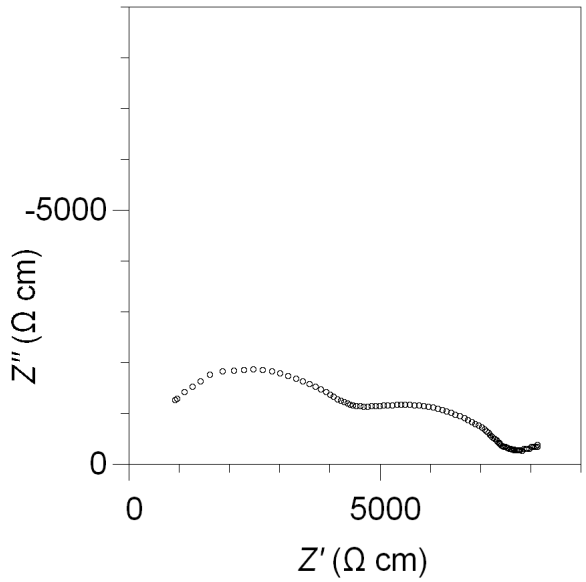

3.10 References

[1] Goodenough, J. B.; Ruiz-Diaz, J. E.; Zhen, Y. S. *Solid State Ionics* **1990**, *44*, 21.
[2] Greaves, C.; Slater, P. R. *J. Mater. Chem.* **1991**, *1*, 17.
[3] Greaves, C.; Slater, P. R. *Physica C* **1991**, *175*, 172.
[4] Slater, P. R.; Greaves, C.; Slaski, M.; Muirhead, C. M. *Physica C* **1993**, *208*, 193.
[5] Miyazaki, Y.; Yamane, H.; Ohnishi, N.; Kajitani, T.; Hiraga, K.; Morii, Y.; Funahashi, S.; Hirai, T. *Physica C* **1992**, *198*, 7.
[6] Maignan, A.; Hervieu, M.; Michel, C.; Raveau, B. *Physica C* **1993**, *208*, 116.
[7] Kinoshita, K.; Yamada, T. *Nature* **1992**, *357*, 313.
[8] Omata, T.; Fuke, T.; Otsuka-Yao-Matsuo, S. *Solid State Ionics* **2006**, *177*, 2447.
[9] Abakumov, A. M.; Rossell, M. D.; Gutnikova, O. Y.; Drozhzhin, O. A.; Leonova, L. S.; Dobrovolsky, Y. A.; Istomin, S. Y.; Tendeloo, G. V.; Antipov, E. V. *Chem. Mater.* **2008**, *20*, 4457.
[10] Larson, A. C.; Von Dreele, R. B. *Los Alamos National Laboratory Report LAUR* **1994**, 86-748.
[11] Mancini, A.; Shin, J. F.; Orera, A.; Slater, P. R.; Tealdi, C.; Ren, Y.; Page, K. L.; Malavasi, L. *Dalton T.* **2012**, *41*, 50.
[12] Malavasi, L.; Kim, H.; Billinge, S. J. L.; Proffen, T.; Tealdi, C.; Flor, G. *J. Am. Chem. Soc.* **2007**, *129*, 6903.
[13] Mackenzie, K. J. D.; Smith, M. E. *Multinuclear Solid State NMR of Inorganic Materials*, Pergamon Materials series, Permagon, Oxford, **2002**
[14] Rolle, A.; Daviero-Minaud, S.; Roussel, P.; Rubbens, A.; Vannier, R. N. *Solid State Ionics* **2008**, *179*, 771.
[15] Karlsson, M.; Matic, A.; Knee, C. S.; Ahmed, I.; Eriksson, S. G.; Börjesson, L. *Chem. Mater.* **2008**, *20*, 3480.
[16] Karlsson, M.; Ahmed, I.; Matic, A.; Eriksson, S. G. *Solid State Ionics* **2010**, *181*, 126.
[17] Zhang, G. B.; Smyth, D. M. *Solid State Ionics* **1995**, *82*, 153.
[18] Schober, T.; Friedrich, J. *Solid State Ionics* **1998**, *113*, 369.
[19] Zakowsky, N.; Williamson, S.; Irvine, J. T. S. *Solid State Ionics* **2005**, *176*, 3019.
[20] Lu, J.; Wang, L.; Fan, L.; Li, Y.; Dai, L.; Guo, H. *J. Rare Earth.* **2008**, *26*, 505.
[21] Magi, M.; Lippmaa, E.; Samoson, A.; Engelhardt, G.; Grimmer, A. R. *J. Phys. Chem.* **1984**, *88*, 1518.
[22] Aoki, M.; Chiang, Y.-M.; Kosacki, I.; Lee, L. J.-R.; Tuller, H.; Liu, Y. *J. Am. Ceram. Soc.* **1996**, *79*, 1169.
[23] Badwal, S. P. S.; Ciacchi, F. T.; Rajendran, S.; Drennan, J. *Solid State Ionics* **1998**, *109*, 167.
[24] Appel, C. C.; Bonanos, N. *J. Eur. Ceram. Soc.* **1999**, *19*, 847.
[25] Kreuer, K. D. *Ann. Rev. Mater. Res.* **2003**, *33*, 333.
[26] Yi, J.; Schroeder, M.; Weirich, T.; Mayer, J. *Chem. Mater.* **2010**, *22*, 6246.
[27] Needs, R. L.; Weller, M. T. *J. Solid State Chem.* **1998**, *139*, 422.

Chapter 4 Oxyanion Doping in $Ba_2Sc_2O_5$

4.1 Introduction

In the previous chapter, the effect of oxyanion doping on the stabilisation of the high symmetry cubic phase of $Ba_2In_2O_5$ and the corresponding positive influence on conductivity and CO_2 stability has been shown. In this chapter, the oxyanion doping strategy has been extended to the Sc analogue, $Ba_2Sc_2O_5$, system. Previous reports on $Ba_2Sc_2O_5$ stated that this phase is unstable above 1000 °C, resulting in the formation of $Ba_3Sc_4O_9$ after heating at higher temperature [1,2]. This thermal instability prohibited the sintering of this phase, and hence its application as a fuel cell electrolyte. Thus the possible improvement of the thermal stability with oxyanion doping was a key aspect for this study. The successful stabilisation of phosphate and sulphate doped $Ba_2Sc_2O_5$ and their conductivities and CO_2 stabilities are shown. Furthermore, evidence is provided to indicate the previously reported undoped $Ba_2Sc_2O_5$ is actually a carbonate doped $Ba_2Sc_2O_5$, which accounts for its low thermal stability.

4.2 Experimental

High purity $BaCO_3$, Sc_2O_3, $NH_4H_2PO_4$, $(NH_4)_2SO_4$ and SiO_2 were used to prepare $Ba_2Sc_{2-x}P_xO_{5+x}$ and $Ba_2Sc_{2-x}Si_xO_{5+x/2}$ samples. A small (3%) excess of $BaCO_3$ was employed, in order to overcome Ba loss at elevated temperatures. Without this small Ba excess, low levels of Ba deficient impurity phases, such as $Ba_3Sc_4O_9$, were observed after sintering, as has been seen in other studies synthesising similar Ba containing phases [2-4]. The powders were intimately ground and heated initially to 900°C for 12h. They were then ball-milled (350 rpm for 1 hour, Fritsch Pulverisette 7 Planetary Mill) and reheated to 1000 °C for a further 12h. The resulting powders were then ball-milled a second time and pressed as pellets (1.3 cm diameter) and sintered at 1500 °C for 10h. The pellets were covered in sample powder and the

crucible was covered with a lid to limit the amount of Ba loss during the sintering process. Following the structural studies on the undoped $Ba_2Sc_2O_5$ system, which suggested it contained carbonates, studies into the possible preparation of a nitrate doped system were performed. For the preparation of these nitrate doped $Ba_2Sc_2O_5$, a precursor suspension was prepared by dissolving $Ba(NO_3)_2$ and NH_4NO_3 in deionised water to which Sc_2O_3 was added. This suspension was sonicated and heated initially to 600°C for 12h in air. It was then ball-milled and reheated to 1000 °C for a further 12h in N_2. For all products, powder X-ray diffraction (Bruker D8 diffractometer with Cu $K_{\alpha 1}$ radiation = 1.5406 Å) was used to demonstrate phase purity. For the detailed information on the structure for $Ba_2Sc_{1.6}P_{0.4}O_{5.4}$, neutron diffraction data (wave length of 1.1551 Å) were recorded on diffractometer HRPT at the SINQ, Paul Scherrer Institut. All structural refinements employed the GSAS suite of Rietveld refinement software [5].

Raman spectroscopy measurements were made in order to provide further evidence for the successful incorporation of phosphate, sulphate, silicate, carbonate and nitrate. These measurements utilised a Renishaw inVia Raman microscope with excitation using a Cobolt Samba CW 532 nm DPSS Laser. In addition, ^{31}P and ^{29}Si NMR data were collected to gain further information about the P and Si environments. These spectra were obtained using a Varian VNMRS instrument operating at 161.87 MHz for ^{31}P and 79.44 MHz for ^{29}Si. Spectral referencing was with respect to 85% H_3PO_4 and tetramethylsilane. The data were collected by the EPSRC Solid state NMR service at Durham University.

The CO_2 stability of samples was determined through two sets of experiments. In the first set of experiments, samples were heated at temperatures between 600 and 800 °C for 12 hours in a tube furnace under flowing CO_2 gas, and the samples were analysed for partial decomposition by X-ray diffraction. In the second experiment samples were analysed using thermogravimetric analysis (Netzsch STA 449 F1 Jupiter Thermal Analyser). Samples were

heated at 10 °C min^{-1} to 1000 °C in 1:1 CO_2 and N_2 mixture to determine at what temperature CO_2 pick up occurred.

The water contents of hydrated samples were determined from thermogravimetric analysis (Netzsch STA 449 F1 Jupiter Thermal Analyser). Samples were heated at 10 °C min^{-1} to 1000 °C in N_2, and the water content was determined from the observed mass loss.

For the conductivity measurements, the sintered pellets (>85% theoretical density) were coated with Pt paste, and then heated to 800 °C for 1 hour to ensure bonding to the pellet. Conductivities were then measured by AC impedance measurements (Hewlett Packard 4182A impedance analyser) in the range from 0.1 to 10^3 kHz. Measurements were made in dry and wet N_2 (in which the gas was bubbled at room temperature through water) to identify any protonic contribution to the conductivity. Measurements were also made in dry O_2 to determine if there was a p-type electronic contribution to the conductivity.

The impedance data generally showed partially resolved semicircles in both dry and wet atmospheres, whose capacitances were consistent with the bulk and grain boundary responses respectively (Appendix 4.1).

4.3 Phosphate doping: $Ba_2Sc_{2-x}P_xO_{5+x}$

4.3.1 Structural study

It has been previously reported that undoped $Ba_2Sc_2O_5$ is unstable at temperatures above 1000 °C [1]. In agreement with this, the preparation of this system (heating at 1000 °C for 3 days) resulted in a material related to perovskite, having broad X-ray diffraction peaks, which turned into a material showing sharp $Ba_3Sc_4O_9$ peaks after sintering at 1300 °C without any trace of perovskite phase (Fig. 4.1). This nominally undoped phase showed a calculated cell parameter of 4.128 Å, which is in agreement with the previous report (4.13 Å) [2]. The best quality samples prepared in these previous studies were made with a large excess of Ba

(Ba:Sc ratio of 1.3:1), and in the present study, similar high levels of Ba (and reaction temperature limited to 1000 °C) were required to prepare the perovskite without any additional oxyanion (phosphate, sulphate, silicate) doping.

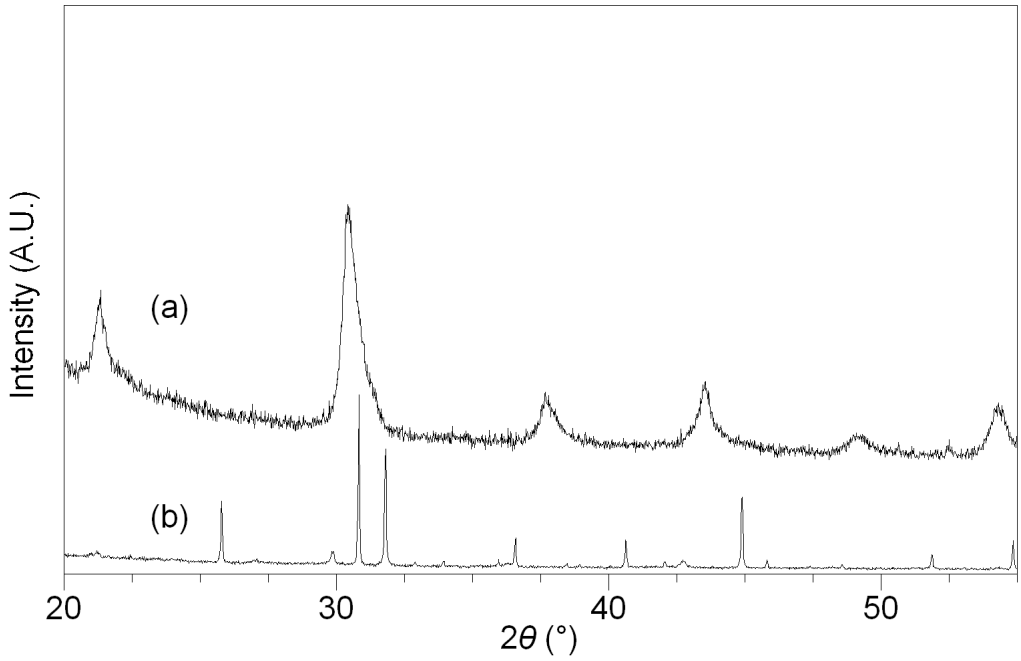

Fig. 4.1 XRD patterns for $Ba_2Sc_2O_5$ fired at (a) 1000 ℃ and (b) 1300 ℃.

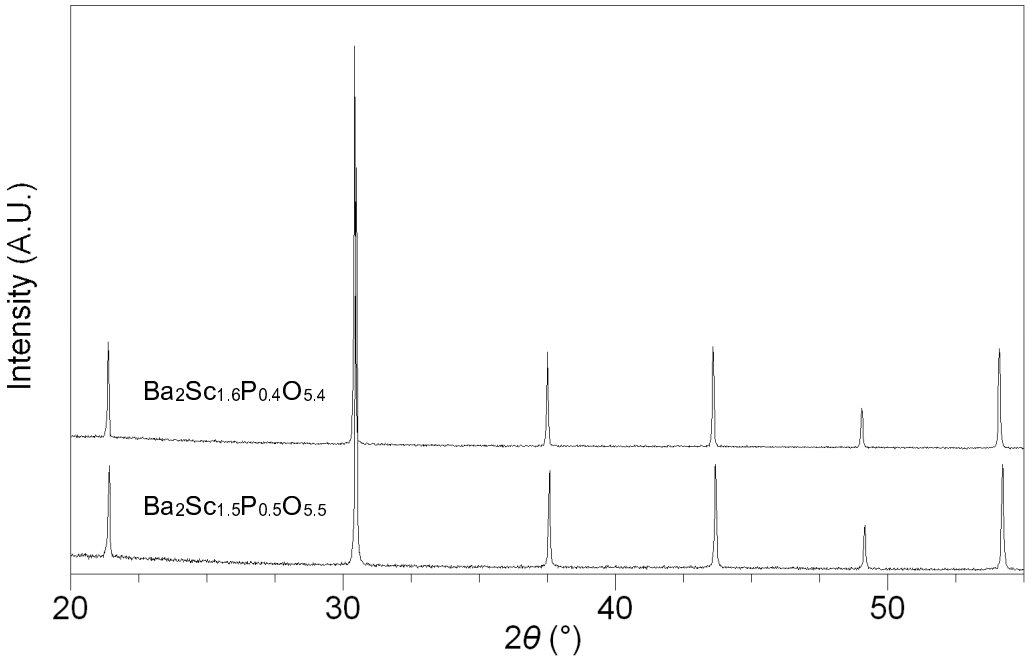

Fig. 4.2 XRD patterns for $Ba_2Sc_{1.6}P_{0.4}O_{5.4}$ and $Ba_2Sc_{1.5}P_{0.5}O_{5.5}$.

On the other hand, X-ray diffraction patterns of phosphate incorporated samples showed the emergence of perovskite peaks along with a reduction in the $Ba_3Sc_4O_9$ peaks after heating to 1300 °C. Thus, single phase cubic perovskite, $Ba_2Sc_{2-x}P_xO_{5+x}$, were successfully prepared in the range $0.4 \leq x \leq 0.5$ (Fig. 4.2). X-ray diffraction patterns of samples for $x < 0.4$ still showed peaks due to $Ba_3Sc_4O_9$, while samples of $x > 0.5$ showed the formation of phosphate rich impurities, i.e. $Ba_5(PO_4)_3(OH)$. Therefore, further work focused on the compositions $Ba_2Sc_{1.6}P_{0.4}O_{5.4}$ and $Ba_2Sc_{1.5}P_{0.5}O_{5.5}$. Preliminary structure refinement using X-ray diffraction data indicated B site occupancies of 1.59(2) Sc and 0.41(2) P for the x = 0.4 sample, and 1.50(2) Sc and 0.50(2) P, for the x = 0.5 sample, consistent with those expected (Fig. 4.3, 4.4 and table 4.1, 4.2). The refinement using neutron diffraction data of $Ba_2Sc_{1.6}P_{0.4}O_{5.4}$ also showed the same occupancies of Sc and P but with a lower than expected oxygen occupancy of 5.12(1) (Fig. 4.5 and table 4.3). This lower oxygen occupancy suggests that not all the oxygen sites have been located, for example the PO_4^{3-} oxygens, since the P-O bond would be much smaller than Sc-O, and hence significantly displaced from the ideal oxygen site. In an attempt to locate these additional oxygen sites, possible strategies to achieve tetrahedral coordination for the P in the perovskite structure were considered. In particular, the P site was moved towards centre of the xy plane to form a tetrahedron with adjacent two oxygen atoms on the x and y axes, and the oxygen atoms along the z axis were moved towards the origin to make up sensible bond lengths and angle with the P site (Fig. 4.7). The refinement of this arrangement resulted in a noticeable increase in the agreement between the model and experimental data, but still there was a lower oxygen content and very high atomic displacement parameters, which suggested the presence of other similar sites to accommodate the smaller tetrahedral phosphate group (Fig. 4.6 and table 4.4, 4.5). This is most likely related to a range of phosphate orientations in the structure and would suggest that the structure of $Ba_2Sc_{1.6}P_{0.4}O_{5.4}$ contains a significant level of distortion from the perfect cubic

perovskite. Neutron total scattering and pair distribution function (PDF) analysis would be useful to enlighten this issue further.

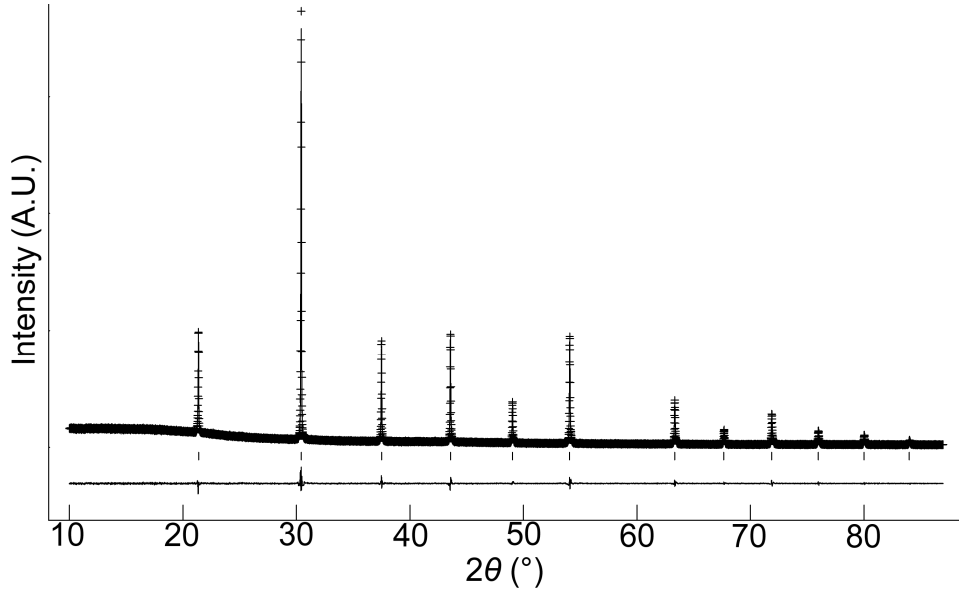

Fig. 4.3 Observed (cross), calculated (line), and difference plots (observed – calculated) of $Ba_2Sc_{1.6}P_{0.4}O_{5.4}$ from the Rietveld refinement for room temperature X-ray diffraction data.

Table 4.1 Refined structural parameters for $Ba_2Sc_{1.6}P_{0.4}O_{5.4}$ using cubic $Pm\bar{3}m$ (221) space group from room temperature X-ray diffraction data.

		a (Å)		R_{wp}	R_p	χ^2
		4.1504 (1)		5.15	3.70	1.83
		x	y	z	Fractional occupancy	U_{iso} (Å^2 x 100)
Ba	1b	½	½	½	1.00	2.22 (2)
Sc	1a	0	0	0	0.794 (8)	2.67 (6)
P	1a	0	0	0	0.206 (8)	2.67 (6)
O	3d	0	0	½	0.896 (5)	3.6 (1)

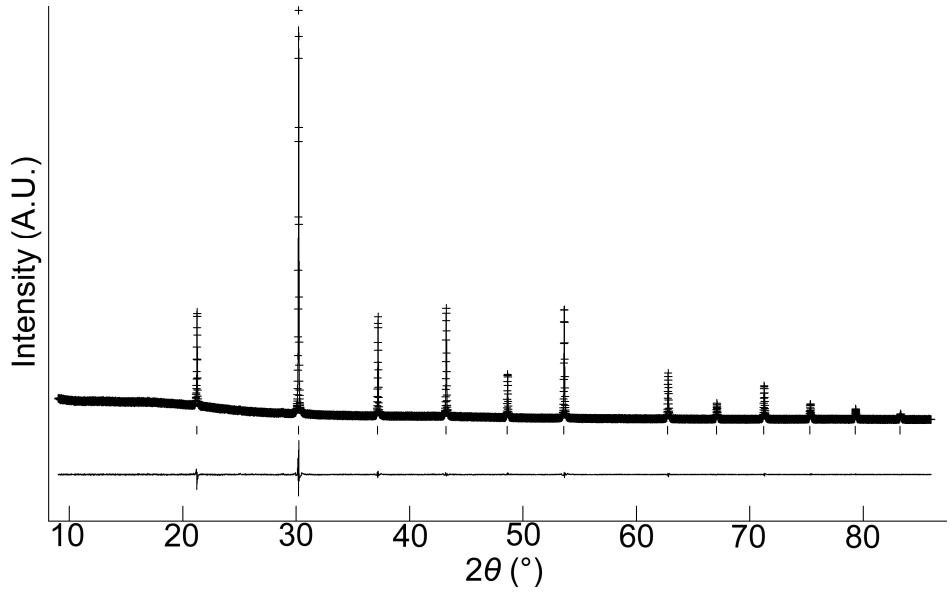

Fig. 4.4 Observed (cross), calculated (line), and difference plots (observed – calculated) of $Ba_2Sc_{1.5}P_{0.5}O_{5.5}$ from the Rietveld refinement for room temperature X-ray diffraction data.

Table 4.2 Refined structural parameters of $Ba_2Sc_{1.5}P_{0.5}O_{5.5}$ using cubic $Pm\bar{3}m$ (221) space group from room temperature X-ray diffraction data.

		a (Å)		R_{wp}	R_p	χ^2
		4.1404 (1)		4.00	2.71	2.44
		x	y	z	Fractional occupancy	U_{iso} (Å^2 x 100)
Ba	1b	½	½	½	1.000	1.88 (1)
Sc	1a	0	0	0	0.748 (7)	2.59 (5)
P	1a	0	0	0	0.252 (7)	2.59 (5)
O	3d	0	0	½	0.917 (4)	3.9 (1)

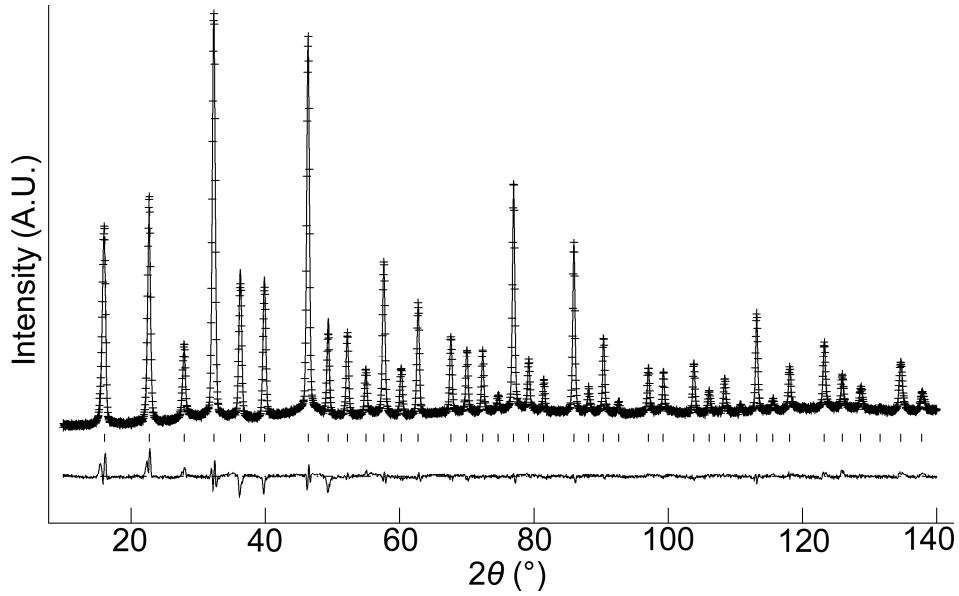

Fig. 4.5 Observed (cross), calculated (line), and difference plots (observed – calculated) of $Ba_2Sc_{1.6}P_{0.4}O_{5.4}$ from the Rietveld refinement for room temperature neutron diffraction data.

Table 4.3 Refined structural parameters of $Ba_2Sc_{1.6}P_{0.4}O_{5.4}$ using cubic $Pm\bar{3}m$ (221) space group from room temperature neutron diffraction data.

		a (Å)		R_{wp}	R_p	χ^2
		4.1504(1)		3.38	2.48	4.64
		x	y	z	Fractional occupancy	U_{iso} (Å^2 x 100)
Ba	1b	½	½	½	1.00	1.66 (2)
Sc	1a	0	0	0	0.794 (1)	1.77 (1)
P	1a	0	0	0	0.206 (1)	1.77 (6)
O	3d	0	0	½	0.854 (2)	2.35 (1)

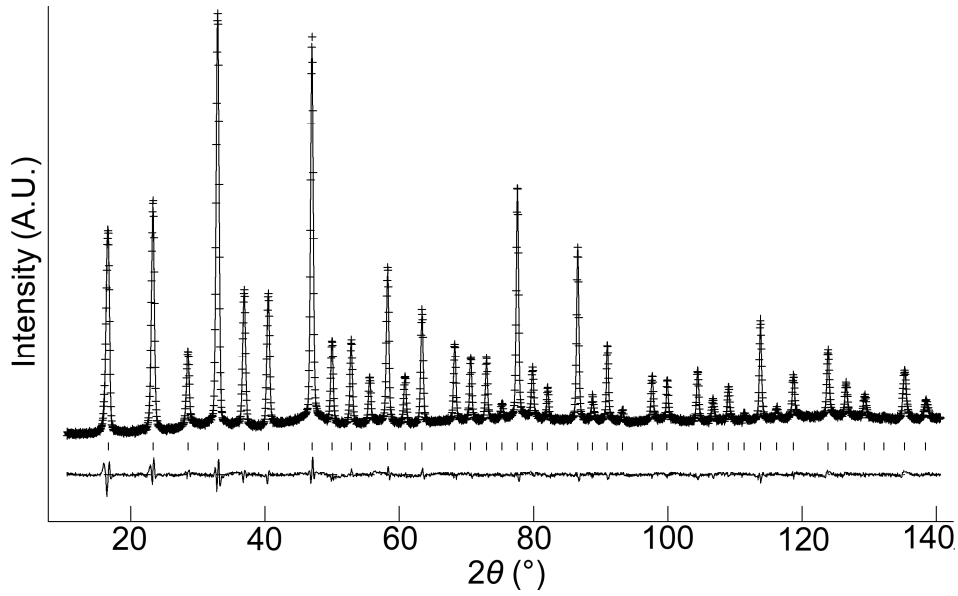

Fig. 4.6 Observed (cross), calculated (line), and difference plots (observed – calculated) of $Ba_2Sc_{1.6}P_{0.4}O_{5.4}$ from the Rietveld refinement for room temperature neutron diffraction data with new P site.

Table 4.4 Refined structural parameters of $Ba_2Sc_{1.6}P_{0.4}O_{5.4}$ using cubic $Pm\bar{3}m$ (221) space group from room temperature neutron diffraction data with new P site coordinates

		a (Å)	R_{wp}	R_p	χ^2
		4.1504(1)	2.75	2.11	3.06
		x	y	z	Fractional occupancy	U_{iso} (Å^2 x 100)
Ba	1b	½	½	½	1.00	1.90 (1)
Sc	1a	0	0	0	0.796 (1)	1.51 (1)
P	12i	0.140(3)	0.140(3)	0	0.017 (1)	11.8 (15)
O(1)	3d	0	0	½	0.812 (1)	2.35 (1)
O(2)	6e	0	0	0.249(6)	0.027 (1)	11.4 (13)

Table 4.5 Selected bond lengths and angles from refinement data (table 4.4).

Bond length (Å)		Bond angle (°)	
P-O(1)	1.605(1)	O(1)-P-O(1)	132.4(1)
P-O(2)	1.322(1)	O(2)-P-O(2)	103.2(1)
		O(1)-P-O(2)	104.5(1)

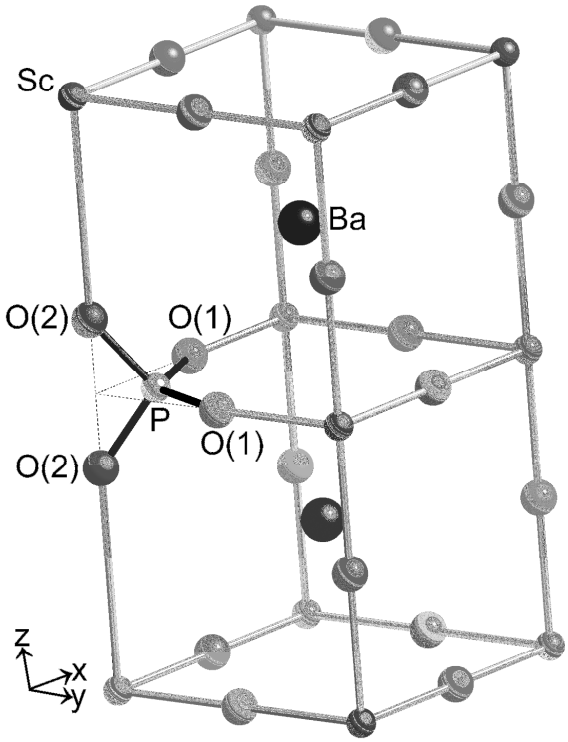

Fig. 4.7 The relocation of P and O(2) to make a tetrahedron.

Table 4.6 Cell parameter data for P doped $Ba_2Sc_2O_5$

Sample (nominal composition)	Unit cell parameters (Å) a_0	Unit cell volume (Å^3)
$Ba_2Sc_2O_5$	4.128(1)	70.34(3)
$Ba_2Sc_{1.6}P_{0.4}O_{5.4}$	4.150(1)	71.49(3)
$Ba_2Sc_{1.5}P_{0.5}O_{5.5}$	4.140(1)	70.98(3)

A particularly interesting point from the refinements was that the cell parameters obtained were greater than that of "undoped" $Ba_2Sc_2O_5$ (table 4.6). This is in contrast with the result expected due to the size difference between P^{5+} and Sc^{3+}, from which it would be predicted that the phosphate doped samples would be smaller than the undoped one, as observed in the phosphate doped $Ba_2In_2O_5$ studies. This fact caused as to re-evaluate the undoped $Ba_2Sc_2O_5$ system. The thermal instability of this phase has been shown in this and previous studies [2], with both studies showing that heating above 1000 °C led eventually to it converting to $Ba_3Sc_4O_9$. We postulate that this thermal instability, and the smaller cell parameter compared to the phosphate doped samples, are caused by the incorporation of carbonate on the Sc site, and thus the "undoped" $Ba_2Sc_2O_5$ is actually carbonate doped phase, $Ba_2Sc_{2-x}C_xO_{5+x/2}$. Certainly, the incorporation of smaller C^{4+} in Sc^{3+} site would result in a smaller cell volume, and the presence of carbonate group in the structure is further evidenced by Raman spectroscopy studies. The spectra contained the intense broad peak at ≈ 1064 cm^{-1} (Fig. 4.8). The shape of the peak is asymmetrical with a clear presence of a shoulder at lower wavenumber, which is consistent with that of unreacted $BaCO_3$, while the bulk of the peak is believed to be due to the carbonate within the perovskite. The partial substitution of Sc with carbonate would also explain the necessity for the use of a high Ba:Sc ratio to achieve the best quality samples.

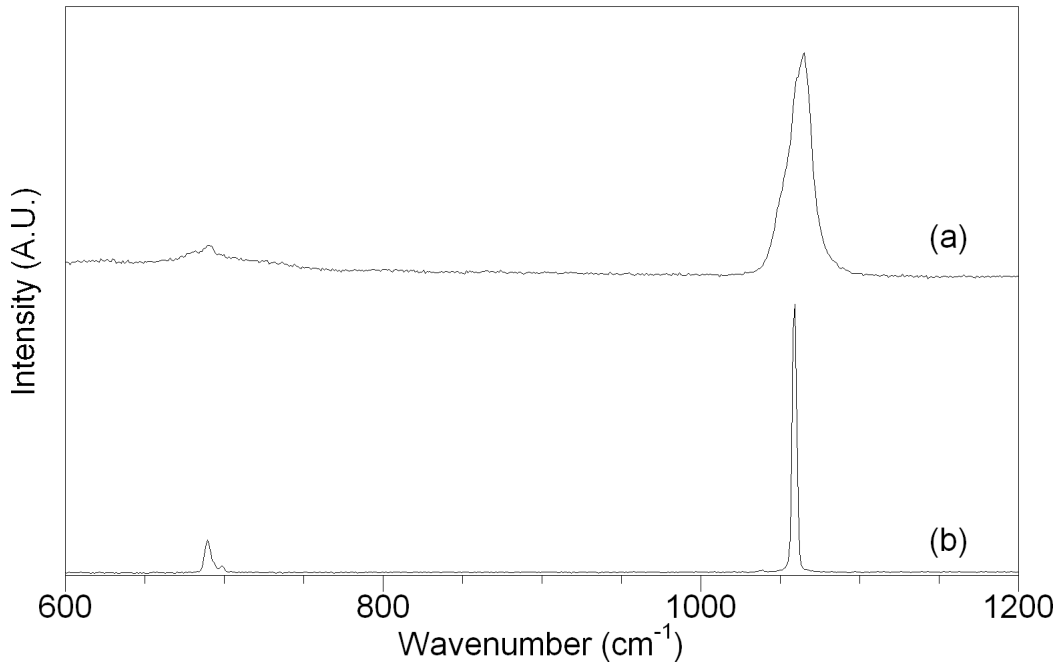

Fig. 4.8 Raman spectra of (a) "undoped" $Ba_2Sc_2O_5$ and (b) $BaCO_3$.

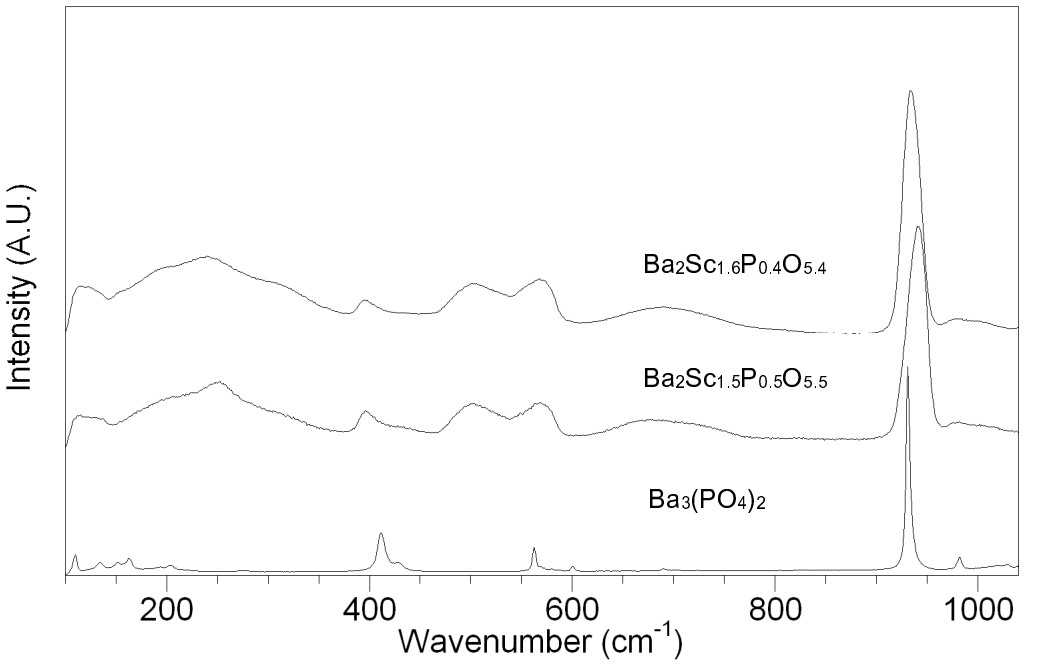

Fig. 4.9 Raman spectra of $Ba_2Sc_{1.6}P_{0.4}O_{5.4}$ and $Ba_2Sc_{1.5}P_{0.5}O_{5.5}$. For comparison, Raman spectrum for $Ba_3(PO_4)_2$ is included.

The Raman spectra for the phosphate doped samples are given in Fig. 4.9. On incorporation of phosphate, there is the appearance of bands at around 930 cm^{-1}, and the position of the newly emerged bands are in a similar position to the bands observed for $Ba_3(PO_4)_2$, consistent with the phosphate group being mainly coordinated to Ba. In addition, there was a small peak shift to higher wavenumber with greater P level which is similar to the results observed for phosphate doped $Ba_2In_2O_5$ studies. As noted earlier, the presence of some Raman bands indicates that while the average structure determined in diffraction studies is cubic, there are considerable local distortions away from cubic symmetry as was the case for phosphate doped $Ba_2In_2O_5$.

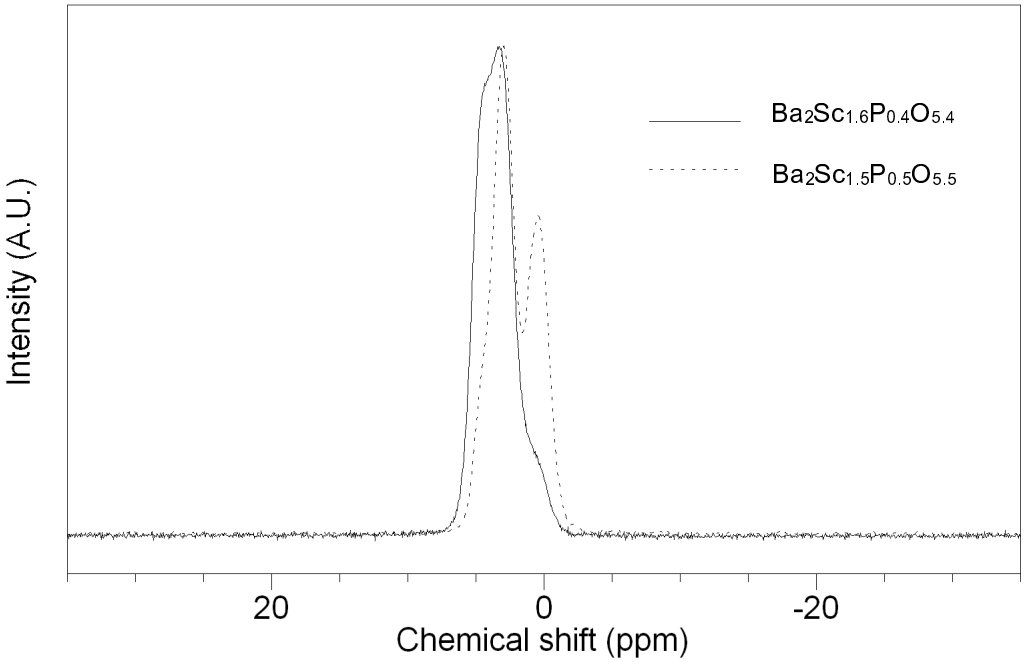

Fig. 4.10 ^{31}P NMR spectra for $Ba_2Sc_{1.6}P_{0.4}O_{5.4}$ (continuous line) and $Ba_2Sc_{1.5}P_{0.5}O_{5.5}$ (broken line).

The ^{31}P NMR data for the phosphate doped samples are given in Fig. 4.10. The data show peaks with chemical shifts ranged from 0.4 to 4.8 ppm which is in the typical region for an alkaline earth orthophosphate [6]. There are three peaks with slight chemical shift difference,

which indicate the presence of more than one phosphate environment. This maybe due to the presence of local distortion away from ideal cubic symmetry which produces local variation in phosphate content and the change in phosphate environments accordingly. The intensity variations of the peaks with different P level is given in table 4.7 showing a significant reduction in the intensity of the peak at higher chemical shift (≈ 4.8 ppm) with increasing P level.

Table 4.7 ^{31}P NMR data for P doped $Ba_2Sc_2O_5$

Sample	Peak position (ppm)	Relative intensity (%)
$Ba_2Sc_{1.6}P_{0.4}O_{5.4}$	1.1	12.1
	3.2	48.9
	4.8	39.0
$Ba_2Sc_{1.5}P_{0.5}O_{5.5}$	0.4	37.9
	2.9	51.9
	4.6	10.3

4.3.2 Conductivity measurements

The conductivity measurements of these phosphate doped samples are given in Fig. 4.11 and table 4.8. As in the analogue system, $Ba_2In_2O_5$, a significant p-type contribution to the conduction was expected, and the initial measurements were done in N_2 to eliminate this p-type contribution. At low temperature, a large grain boundary contribution was observed which became less significant at higher temperature (Table 4.8). Both samples showed high bulk conductivities, which were enhanced further in wet N_2 through a protonic contribution to the conduction. However, the total conductivities at low temperature were lower than for P doped $Ba_2In_2O_5$ due to the significant grain boundary contribution mentioned above. $Ba_2Sc_{1.5}P_{0.5}O_{5.5}$ sample showed a lower conductivity compared to $Ba_2Sc_{1.6}P_{0.4}O_{5.4}$, most likely due to the lower oxygen vacancy concentration. While the low temperature grain boundary

conductivity was low, the bulk conductivity of 5.9 x 10^{-3} S cm^{-1} at 500 °C in wet N_2 for $Ba_2Sc_{1.6}P_{0.4}O_{5.4}$ is comparable with other proton conducting perovskites [7, 8]. The conductivities in dry O_2 were higher at elevated temperatures than those in dry N_2, which confirms the presence of a p-type contribution as expected. (Fig. 4.12).

Table 4.8.a Bulk conductivity data for P doped $Ba_2Sc_2O_5$.

Sample (nominal composition)	Conductivity (S cm^{-1})		
	500 °C		800 °C
	Dry	Wet	Dry
$Ba_2Sc_{1.6}P_{0.4}O_{5.4}$	2.9 x 10^{-3}	5.9 x 10^{-3}	7.9 x 10^{-3}
$Ba_2Sc_{1.5}P_{0.5}O_{5.5}$	9.0 x 10^{-4}	1.3 x 10^{-3}	4.5 x 10^{-3}

Table 4.8.b Total conductivity data for P doped $Ba_2Sc_2O_5$ (Grain boundary resistance was insignificant compared to that of the bulk at 800 °C).

Sample (nominal composition)	Conductivity (S cm^{-1})		
	500 °C		800 °C
	Dry	Wet	Dry
$Ba_2Sc_{1.6}P_{0.4}O_{5.4}$	1.2 x 10^{-3}	2.3 x 10^{-3}	7.9 x 10^{-3}
$Ba_2Sc_{1.5}P_{0.5}O_{5.5}$	4.4 x 10^{-4}	6.5 x 10^{-4}	4.5 x 10^{-3}

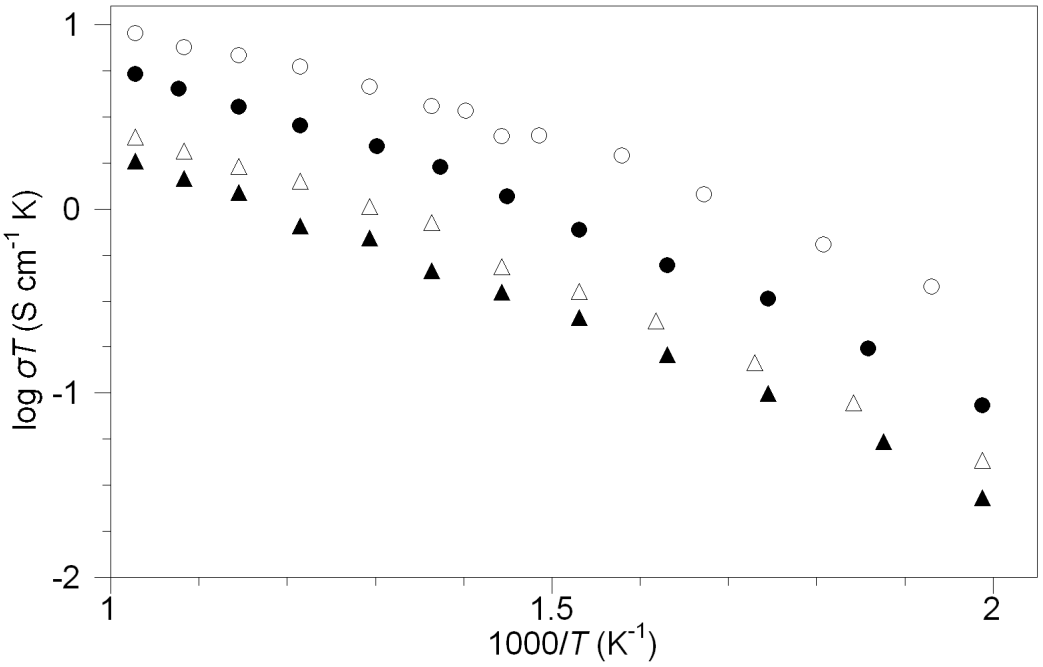

Fig. 4.11 Bulk conductivity data for $Ba_2Sc_{1.6}P_{0.4}O_{5.4}$ in dry N_2 (filled circle) and wet N_2 (open circle) and for $Ba_2Sc_{1.5}P_{0.5}O_{5.5}$ in dry N_2 (filled triangle) and wet N_2 (open triangle).

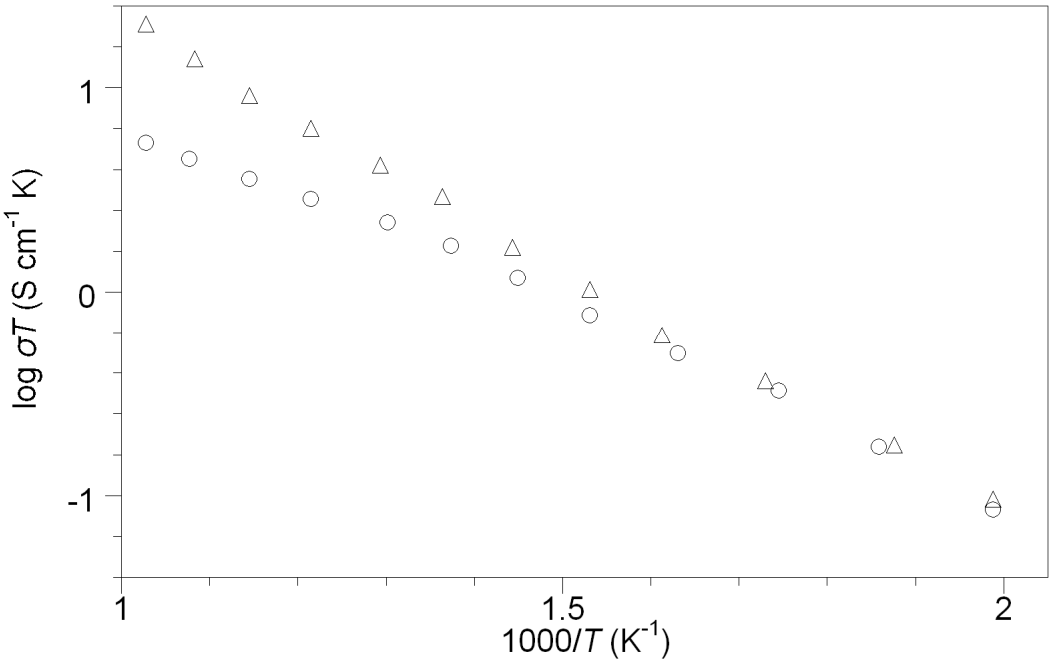

Fig. 4.12 Bulk conductivity data for $Ba_2Sc_{1.6}P_{0.4}O_{5.4}$ in dry N_2 (circle) and dry O_2 (triangle).

4.3.3 Water incorporation study

For the determination of the level of water incorporated, the samples were heated under wet N_2 to 800 °C, before slow cooling (0.4 °C min^{-1}) to room temperature. The water contents were then determined by TGA measurements, which gave values of 0.12 and 0.07 for $Ba_2Sc_{1.6}P_{0.4}O_{5.4}$ and $Ba_2Sc_{1.5}P_{0.5}O_{5.5}$ respectively. These relatively low water contents can be correlated to the tetrahedral geometry of phosphate, which requires the presence of oxygen vacancies around to maintain this tetrahedral coordination. Thus the complete filling of all the available oxygen vacancy sites with water is not possible, as also observed in oxyanion doped $Ba_2In_2O_5$.

4.3.4 CO_2 stability results

X-ray diffraction data for the $Ba_2Sc_{1.6}P_{0.4}O_{5.4}$ and $Ba_2Sc_{1.5}P_{0.5}O_{5.5}$ samples heated to 600 °C in CO_2 showed no evidence of $BaCO_3$ formation (Fig. 4.13) unlike the perovskite $BaCe_{0.9}Y_{0.1}O_{2.95}$, which showed a significant level of $BaCO_3$ formation. On increasing the heating temperature to 800 °C, the appearance of small $BaCO_3$ peaks were, however, observed. The TG profiles are given in Fig. 4.14 and they provide further evidence regarding the relative stability towards CO_2. $BaCe_{0.9}Y_{0.1}O_{2.95}$ showed a clear mass increase ($BaCO_3$ formation by CO_2 pick up) above 500 °C, while $Ba_2Sc_{1.6}P_{0.4}O_{5.4}$ and $Ba_2Sc_{1.5}P_{0.5}O_{5.5}$ samples showed generally flatter TG profile, with a significant mass change observed only above 800 °C. Thus the results indicated that the phosphate doped $Ba_2Sc_2O_5$ show improved stability towards CO_2, though at higher temperature, they still show some instability.

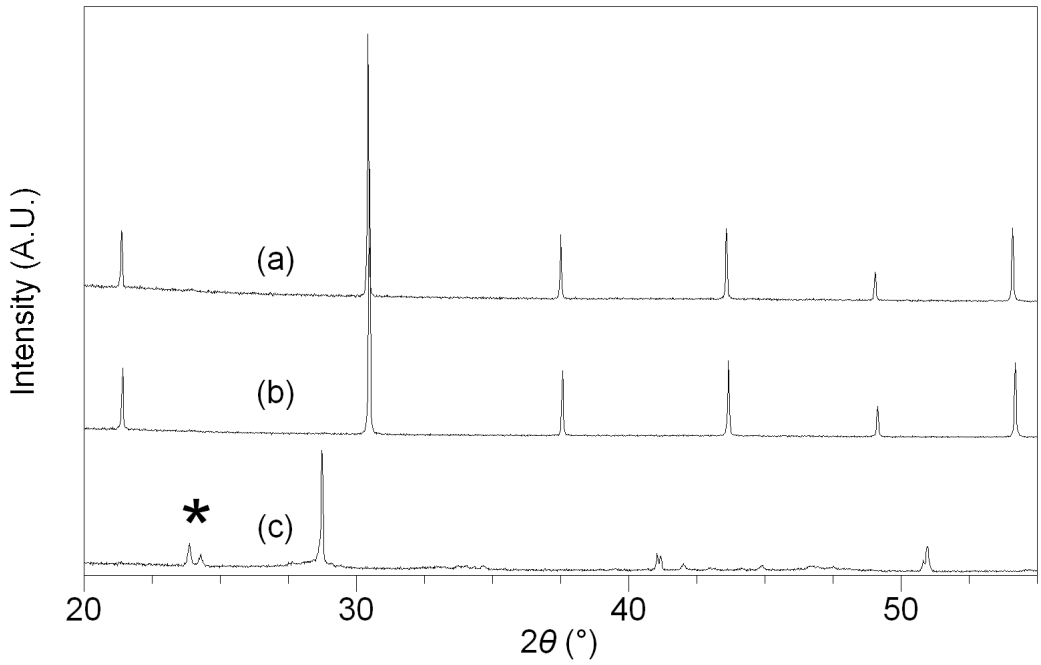

Fig. 4.13 XRD patterns for (a) $Ba_2Sc_{1.6}P_{0.4}O_{5.4}$, (b) $Ba_2Sc_{1.5}P_{0.5}O_{5.5}$ and (c) $BaCe_{0.9}Y_{0.1}O_{2.95}$ after heating in CO_2 at 600 °C for 12h (main $BaCO_3$ impurity peaks marked *).

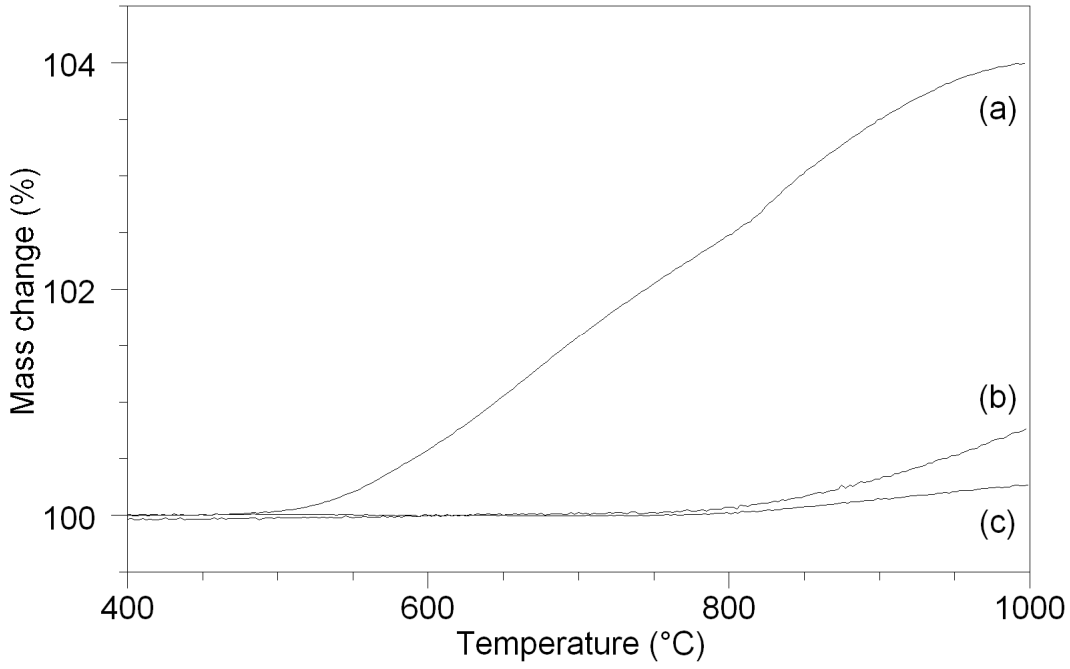

Fig. 4.14 TG profiles (10 °C min^{-1} to 1000 °C in 1:1 CO_2 and N_2 mixture) for (a) $BaCe_{0.9}Y_{0.1}O_{2.95,}$ (b) $Ba_2Sc_{1.6}P_{0.4}O_{5.4}$ and (c) $Ba_2Sc_{1.5}P_{0.5}O_{5.5.}$

4.4 Sulphate doping: $Ba_2Sc_{2-x}S_xO_{5+3x/2}$

4.4.1 Structural study

After the successful incorporation of phosphate in $Ba_2Sc_2O_5$, the preparation of sulphate doped samples have been attempted. As for the phosphate doping, at low level of sulphate ($Ba_2Sc_{2-x}S_xO_{5+3x/2}$, $x < 0.4$), peaks due to $Ba_3Sc_4O_9$ were seen in the X-ray diffraction patterns. The intensity of these peaks decreased with an increase in S content and they were not observed for the sample, $x = 0.4$, while samples of $x > 0.4$ showed the formation of sulphate rich impurities, i.e. $BaSO_4$. Preliminary structure refinement using X-ray diffraction data of single phase $Ba_2Sc_{1.6}S_{0.4}O_{5.6}$ indicated B site occupancies of 1.58(2) Sc and 0.42(2) S, consistent with those expected (Fig. 4.15 and table 4.9). A cell parameter of 4.168 Å was obtained and this value is slightly greater than those of phosphate doped systems, which is similar to observed for phosphate and sulphate doped $Ba_2In_2O_5$ studies.

The Raman spectrum for the $Ba_2Sc_{1.6}S_{0.4}O_{5.6}$ sample is given in Fig. 4.16. On incorporation of sulphate, there is the appearance of broad bands in the range 985-1000 cm^{-1}, and the position of the newly emerged bands are in a similar position to the bands observed for $BaSO_4$, consistent with the sulphate group being mainly coordinated to Ba. The presence of multiple bands indicates the presence of more than one sulphate environments in the structure as evidenced in the NMR study for the phosphate doped system. Also the presence of some Raman bands indicates that while the average structure determined in diffraction studies is cubic, there are local distortions away from cubic symmetry as was the case of sulphate doped $Ba_2In_2O_5$.

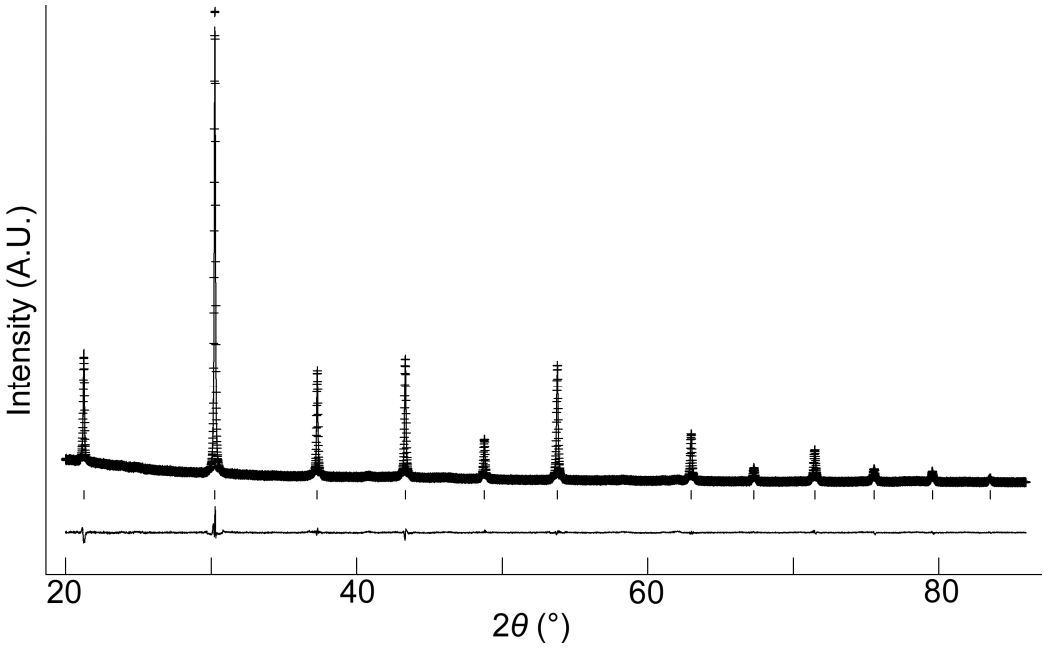

Fig. 4.15 Observed (cross), calculated (line), and difference plots (observed – calculated) of $Ba_2Sc_{1.6}S_{0.4}O_{5.6}$ from the Rietveld refinement for room temperature X-ray diffraction data.

Table 4.9 Refined structural parameters for $Ba_2Sc_{1.6}S_{0.4}O_{5.6}$ using cubic $Pm\bar{3}m$ (221) space group from room temperature X-ray diffraction data.

		a (Å)		R_{wp}	R_p	χ^2
		4.1679 (1)		3.77	2.76	2.16
		x	y	z	Fractional occupancy	U_{iso} (Å^2 x 100)
Ba	1b	½	½	½	1.000	2.78 (1)
Sc	1a	0	0	0	0.792 (7)	2.56 (4)
S	1a	0	0	0	0.208 (7)	2.56 (4)
O	3d	0	0	½	0.922 (4)	3.53 (9)

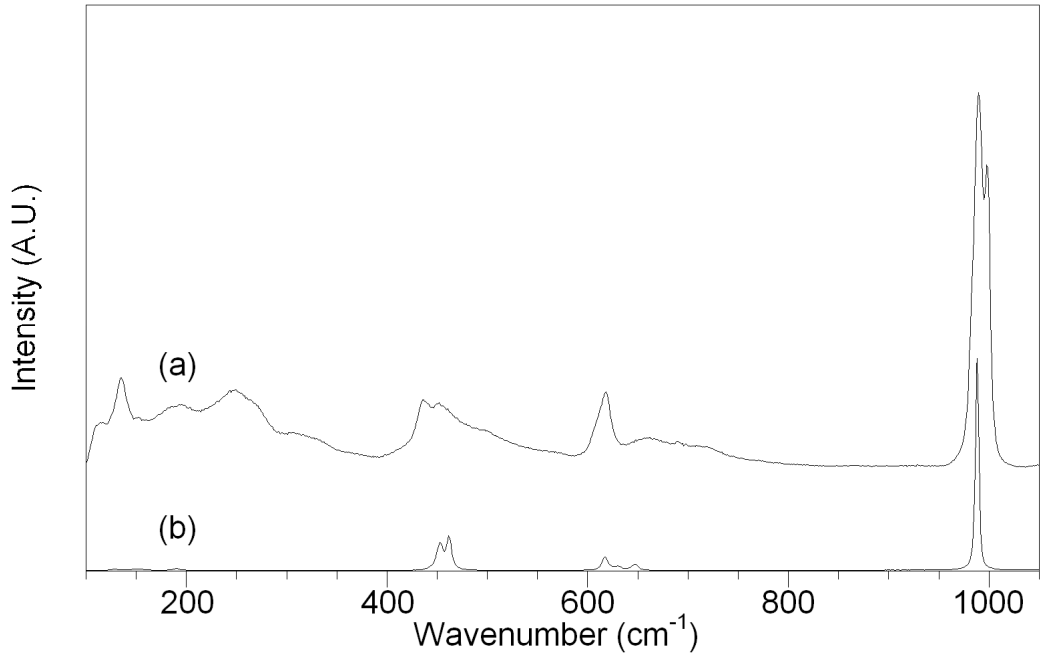

Fig. 4.16 Raman spectra of (a) $Ba_2Sc_{1.6}S_{0.4}O_{5.6}$ and (b) $BaSO_4$.

4.4.2 Conductivity measurements

The conductivity measurements for $Ba_2Sc_{1.6}S_{0.4}O_{5.6}$ sample in N_2 are given in table 4.10. At low temperature, a large grain boundary contribution was observed, which became less significant at higher temperature. The sample showed slightly lower conductivity than the phosphate doped sample, which was also the case for the analogous $Ba_2In_2O_5$ series, and there was no enhancement of the conductivity in wet N_2.

Table 4.10 Conductivity data for $Ba_2Sc_{1.6}S_{0.4}O_{5.6}$ (Grain boundary resistance was insignificant compared to that of bulk at 800 °C).

Conductivity (S cm^{-1})		
500 °C		800 °C
Bulk	Total	Total
8.9×10^{-4}	3.9×10^{-4}	3.5×10^{-3}

4.5 Silicate doping: $Ba_2Sc_{2-x}Si_xO_{5+x/2}$

After the successful incorporation of phosphate in $Ba_2Sc_2O_5$, the preparation of silicate doped samples was attempted. As for the phosphate and sulphate doping, at low level of silicate incorporation levels ($Ba_2Sc_{2-x}Si_xO_{5+x/2}$, x< 0.6), peaks due to $Ba_3Sc_4O_9$ were seen in the X-ray diffraction patterns. The intensity of these peaks decreased with increase in Si content and they were not observed for the sample, x = 0.6. However, a small impurity of Ba_2SiO_4 was observed instead at this level of Si doping (Fig. 4.17), and complete elimination of this impurity was not successful. Cell parameters were determined and a value of 4.123 Å was obtained through the refinement of X-ray diffraction data (Fig. 4.18 and table 4.11). This is slightly smaller than those of phosphate doped systems which is similar to observed for phosphate and silicate doped $Ba_2In_2O_5$. The refinement also indicated the Si content of 0.52(2), which is lower than the nominal value of 0.6 in the starting composition, the lower value accounting for the presence of small Ba_2SiO_4 impurities.

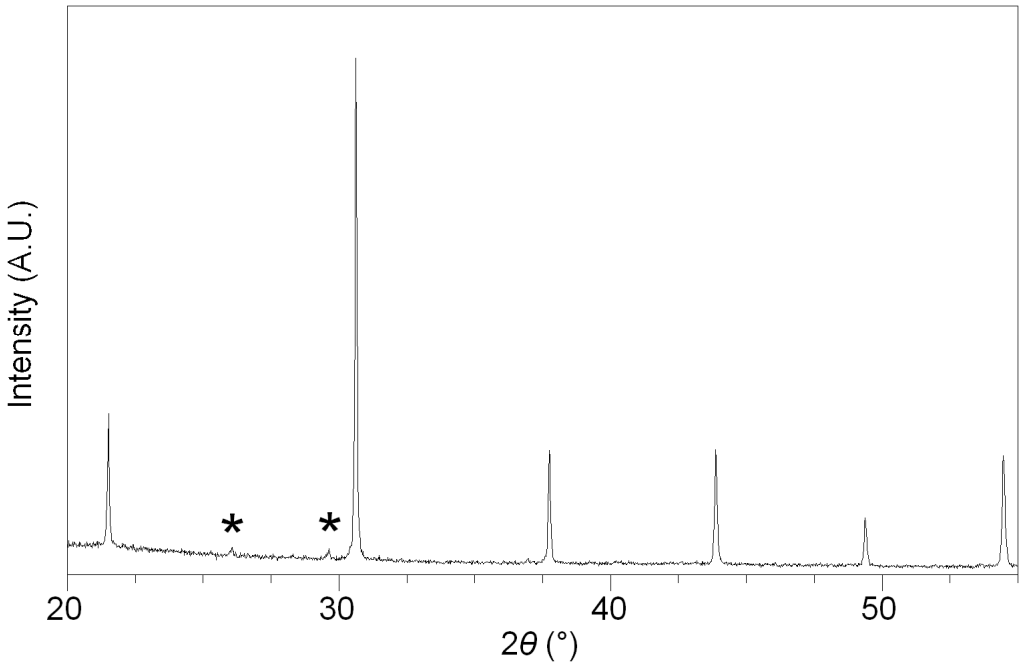

Fig. 4.17 XRD patterns for $Ba_2Sc_{1.4}Si_{0.6}O_{5.3}$ (Ba_2SiO_4 impurity peaks marked *).

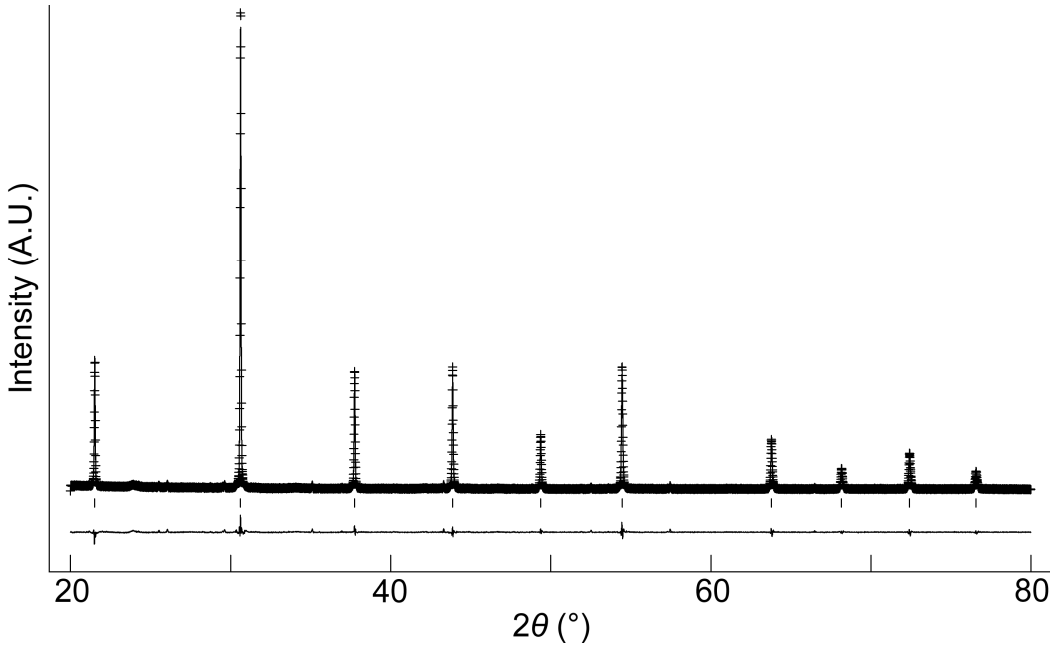

Fig. 4.18 Observed (cross), calculated (line), and difference plots (observed – calculated) of $Ba_2Sc_{1.4}Si_{0.6}O_{5.3}$ from the Rietveld refinement for room temperature X-ray diffraction data.

Table 4.11 Refined structural parameters for $Ba_2Sc_{1.4}Si_{0.6}O_{5.3}$ using cubic $Pm\bar{3}m$ (221) space group from room temperature X-ray diffraction data.

		a (Å)		R_{wp}	R_p	χ^2
		4.1225 (1)		8.72	6.07	2.81
		x	y	z	Fractional occupancy	U_{iso} (Å^2 x 100)
Ba	1b	½	½	½	1.000	1.69 (2)
Sc	1a	0	0	0	0.739 (8)	3.12 (7)
Si	1a	0	0	0	0.261 (8)	3.12 (7)
O	3d	0	0	½	0.874 (5)	3.60 (10)

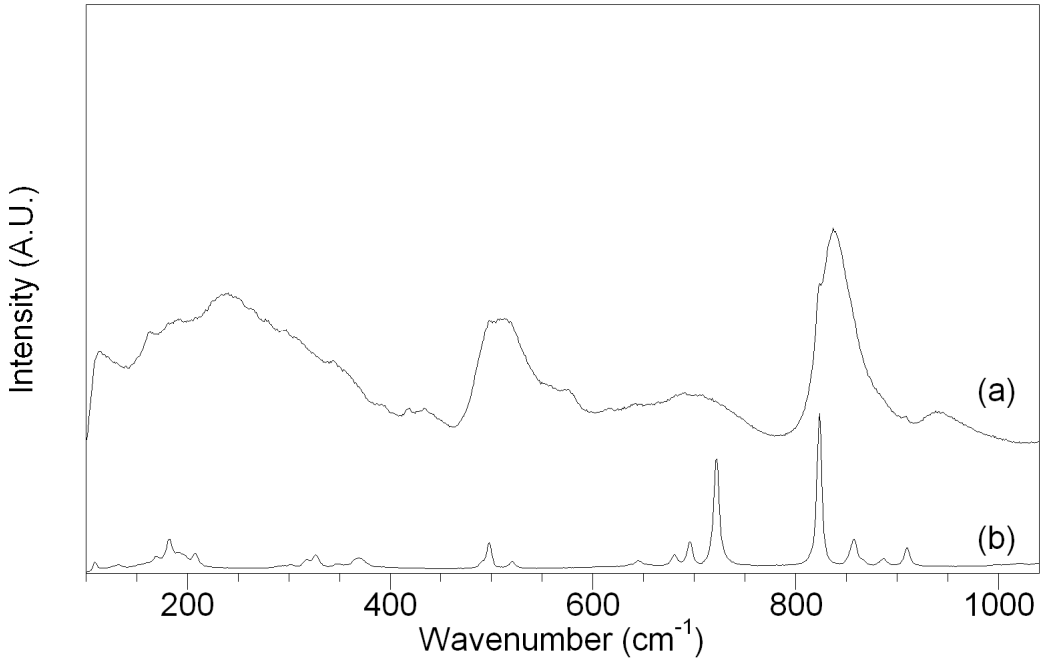

Fig. 4.19 Raman spectra of (a) $Ba_2Sc_{1.4}Si_{0.6}O_{5.3}$ and (b) Ba_2SiO_4.

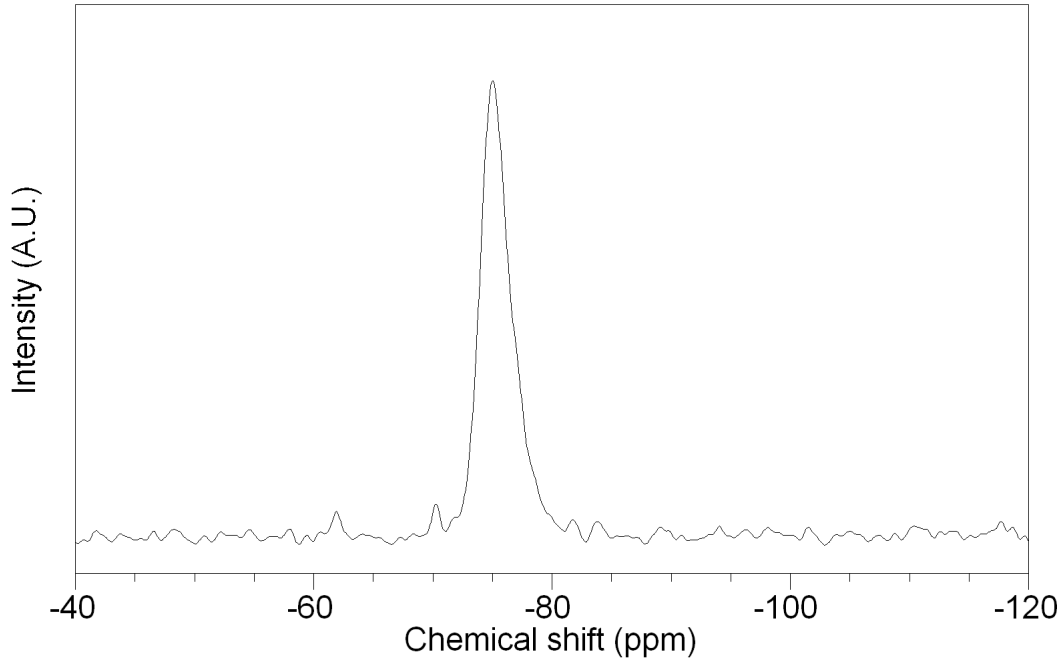

Fig. 4.20 ^{29}Si NMR spectrum for $Ba_2Sc_{1.4}Si_{0.6}O_{5.3.}$

The Raman spectrum for the x = 0.6 sample is given in Fig. 4.19. On incorporation of silicate, there is the appearance of bands in the range 800-900 cm^{-1} consistent with the presence of SiO_4^{4-}. The ^{29}Si NMR spectrum for the sample is given in Fig. 4.20. It shows the presence of a broad peak, which consists of a main peak at -74.9 ppm, with a shoulder at -76.7 ppm (intensity ratio 7:3). The chemical shift of the peaks are that of the typical tetrahedral $Si(Q^0)$ which is similar to the silicate doped $Ba_2In_2O_5$ studies. A weak peak at around -70 ppm is also shown, which is consistent with the presence of small Ba_2SiO_4 impurity. The conductivity of this sample was not measured due to the impure nature.

4.6 Nitrate doping

As noted earlier, work suggested that the parent $Ba_2Sc_2O_5$ was actually an oxide carbonate, $Ba_2Sc_{2-x}C_xO_{5+x/2}$, which accounted for the poor thermal stability. As a result of this observation, an attempt to synthesise a nitrate analogue, $Ba_2Sc_{2-x}N_xO_{5+x}$ has been made. X-ray diffraction data for both firing stages and calculated cell parameters are shown in Fig. 4.21 and table 4.12. X-ray diffraction data for the sample fired at 600 °C showed the emergence of very sharp cubic perovskite peaks having significantly smaller cell volume than $Ba_2Sc_{2-x}C_xO_{5+x/2}$, along with $BaCO_3$ and Sc_2O_3 peaks. The peaks corresponding to unreacted Sc_2O_3 were reduced by an increase in the Ba:Sc ratio (4:1) and can most likely be accounted for by the sluggish reactivity of Sc_2O_3 at low temperature. The reduction of $BaCO_3$ peaks were observed for the sample fired at 1000 °C in N_2 while the peaks for the cubic perovskite phase were broadened, which resulted in the small increase in cell volume. Hence, it is postulated that the perovskite phase formed at 600 °C firing stage is nitrate doped $Ba_2Sc_2O_5$ and there was a partial loss of the nitrate groups from the structure at 1000 °C, with possible replacement by carbonate.

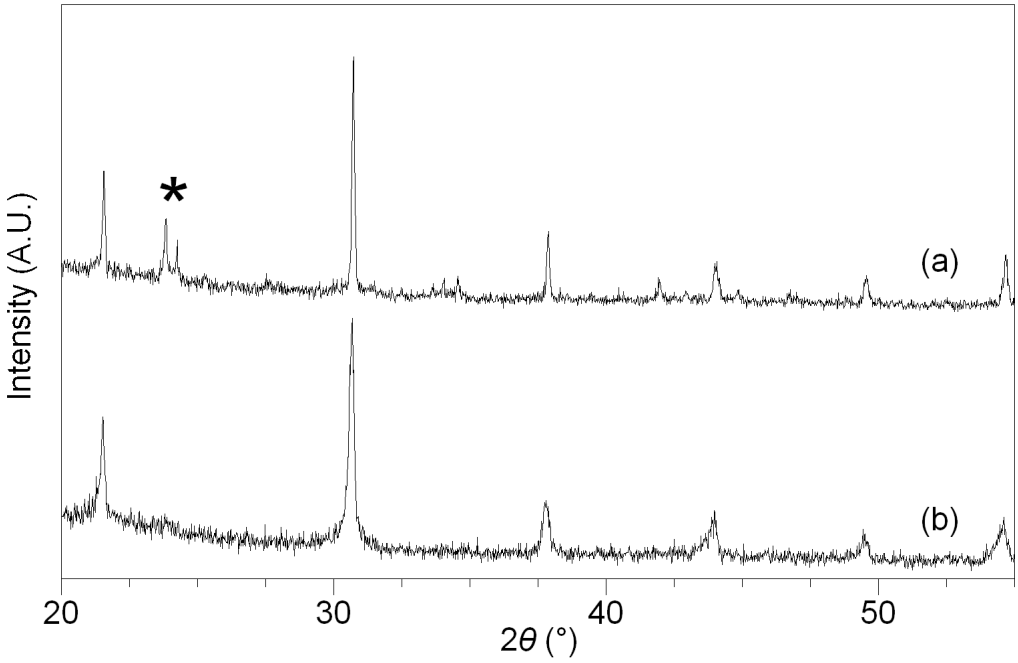

Fig. 4.21 XRD patterns for N doped $Ba_2Sc_2O_5$ fired at (a) 600 ℃ in air and (b) 1000 ℃ in N_2 (Peaks due to $BaCO_3$ is highlighted).

Table 4.12 Cell parameter data for N doped $Ba_2Sc_2O_5$

Sample (nominal composition)	Unit cell parameters (Å)	Unit cell volume (Å^3)
	a_0	
$Ba_2Sc_2O_5$	4.128(1)	70.34(3)
N doped, fired at 600 °C	4.103(1)	69.06(2)
N doped, fired at 1000 °C	4.109(1)	69.37(2)

The presence of a nitrate group in the structure is also evidenced by Raman spectroscopy studies. The spectra for the sample fired at 600 °C in air contained the intense broad double band centred at ≈ 1055 cm^{-1} (Fig. 4.22) with the region at 1059 cm^{-1} most likely corresponding to that of $BaCO_3$ impurity while the broad feature at lower wavenumber is consistent with the presence of nitrate. The spectra for the sample fired at 1000 °C in N_2 showed the reduction in the intensity in the lower wavenumber region while showing an

increase in the intensity in the peak at higher wavenumber. These changes suggest the loss of nitrate from the structure at higher firing temperature due to the possible replacement of carbonate from the decomposition of $BaCO_3$, which is in agreement with the small increase in the cell parameter. The spectra still contained the sharper feature which could correspond to $BaCO_3$ impurity, although X-ray diffraction data showed no significant peaks due to $BaCO_3$, and thus any $BaCO_3$ present is mostly poorly crystalline.

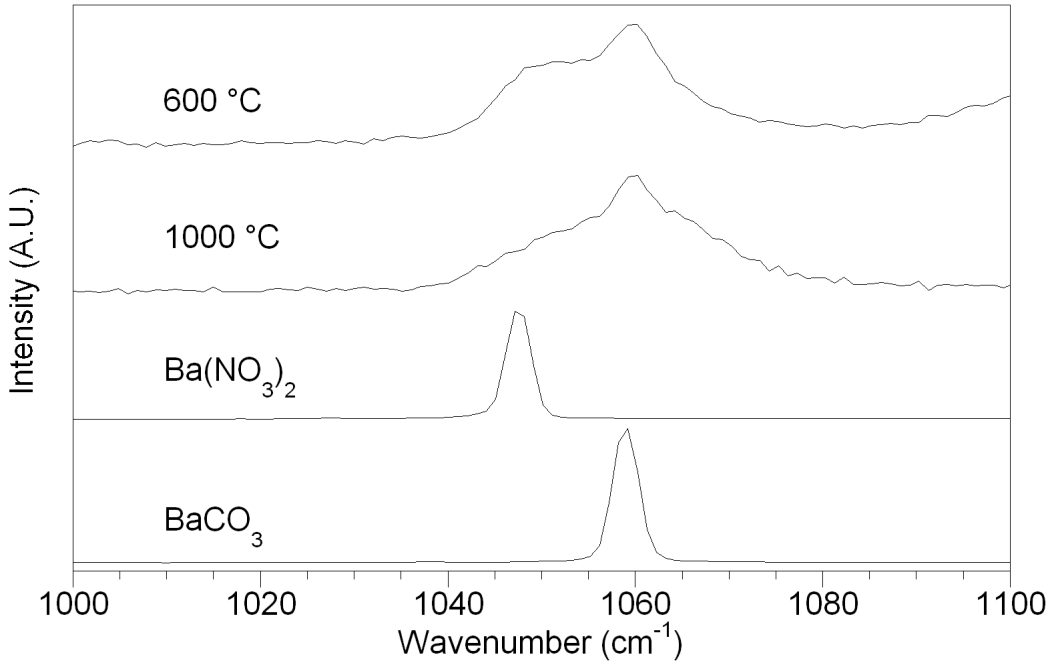

Fig. 4.22 Raman spectra for N doped $Ba_2Sc_2O_5$ fired at 600 and 1000 °C along with $Ba(NO_3)_2$ and $BaCO_3$ for comparison.

4.7 Conclusions

The results show the successful introduction of phosphate, sulphate and silicate into $Ba_2Sc_2O_5$. While single phase phosphate and sulphate doped $Ba_2Sc_2O_5$ samples ($Ba_2Sc_{1.6}P_{0.4}O_{5.4}$, $Ba_2Sc_{1.5}P_{0.5}O_{5.5}$ and $Ba_2Sc_{1.6}S_{0.4}O_{5.6}$) can be prepared, small Ba_2SiO_4 impurities are present in the silicate sample $Ba_2Sc_{1.4}Si_{0.6}O_{5.3}$. Furthermore, this work suggests that even "undoped" $Ba_2Sc_2O_5$ contains oxyanions, in this case carbonate, which explains the

previously reported thermal instability of this phase.

The phosphate doped systems showed good thermal stability along with high oxide ion conductivity. Significant proton contribution in wet atmospheres is also shown. Moreover, the doped samples show higher CO_2 stability than doped $BaCeO_3$. The work further emphasize the potential of this oxyanion doping strategy in perovskite related phases, with regards to the formation of new phases with high conductivities and high CO_2 stability.

4.8 Appendices

Appendix 4.1 Impedance spectra for $Ba_2Sc_{1.6}P_{0.4}O_{5.4}$ in dry N_2 at 300 ℃ showing typical bulk and grain boundary semicircles

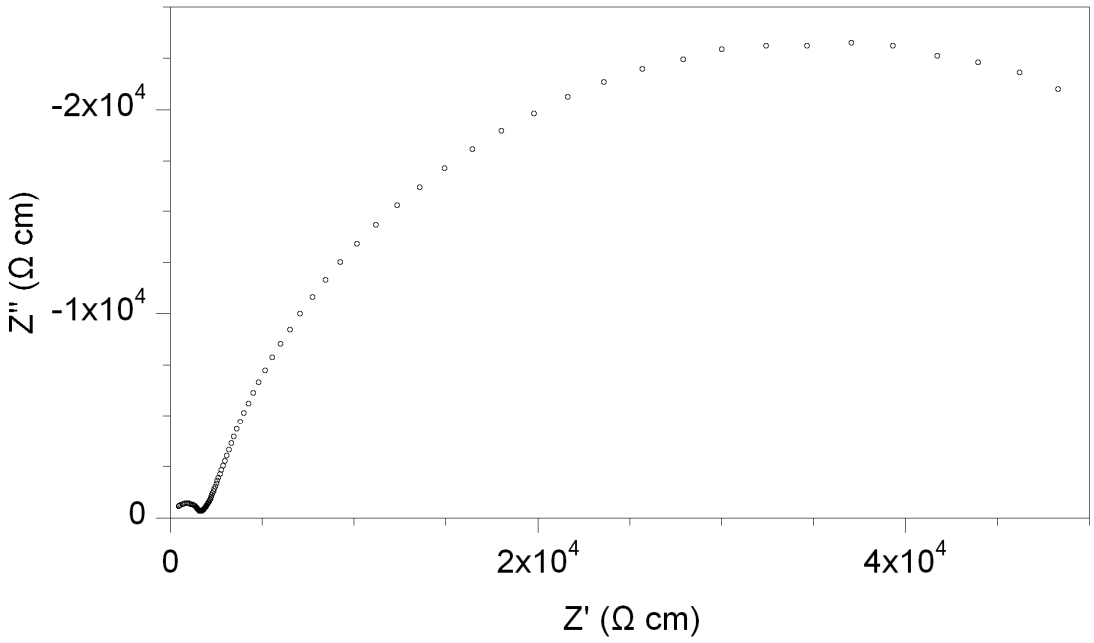

4.9 References

[1] Kwestroo, W.; van Hal, H. A. M.; Langereis, C. *Mater. Res. Bull.* **1974**, *9*, 1623.
[2] Omata, T.; Fuke, T.; Otsuka-Yao-Matsuo, S. *Solid State Ionics* **2006**, *177*, 2447.
[3] Shin, J. F.; Apperley, D. C.; Slater, P. R. *Chem. Mater.* **2010**, *22*, 5945.
[4] Abakumov, A. M.; Rossell, M. D.; Gutnikova, O. Y.; Drozhzhin, O. A.; Leonova, L. S.; Dobrovolsky, Y. A.; Istomin, S. Y.; Tendeloo, G. V.; Antipov, E. V. *Chem. Mater.* **2008**, *20*, 4457.
[5] Larson, A. C.; Von Dreele, R. B. *Los Alamos National Laboratory Report LAUR* **1994**, 86-748.
[6] Mackenzie, K. J. D.; Smith, M. E. *Multinuclear Solid State NMR of Inorganic Materials*, Pergamon Materials series, Permagon, Oxford, **2002**
[7] Goodenough, J. B. *Ann. Rev. Mater. Res.* **2003**, *33*, 91.
[8] Kreuer, K. D. *Ann. Rev. Mater. Res.* **2003**, *33*, 333.

Chapter 5 Y/Yb Doping in $Ba_2In_2O_5$

5.1 Introduction

The studies presented in chapter 3 have demonstrated that oxyanion (phosphate, sulfate, silicate) doping is successful in enhancing the oxide ion conductivity in $Ba_2In_2O_5$ and related phases through the introduction of disorder, along with enhancing the stability towards CO_2 (poor CO_2 stability is a key issue for applications of many potential proton conducting electrolytes). However, the high cost of In is one of the issues for technological applications, as well as the tendency for In^{3+} to reduce at high temperatures under reducing conditions, thus raising the necessity to investigate strategies to reduce the In content. In this respect Y, Yb doping in $Ba_2In_2O_5$ have been examined. Previous studies have shown Y substitution up to 35% in $Ba_2In_2O_5$ and a similar solubility limit of Yb into the related $Ba_{0.6}Sr_{0.4}LaIn_2O_{5.5}$ [1, 2]. In this chapter, we expand such studies to investigate the CO_2 stability of such systems, as well as the possible incorporation of higher levels of Y, Yb through co-doping with phosphate.

5.2 Experimental

High purity $BaCO_3$, In_2O_3, La_2O_3, Y_2O_3, Yb_2O_3, and $NH_4H_2PO_4$ were used to prepare $Ba_{2-z}La_zIn_{2-x-y}M_yP_xO_{5+x+z/2}$ (M=Y, Yb) samples. A small (3%) excess of $BaCO_3$ was employed, in order to overcome Ba loss at elevated temperatures, and eliminate Ba deficient impurity phases, such as $Ba_3In_4O_9$, as has been seen in other studies synthesising similar Ba containing phases [3, 4]. The powders were intimately ground and heated initially to 1000°C for 12 hours. They were then ball-milled (350 rpm for 1 hour, Fritsch Pulverisette 7 Planetary Mill) and reheated to 1000°C for 50 hours. The resulting powders were then ball-milled a second time and pressed as pellets (1.3 cm diameter) and sintered at 1400°C for 10 hours. The

pellets were covered in sample powder and the crucible was covered with a lid to limit the amount of Ba loss during the sintering process. Powder X-ray diffraction (Bruker D8 diffractometer with Cu $K\alpha_1$ radiation = 1.5406 Å) was used to demonstrate phase purity as well as for preliminary structure determination. For the latter, the GSAS suite of programs was used [5].

The CO_2 stability of samples was determined using thermogravimetric analysis (Netzsch STA 449 F1 Jupiter Thermal Analyser). Samples were heated at 10 $^{\circ}C\ min^{-1}$ to 1000 $^{\circ}C$ in a 1:1 CO_2 and N_2 mixture to determine at what temperature CO_2 pick up occurred. In addition further stability studies were performed by heating samples at 600$^{\circ}C$ for 12 hours in a tube furnace under flowing CO_2 gas.

Raman spectroscopy measurements were made in order to provide further evidence for the successful incorporation of phosphate. These measurements utilised a Renishaw inVia Raman microscope with excitation using a Cobolt Samba CW 532 nm DPSS Laser.

The water contents of hydrated samples were determined from thermogravimetric analysis (Netzsch STA 449 F1 Jupiter Thermal Analyser). Samples were heated at 10$^{\circ}C\ min^{-1}$ to 1000$^{\circ}C$ in N_2, and the water content was determined from the observed mass loss.

For the conductivity measurements, the sintered pellets were coated with Pt paste, and then heated to 800°C for 1 hour to ensure bonding to the pellet. Conductivities were then measured by AC impedance measurements (Hewlett Packard 4182A impedance analyser) in the range from 0.1 to 10^3 kHz. Measurements were made in dry N_2 and wet N_2 (in which the gas was bubbled at room temperature through water) to identify any protonic contribution to the conductivity.

The impedance data showed generally a single broad semicircle in both dry and wet atmospheres. The capacitance of the broad semicircle was typical of a bulk response,

suggesting that the resistance of the grain boundary was small compared to that of the bulk (Appendix 5.1).

5.3 Yttrium and Ytterbium doped $Ba_2In_2O_5$: $Ba_2In_{2-y}(Y/Yb)_yO_5$ (y = 0, 0.4, 0.7)

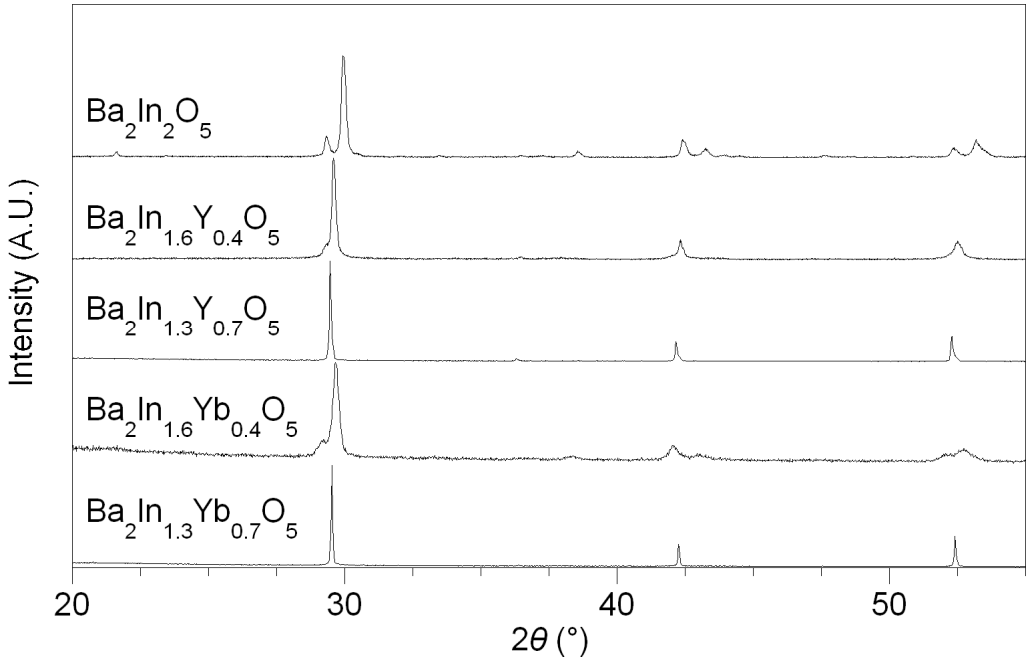

Fig. 5.1 XRD patterns for $Ba_2In_{2-y}(Y/Yb)_yO_5$

Initially, the determination of the solid solution limits for Y, Yb doping in $Ba_2In_2O_5$ was examined. The results indicated that single phase samples of $Ba_2In_{2-y}M_yO_5$ (M=Y, Yb) could be obtained for $0 \leq y \leq 0.7$, while Y, Yb excess phases (e.g. $Ba_3(Y/Yb)_4O_9$) were observed for higher levels of Y, Yb. These solid solution limits for Y, Yb in the $Ba_2In_2O_5$ structure are in agreement with those previously reported by Noirault *et al.* for Y doped systems, and for Yb doping by Kakinuma *et al.* in the related $Ba_{0.6}Sr_{0.4}LaIn_2O_{5.5}$ [1, 2]. The X-ray data showed a reduction in the orthorhombic splitting on Y, Yb incorporation, and a transition to cubic symmetry for the highest Y, Yb levels, suggesting the introduction of disorder on the oxygen sublattice through Y, Yb doping (Fig. 5.1). The structure refinement for the y = 0.7 samples

showed B site occupancies (1.30(1) In and 0.70(1) Y and 1.30(1) In and 0.70(1) Yb) consistent with those expected for the nominal starting composition (Appendix 5.2 and 5.3). The cell parameters showed an increase (comparing equivalent cells) on Y, Yb incorporation, which is consistent with the larger sizes of Y^{3+}/Yb^{3+} compared to In^{3+} (Table 5.1).

Table 5.1 Cell parameter data for $Ba_2In_{2-y}(Y/Yb)_yO_5$

Sample (nominal composition)	Unit cell parameters (Å)			Unit cell volume (Å^3)
	a	b	c	
$Ba_2In_2O_5$	6.089(2)	16.736(8)	5.963(2)	607.6(2)
$Ba_2In_{1.6}Y_{0.4}O_5$	6.025(3)	17.135(9)	6.040(2)	623.5(3)
$Ba_2In_{1.3}Y_{0.7}O_5$	4.280(1)	-	-	78.38(4)
$Ba_2In_{1.6}Yb_{0.4}O_5$	6.118(2)	16.817(9)	6.005(3)	617.8(4)
$Ba_2In_{1.3}Yb_{0.7}O_5$	4.264(1)	-	-	77.53(4)

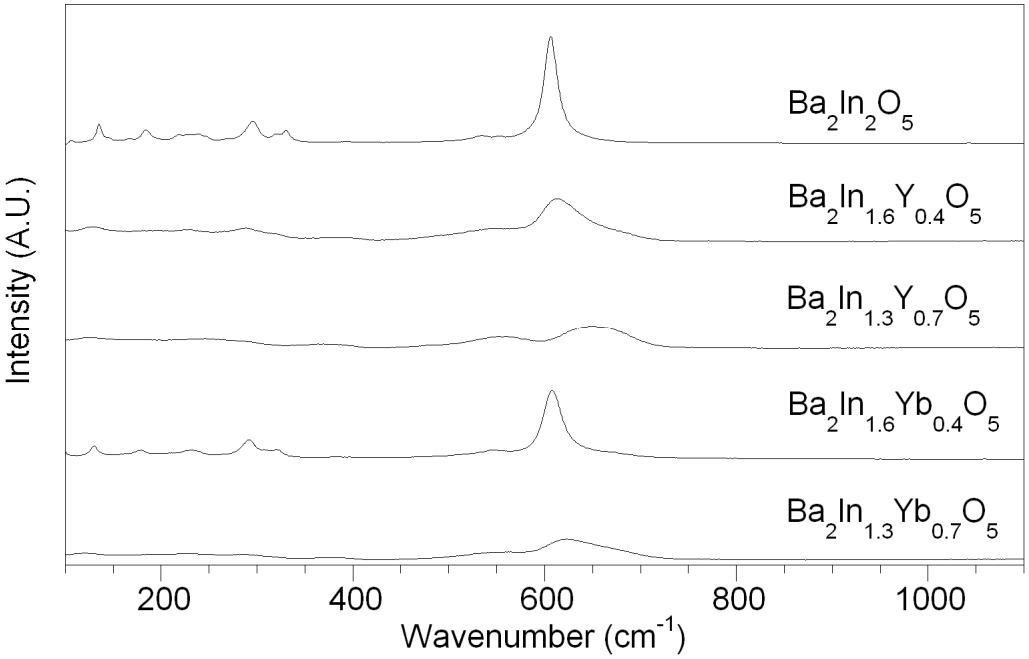

Fig. 5.2 Raman spectra of $Ba_2In_{2-y}(Y/Yb)_yO_5$

The Raman spectra for the y = 0, 0.4, 0.7 samples are given in Fig. 5.2. On incorporation of Y, Yb, there is the reduction in the intensity of In-O bands, mostly notable for the band at 600 cm^{-1}, which broadened with higher level of Y/Yb incorporation while the intensity of the band at 550 cm^{-1} was more significant. These changes are in agreement with previous studies of the introduction of oxygen disorder by oxyanion doping (chapter 3 and 4). The presence of some bands indicates that while the average structure determined in diffraction studies for y = 0.7 samples is cubic, there are considerable local distortions away from cubic symmetry as observed in the oxyanion doped $Ba_2M_2O_5$ (M = Sc, In) samples in chapter 3 and 4.

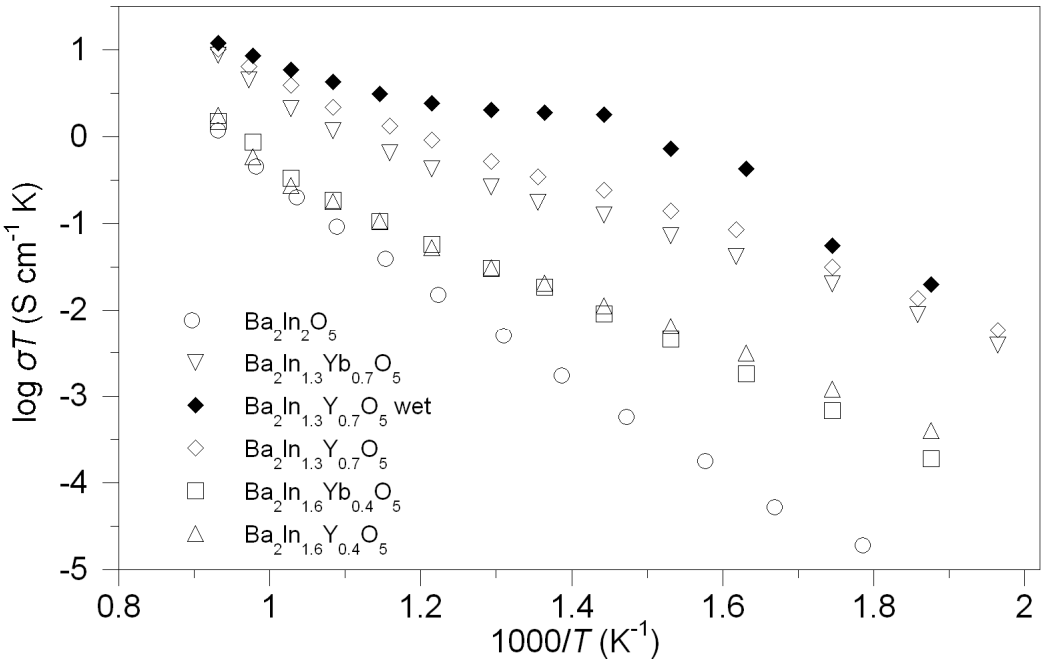

Fig. 5.3 Conductivity data in dry N_2 for $Ba_2In_{2-y}(Y/Yb)_yO_5$. Conductivity data in wet N_2 for $Ba_2In_{1.3}Y_{0.7}O_5$ (filled diamond) is also shown.

Table 5.2 Bulk conductivity data for $Ba_2In_{2-y}(Y/Yb)_yO_5$

Sample (nominal composition)	Conductivity (S cm^{-1})		
	500 °C		800 °C
	Wet	Dry	
$Ba_2In_2O_5$	3.2×10^{-5}	6.5×10^{-6}	1.1×10^{-3}
$Ba_2In_{1.6}Y_{0.4}O_5$	1.8×10^{-4}	4.0×10^{-5}	1.7×10^{-3}
$Ba_2In_{1.3}Y_{0.7}O_5$	2.6×10^{-3}	6.7×10^{-4}	9.5×10^{-3}
$Ba_2In_{1.6}Yb_{0.4}O_5$	1.7×10^{-4}	3.9×10^{-5}	1.4×10^{-3}
$Ba_2In_{1.3}Yb_{0.7}O_5$	4.6×10^{-4}	3.4×10^{-4}	8.1×10^{-3}

The conductivity data showed that there is an enhancement in the conductivity in dry N_2 on Y, Yb doping (Fig. 5.3, table 5.2), in agreement with the above conclusions regarding the increase in disorder on the oxygen sublattice, with a further enhancement owing to a protonic contribution on changing to wet N_2, similar to the studies presented in chapter 3 and 4. Following on from these conductivity studies, the CO_2 stability on Y, Yb incorporation was studied: undoped $Ba_2In_2O_5$ is known to have comparatively poor CO_2 stability, showing a significant mass increase above 600 °C in the TG profile on heating in a 1:1 CO_2 and N_2 gas mixture. The Y, Yb doped samples exhibited similar low stability (Fig. 5.4), with the temperature for the first observed mass increases being slightly lower, at 550°C, for both $Ba_2In_{1.3}Y_{0.7}O_5$ and $Ba_2In_{1.3}Yb_{0.7}O_5$, while the overall mass increases were slightly lower (Fig. 5.4). X-ray diffraction data of the samples heated under CO_2 in a tube furnace at 600°C showed the presence of significant amounts of $BaCO_3$ impurity, with the highest levels of $BaCO_3$ observed for undoped $Ba_2In_2O_5$ (Fig. 5.5) in agreement with the highest mass increase from the TGA results.

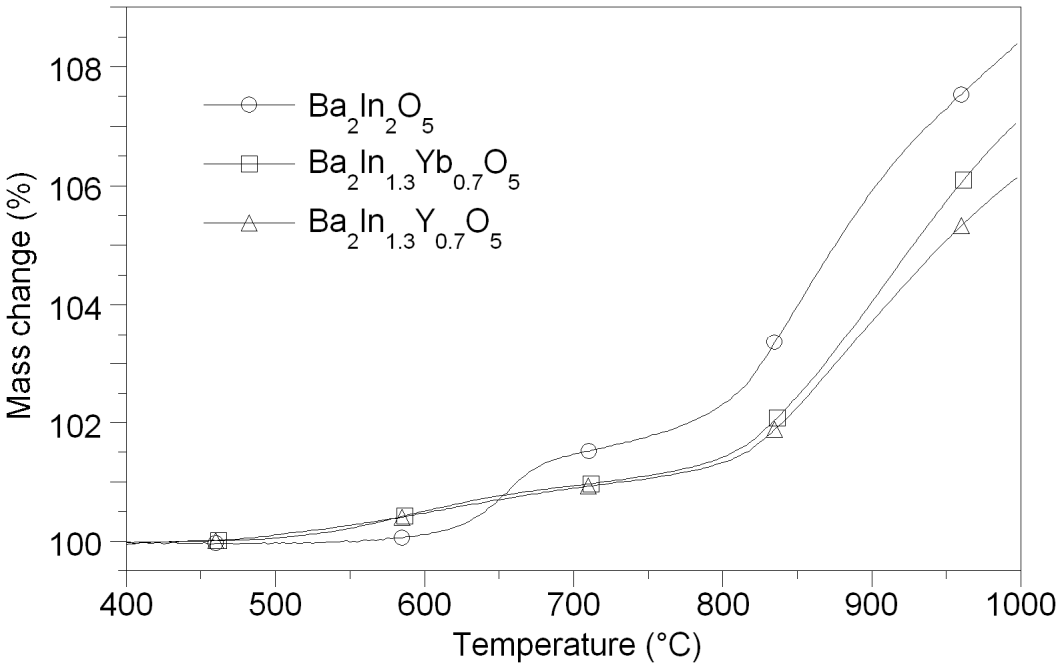

Fig. 5.4. TG profiles (10 ℃ min^{-1} to 1000 ℃ in 1:1 CO_2 and N_2 mixture) for $Ba_2In_{1.3}(Y/Yb)_{0.7}O_5$.

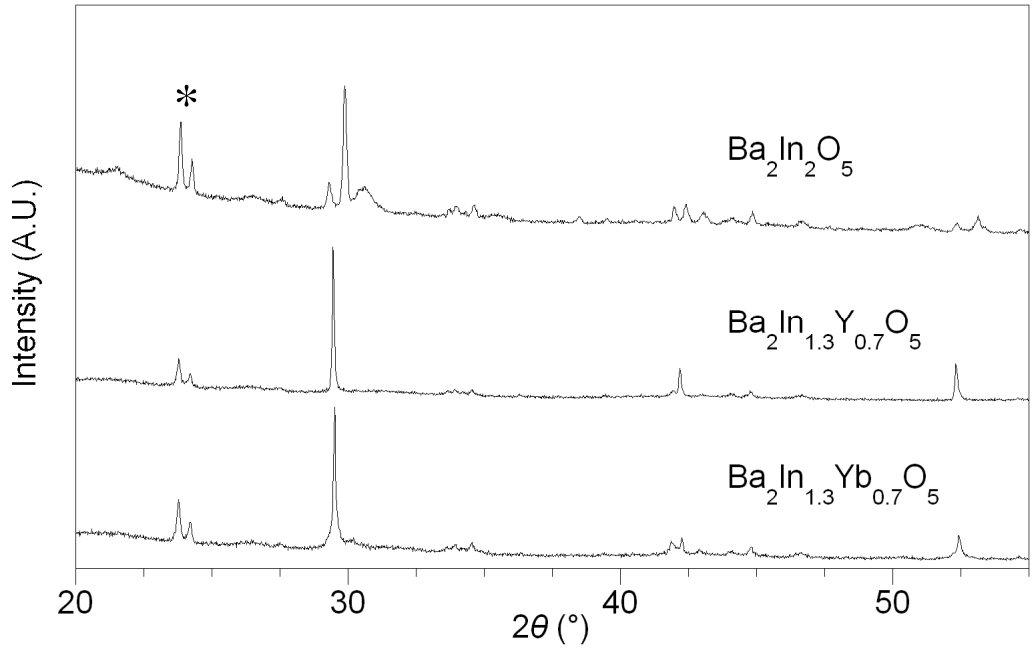

Fig. 5.5 XRD patterns for $Ba_2In_2O_5$ and $Ba_2In_{1.3}(Y/Yb)_{0.7}O_5$ after heating in CO_2 at 600 ℃ for 12h (Peaks due to $BaCO_3$ are highlighted).

For the determination of the maximum level of water incorporated in these samples, they were heated under wet N_2 to 800°C, then cooled slowly (0.4 °C min^{-1}) to room temperature. The water content of these hydrated samples was then determined by thermogravimetric analysis, which resulted in values of 1 H_2O per formula unit, indicating the complete filling of the oxide ion vacancies.

5.4 Y/Yb doped $Ba_2In_2O_5$ systems co-doped with La, P

In order to increase the maximum incorporation level of Y, Yb, as well as enhance the CO_2 stability, co-doping with phosphate was examined. The results showed that quite high levels of phosphate were required to increase the Y/Yb content further, with it proving to be possible to prepare single phase samples with composition $Ba_2In_{0.5}(Y/Yb)P_{0.5}O_{5.5}$ (Fig. 5.6, table 5.3). The Raman spectra for these co-doped samples confirmed the presence of phosphate, as exemplified by the emergence of a peak at 940 cm^{-1}, in line with prior studies on phosphate doped $Ba_2M_2O_5$ (M = In, Sc) in chapter 3 and 4 (Fig. 5.7).

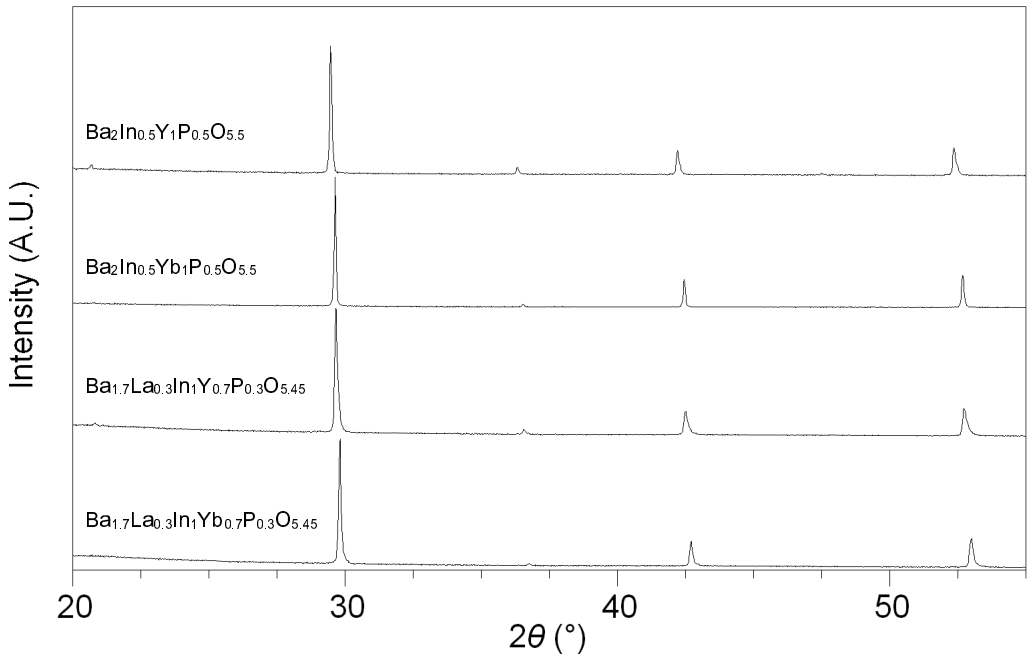

Fig. 5.6 XRD patterns for La and/or P and/or Y/Yb co-doped $Ba_2In_2O_5$

Table 5.3 Cell parameter data for La and/or P co-doped $Ba_2In_{2-y}(Y/Yb)_yO_5$

Sample (nominal composition)	Unit cell parameters (Å)			Unit cell volume (Å^3)
	a	b	c	
$Ba_2In_2O_5$	6.089(2)	16.736(8)	5.963(2)	607.6(2)
$Ba_2In_{0.5}Y_1P_{0.5}O_{5.5}$	4.269(1)	-	-	77.78(4)
$Ba_2In_{0.5}Yb_1P_{0.5}O_{5.5}$	4.244(1)	-	-	76.43(4)
$Ba_{1.7}La_{0.3}In_1Y_{0.7}P_{0.3}O_{5.45}$	4.241(1)	-	-	76.25(4)
$Ba_{1.7}La_{0.3}In_1Yb_{0.7}P_{0.3}O_{5.45}$	4.221(1)	-	-	75.23(4)
$Ba_2Y_{1.5}P_{0.5}O_{5.5}$	4.290(1)	-	-	78.92(5)
$Ba_2Yb_{1.5}P_{0.5}O_{5.5}$	4.251(1)	-	-	76.81(4)

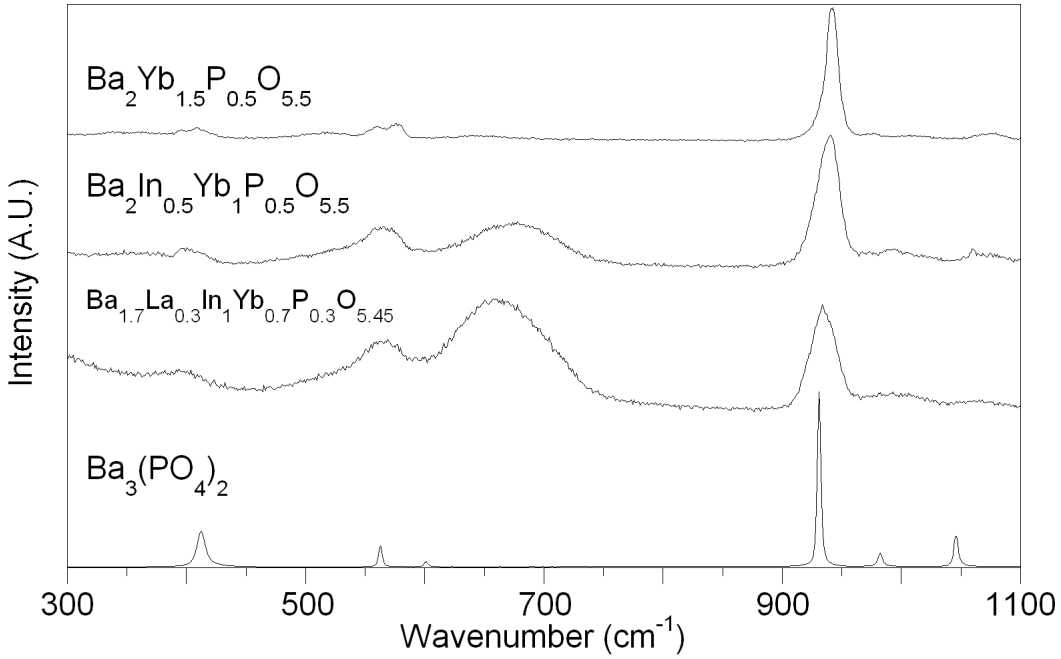

Fig. 5.7 Raman spectra of $Ba_2Yb_{1.5}P_{0.5}O_{5.5}$, $Ba_2In_{0.5}Yb_1P_{0.5}O_{5.5}$, $Ba_{1.7}La_{0.3}In_1Yb_{0.7}P_{0.3}O_{5.45}$ and $Ba_3(PO_4)_2$

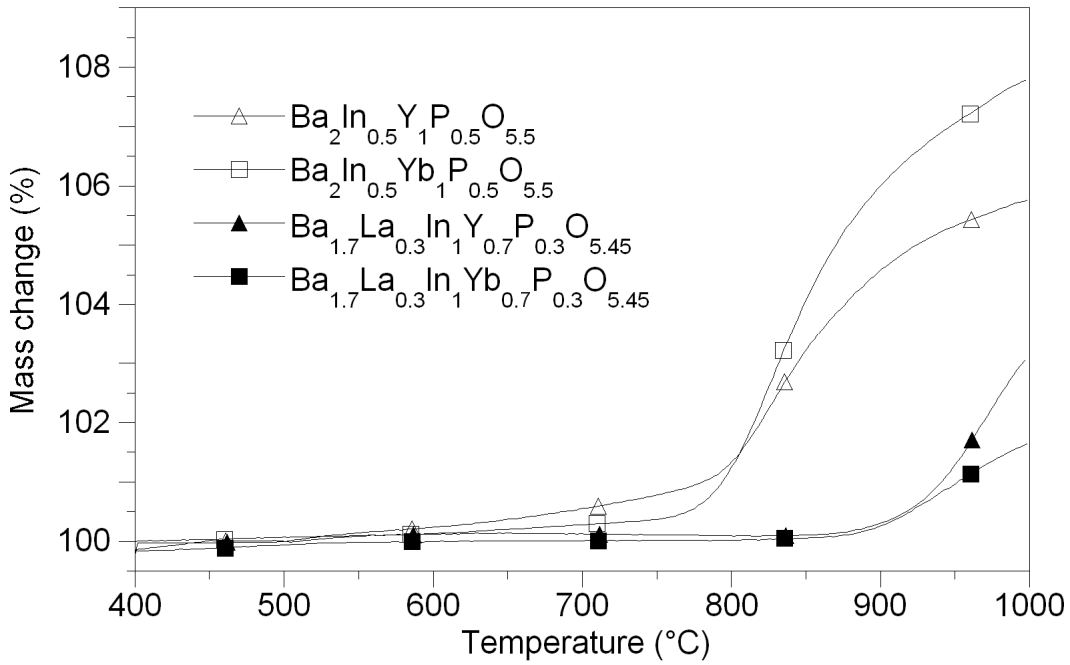

Fig. 5.8 TG profiles (10 ℃ min^{-1} to 1000 ℃ in 1:1 CO_2 and N_2 mixture) for La and/or P and Y/Yb co-doped $Ba_2In_2O_5$

While the previous studies for Y, Yb doped $Ba_2In_2O_5$ showed a small decrease in the onset temperature of CO_2 pick-up, the phosphate co-doped samples, despite the higher Y, Yb levels, resulted in a small increase in this temperature, with the $Ba_2In_{0.5}YbP_{0.5}O_{5.5}$ sample only showing a mass increase above 700 °C (Fig. 5.8 and 5.9). This was also observed for phosphate doped $Ba_2In_2O_5$ studies, and it was proposed that the incorporation of phosphate reduces the basicity of the system, thus resulting in the enhancement in CO_2 stability. Although the phosphate co-doping showed a beneficial effect in terms of the CO_2 stability, it proved to be detrimental on the conductivity (Table 5.4). This is most likely caused by the decrease in the oxide ion vacancy level due to the doping of higher valent P, and the presence of oxygen vacancy trapping around the phosphorus, due to its preference to be incorporated as a tetrahedral PO_4^{3-} ion. Further increases in the Y, Yb content in the presence of phosphate proved to be possible and the complete replacement of In with Y, Yb was successful, resulting

in the samples with nominal starting composition $Ba_2(Y/Yb)_{1.5}P_{0.5}O_{5.5}$. However, the presence of $Ba_3(Y/Yb)_4O_9$ impurities cannot be avoided in the synthesis of these particular phases, despite increasing the $BaCO_3$ excess to >10%.

Table 5.4 Bulk conductivity data for La and/or P co-doped $Ba_2In_{2-y}(Y/Yb)_yO_5$

Sample (nominal composition)	Conductivity (S cm^{-1})		
	500 °C		800 °C
	Wet	Dry	
$Ba_2In_{0.5}Y_1P_{0.5}O_{5.5}$	4.5 x 10^{-4}	1.7 x 10^{-4}	4.4 x 10^{-4}
$Ba_2In_{0.5}Yb_1P_{0.5}O_{5.5}$	6.6 x 10^{-4}	2.0 x 10^{-4}	6.1 x 10^{-4}
$Ba_{1.7}La_{0.3}In_1Y_{0.7}P_{0.3}O_{5.45}$	3.3 x 10^{-4}	9.8 x 10^{-5}	1.5 x 10^{-3}
$Ba_{1.7}La_{0.3}In_1Yb_{0.7}P_{0.3}O_{5.45}$	2.7 x 10^{-4}	8.3 x 10^{-5}	1.3 x 10^{-3}

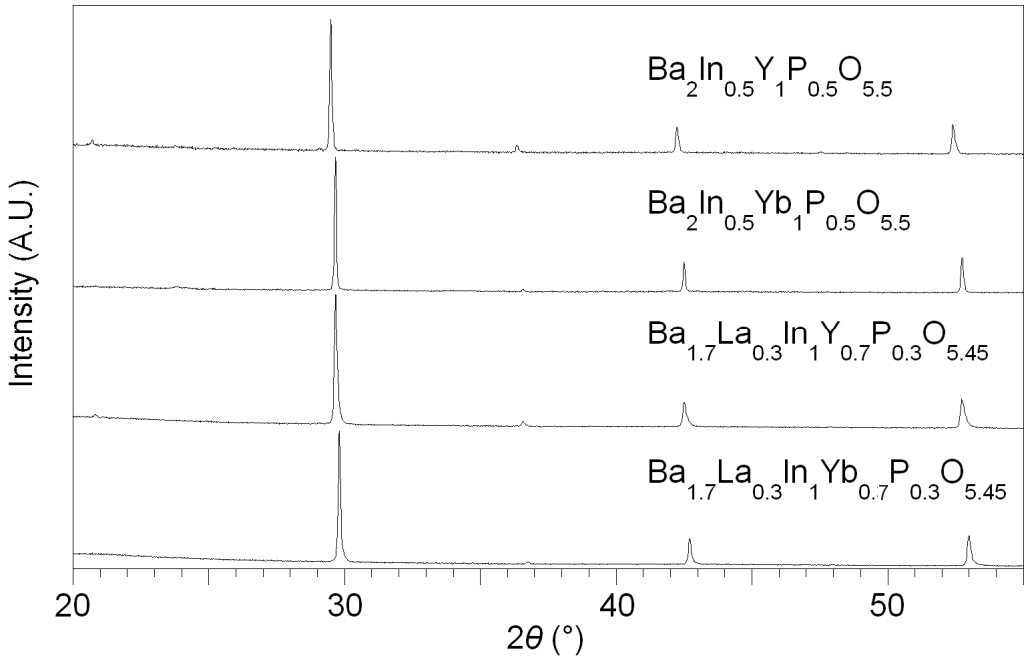

Fig. 5.9 XRD patterns for La and/or P and Y/Yb co-doped $Ba_2In_2O_5$ after heating in CO_2 at 600 °C for 12h, showing no evidence for $BaCO_3$ formation unlike for samples without P doping (see Fig. 5.5).

The structure refinement using X-ray diffraction data for $Ba_2Yb_{1.5}P_{0.5}O_{5.5}$ (Appendix 5.4) indicated an Yb content of 1.47(1), which is similar to the nominal value of 1.5 in the starting composition. No further analysis was performed on these samples due to the impure nature.

In order to improve the CO_2 stability further, additional co-doping with La was examined, as the previous studies of La and phosphate doping in $Ba_2In_2O_5$ resulted in a large enhancement in the CO_2 stability (Chapter 3). To accommodate the additional La, the phosphate level had to be reduced and single phase samples of composition $Ba_{1.7}La_{0.3}In_1(Y/Yb)_{0.7}P_{0.3}O_{5.45}$ were prepared as shown by X-ray diffraction data (Fig. 5.6). In agreement with the prior studies, the results here showed a further improvement in the CO_2 stability of these samples, with TGA showing a mass increase on heating in a 1:1 CO_2/N_2 gas mixture only at temperatures above $\approx 900^{\circ}C$ (Fig. 5.8). However, the conductivity was significantly lower compared to both samples with and without phosphate (Table 5.4).

5.5 Conclusions

It has been shown that up to 35% Y, Yb can be incorporated into $Ba_2In_2O_5$ leading to an improvement in the low temperature conductivity as a result of the introduction of disorder on the oxygen sublattice. Higher levels of Y, Yb incorporation are possible through co-doping with phosphate. These co-doped samples showed a small improvement in the CO_2 stability, although there was a detrimental effect on the conductivity. The CO_2 stability could be improved further through co-doping on the Ba site with La. However, it was again shown to be at the detriment of the conductivity, indicating the difficulties of achieving both high conductivity and CO_2 stability in such perovskite systems.

5.6 Appendices

Appendix 5.1 Impedance spectra at 260 ℃ for $Ba_2In_{1.3}Yb_{0.7}O_5$ in dry and wet N_2 showing a single semicircle.

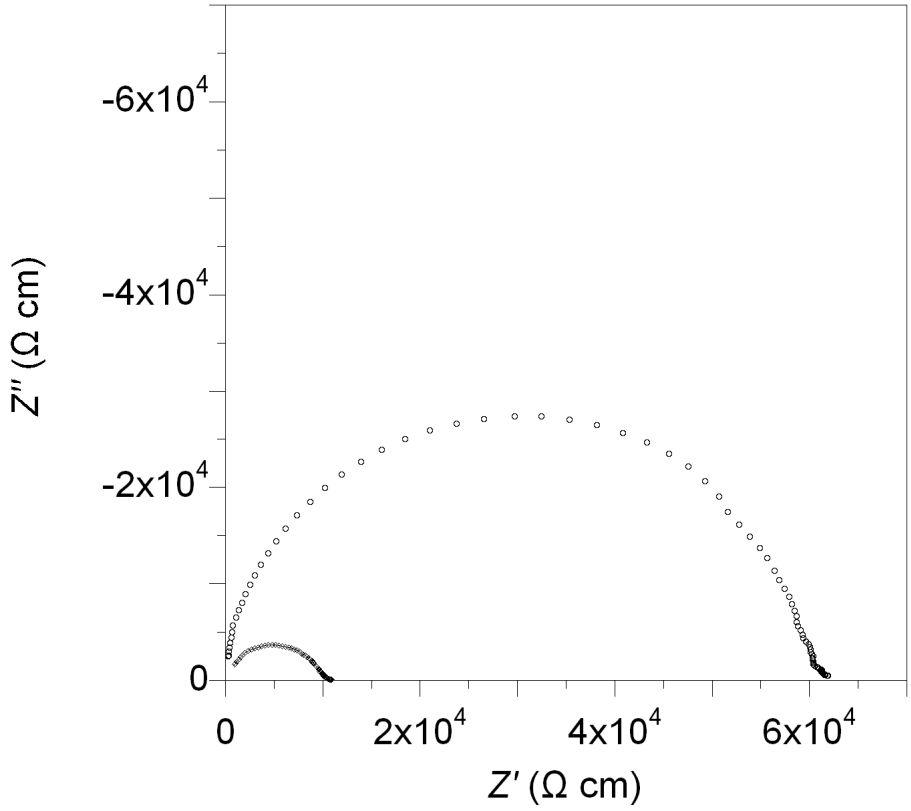

Appendix 5.2.a Observed (cross), calculated (line), and difference plots (observed – calculated) of $Ba_2In_{1.3}Y_{0.7}O_5$ from the Rietveld refinement for room temperature X-ray diffraction data.

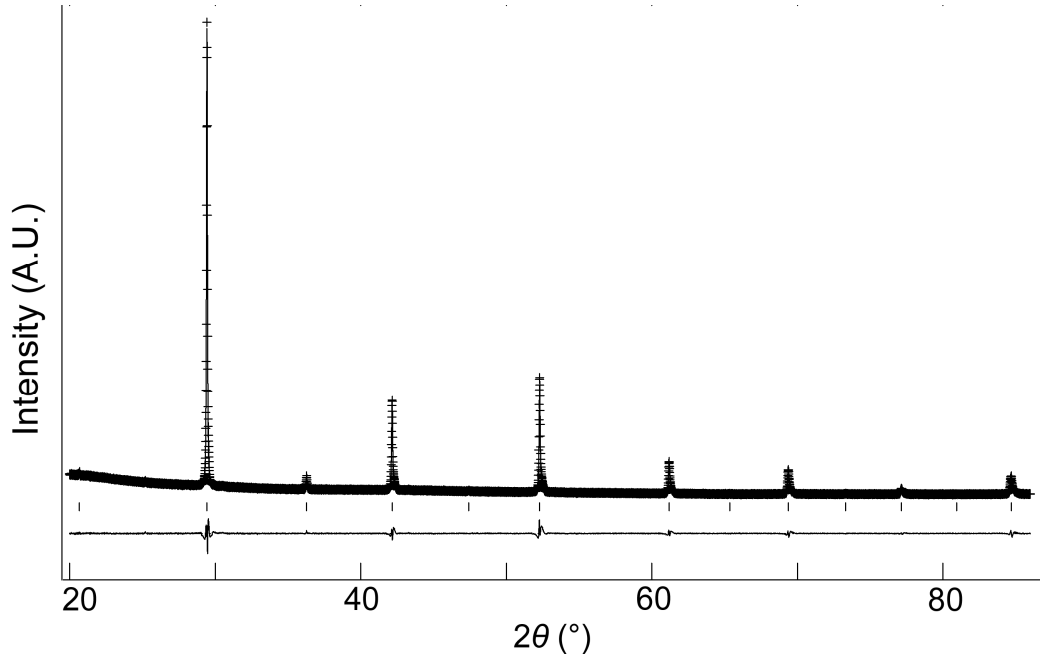

Appendix 5.2.b Refined structural parameters for $Ba_2In_{1.3}Y_{0.7}O_5$ using cubic $Pm\bar{3}m$ (221) space group from room temperature X-ray diffraction data.

		a (Å)	R_{wp}	R_p	χ^2
		4.2800 (1)	5.18	3.05	4.21

		x	y	z	Fractional occupancy	U_{iso} (Å^2 x 100)
Ba	1b	½	½	½	1.000	3.73 (7)
In	1a	0	0	0	0.651 (8)	4.08 (9)
Y	1a	0	0	0	0.349 (8)	4.08 (9)
O	3d	0	0	½	0.833 (11)	8.69(34)

Appendix 5.3.a Observed (cross), calculated (line), and difference plots (observed – calculated) of $Ba_2In_{1.3}Yb_{0.7}O_5$ from the Rietveld refinement for room temperature X-ray diffraction data.

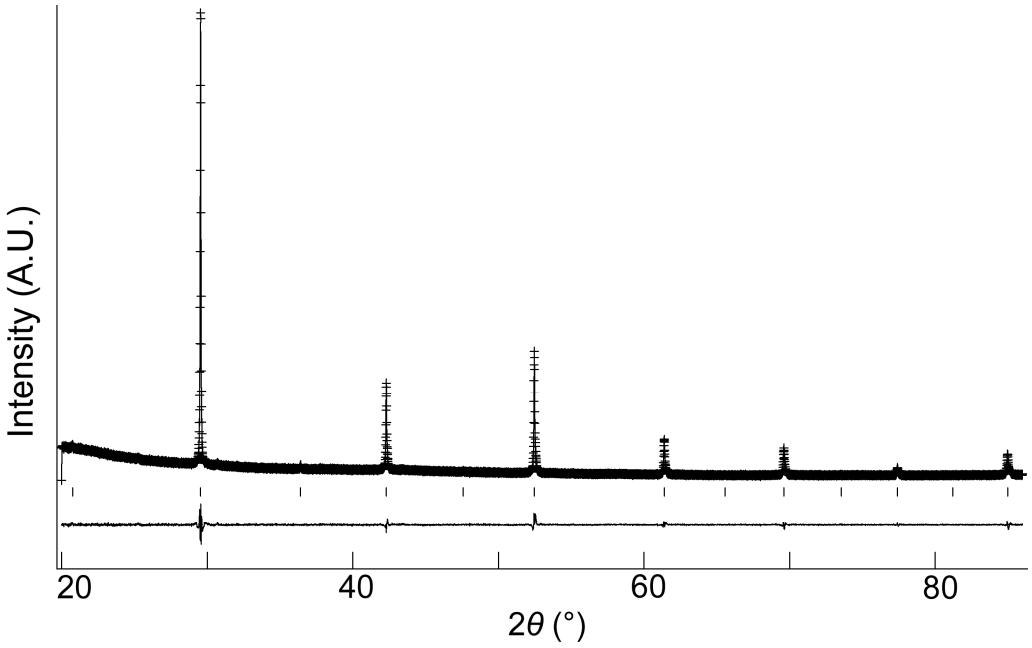

Appendix 5.3.b Refined structural parameters for $Ba_2In_{1.3}Yb_{0.7}O_5$ using cubic $Pm\bar{3}m$ (221) space group from room temperature X-ray diffraction data.

		a (Å)	R_{wp}	R_p	χ^2
		4.2641 (1)	5.59	3.99	1.97

		x	y	z	Fractional occupancy	U_{iso} (Å^2 x 100)
Ba	1(b)	½	½	½	1.000	3.26 (14)
In	1(a)	0	0	0	0.650 (8)	2.92 (14)
Yb	1(a)	0	0	0	0.350 (8)	2.92 (14)
O	3(d)	0	0	½	0.829 (15)	6.72 (41)

Appendix 5.4.a Observed (cross), calculated (line), and difference plots (observed – calculated) of $Ba_2Yb_{1.5}P_{0.5}O_{5.5}$ from the Rietveld refinement for room temperature X-ray diffraction data.

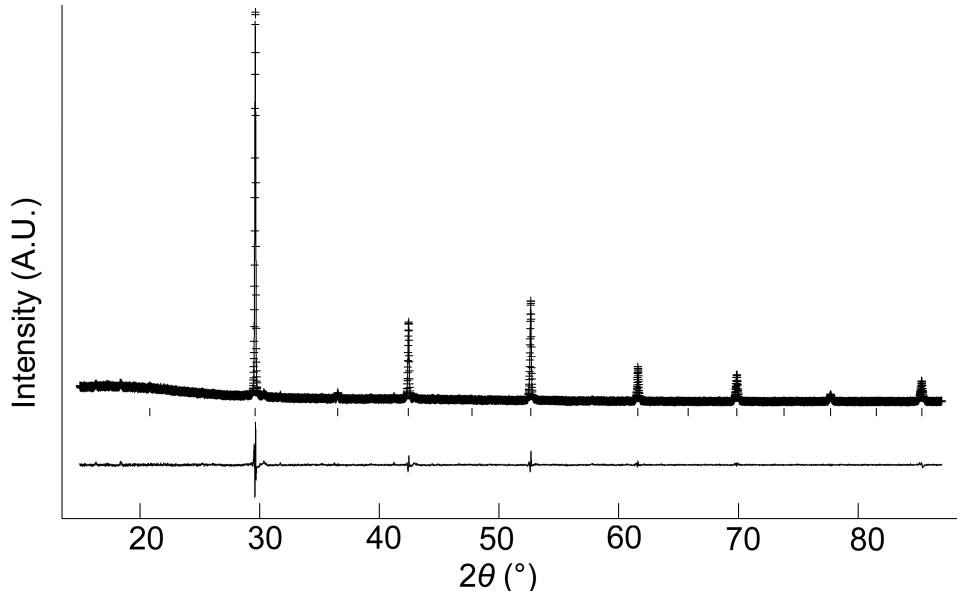

Appendix 5.4.b Refined structural parameters for $Ba_2Yb_{1.5}P_{0.5}O_{5.5}$ using cubic $Pm\bar{3}m$ (221) space group from room temperature X-ray diffraction data.

		a (Å)	R_{wp}	R_p	χ^2
		4.2508 (1)	7.35	5.41	2.04

		x	y	z	Fractional occupancy	U_{iso} (Å^2 x 100)
Ba	1(b)	½	½	½	1.000	1.99 (10)
Yb	1(a)	0	0	0	0.733 (8)	2.42 (12)
P	1(a)	0	0	0	0.267 (8)	2.42 (12)
O	3(d)	0	0	½	0.932 (15)	6.93 (38)

5.7 References

[1] Kakinuma, K.; Waki, T.; Yamamura, H.; Atake, T. *J. Ceram. Soc. Jp.* **2009**, *117*, 529.

[2] Noirault, S.; Quarez, E.; Piffard, Y.; Joubert, O. *Solid State Ionics.* **2009**, *180*, 1157.

[3] Omata, T.; Fuke, T.; Otsuka-Yao-Matsuo, S. *Solid State Ionics* **2006**, *177*, 2447.

[4] Abakumov, A. M.; Rossell, M. D.; Gutnikova, O. Y.; Drozhzhin, O. A.; Leonova, L. S.; Dobrovolsky, Y. A.; Istomin, S. Y.; Tendeloo, G. V.; Antipov, E. V. *Chem. Mater.* **2008**, *20*, 4457.

[5] Larson, A. C.; Von Dreele, R. B. *Los Alamos National Laboratory Report LAUR* **1994**, 86-748.

Chapter 6 Conductivity and the Effect of Long Term Annealing Studies of Apatite-type Al-doped Neodymium Silicate Single Crystals and Polycrystalline Lanthanum Silicates

6.1 Introduction

Apatite-type silicates have attracted a considerable amount of interest for SOFC electrolyte applications owing to their high oxide ion conductivity [1, 2]. In order to understand the conduction properties of these systems further, various lanthanide containing apatite silicate singles crystals have been prepared and shown to display significant anisotropic conduction, with the conductivity parallel to the c-axis being about an order of magnitude higher than perpendicular to the c-axis [3-5]. Although doping studies on the Si site in these systems in polycrystalline samples have shown improved conductivity, there have been no such studies with single crystals, with the only doping studies being the examination of Sr doped neodymium silicate single crystals [6]. Thus, the preparation of single crystals containing the lower valent cation Al on the Si site has been attempted.

In this chapter, the fundamental measurement of the oxide ion conductivity of these Al-doped neodymium silicate single crystals is reported. Preliminary results indicated the presence of a second semicircle in the impedance plot, which was not previously reported. To identify the origin of this additional impedance response, conductivity data for single crystals annealed at 950 °C for 1-3 months were also recorded.

For fuel cell electrolyte applications, along with high ionic conductivity, and negligible electronic conductivity, the long term stability at fuel cell operating temperature is required. And thus similar annealing studies to the $Nd_{9.33+x/3}Si_{6-x}Al_xO_{26}$ single crystals were carried out for practical electrolyte materials: $La_{9.67}Si_6O_{26.5}$ and $La_{10}Si_5GaO_{26.5}$. A combination of techniques including X-ray powder diffraction, AC impedance measurements and ^{29}Si NMR

spectroscopy has been employed to study, in detail, the effect of this long term thermal treatment on structure and oxide ion conductivity of these apatite silicates. In particular, the effect of long term thermal treatment on conductivity is discussed in terms of structural considerations. In addition, evidence for a beneficial outcome of long term thermal treatment, in terms of total conductivity below 400 °C, is also provided.

6.2 Experimental

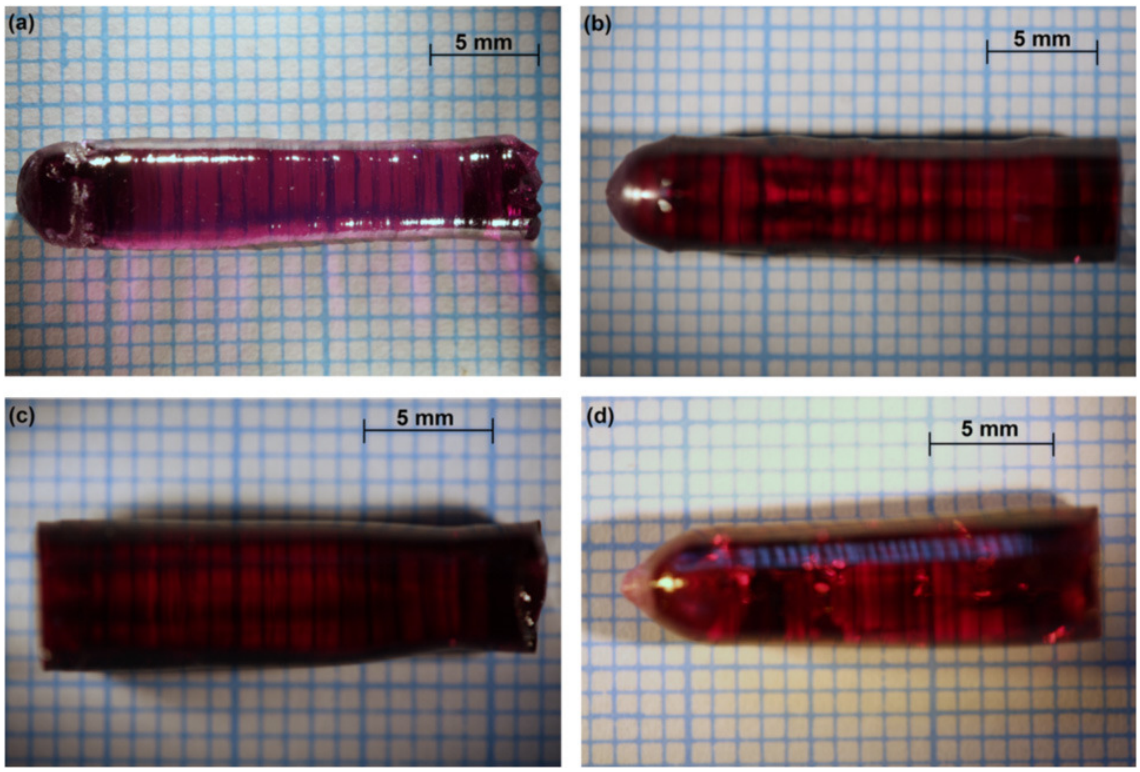

Fig. 6.1 Single crystals of (a) $Nd_{9.33}Si_6O_{26}$, (b) $Nd_{9.50}Al_{0.5}Si_{5.5}O_{26}$, (c) $Nd_{9.67}AlSi_5O_{26}$ and (d) $Nd_{9.83}Al_{1.5}Si_{4.5}O_{26}$ grown along the c-axis. Reproduced with permission from [7].

The single crystals ($Nd_{9.33+x/3}Si_{6-x}Al_xO_{26}$: x = 0, 0.5, 1.0, 1.5) were prepared using the floating-zone method in an argon atmosphere at a growth rate of 5mm h^{-1} by the research group of Prof. T. White at Nanyang Technological University in Singapore (detailed synthesis

procedure is given in An *et al.* [7]). The crystals, grown along the c-axis, were cut into hexagonal discs and the surfaces of the discs were polished. The phase purity was established through X-ray powder diffraction for the powder obtained from pieces of crushed single crystals.

The excess oxygen containing $La_{10}Si_5GaO_{26.5}$ and $La_{9.67}Si_6O_{26.5}$ polycrystalline samples were prepared using high purity La_2O_3, SiO_2 and Ga_2O_3. The correct stoichiometric mixtures were heated for 12 hours at 1200 ºC, with a second firing at 1350 ºC for a further 12 hours. They were then ball-milled (350 rpm for 1 hour, Fritsch Pulverisette 7 Planetary Mill) and pressed as pellets (1.3 cm diameter) and sintered at 1600°C for 2 hours. Powder X-ray diffraction (Bruker D8 diffractometer with Cu $K_{\alpha 1}$ radiation = 1.5406 Å) was used to demonstrate phase purity.

For the conductivity measurements, the crystal discs and sintered pellets were coated with Pt paste, and then heated to 800 °C for 1 hour to ensure bonding to the disc. Conductivities were then measured by AC impedance measurements (Hewlett Packard 4182A impedance analyser) in the range from 0.1 to 10^3 kHz with the voltage perturbation of 100 mV. Measurements were made in air and the data were analysed using *ZView* software, which estimates the resistance and capacitance values associated with equivalent circuits (to represent the materials) through the complex nonlinear least squares fitting [8]. After the measurement, the samples were annealed at 950 ºC for a month, and the conductivity measurements were performed again. The procedure was repeated for the total annealing time of 3 months.

^{29}Si NMR data for the as prepared and 3 months annealed $La_{10}Si_5GaO_{26.5}$ and $La_{9.67}Si_6O_{26.5}$ polycrystalline samples were collected to gain further information about the Si environment. These spectra were obtained using a Varian Unity Inova operating at 59.56 MHz, and spectral

referencing was with respect to tetramethylsilane. The data were collected by the EPSRC Solid state NMR service at Durham University.

6.3 Conductivity data for the as prepared single crystals

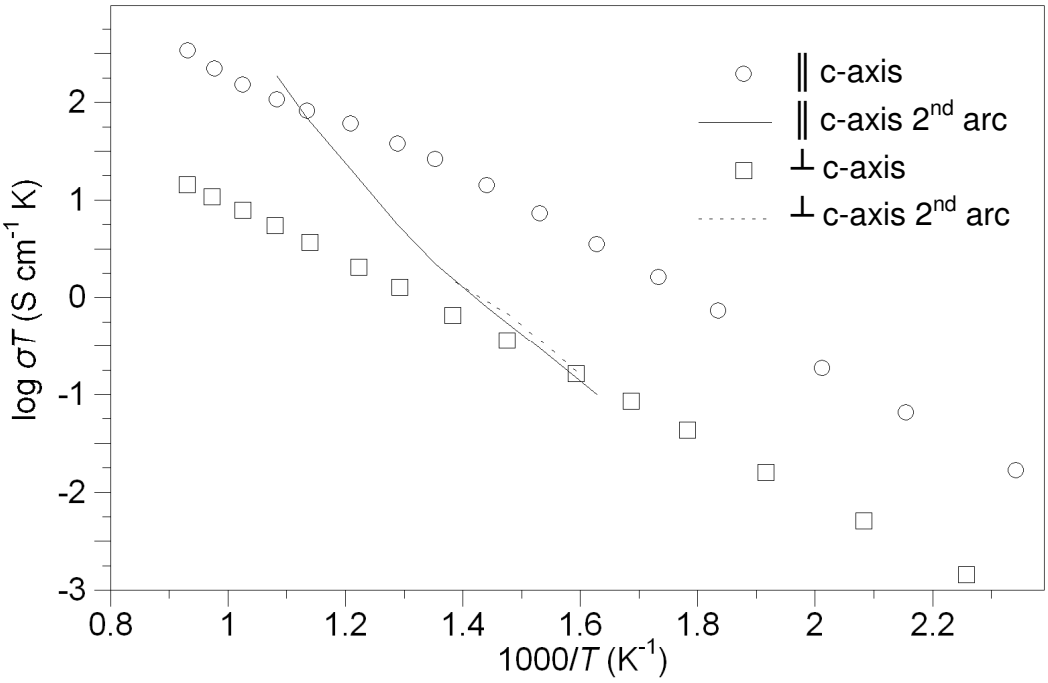

Fig. 6.2 Conductivity plots for a $Nd_{9.33}Si_6O_{26}$ single crystal, parallel and perpendicular to the c-axis.

Table 6.1 Bulk conductivity data for Al-doped neodymium silicate single crystals parallel to the c-axis

Composition	σ (S cm^{-1}) at 500 °C	E_a (eV)
$Nd_{9.33}Si_6O_{26}$	5.2 x 10^{-2}	0.63
$Nd_{9.33}Si_6O_{26}$ (⊥ c-axis)	1.6 x 10^{-3}	0.60
$Nd_{9.5}Si_{5.5}Al_{0.5}O_{26}$	3.7 x 10^{-2}	0.71
$Nd_{9.67}Si_5Al_1O_{26}$	1.6 x 10^{-2}	0.81
$Nd_{9.83}Si_{4.5}Al_{1.5}O_{26}$	6.9 x 10^{-3}	0.82

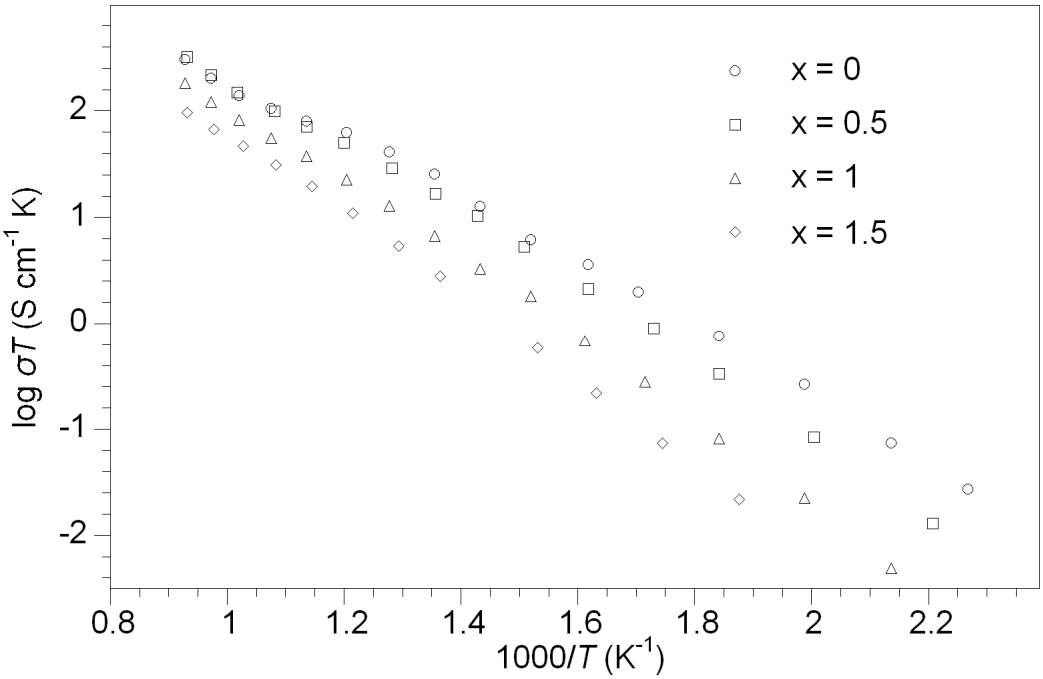

Fig. 6.3 Conductivity plots for $Nd_{9.33+x/3}Si_{6-x}Al_xO_{26}$ single crystals, parallel to the c-axis.

The conductivities (parallel and perpendicular to the c-axis) of $Nd_{9.33}Si_6O_{26}$ are shown in Fig. 6.2 and table 6.1 and they are in agreement with those previous reported [4]. The conductivities parallel to the c-axis for the Al doped single crystals are given in Fig. 6.3 and table 6.1 and this represents the first such conductivity study of a single crystal doped on the Si site. The single crystals showed a decrease in the conductivity with increase in Al level, in contrast to the previous studies on polycrystalline Al doped lanthanum silicates, where a conductivity enhancement was observed. The enhanced conductivity in the latter case was attributed to there being an optimum cation vacancy level to ensure high oxide ion conductivity [9]. The difference in the trend for the single crystals may have arisen from the different size of the rare earth cation: neodymium to lanthanum. Thus further doping studies with similar trivalent cations (e.g. Ga, B) are required to elucidate this issue further. In line with the effect of the smaller rare earth, Nd, studies by Slater et al. also showed a reduction in conductivity for polycrystalline samples on Ga doping in $Nd_{9.33}Si_6O_{26}$ [10]. In addition to the

observed reduction in the conductivity of the single crystals, the activation energy was increased with increase in Al content (table 6.1).

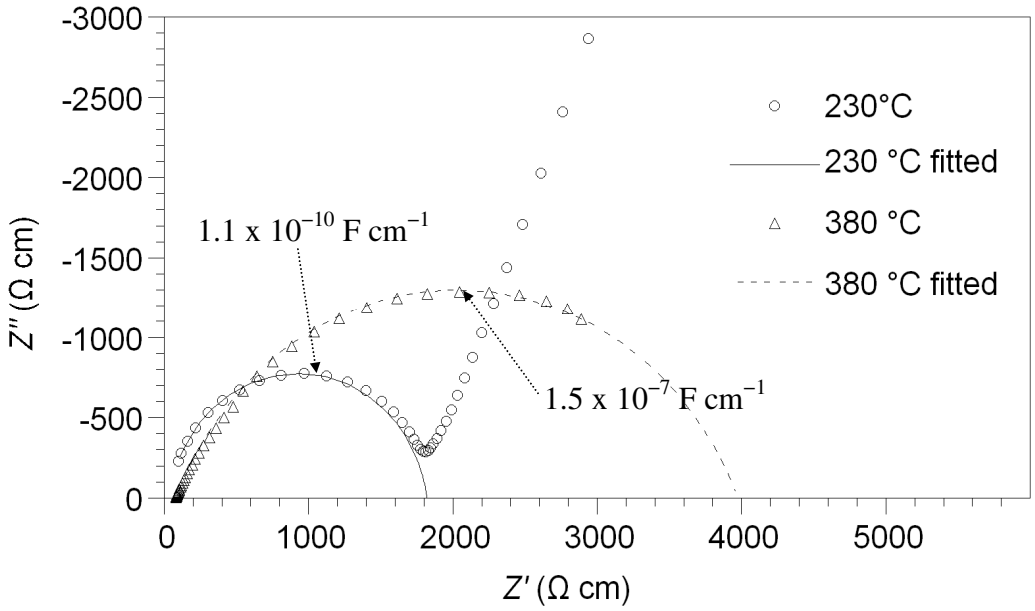

Fig. 6.4 Impedance plots for a $Nd_{9.33}Si_6O_{26}$ single crystal parallel to the c-axis at 230 and 380 °C showing a bulk and an additional semicircle with corresponding capacitance values.

An interesting feature from the impedance spectra for the single crystals was the appearance of a semicircle at lower frequency as shown in the impedance plot measured along the c-axis at 380 °C for $Nd_{9.33}Si_6O_{26}$, having the capacitance value 1.5 x 10^{-7} F cm^{-1}, which is slightly larger than a typical value for a grain boundary response and may be correlated with a surface layer effect [12] (Fig. 6.4): a similar extra semicircle was also present in the measurement along the ab plane and its conductivity was also similar (Fig. 6.2). The presence of a second semicircle was not reported in previous studies of single crystals, although in these earlier studies, the impedance plot reported was only at 100 °C, with no higher temperature data given [4]. This second semicircle was also shown in the Al doped single crystals and its origin is not clear, since there should be no grain boundary component in a

true single crystal. One possibility is that this secondary resistive component is associated with stacking faults/dislocations or boundaries between regions of different cation vacancy content in the single crystal. To verify this hypothesis, long term annealing (at 950 °C) studies were conducted in the hope that any stacking faults/dislocations/inhomogeneity in cation content in a single crystal would be annealed out over time.

In addition, it should be noted that the capacitance value for the bulk response shown in Fig. 6.4 is slightly higher than that for a conventional ceramic sample, but this high capacitance in a single crystal was previously observed in other single crystal studies and rationalised by the ready local displacement of the charge carrier [13].

6.4 Effect of long term heat treatment on the conductivity of single crystals of $Nd_{9.33}Si_6O_{26}$ and $Nd_{9.5}Si_{5.5}Al_{0.5}O_{26}$

The conductivities of the single crystals were remeasured after annealing at 950 °C over 3 months. The data showed that the lower frequency semicircle was not observed anymore for $Nd_{9.33}Si_6O_{26}$ after annealing for 2 months (Fig. 6.5), which suggested that this may indeed be due to stacking faults/dislocations/inhomogeneity effects. However, the data also showed that the bulk conductivity along the c-axis decreased, as illustrated by the increase in the size of semicircle in the impedance plots measured along the c-axis at 300 °C upon annealing (Fig. 6.6 and 6.7). The origin of this reduction in bulk conductivity is unclear, but it may be due to the reduced disordering of oxide ion defects in the lattice as a result of the reduction in cation lattice inhomogeneity.

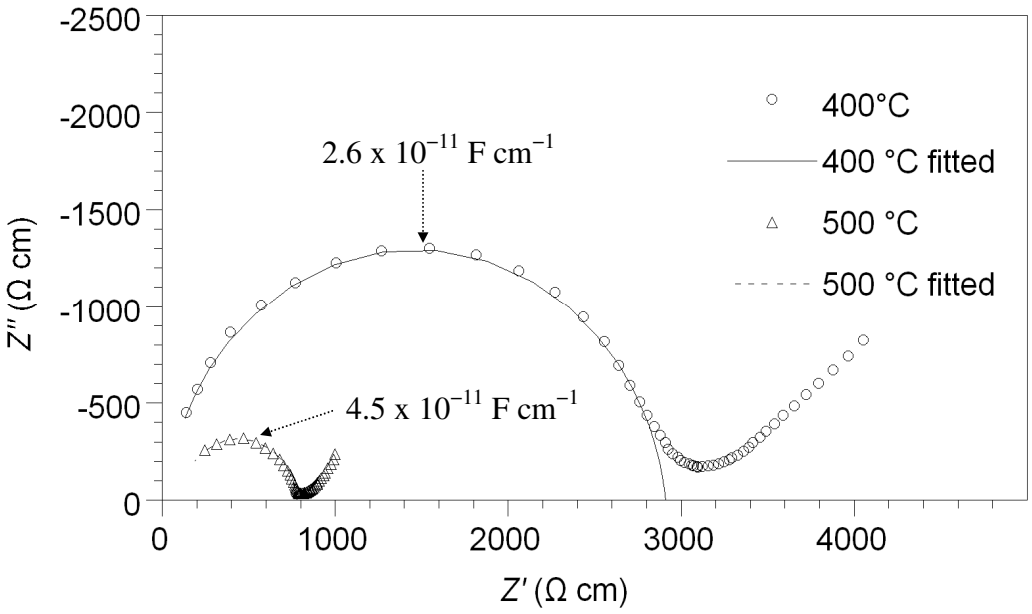

Fig. 6.5 Impedance plots for a $Nd_{9.33}Si_6O_{26}$ single crystal annealed for 2 months parallel to the c-axis at 400 and 500 ℃ showing no evidence of the additional semicircle which was present for the as prepared sample.

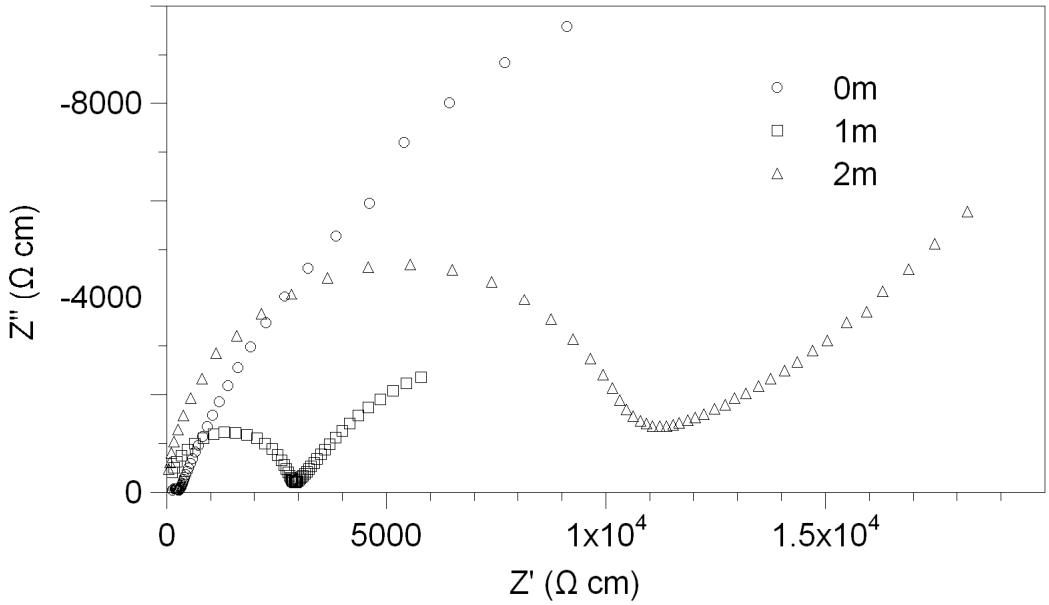

Fig. 6.6 Impedance plots at 300 ℃ parallel to the c-axis for a $Nd_{9.33}Si_6O_{26}$ single crystal annealed at 950 ℃ for various durations (in months) showing the increase in the size of semicircle corresponding to the bulk conduction process.

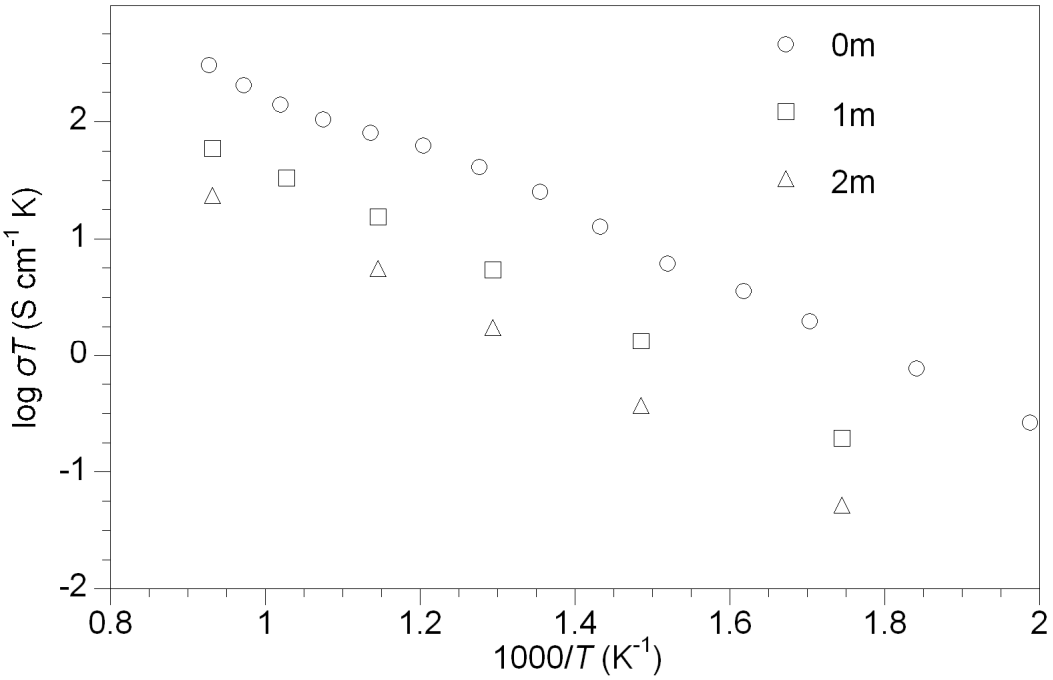

Fig. 6.7 Bulk conductivity plots for a $Nd_{9.33}Si_6O_{26}$ single crystal annealed at 950 ℃ for various durations (in months).

In addition to the effect of long term annealing on the conductivity of $Nd_{9.33}Si_6O_{26}$, the conductivity of similarly annealed Al doped $Nd_{9.5}Si_{5.5}Al_{0.5}O_{26}$ was also examined and the impedance plots of $Nd_{9.5}Si_{5.5}Al_{0.5}O_{26}$ measured along the c-axis at 300 °C are given in Fig. 6.8. These data showed the same reduction in bulk conductivity and disappearance of the second semicircle. However, in this $Nd_{9.5}Si_{5.5}Al_{0.5}O_{26}$ single crystal, there was an appearance of yet another resistive component at lower frequency with the capacitance value typical for a grain boundary/impurity response (2.6 x 10^{-8} F cm^{-1}), with the size of this semicircle increasing upon annealing (Fig. 6.8). This semicircle may be due to the precipitation of a secondary phase such as $NdAlO_3$, as $LaAlO_3$ has been reported as a common secondary phase in the preparation of Al doped lanthanum silicate samples [14, 15]. However, there was no evidence of such an additional phase in the X-ray diffraction data after annealing collected by T. White group and co-workers. Thus further annealing studies, possibly in conjunction with similar studies on polycrystalline Al doped neodymium silicate are required to explain this

issue. Overall, the results showed that the total conductivity parallel to the c-axis of the $Nd_{9.5}Si_{5.5}Al_{0.5}O_{26}$ single crystal decreased upon annealing (Fig. 6.9).

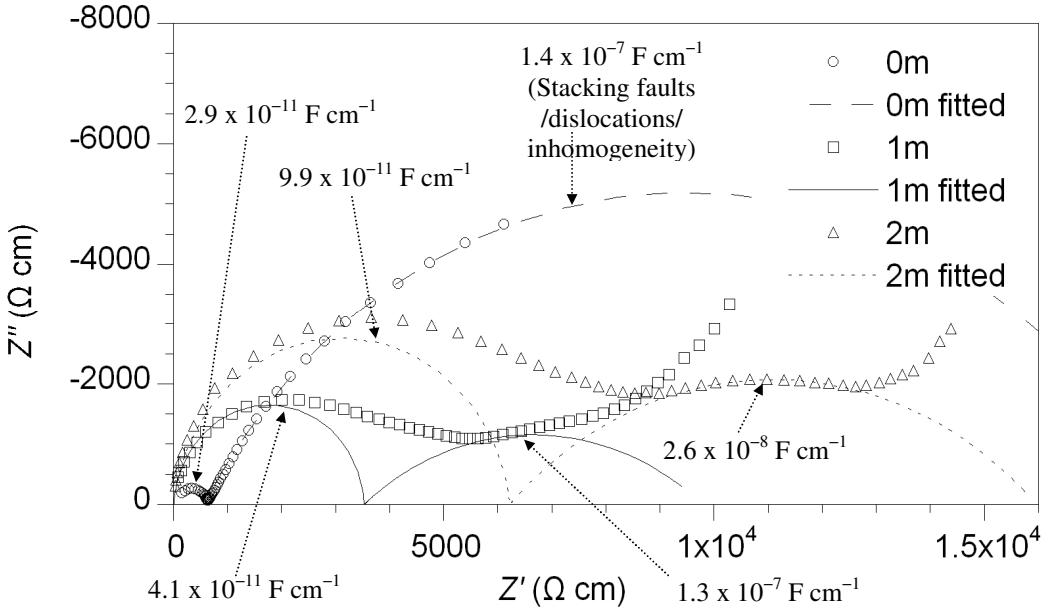

Fig. 6.8 Impedance plots at 300 °C for a $Nd_{9.5}Si_{5.5}Al_{0.5}O_{26}$ single crystal annealed at 950 °C for various durations (in months), showing the emergence of a further semicircle.

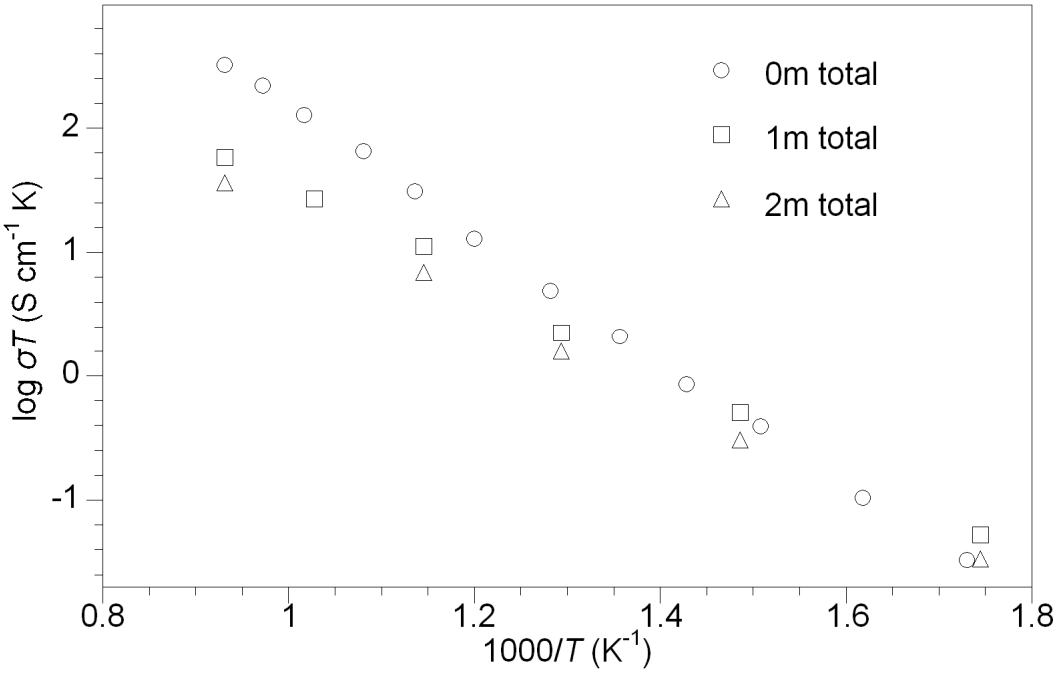

Fig. 6.9 Total conductivity plots for a $Nd_{9.5}Si_{5.5}Al_{0.5}O_{26}$ single crystal annealed at 950 °C for various durations (in months).

6.5 Effect of long term heat treatment on the conductivity of polycrystalline $La_{10}Si_5GaO_{26.5}$ and $La_{9.67}Si_6O_{26.5}$

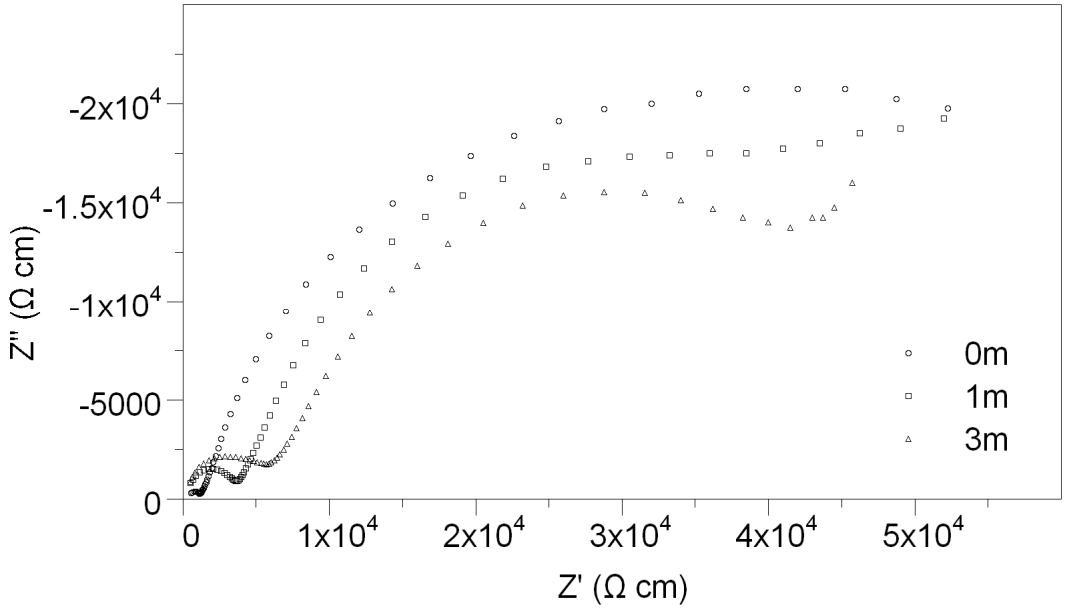

Fig. 6.10 Impedance plots at 300 ℃ for poly-crystalline $La_{10}Si_5GaO_{26.5}$ samples annealed at 950 ℃ for various durations (in months) showing the increase in the size of the semicircle corresponding to the bulk conduction and decrease in the size of semicircle corresponding to the grain boundary conduction.

Table 6.2 Total conductivity data for $La_{10}Si_5GaO_{26.5}$ samples after annealing at 950 ℃ for various durations

	Conductivity (S cm^{-1})	
	400 °C	600 °C
As prepared	1.42×10^{-4}	7.91×10^{-3}
1 month	1.44×10^{-4}	5.57×10^{-3}
2 months	1.95×10^{-4}	5.14×10^{-3}
3 months	2.14×10^{-4}	4.96×10^{-3}

The conductivity data obtained for as prepared $La_{10}Si_5GaO_{26.5}$ were in agreement with the previously reported values [11]. The impedance plots at 300 °C given in Fig. 6.10 showed the

significant decrease in bulk conductivity upon annealing, similar to the results from neodymium silicate single crystals. At the same time, there is an improvement in the grain boundary conductivity as the size of the low frequency semicircle decreased upon annealing (Fig. 6.10). Significantly, this resulted in a small enhancement in total conductivity below 400 °C because the improvement in grain boundary conductivity outweighed the decrease in bulk conductivity (Fig. 6.11 and table 6.2) which at higher temperature the situation was reversed. The other annealed sample, $La_{9.67}Si_6O_{26.5}$, showed a similar result to $La_{10}Si_5GaO_{26.5,}$ exhibiting an improvement in total conductivity below 400 °C (Fig. 6.12). The reduction in the bulk conductivity may be caused by the reduced disordering of defects in the lattice and the enhancement in the grain boundary conductivity may be caused by the reduction/disappearance of the contribution of stacking faults/dislocations/inhomogeneity to grain boundary conductivity as observed in the single crystal studies.

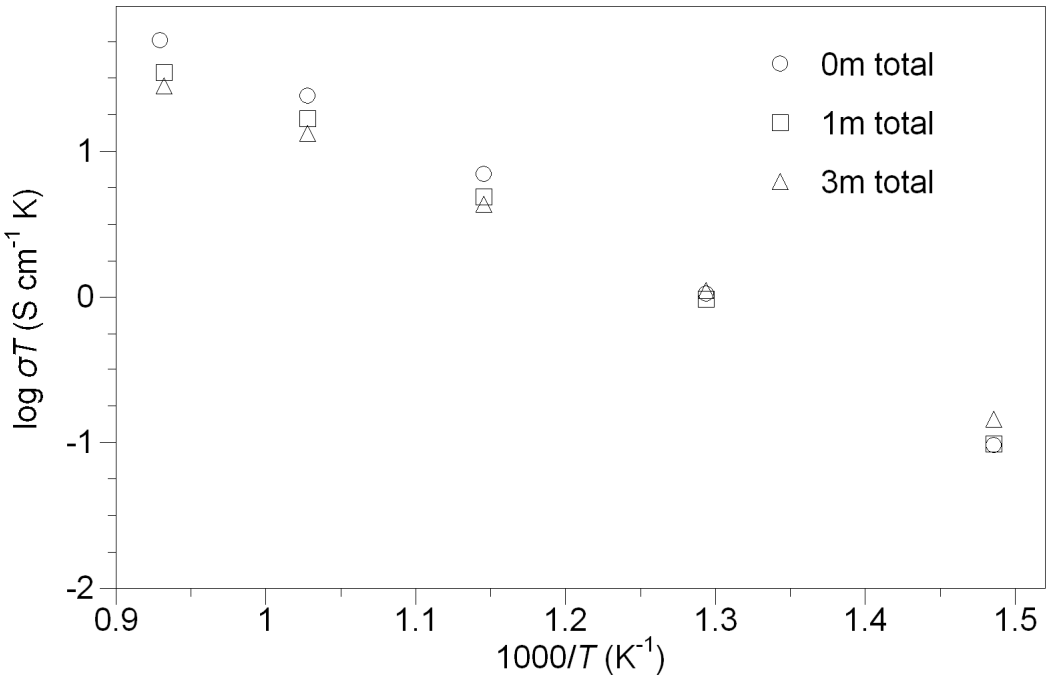

Fig. 6.11 Conductivity plots for $La_{10}Si_5GaO_{26.5}$ samples annealed at 950 ℃ for various durations (in months) showing the total conductivity change.

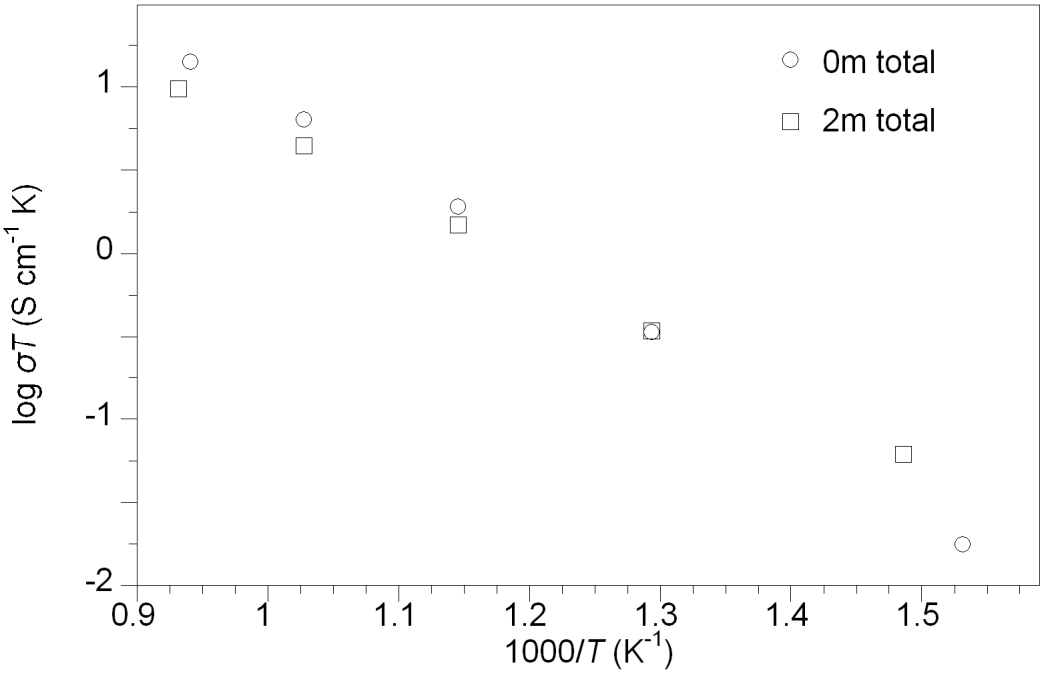

Fig. 6.12 Conductivity plots for $La_{9.67}Si_6O_{26.5}$ samples annealed at 950 ℃ for various durations (in months) showing the total conductivity change.

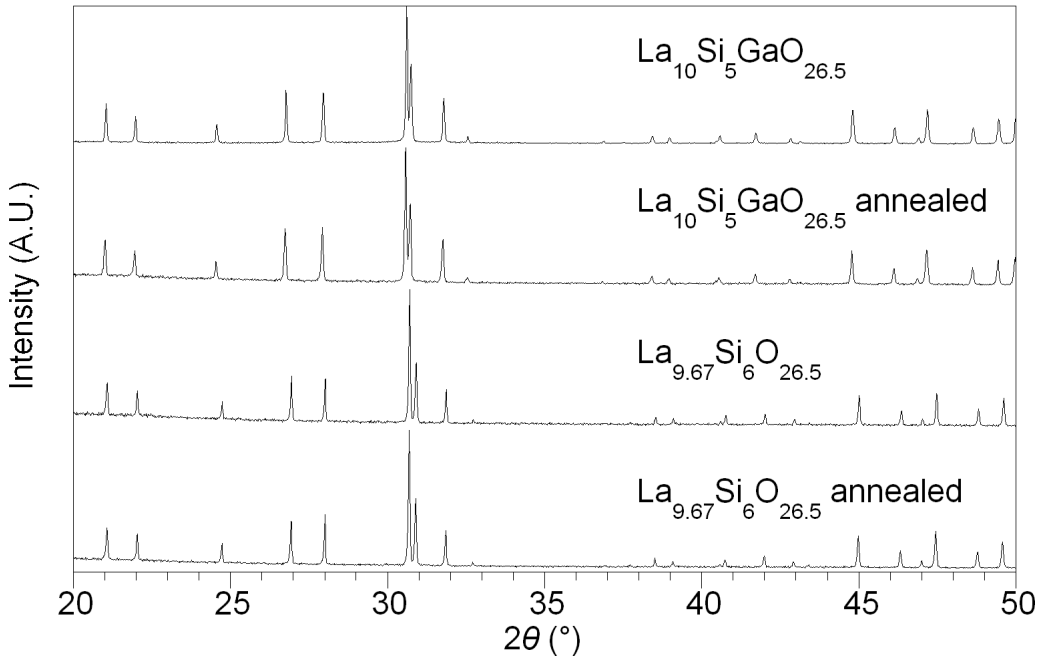

Fig. 6.13 X-ray diffraction data for as prepared and annealed (at 950 ℃ for 3 months) $La_{10}Si_5GaO_{26.5}$ and $La_{9.67}Si_6O_{26.5}$.

Table 6.3 Cell parameters for as prepared and annealed (at 950 °C for 3 months) $La_{10}Si_5GaO_{26.5}$ and $La_{9.67}Si_6O_{26.5}$.

Sample (nominal composition)	Unit cell parameters (Å)			Unit cell volume ($Å^3$)
	a	b	c	
$La_{10}Si_5GaO_{26.5}$	9.743(1)	-	7.242(1)	595.4(1)
$La_{10}Si_5GaO_{26.5}$ annealed	9.744(1)	-	7.240(1)	595.4(1)
$La_{9.67}Si_6O_{26.5}$	9.703(1)	-	7.179(1)	585.3(1)
$La_{9.67}Si_6O_{26.5}$ annealed	9.717(1)	-	7.187(1)	587.7(1)

The structural change after 3 months of annealing was examined by X-ray diffraction and ^{29}Si NMR data. No second phase was observed in the X-ray diffraction data for both $La_{10}Si_5GaO_{26.5}$ and $La_{9.67}Si_6O_{26.5}$ (Fig. 6.13). The calculated cell parameters for as prepared and annealed $La_{10}Si_5GaO_{26.5}$ samples were the same, while those of $La_{9.67}Si_6O_{26.5}$ showed a slight increase for the annealed sample (Table 6.3). The ^{29}Si NMR data for $La_{10}Si_5GaO_{26.5}$ and $La_{9.67}Si_6O_{26.5}$ are given in Fig. 6.14 and table 6.4. The ^{29}Si NMR data for the as prepared $La_{10}Si_5GaO_{26.5}$ sample showed two peaks at −77.8 and −80.8 ppm in agreement with previous reports, which were associated with two different Q^0 SiO_4 units, the latter associated with a SiO_4 group near an interstitial oxide ion [16]. Upon annealing, there was only a slight shift of the second peak towards higher field indicating a small bond strength change without any significant change in the intensity. The ^{29}Si NMR data for as prepared $La_{9.67}Si_6O_{26.5}$ samples showed four peaks at −77.7, −79.3, −81.2 and −84.9 ppm in agreement with previous reports, which were assigned to Q^0 SiO_4 units with different environments and a possible Q^1 Si_2O_7 unit for the peak at −84.9 ppm [17, 18]. Upon annealing, most notably, a very broad peak at −111.6 ppm was observed and assigned to Q^4 SiO_2. If only Si drops out from the structure, then an overall increase in the La and excess oxygen content would be expected with a consequential increase in the cell volume. This was actually observed in the X-ray diffraction

data for the annealed sample, although there was no significant evidence for the presence of SiO_2 in the data, which suggests that the SiO_2 might not be crystalline. Excluding the contribution of the SiO_2 peak from the relative intensity, the corrected relative intensity showed no significant change upon annealing. However, the annealing leads to an increase in the La:Si ratio in the bulk material, then an enhancement in conductivity might have been expected due to the increased interstitial oxide ion content, whereas the reverse was observed. Thus the origins of the observed conductivity change are still not fully explained.

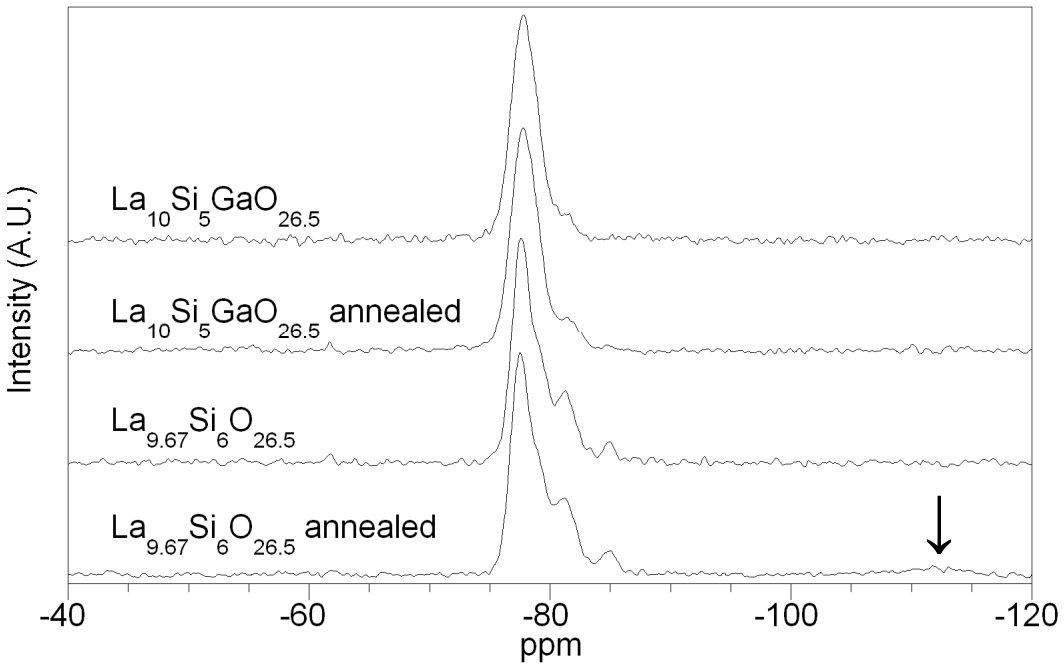

Fig. 6.14 ^{29}Si NMR data for as prepared and annealed (at 950 ℃ for 3 months) $La_{10}Si_5GaO_{26.5}$ and $La_{9.67}Si_6O_{26.5}$ (SiO_2 peak is highlighted).

Table 6.4 ^{29}Si NMR data for as prepared and annealed (at 950 ℃ for 3 months) $La_{10}Si_5GaO_{26.5}$ and $La_{9.67}Si_6O_{26.5}$. The relative intensity was obtained by the deconvolution of the spectra in Fig. 6.14 (uncertainty = ± 2 %). The corrected relative intensity for the annealed $La_{9.67}Si_6O_{26.5}$ was calculated by removing the contribution of the intensity of the SiO_2 peak at -111.6 ppm for the comparison with the relative intensity of the peaks for the as prepared sample.

Sample		Peak position (ppm)	Relative intensity (%)	Corrected relative intensity (%)
$La_{10}Si_5GaO_{26.5}$	As prepared	-80.8	11.7	-
		-77.8	88.3	
	Annealed	-81.3	13.7	-
		-77.9	86.3	
$La_{9.67}Si_6O_{26.5}$	As prepared	-84.9	3.5	-
		-81.2	23.4	
		-79.3	13.2	
		-77.7	59.9	
	Annealed	-111.6	4.7	-
		-84.9	5.0	5.2
		-81.1	25.1	26.3
		-79.2	13.2	13.9
		-77.5	52.1	54.7

6.6 Conclusions

The conductivity of Al doped neodymium silicates single crystals has been reported for the first time and showed a decrease with increasing Al level. Due to the presence of a second semicircle in the impedance plots, the effect of long term (1-3 months) heat treatment at 950 °C was also examined for $Nd_{9.33}Si_6O_{26}$ and $Nd_{9.5}Si_{5.5}Al_{0.5}O_{26}$ single crystals. The annealing treatment was shown to eliminate this second semicircle: thus its cause is suggested to be due to stacking faults/dislocations/sample inhomogeneity in the single crystals which are annealed out over time. The data showed that there was also a general decrease in the conductivity for $Nd_{9.5}Si_{5.5}Al_{0.5}O_{26}$ single crystal along with the appearance of a third

semicircle at lower frequency with the capacitance value for a typical grain boundary/impurity response. The origin of this semicircle is not clear and further systematic studies utilising other lower valent cation (i.e. Ga, B) doped single crystals in conjunction with polycrystalline samples would be required to elucidate this issue further.

Although, there were only small structural changes from the powder X-ray diffraction and ^{29}Si NMR data for the polycrystalline apatite silicates, there was a general decrease in the bulk conductivity. While the bulk conductivity was decreased, it was evidenced that the long term thermal treatment was beneficial on the total conductivity of the polycrystalline silicates at the temperature lower than 400 °C due to an improvement in grain boundary conductivity. In the next chapter, neutron diffraction studies are reported for such annealed samples in order to try to determine the origin of these effects.

6.7 References

[1] Nakayama, S.; Aono, H.; Sadaoka, Y. *Chem. Lett.* **1995**, *24*, 431.

[2] Nakayama, S.; Sakamoto, M.; Highchi, M.; Kodaira, K. *J. Mater. Sci. Lett.* **2000**, *19*, 91.

[3] Nakayama, S.; Highchi, M. *J. Mater. Sci. Lett.* **2001**, *20*, 913.

[4] Nakayama, S.; Sakamoto, M.; Higuchi, M.; Kodaira, K.; Sato, M.; Kakita, S.; Suzuki, T.; Itoh, K. *J. Eur. Ceram. Soc.* **1999**, *19*, 507.

[5] Nakayama, S.; Sakamoto, M.; Highchi, M.; Kodaira, K. *J. Mater. Sci. Lett.* **2000**, *19*, 91.

[6] Masubuchi, Y.; Higuchi, M.; Katase, H.; Takeda, T.; Kikkawa, S.; Kodaira, K.; Nakayama, S. *Solid State Ionics.* **2004**, *166*, 213.

[7] An, T.; Baikie, T.; Wei, F. X.; Li, H. N.; Brink, F.; Wei, J.; Ngoh, S. L.; White, T. J.; Kloc, C. *J. Cryst. Growth* **2011**, *333*, 70.

[8] Johnson, D. *ZView: a Software Program for IES Analysis, Version 3.1c*, Scribner Associates Inc., **2007**.

[9] Abram, E. J.; Sinclair, D. C.; West, A. R. *J. Mater. Chem.* **2001**, *11*, 1978.

[10] Slater, P. R.; Tolchard, J. R.; Sansom J. E. H. *Proc. RTST2005* **2005**, 2, 1.

[11] Sansom, J. E. H.; Tolchard, J. R.; Slater, P. R.; Islam, M. S. *Solid State Ionics.* **2004**, *167*, 17.

[12] Irvine, J. T. S.; Sinclair, D. C.; West, A. R. *Adv. Mater.* **1990**, *2*, 132.

[13] Sinclair, D. C.; West, A. R. *Phys. Rev. B* **1989**, *39*, 13486.

[14] Kharlamova, T.; Pavlova, S.; Sadykov, V.; Chaikina, M.; Krieger, T.; Lapina, O.; Khabibulin, D.; Ishchenko, A.; Zaikovskii, V.; Argirusis, C.; Frade, J. *Eur. J. Inorg. Chem.* **2008**, 939.

[15] Kharlamova, T.; Pavlova, S.; Sadykov, V.; Krieger, T.; Batuev, L.; Muzykantov, V.; Uvarov, N.; Argirusis, C. *Solid State Ionics.* **2009**, *180*, 796.

[16] Sansom, J. E. H.; Tolchard, J. R.; Islam, M. S.; Apperley, D.; Slater, P. R. *J. Mater. Chem.* **2006**, *16*, 1410.

[17] Madani, A.; Sobrados, I.; Inoubli, A.; Chefi, S.; Kahlaoui, M.; Sanz, J. *Ionics* **2010**, *16*, 723.

Chapter 7 Structural Features of Apatite Silicates with high Oxygen Excess: the Effect of Hydration and Long Term Annealing

7.1 Introduction

Apatite-type silicates have been an active subject of research for fuel cell electrolyte applications owing to their high oxide ion conductivity [1, 2]. The numerous conduction mechanisms proposed for apatite-type silicates and the pivotal role of the interstitial oxide ion were discussed in detail in chapter 1.4. While there is general agreement relating to the location of the interstitial site for the apatite-type germanates (located adjacent to Ge leading to the formation of 5 coordinate Ge) [3-6], a range of sites have been suggested for the silicate apatites [7-10], although there is growing support for a position near the channel centre [10-12]. One of the difficulties with locating these interstitial oxide ion sites is the generally low levels of interstitial oxide ion, especially for the silicates, where prior studies have suggested a maximum limit close to 0.5 O per formula unit [7]. In order to improve our ability to accurately locate the interstitial site, a higher oxygen excess would be beneficial. In this respect, it has been shown that the interstitial oxide ion content can be increased through water incorporation for the apatite germanates [13, 14], and the same strategy to increase the interstitial oxide ion content for the silicates has been examined in this work. While only low levels of water can be incorporated in cation stoichiometric apatite silicates, e.g. $La_{8+x}A_{2-x}Si_6O_{26+x/2}$ (A = Ca, Sr, Ba), significant water incorporation for systems containing oxygen excess and cation vacancies, i.e. $La_{9.33+x}Si_6O_{26+3x/2}$ was achieved. In particular, the work here has highlighted that systems with $x > 0.17$ can accommodate higher levels of water than samples with low values of x. In this chapter, the successful incorporation of water in the system, $La_{9.6}Si_6O_{26.4}$, is reported and the structure, especially the location of the interstitial

oxide ion site is analysed. In addition, the structural change upon annealing for a month is investigated to rationalize the cause of the decrease in the bulk conductivity for the apatite-type single crystals and polycrystalline samples upon long term annealing studies, as shown in the previous chapter.

7.2 Experimental

$La_{9.6}Si_6O_{26.4}$ was prepared as follows. High purity La_2O_3, and SiO_2 were ground together in the correct stoichiometric ratio and heated for 12 hours at 1350 ºC, with a second firing at 1350 ºC for a further 12 hours. Between firings the sample was reground to ensure a homogeneous mixture. The sample was then divided into two equal weight batches (≈ 12g). Batch 1 was used as prepared while batch 2 was annealed at 950 ºC for a month. In both cases, phase purity was established through X-ray powder diffraction (Bruker D8 diffractometer with Cu $K_{\alpha 1}$ radiation = 1.5406 Å).

For the water incorporation, a portion (≈ ⅓ of each batch) of the samples was heated in water in a hydrothermal vessel (model 4749 Parr digestion vessel with 23 ml capacity) at 200°C for 48 hours ($pH_2O \approx 15$ atm), as described previously [14]. The water contents were assessed through thermogravimetric analysis (Netzsch STA 449 F1 Jupiter Thermal Analyser). The TGA experiments were carried out in N_2 with a heating rate of 10 °C/min up to 700 °C.

The structures of both as prepared and hydrated samples were determined by refinement using neutron diffraction data, which were collected on diffractometer HRPT at the SINQ, Paul Scherrer Institut. All structural refinements employed the GSAS suite of Rietveld refinement software [15].

The metaprism twist angle, φ of the LaO_6 units was calculated using the equation based on cosine rule (geometry for the La, O_1 and O_2 are given in chapter 1.4.4) [16]:

$$\cos\varphi = \frac{(G_3 - G_1)^2 + (H_3 - H_1)^2 + (G_1 - G_2)^2 + (H_1 - H_2)^2 - (G_2 - G_3)^2 - (H_2 - H_3)^2}{2\{[(G_3 - G_1)^2 + (H_3 - H_1)^2] \times [(G_1 - G_2)^2 + (H_1 - H_2)^2]\}^{\frac{1}{2}}}$$

where $G_1 = 0.866 x_{\mathrm{La}}$, $H_1 = y_{\mathrm{La}} - 0.5 x_{\mathrm{La}}$;

$G_2 = 0.866 x_{\mathrm{O_1}}$, $H_2 = y_{\mathrm{O_1}} - 0.5 x_{\mathrm{O_1}}$;

$G_3 = 0.866 x_{\mathrm{O_2}}$, $H_3 = y_{\mathrm{O_2}} - 0.5 x_{\mathrm{O_2}}$.

In order to gain additional information on the thermal stability of the water in the apatite structure, the hydrated sample was investigated further through high temperature X-ray diffraction, utilising a Bruker D8 diffractometer. Measurements were made between 50 and 550 °C in air.

7.3 As prepared $La_{9.6}Si_6O_{26.4}$

Among the various space groups reported to be exhibited by apatite systems [16], space groups $P6_3$ and $P\bar{3}$ were analysed initially, as these are the most widely reported space groups used to describe oxygen excess apatite-type silicates [17]. The initial structural refinement using both symmetries showed similar R-factor values, and thus the higher symmetry space group $P6_3$ was chosen for the full structural refinement. Because there is no special position in terms of the z coordinate in this space group, it was required to constrain the z coordinate of the channel oxygen to a value of ¼ to provide a fixed origin in z. In the initial structure refinement, there was no evidence of any cation vacancy ordering phenomena involving the La(1) and La(2) sites [18], and so to avoid errors involving the high degree of correlation between these sites, their fractional occupancy and thermal parameters were constrained to be equal. Among the various interstitial oxide ion sites reported in apatite silicates, two sites at channel periphery (0.037, 0.277, 0.584) [17] and near channel centre (0.018, 0.050, 0.573) [12] was tested initially. The refinement for both sites showed an improved fit compared to

the model without any interstitial oxide ion (R_{wp} = 2.18) but the interstitial oxide ion positioned near channel centre resulted in a better fit (R_{wp} = 2.08) over channel periphery site (R_{wp} = 2.13), and thus the full structural refinement was continued with the interstitial oxide ion near the channel centre.

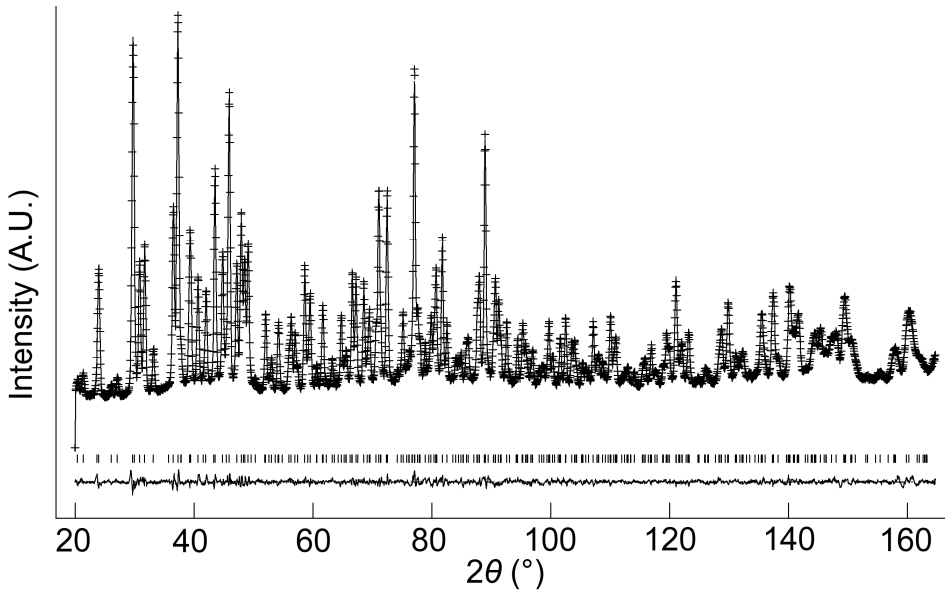

Fig. 7.1 Observed (cross), calculated (line) and difference plots of as prepared $La_{9.6}Si_6O_{26.4}$ from the Rietveld refinement from room temperature neutron diffraction data

Table 7.1.a Refined structural parameters of as prepared $La_{9.6}Si_6O_{26.4}$ with hexagonal *P6₃* (173) space group, from room temperature neutron diffraction data

Space group	a/b (Å)	c (Å)	R_{wp}	R_p	χ^2
P6₃	9.72441(4)	7.18726(5)	2.00	1.58	3.299
Atom	Site	x	y	z	U_{iso} x 100 (Å)	SOF
La(1)	2b	⅓	⅔	-0.0161(5)	1.28(2)	0.874(2)
La(2)	2b	⅔	⅓	-0.0139(5)	1.28(2)	0.874(2)
La(3)	6c	0.2286(1)	-0.0119(1)	0.2427(5)	1.09(1)	1
Si	6c	0.4028(2)	0.3725(1)	0.2488(5)	0.69(2)	1
O(1)	6c	0.3235(2)	0.4847(2)	0.2429(9)		1
O(2)	6c	0.5948(1)	0.4729(2)	0.2438(10)		1
O(3)	6c	0.3531(4)	0.2580(5)	0.0592(8)		1
O(4)	6c	0.6643(6)	0.7466(5)	0.9204(7)		1
O(5)	2a	0	0	¼		0.853(5)
O(6)	6c	0.0033(23)	0.0193(41)	0.4049(21)		0.092(3)
100 x	U_{11}	U_{22}	U_{33}	U_{12}	U_{13}	U_{23}
O(1)	2.98(7)	2.51(7)	2.43(9)	2.38(7)	-1.64(20)	-0.52(21)
O(2)	1.01(6)	0.98(5)	2.47(7)	0.37(5)	0.37(20)	0.30(21)
O(3)	2.22(11)	1.84(14)	1.75(14)	1.29(11)	-0.80(9)	-0.51(14)
O(4)	8.27(20)	1.18(14)	1.59(15)	2.08(16)	-2.73(12)	-0.84(15)
O(5)	0.28(5)	0.27(5)	13.4(3)	0.14(3)	0	0
O(6)	8.9(18)	33.8(36)	8.3(15)	13.7(24)	15.0(16)	19.3(24)

Table 7.1.b Selected bond distances for as prepared $La_{9.6}Si_6O_{26.4}$

Bond	Bond distance (Å)
Si-O(1)	1.620(1)
Si-O(2)	1.618(1)
Si-O(3)	1.674(1)
Si-O(4)	1.587(1)
La(1)-O(1) (x3)	2.535(1)
La(1)-O(2) (x3)	2.503(1)
La(1)-O(4) (x3)	2.944(1)
La(2)-O(1) (x3)	2.453(1)
La(2)-O(2) (x3)	2.591(1)
La(2)-O(3) (x3)	2.806(1)
La(3)-O(1)	2.762(1)
La(3)-O(2)	2.519(1)
La(3)-O(3)	2.630(1), 2.476(1)
La(3)-O(4)	2.464(1), 2.586(1)
La(3)-O(5)	2.284(1)
O(6)-La(3)	2.632(1), 2.677(1), 2.405(1)
O(6)-O(5)	1.136(1)

Fig. 7.2 The anisotropic thermal ellipsoids around the apatite channel position of as prepared $La_{9.6}Si_6O_{26.4}$, viewed down the c-axis.

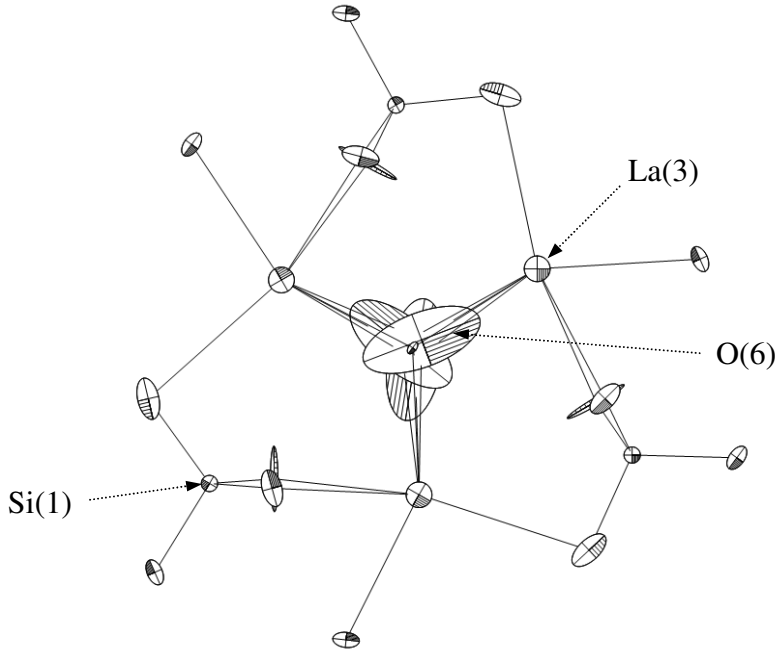

The structural parameters of the as prepared $La_{9.6}Si_6O_{26.4}$ sample using neutron diffraction data are given table 7.1, with the observed, calculated and difference profiles in Fig. 7.1. The data indicated a refined composition of $La_{9.50}Si_6O_{26.26}$, close to that expected from the starting stoichiometry. The structural data generally agrees with the previously reported sample of similar composition, $La_{9.67}Si_6O_{26.5}$ [17], including high thermal displacement parameters for O(4) (silicate oxygen near the channel) and O(5) (channel oxygen), which suggests significant local structural disorder. However, in this study, the interstitial oxide ion, O(6) appeared to be located near the channel centre site (0.003, 0.019, 0.405) rather than channel periphery. This result is similar to the position observed by Bechade *et al*. and others [10-12]. In this model, Bechade *et al*. proposed a defect complex ($O_i''-V_O^{\bullet\bullet}-O_i''$) (Fig. 1.4.6 in chapter 1), and in the present study, a similar complex can be proposed. The observed length scale in this study for this complex is 2.27 Å which is smaller than the predicted value of 2.93 Å from the modelling

work [10]. However, it should be noted that the thermal displacement parameter for O(6) is very high perpendicular to the channel (U_{22} = 34 Å^2). This suggests significant local displacement from the refined position: which may hence allow an increase in the O_i''–$V_O^{\bullet\bullet}$ length. Overall it would suggest the presence of various interstitial oxide ion sites with differing displacements from the channel centre. In particular, the anisotropic thermal ellipsoids for the O(6) are directed towards channel lanthanum, La(3) (Fig. 7.2), which is not unexpected as O(6) is highly underbonded (−1.08), and so some displacement might be expected to aid the stability of this oxide ion site.

7.4 Hydrated $La_{9.6}Si_6O_{26.4}$

The structural parameters for hydrated $La_{9.6}Si_6O_{26.4}$ are given in table 7.2 with the observed, calculated and difference profiles in Fig. 7.3. It was not possible to locate the proton site, most likely due to the presence of a range of different H sites and significant local displacement in these positions. In this respect, further studies at low temperature (≈ 4K) would be required, as has been performed to locate the proton sites in perovskite systems. The data indicated a refined composition of $La_{9.53}Si_6O_{26.98}$ (excluding protons) showing a significant increase in the O content. If we assume that this extra O is charge balanced by protons, the composition of $La_{9.53}Si_6O_{26.98}H_{1.37}$ is obtained. Apart from the increased O content, the major difference to the as prepared sample is the deviation of the interstitial oxide ion site further away from the channel centre (0.133, 0.143, 0.419). This displaced interstitial oxide ion site is still closer to the channel centre than the channel periphery. It can be proposed that the additional displacement from the channel centre is required to accommodate more anions in the structure, and the data showed that further structure distortion accompanied the water incorporation. In particular, the calculated average metaprism twist angle of LaO_6 was decreased from 22.24°

to 21.68°, in order to expand the channel size to allow the accommodation of the extra oxide ions, resulting in an increase in the cell size along a/b and decrease in c. These cell parameters changes can be elegantly demonstrated using high temperature X-ray diffraction data (Fig. 7.4). Such data show that there is a steep decrease in the size of a/b and increase in c at around 210 °C, on heating the hydrated sample (due to water loss), while the as prepared sample showed a linear increase over the temperature range. This single stage dehydration process also can be easily noticed on the plot of cell volume change with temperature.

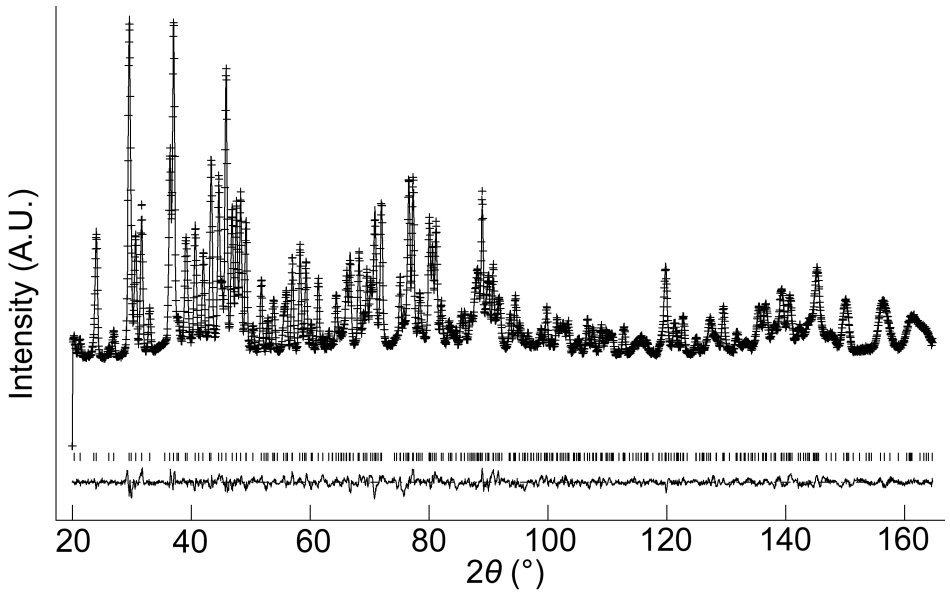

Fig. 7.3 Observed (cross), calculated (line) and difference plots of hydrated $La_{9.6}Si_6O_{26.4}$ from the Rietveld refinement for room temperature neutron diffraction data.

Table 7.2.a Refined structural parameters of hydrated $La_{9.6}Si_6O_{26.4}$ with hexagonal *P6₃* (173) space group, from room temperature neutron diffraction data

Space group	a/b (Å)	c (Å)	R_{wp}	R_p	χ^2
P6₃	9.79242(10)	7.17565(9)	2.47	1.93	5.309
Atom	Site	x	y	z	U_{iso} x 100 (Å)	SOF
La(1)	2b	⅓	⅔	0.0058(9)	1.93(4)	0.882(3)
La(2)	2b	⅔	⅓	0.0028(9)	1.93(4)	0.882(3)
La(3)	6c	0.2360(1)	-0.0077(2)	0.2438(6)	1.28(2)	1
Si	6c	0.4032(3)	0.3757(3)	0.2475(12)	1.51(5)	1
O(1)	6c	0.3269(3)	0.4877(3)	0.24941(8)		1
O(2)	6c	0.5939(2)	0.4724(3)	0.2515(9)		1
O(3)	6c	0.3624(4)	0.2649(6)	0.0628(6)		1
O(4)	6c	0.6664(6)	0.7494(6)	0.9169(6)		1
O(5)	2a	0	0	¼		0.890(11)
O(6)	6c	0.1334(20)	0.1425(12)	0.4192(17)		0.200(7)
100 x	U_{11}	U_{22}	U_{33}	U_{12}	U_{13}	U_{23}
O(1)	6.09(17)	4.29(17)	0.71(10)	4.70(15)	-1.62(25)	-2.36(18)
O(2)	2.06(12)	1.74(11)	2.25(12)	0.04(10)	-0.99(30)	-0.97(31)
O(3)	5.29(24)	4.75(27)	0.64(16)	4.03(23)	0.79(14)	0.17(16)
O(4)	8.46(29)	1.82(20)	2.18(18)	2.34(23)	-3.68(15)	-1.09(19)
O(5)	1.64(15)	1.64(15)	22.5(8)	0.82(7)	0	0
O(6)	8.5(13)	0.20(58)	3.09(71)	3.07(66)	0.52(70)	-2.21(51)

Table 7.2.b Selected bond distances for hydrated $La_{9.6}Si_6O_{26.4}$

Bond	Bond distance (Å)
Si-O(1)	1.609(1)
Si-O(2)	1.618(1)
Si-O(3)	1.628(1)
Si-O(4)	1.614(1)
La(1)-O(1) (x3)	2.455(1)
La(1)-O(2) (x3)	2.580(1)
La(1)-O(4) (x3)	3.010(1)
La(2)-O(1) (x3)	2.505(1)
La(2)-O(2) (x3)	2.552(1)
La(2)-O(3) (x3)	2.740(1)
La(3)-O(1)	2.830(1)
La(3)-O(2)	2.479(1)
La(3)-O(3)	2.651(1), 2.520(1)
La(3)-O(4)	2.483(1), 2.538(1)
La(3)-O(5)	2.350(1)
O(6)-La(3)	2.489(1), 2.302(1), 2.538(1)
O(6)-O(4)	1.698(1)
O(6)-O(5)	1.818(1)

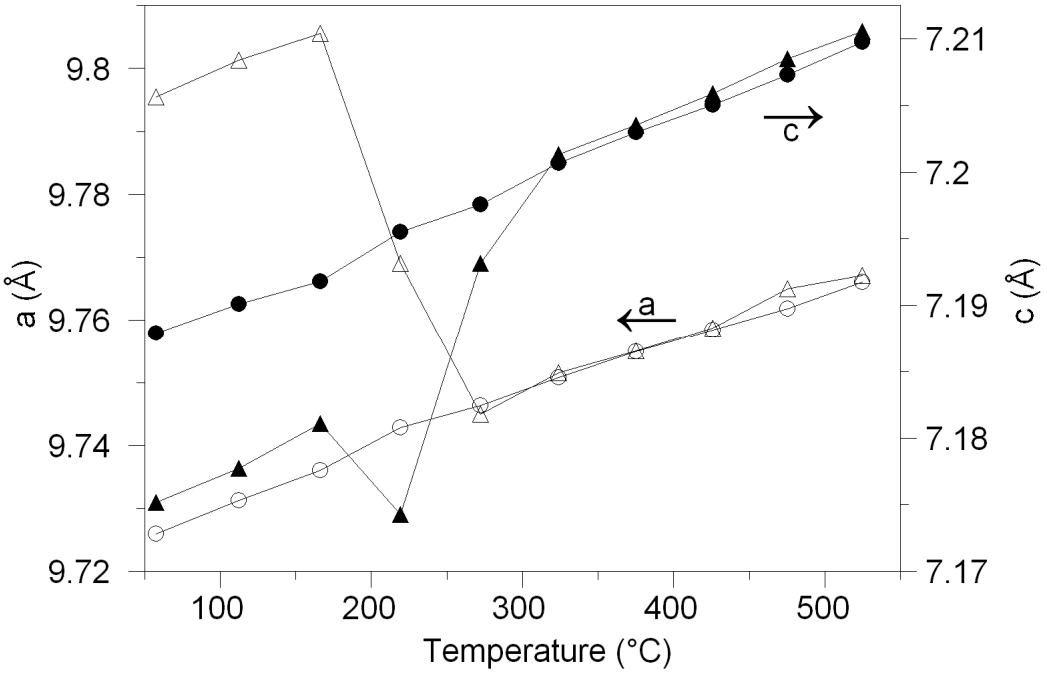

Fig. 7.4.a Cell parameter variation versus temperature for the as prepared (circle) and hydrated (triangle) $La_{9.6}Si_6O_{26.4}$ on heating.

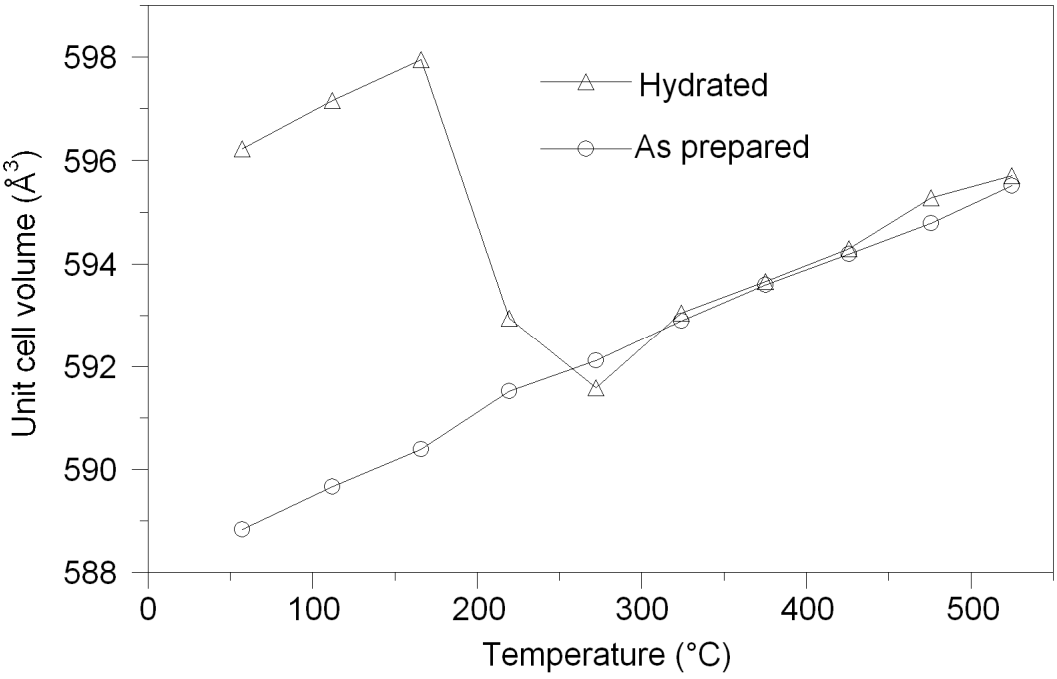

Fig. 7.4.b Cell volume variation versus temperature for the as prepared (circle) and hydrated (triangle) $La_{9.6}Si_6O_{26.4}$ on heating.

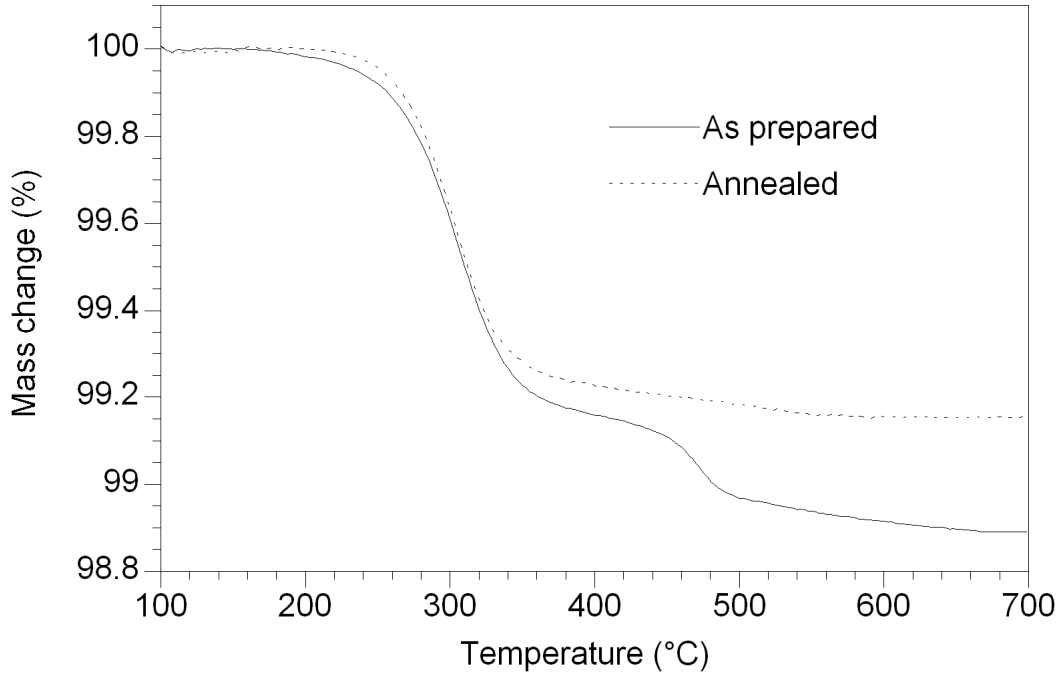

Fig. 7.5 TG profile of hydrated $La_{9.6}Si_6O_{26.4}$

The water content of hydrated sample was determined by TGA measurements (Fig. 7.5). Unlike the single stage dehydration suggested by the high temperature X-ray diffraction data, there was evidence for a two stage water loss from the TGA data: firstly there was an abrupt loss in mass at around 280 °C with a second mass loss at around 470 °C. Since high temperature X-ray diffraction data did not show any change at higher temperature, the second mass loss was attributed to the decomposition of an impurity phase (most likely amorphous), since the structure refinement indicated a lower La content than the starting ratio, it was presumed that this may be $La(OH)_3$ [19]:

$$2La(OH)_3 \xrightarrow{280°C} 2LaOOH + 2H_2O\uparrow \xrightarrow{470°C} La_2O_3 + H_2O\uparrow$$

Firstly, the mass of LaOOH was worked out from the mass loss at 470 °C and subsequently, the mass of $La(OH)_3$ was calculated. Eliminating the contribution of the above process, the calculated level of water incorporated was 0.75 H_2O per formula unit, which agreed with the composition $La_{9.5}Si_6O_{26.26}.0.75H_2O$ and the calculated interstitial content (≈ 1 O per formula

unit) from the diffraction studies. The dehydration temperature difference between X-ray diffraction study and the TGA result is due to the dynamic nature of the TGA measurement.

7.5 Annealed $La_{9.6}Si_6O_{26.4}$

In order to determine the effect of long term (1 month) heat treatment at 950 °C, the structure of annealed $La_{9.6}Si_6O_{26.4}$ was examined using neutron diffraction data. The structural parameters are given in table 7.3 with the observed, calculated and difference profiles in Fig. 7.6. The data indicated a refined composition of $La_{9.46}Si_6O_{26.16}$. Overall, there was no significant structural difference to the as prepared sample, apart from the slightly lower La content and consequently lower interstitial oxide ion occupancy, and the slight expansion in the a/b axis. The lower occupancy of La and O was accompanied by a slight increase in the average metaprism twist angle (22.24° → 22.43°), corresponding to the closing of the channel due to the lower anion content. Although there was no evidence for the presence of a secondary phase in the diffraction pattern, it is possible that lanthanum was lost from the structure as a form of La_2SiO_5 (amorphous), which is a common impurity in apatite-type silicates [20]:

$$La_{9.5}Si_6O_{26.26} \rightarrow 0.095La_2SiO_5 + 0.98La_{9.46}Si_6O_{26.16}$$

Table 7.3.a Refined structural parameters of annealed $La_{9.6}Si_6O_{26.4}$ with hexagonal *P6₃* (173) space group, from room temperature neutron diffraction data.

Space group	a/b (Å)	c (Å)	R_{wp}	R_p	χ^2
P6₃	9.72969(4)	7.18835(5)	2.34	1.83	3.105
Atom	Site	x	y	z	U_{iso} x 100 (Å)	SOF
La(1)	2b	⅓	⅔	-0.0161(6)	1.22(1)	0.864(2)
La(2)	2b	⅔	⅓	-0.0143(6)	1.22(1)	0.864(2)
La(3)	6c	0.2300(1)	-0.0116(1)	0.2415(5)	1.06(1)	1
Si	6c	0.4025(2)	0.3723(2)	0.2485(6)	0.71(3)	1
O(1)	6c	0.3233(2)	0.4846(2)	0.2425(8)		1
O(2)	6c	0.5942(1)	0.4727(1)	0.2425(8)		1
O(3)	6c	0.3535(3)	0.2588(4)	0.0588(5)		1
O(4)	6c	0.6644(5)	0.7473(4)	0.9201(6)		1
O(5)	2a	0	0	¼		0.849(5)
O(6)	6c	0.0018(21)	0.0058(45)	0.3959(20)		0.077(2)
100 x	U_{11}	U_{22}	U_{33}	U_{12}	U_{13}	U_{23}
O(1)	3.09(8)	2.57(8)	2.34(9)	2.45(7)	-0.62(22)	-1.64(23)
O(2)	0.94(6)	1.16(6)	2.28(8)	0.35(6)	0.27(21)	0.45(21)
O(3)	2.37(12)	2.03(15)	1.64(16)	1.42(12)	-0.71(10)	-0.89(14)
O(4)	8.09(21)	0.96(14)	1.57(17)	1.80(16)	-0.64(12)	-2.83(15)
O(5)	0.06(6)	0.06(6)	13.1(3)	0.03(3)	0	0
O(6)	7.26(28)	35.3(41)	5.59(17)	13.3(28)	18.7(16)	14.0(30)

Table 7.3.b Selected bond distances for annealed $La_{9.6}Si_6O_{26.4}$

Bond	Bond distance (Å)
Si-O(1)	1.622(1)
Si-O(2)	1.617(1)
Si-O(3)	1.667(1)
Si-O(4)	1.594(1)
La(1)-O(1) (x3)	2.536(1)
La(1)-O(2) (x3)	2.510(1)
La(1)-O(4) (x3)	2.945(1)
La(2)-O(1) (x3)	2.456(1)
La(2)-O(2) (x3)	2.588(1)
La(2)-O(3) (x3)	2.806(1)
La(3)-O(1)	2.761(1)
La(3)-O(2)	2.513(1)
La(3)-O(3)	2.633(1), 2.483(1)
La(3)-O(4)	2.455(1), 2.583(1)
La(3)-O(5)	2.294(1)
O(6)-La(3)	2.560(1), 2.580(1), 2.505(1)
O(6)-O(5)	1.050(1)

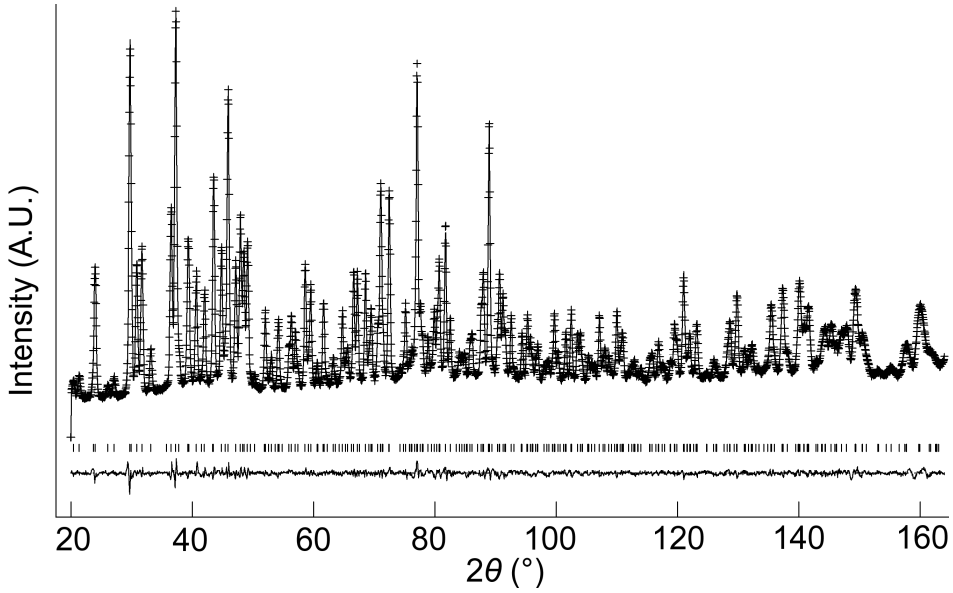

Fig. 7.6 Observed (cross), calculated (line) and difference plots of annealed $La_{9.6}Si_6O_{26.4}$ from the Rietveld refinement for room temperature neutron diffraction data.

The structural parameters for the annealed-hydrated $La_{9.6}Si_6O_{26.4}$ sample are given in table 7.4 with the observed, calculated and difference neutron diffraction profiles in Fig. 7.7. These data show a refined composition of $La_{9.46}Si_6O_{27.03}$ (excluding protons) or $La_{9.46}Si_6O_{27.03}H_{1.68}$ (with protons). As before, there were no significant structural differences compared to the as prepared hydrated sample apart from the very high atomic displacement parameter along the x-axis for O(6), which is suggestive of the presence of multiple interstitial sites. The level of water incorporated was also higher, which may be related to the lower occupancy of the interstitial oxide ion for the annealed sample. The calculated level of water incorporated by the TGA measurement was 0.88 H_2O per formula unit, which agreed with the calculated interstitial content from the diffraction studies. Interestingly, the TGA result showed no second mass loss at 470 °C, which suggests no $La(OH)_3$ present. Thus, these impurities have been eliminated in the annealing process. Overall, the structural data indicated only small differences between the samples before and after long term annealing at 950 °C.

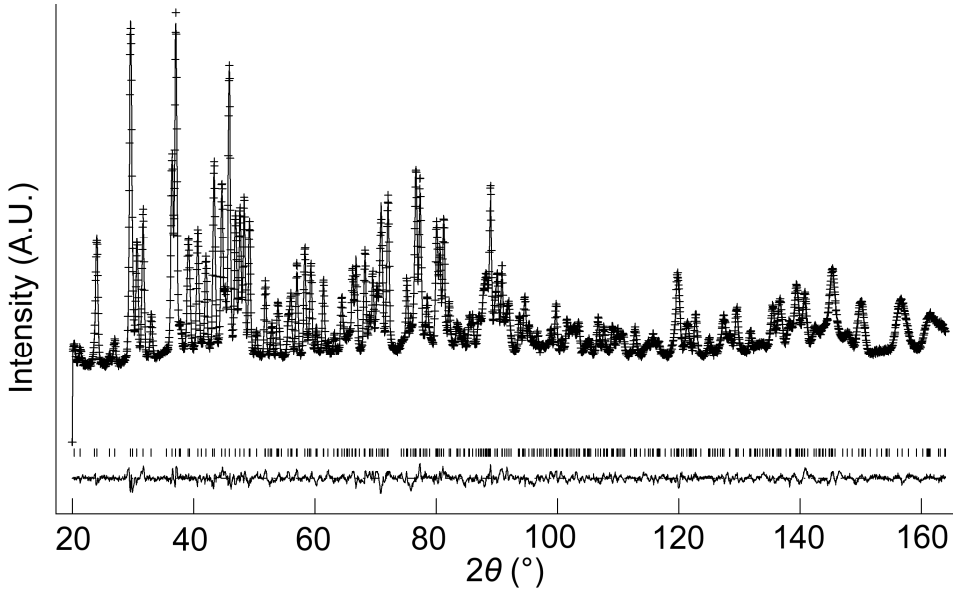

Fig. 7.7 Observed (cross), calculated (line) and difference plots of annealed and hydrated $La_{9.6}Si_6O_{26.4}$ from the Rietveld refinement for room temperature neutron diffraction data.

Table 7.4.a Refined structural parameters of annealed and hydrated $La_{9.6}Si_6O_{26.4}$ with hexagonal *P6₃* (173) space group, from room temperature neutron diffraction data.

Space group	a/b (Å)	c (Å)	R_{wp}	R_p	χ^2
P6₃	9.78693(9)	7.17734(9)	2.66	2.08	5.436

Atom	Site	x	y	z	U_{iso} x 100 (Å)	SOF
La(1)	2b	⅓	⅔	-0.0026(21)	1.83(3)	0.866(3)
La(2)	2b	⅔	⅓	-0.0044(21)	1.83(3)	0.866(3)
La(3)	6c	0.2356(1)	-0.0079(2)	0.2383(19)	1.16(2)	1
Si	6c	0.4024(3)	0.3748(3)	0.2428(20)	1.40(5)	1
O(1)	6c	0.3258(3)	0.4866(3)	0.2471(19)		1
O(2)	6c	0.5935(2)	0.4721(3)	0.2465(21)		1
O(3)	6c	0.3621(5)	0.2640(6)	0.0589(19)		1
O(4)	6c	0.6667(6)	0.7481(6)	0.9142(20)		1
O(5)	2a	0	0	¼		0.884(5)
O(6)	6c	0.1359(21)	0.1462(45)	0.4151(20)		0.211(2)

100 x	U_{11}	U_{22}	U_{33}	U_{12}	U_{13}	U_{23}
O(1)	6.04(17)	4.45(17)	0.79(10)	4.79(15)	-2.06(25)	-2.50(19)
O(2)	1.85(11)	1.69(11)	1.90(11)	0.21(10)	0.13(29)	0.02(30)
O(3)	5.10(23)	4.87(27)	0.79(16)	4.33(22)	-0.41(14)	-0.25(17)
O(4)	7.72(26)	0.90(18)	1.98(17)	0.97(18)	-3.43(14)	-1.16(19)
O(5)	1.30(13)	1.30(13)	21.4(7)	0.66(6)	0	0
O(6)	26.0(31)	0.09(6)	2.08(7)	6.16(11)	0.56(11)	-2.21(5)

Table 7.4.b Selected bond distances for annealed and hydrated $La_{9.6}Si_6O_{26.4}$

Bond	Bond distance (Å)
Si-O(1)	1.606(1)
Si-O(2)	1.620(1)
Si-O(3)	1.626(1)
Si-O(4)	1.614(1)
La(1)-O(1) (x3)	2.489(1)
La(1)-O(2) (x3)	2.563(1)
La(1)-O(4) (x3)	3.006(1)
La(2)-O(1) (x3)	2.483(1)
La(2)-O(2) (x3)	2.563(1)
La(2)-O(3) (x3)	2.745(1)
La(3)-O(1)	2.818(1)
La(3)-O(2)	2.484(1)
La(3)-O(3)	2.643(1), 2.527(1)
La(3)-O(4)	2.466(1), 2.556(1)
La(3)-O(5)	2.347(1)
O(6)-La(3)	2.511(1), 2.296(1), 2.519(1)
O(6)-O(4)	1.675(1)
O(6)-O(5)	1.821(1)

7.6 Conclusions

The refined structural parameters for apatite-type silicate system, $La_{9.6}Si_6O_{26.4}$, containing cation vacancies and oxygen excess, suggested a slightly lower La content with refined composition $La_{9.50}Si_6O_{26.26}$. Hydration of this sample led to an increase in the total oxygen content to approximately 27, i.e. $La_{9.50}Si_6O_{25.61}(OH)_{1.37}$: this represents an approximate 0.69 H_2O per formula unit. The position of the interstitial oxide ion site for the as prepared sample was determined to be close to the channel centre, at (0.003, 0.019, 0.405), rather than at the channel periphery, similar to the reports by Bechade *et al.*[10]. As water was incorporated, a displacement of the oxygen from the channel centre, (0.133, 0.143, 0.419) was observed, which was accompanied by the channel expansion to accommodate the higher level of interstitial oxide ions, evidenced by a cell parameter increase along a/b and a reduction in the LaO_6 metaprism twist angle. Overall, the results indicated that these interstitial oxide ions appear to be located along the channels causing local displacement of the oxide ion in the conventional oxide ion sites (evidenced by the high atomic displacement parameters) in line with the conclusions by Bechade *et al.*. As water is incorporated, and hence more anions introduced, there is insufficient space to accommodate the oxide ions directly along the channel centre, and the interstitial oxide ions are displaced away from the channel centre leading to swelling of the channel. The structure accommodates this swelling through the flexibility of the $La_{3.6}(SiO_4)_6$ framework, through a change in the metaprism twist angle. The results therefore highlights the importance of the metaprism twist angle, and the structural flexibility its' variation allows in these apatite systems. Moreover, the demonstration of the ability to open up or close the channels by the variation in this angle potentially provides some insight into how oxide ion migration can progress along the c direction. The opening of the channel to allow an oxide ion interstitial to more along c, followed by its closure once the

oxide ion has moved, may indicate a mechanism similar to peristalsis, which is observed to move items in the small intestine. The structural data indicated only small differences between the samples before and after long term annealing at 950 °C. There was some indication for a lower La content in the annealed sample. This may suggest that such oxygen excess apatites may be inherently unstable at temperatures lower than their synthesis temperature. The lower La content and hence lower oxygen content, observed after annealing would account for the reduction in bulk conductivity on annealing. Somewhat surprisingly, the reduction in La content was accompanied by a small increase in the cell dimensions, whereas the opposite might have been expected. Overall, therefore the results indicate significant complexities in the structural features of these apatite silicates, warranting further studies for samples with different La:Si rations, including phase diagram studies at different temperatures.

7.7 References

[1] Nakayama, S.; Aono, H.; Sadaoka, Y. *Chem. Lett.* **1995**, *24*, 431.
[2] Nakayama, S.; Sakamoto, M.; Highchi, M.; Kodaira, K. *J. Mater. Sci. Lett.* **2000**, *19*, 91.
[3] Pramana, S. S.; Klooster, W. T.; White, T. J. *Acta Crystallogr. B* **2007**, *63*, 597.
[4] Pramana, S. S.; Klooster, W. T.; White, T. J. *J. Solid State Chem.* **2008**, *181*,1717
[5] Kendrick, E.; Islam, M. S.; Slater, P. R. *Chem. Comm.* **2008**, 715.
[6] Kendrick, E.; Orera, A.; Slater, P. R. *J. Mater. Chem.* **2009**, *19*, 7955.
[7] Kendrick, E.; Islam, M. S.; Slater, P. R. *J. Mater. Chem.* **2007**, *17*, 3104.
[8] Masubuchi, Y.; Higuchi, M; Takeda, T.; Kikkawa, S. *Solid State Ionics* **2006**, *177*, 263.
[9] Ali, R.; Yashima, M.; Matsushita, Y.; Yoshioka, H.; Okoyama, K.; Izumi, F. *Chem. Mater.***2008**, *20*, 5203.
[10] Bechade, E.; Masson, O.; Iwata, T.; Julien, I.; Fukuda, K.; Thomas, P.; Champion, E. *Chem. Mater.* **2009**, *21*, 2508.
[11] León-Reina, L.; Porras-Vázquez, J. M.; Losilla, E. R.; Aranda, M. A. G. *Solid State Ion.* **2006**, *177*, 1307.
[12] Leon-Reina, L.; Porras-Vazquez, J. M.; Losilla, E. R.; Sheptyakov, D. V.; Llobet, A.; Aranda, M. A. G. *Dalton T.* **2007**, 2058.
[13] Panchmatia, P. M.; Orera, A.; Kendrick, E.; Hanna, J. V.; Smith, M. E.; Slater, P. R.; Islam, M. S. *J. Mater. Chem.* **2010**, *20*, 2766.
[14] Orera, A.; Slater, P. R. *Solid State Ionics.* **2010**, *181*, 110.
[15] Larson, A. C.; Von Dreele, R. B. *Los Alamos National Laboratory Report LAUR* **1994**, 86-748.
[16] White, T. J.; Dong, Z. L. *Acta Crystallogr. B* **2003**, *59*, 1.
[17] Tolchard, J. R.; Slater, P. R. *J. Phys. Chem. Solids* **2008**, *69*, 2433.
[18] Tolchard, J. R.; Sansom, J. E. H.; Islam, M. S.; Slater, P. R. *Dalton T.* **2005**, 1273.
[19] Bechade, E.; Julien, I.; Iwata, T.; Masson, O.; Thomas, P.; Champion, E.; Fukuda, K. *J. Eur. Ceram. Soc.* **2008**, *28*, 2717.
[20] Li, L.; Tang, Z. J.; Sun, W. Y.; Wang, P. L. *J. Mater. Sci. Technol.* **1999**, *15*, 439.

Chapter 8 Evaluation of a $La_{0.6}Sr_{0.4}Fe_{0.8}Co_{0.2}O_{3-\delta}$-$La_{10}Si_5GaO_{26.5}$ Composite Cathode Deposited on a $La_{10}Si_5GaO_{26.5}$ Electrolyte

8.1 Introduction

A number of studies have been carried out for the optimisation of apatite silicate electrolytes for SOFC applications including lower temperature sintering to reduce the production cost [1], thin film fabrication to reduce the ohmic losses [2] and diffusion controlled grain growth along the c-axis to maximise their anisotropic conduction [3]. Apart from these studies, concerning only the electrolyte part, the properties involving the electrode and electrolyte interface have been also examined such as thermal expansion coefficient compatibility [4] and area specific resistance (ASR) for a range of electrode materials [1, 5, 6].

It has been reported that the employment of a composite electrode reduces ASR by an increase in porosity and accessible triple phase boundary (TPB) [7]. The electrolyte material in the composite provides the porous support for the electrode material, thus resulting in a more open pore structure, which allows the easy access of the fuel/oxidant gases to the TPB. At the same time, the increased contact area between catalytic sites and ionic conducting phase provides an increased number of charge transfer pathways in a given area. These effects are often analysed by AC impedance spectroscopy, which generally resulted in two semicircles corresponding to the charge transfer at higher frequency and the gas diffusion (and dissociation) at lower frequency [1, 6].

There have been a number of studies carried out to identify the best cathode for apatite electrolytes in terms of ASR, and various optimisation strategies examined, such as the particle sizes of the composite electrode materials [8] and the employment of a buffer layer in between the electrode and electrolyte layers [1]. In order to extend these studies, in this

chapter, the effect of the perovskite/apatite ratio of the composite cathodes applied on an apatite-type silicate electrolyte $La_{10}Si_5GaO_{26.5}$ is reported, as well as the chemical compatibility of the materials involved in the composite cathodes. $La_{10}Si_5GaO_{26.5}$ was chosen as it has been reported to show high oxide ion conductivity, and is cation stoichiometric, and so may help to limit interaction with the perovskite material. In addition to the conventional cathode material $La_{0.6}Sr_{0.4}Fe_{0.8}Co_{0.2}O_{3-\delta}$ (LSCF), a new phosphate doped perovskite material $CaMn_{0.95}P_{0.05}O_{3-\delta}$ (CMP), prepared in our group [9] was analysed. Furthermore, a composite of perovskite and $Ce_{0.9}Gd_{0.1}O_{1.95}$ (CGO) was also examined on this apatite electrolyte.

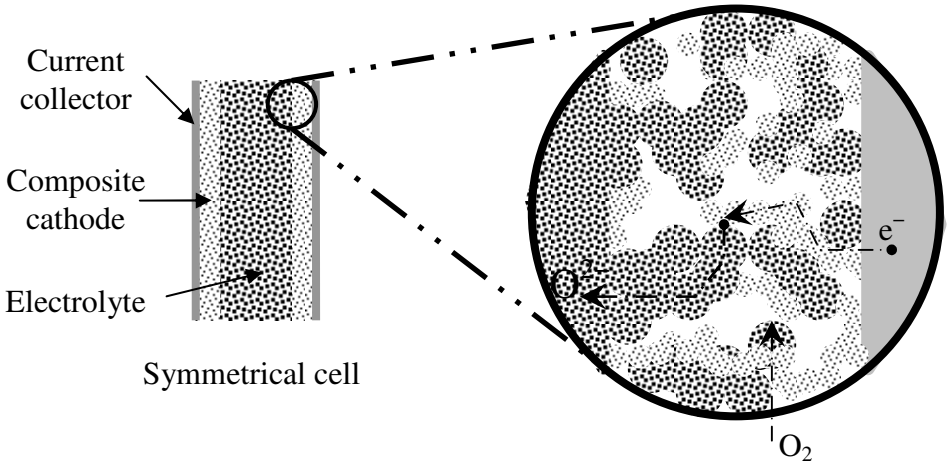

Fig. 8.1 Schematic diagram of a composite cathode deposited on an electrolyte in a symmetrical cell.

8.2 Experimental

For the preparation of the electrolyte material, $La_{10}Si_5GaO_{26.5}$ (LSG), high purity La_2O_3, SiO_2 and Ga_2O_3 were ground together in the correct stoichiometric mixture and heated for 12 hours at 1200 ºC, with a second firing at 1350 ºC for a further 12 hours. Between firings the sample was reground to ensure a homogeneous mixture. They were then ball-milled (350 rpm for 1 hour, Fritsch Pulverisette 7 Planetary Mill) and pressed as pellets (0.8 cm diameter) and

sintered at 1600°C for 2 hours. For the preparation of the cathode material, $CaMn_{0.95}P_{0.05}O_{3-\delta}$ (CMP), high purity $CaCO_3$, MnO_2 and $NH_4H_2PO_4$ were ground together in the correct stoichiometric mixture and heated for 12 hours at 1200 ºC, with a second firing at 1250 ºC for a further 12 hours. Between firings the sample were reground to ensure homogeneous reaction. Powder X-ray diffraction (Bruker D8 diffractometer with Cu $K\alpha_1$ radiation = 1.5406 Å) was used to demonstrate phase purity. The other cathode and electrolyte materials examined, $La_{0.6}Sr_{0.4}Fe_{0.8}Co_{0.2}O_{3-\delta}$ (LSCF) and $Ce_{0.9}Gd_{0.1}O_{1.95}$ (CGO) were obtained from Sigma-Aldrich.

The chemical compatibility between the materials was examined by X-ray diffraction studies. 1:1 wt.% mixtures of materials were ground together and fired to 1000 ºC for 12 h and the data were analysed to reveal any changes in the compounds of the mixture (e.g. cell parameters, the presence of additional phase).

For the preparation of the symmetrical cells for the area specific resistance (ASR) measurements, cathode and electrolyte materials were mixed in amounts from 0 to 50 wt.% electrolyte using a ball-mill (350 rpm for 1 hour), with the addition of the binder material, Decoflux (WB41, Zschimmer and Schwarz). The suspension was painted onto a thin LSG electrolyte pellet (thickness ≈ 0.6 mm) on both sides, and dried in an oven at 100 ºC: this was repeated 3 times to ensure full covering of the surface. The cell was fired to 900 ºC for 2h, and then coated with Pt paste, followed by heating to 800°C for 1 hour to ensure bonding to the cathode surface. ASR measurements were then measured in static air by AC impedance spectroscopy (Solartron SI 1260 impedance/gain phase analyser) in the frequency range from 1 to 10^6 Hz with perturbation of 100 mV. The induction contribution from the measurement rig was corrected by the method described in Macdonald [10]. The impedance data were analysed using *ZView* software, which estimates the resistance and capacitance values associated with equivalent circuits through the complex nonlinear least squares fitting [11].

8.3 Chemical compatibility results

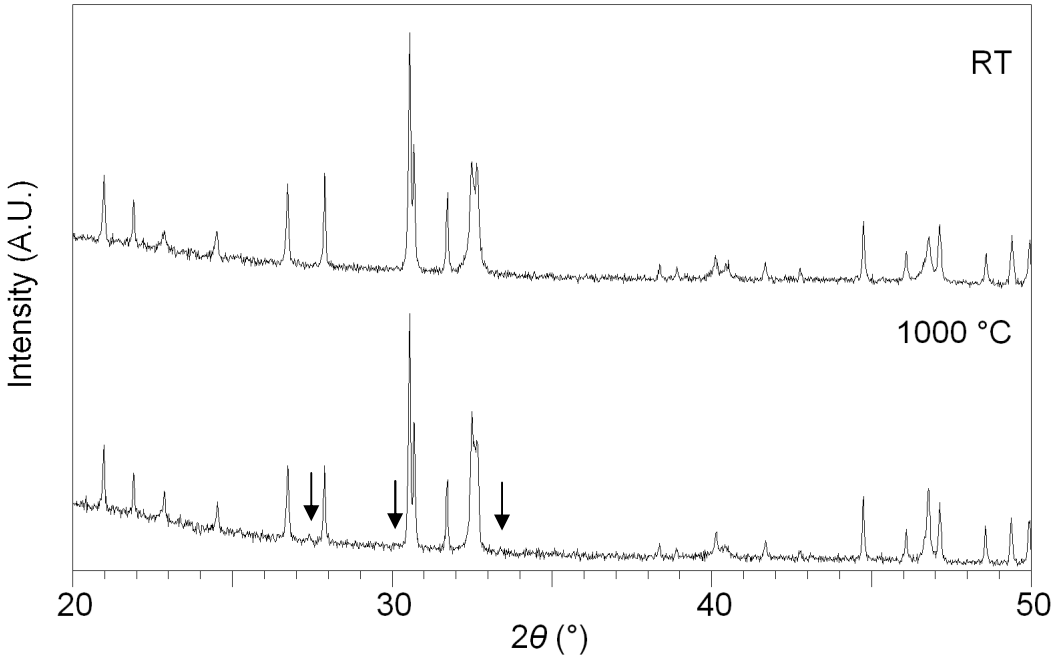

Fig. 8.2 X-ray diffraction patterns for the composite electrode, LSCF-LSG at room temperature and fired at 1000 ℃ for 12h (Peaks due to strontium silicates are highlighted).

The X-ray diffraction data for the LSCF-LSG composites, as mixed and fired at 1000 °C, are given in Fig. 8.2. There was the emergence of small peaks relating to strontium silicates, Sr_2SiO_4 and $SrSiO_3$ which was also seen in the work of Merrero-Lopez *et al.* [1] while showing no significant cell parameter change for both LSG and LSCF. The long term heat treatment resembling SOFC operating condition was carried out at 900 °C for 2 weeks and showed no significant cell parameter change for both LSG and LSCF while the emergence of small peaks due to $SrSiO_3$ was observed in X-ray diffraction data (Fig. 8.3). Overall, limited reactivity between LSCF and LSG was demonstrated.

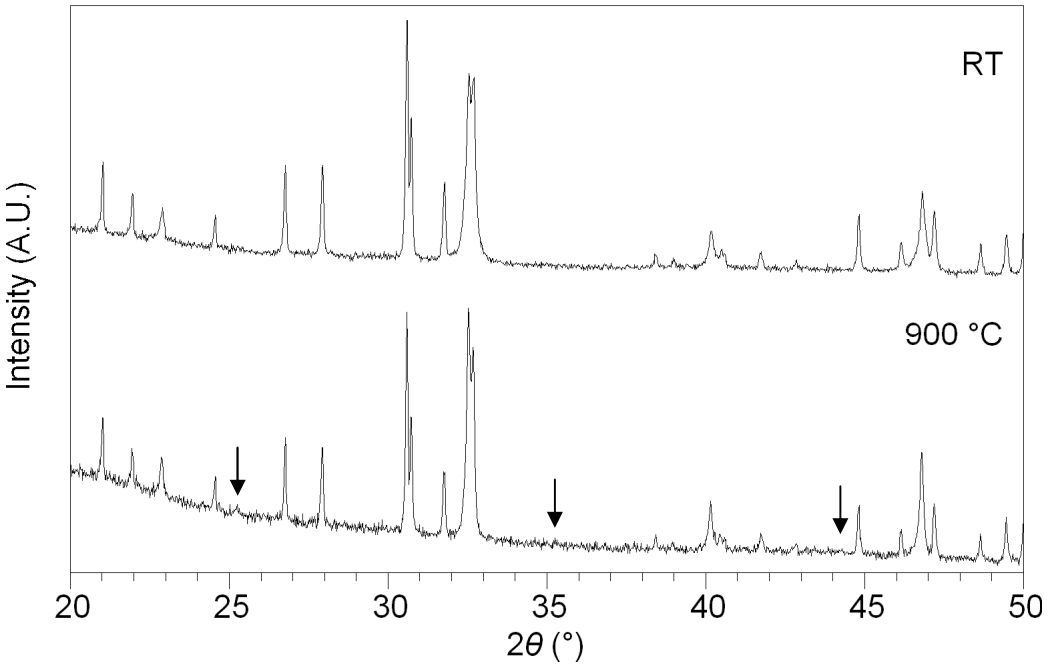

Fig. 8.3 X-ray diffraction patterns for the composite electrode, LSCF-LSG at room temperature and fired at 900 ℃ for 2 weeks (Peaks due to $SrSiO_3$ are highlighted).

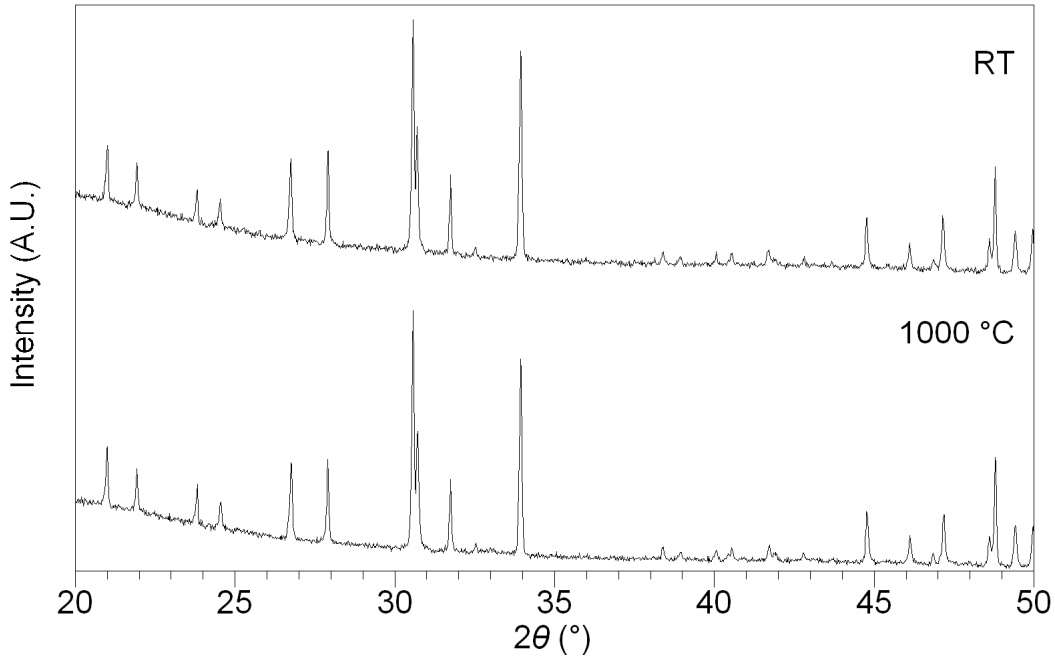

Fig. 8.4 X-ray diffraction patterns for the composite electrode, CMP-LSG at room temperature and fired at 1000 ℃ for 12h.

A compatibility test between LSG and oxyanion doped cathode materials, $CaMn_{0.95}P_{0.05}O_{3-\delta}$ (CMP) was also carried out (Fig. 8.4). There were no peaks due to additional phases observed in the X-ray diffraction data and no significant cell parameter change for both LSG and CMP which indicated no significant reactivity between CMP and LSG.

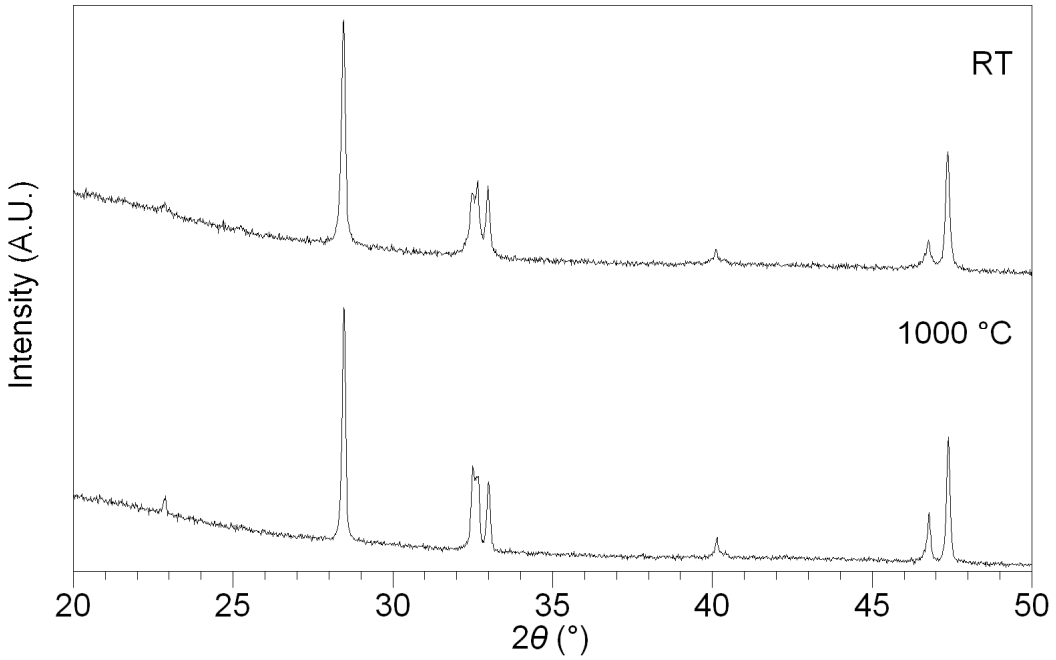

Fig. 8.5 X-ray diffraction patterns for the composite electrode, LSCF-CGO at room temperature and fired at 1000 ℃ for 12h.

CGO is a common electrolyte material for SOFC applications and it has also been used in many studies related to cathode development, and even used as a buffer layer for an apatite-type silicate electrolyte [1]. Thus, CGO was used to prepare LSCF-CGO composite cathodes, and so compatibility tests between LSCF and CGO were carried out (Fig. 8.5 and table 8.1.a). Although there was no evidence to indicate the formation of an additional phase in the X-ray diffraction data, the cell parameter for LSCF decreased dramatically, which suggested a significant level of cation migration as observed in prior studies [1]. The compatibility test

between CGO and LSG was also carried out (Fig. 8.6 and table 8.1.b) because LSG was the electrolyte for the ASR measurement of the composite, and there was a significant reduction in the cell parameter for LSG, although there was no evidence for the formation of any secondary phase. The results therefore indicated that CGO is reactive towards both LSCF and LSG as previously reported [1].

Table 8.1 Cell parameters for composite electrode constituents as mixed and heat treated.

		Composite constituent	Unit cell parameters (Å)			Unit cell volume ($Å^3$)
			a	b	c	
(a)	As mixed	CGO	5.417(1)	-	-	159.0(1)
		LSCF	5.477(1)	-	13.47(1)	349.8(1)
	1000 °C 12h	CGO	5.417(1)	-	-	158.9(1)
		LSCF	5.484(1)	-	13.35(1)	347.6(1)
(b)	As mixed	LSG	9.743(1)	-	7.242(1)	595.3(1)
		CGO	5.414(1)	-	-	158.7(1)
	1000 °C 12h	LSG	9.739(1)	-	7.233(1)	594.1(1)
		CGO	5.414(1)	-	-	158.7(1)

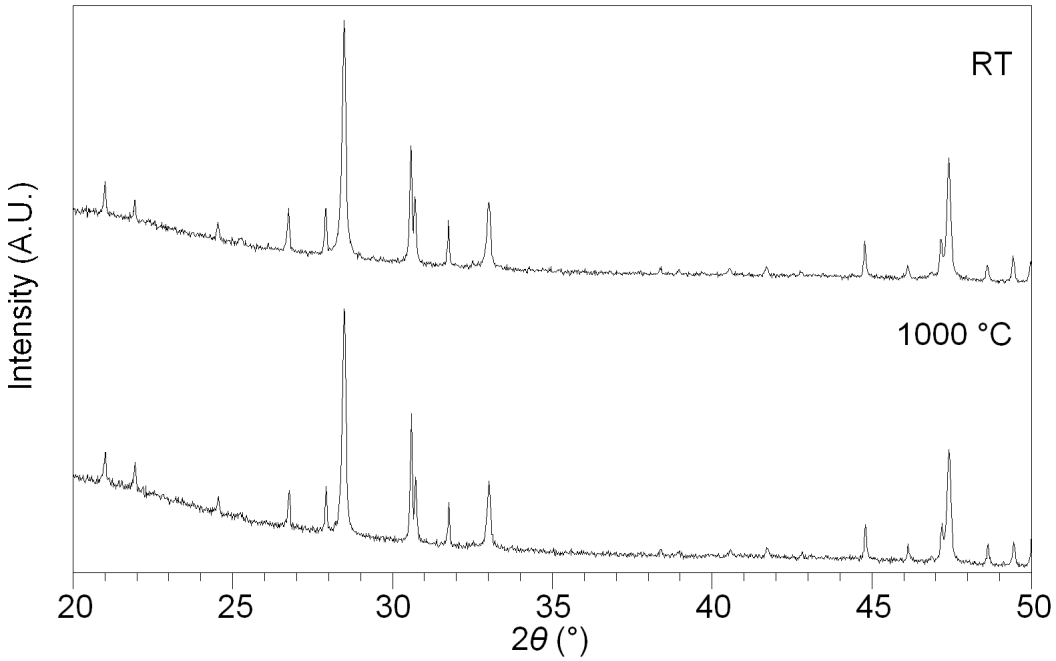

Fig. 8.6 X-ray diffraction patterns for the electrolyte mixture, CGO-LSG at room temperature and fired at 1000 ℃ for 12h.

8.4 Area specific resistance results

The impedance plots for the symmetrical cells showed distorted semicircles which can be interpreted as the overlapping of two semicircles. For example, the impedance plot obtained from the LSCF-LSG composite cathode on the electrolyte showed the overlapping of two semicircles (Fig. 8.7), and these were attributed to the charge transfer, and to the competitive reactions at the TPB (oxygen diffusion, adsorption and dissociation). However, some impedance plots showed severely distorted semicircles, such that the estimation of the resistance and capacitance for each constituent semicircle was not always possible. Thus, only the overall ASR values are reported here.

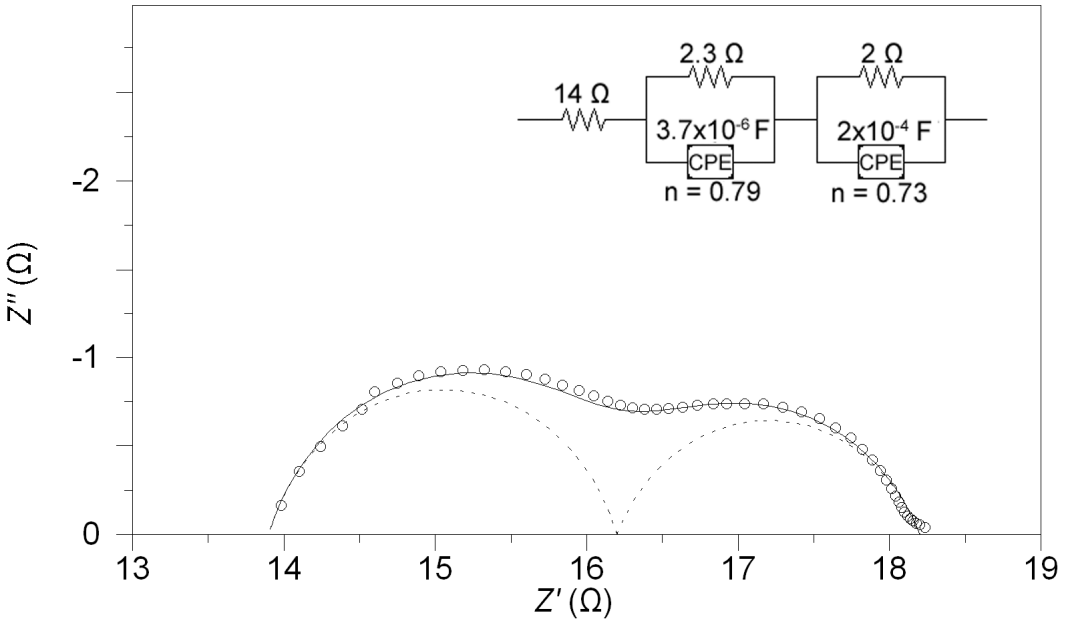

Fig. 8.7 The impedance plot of $La_{0.6}Sr_{0.4}Fe_{0.8}Co_{0.2}O_{3-\delta}$-$La_{10}Si_5GaO_{26.5}$ 1:1 composite on $La_{10}Si_5GaO_{26.5}$ electrolyte having area of 0.44 cm^2, measured at 700 °C in air, and the equivalent model for the fitting.

The ASR data for the LSCF-LSG composite cathode on the LSG electrolyte showed the reduction in the ASR for the 10-30 % LSG containing composite cathode compared to that of LSCF on its own, while the 40-50% LSG composite showed no significant difference to LSCF on its own (Fig. 8.8). The ASR value obtained for the 10 % LSG composite was 0.56 Ω cm^2 at 700 °C which was a significant improvement compared to 1.16 Ω cm^2 for LSCF on its own. There was also no significant change in activation energy (≈ 2.1 eV) for the different compositions and the value is slightly higher than in previous reports for other apatite silicate electrolytes, such as $La_{10}Si_{5.5}Al_{0.5}O_{26.75}$, etc [1, 6].

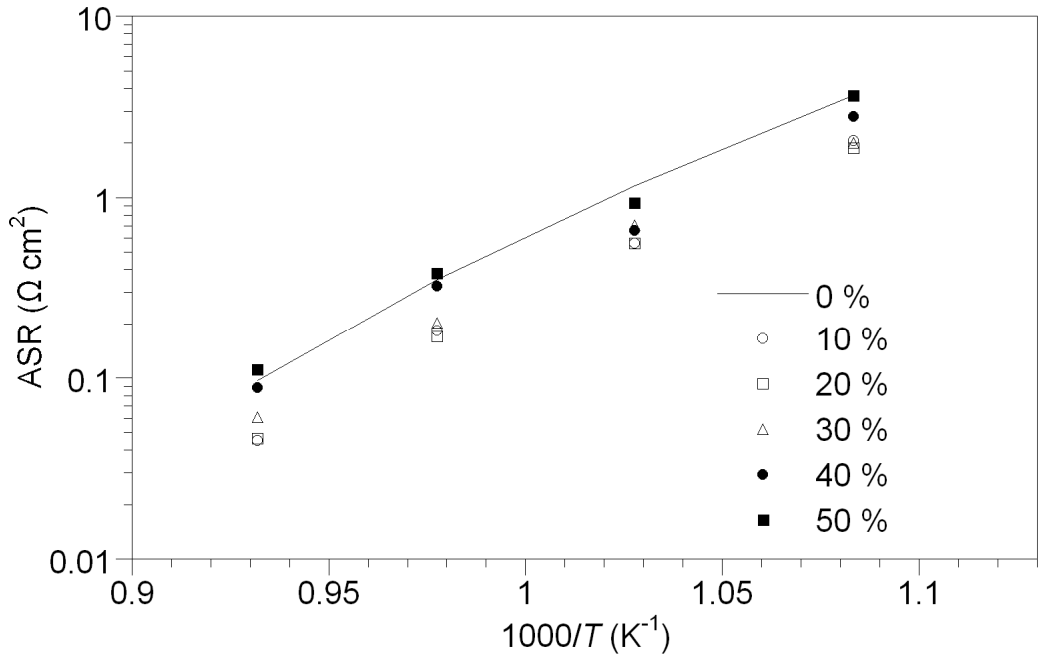

Fig. 8.8 ASR data in static air for composite electrodes, LSCF-LSG mixed in various ratio (percentage given is LSG content). E_a = 2.14 eV for 0% electrolyte.

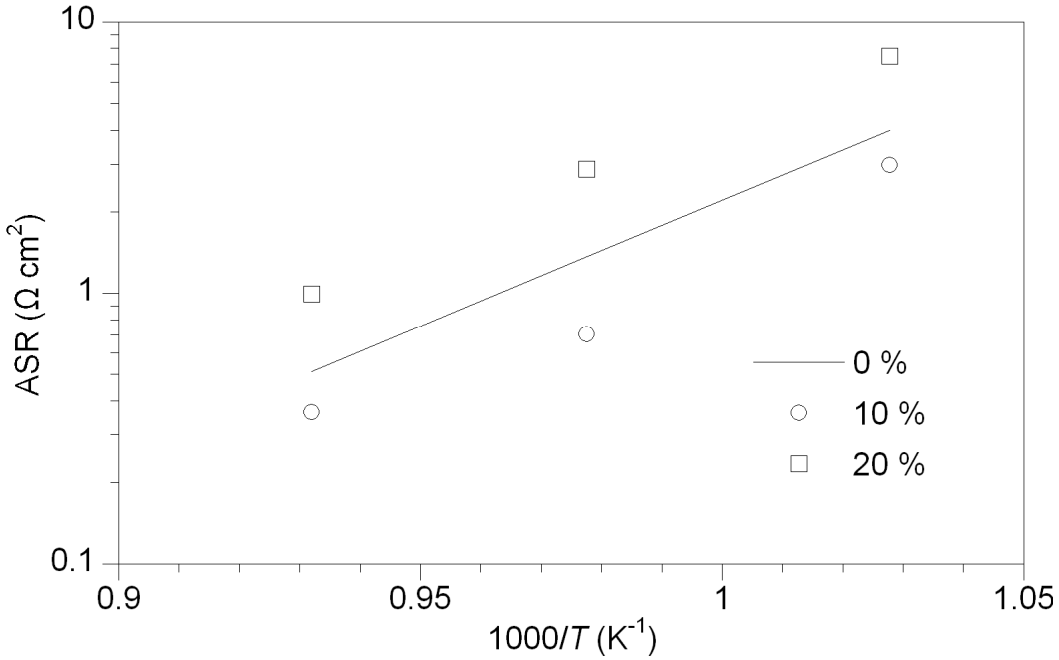

Fig. 8.9 ASR data in static air for composite electrodes, CMP-LSG mixed in various ratio (percentage given is LSG content). E_a = 1.94 eV for 0% electrolyte.

The ASR measurement of the CMP(90%)-LSG(10%) composite cathode on LSG electrolyte showed the slight decrease to 2.98 Ω cm^2 at 700 °C compared to 3.99 Ω cm^2 for CMP on its own. However, further addition of LSG (20 %) was shown to be detrimental to the ASR (Fig. 8.9), which may be due to some Ca, Mn incorporation into the apatite phase. As before, there was no significant change in activation energy (≈ 1.94 eV) on varying electrolyte contents.

Table 8.2 Area specific resistance values for various composite electrodes deposited on $La_{10}Si_5GaO_{26.5}$ electrolyte at 900 °C for 2h.

Composition	Ratio	ASR (Ω cm^2) at 700 °C
LSCF		1.164
LSCF-LSG	90:10	0.560
LSCF-CGO	90:10	0.661
CMP		3.992
CMP-LSG	90:10	2.981

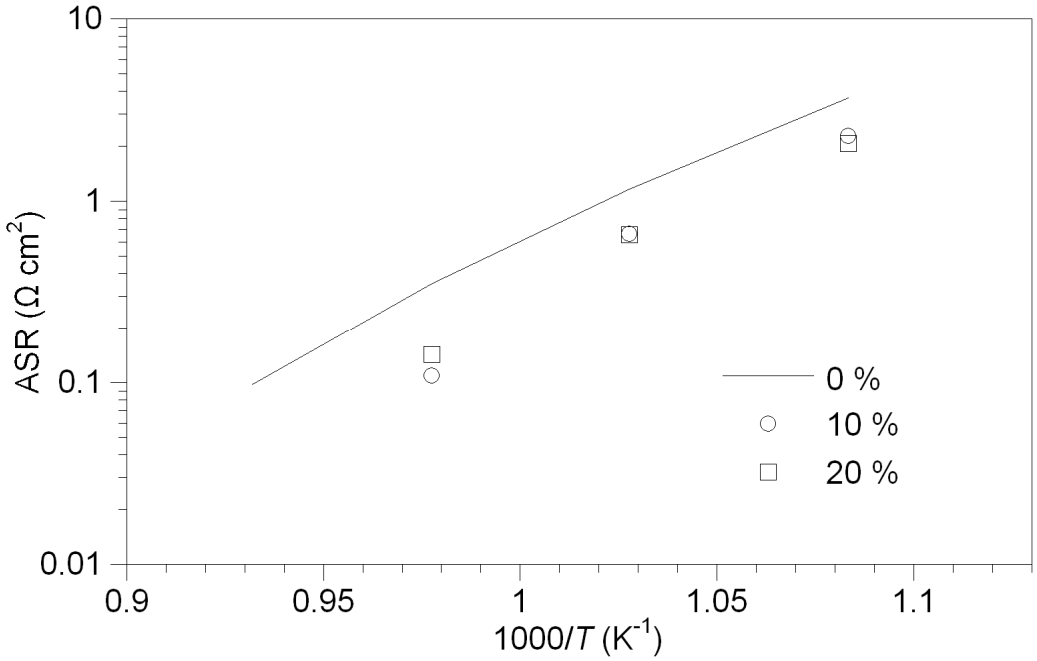

Fig. 8.10 ASR data in static air for composite electrodes, LSCF-CGO mixed in various ratio (percentage given is CGO content).

A CGO-LSCF composite cathode has been reported to be a good system in terms of low ASR [6, 12-14], and this was shown to be true for the ASR measurement on LSG electrolyte showing an ASR value of 0.66 Ω cm^2 at 700 °C (Fig. 8.10 and table 8.2), although there was evidence for the reaction between the LSCF and CGO. Interestingly, no ASR value variation was observed with varying the CGO ratio: essentially similar values were obtained from 0 % to 50 % CGO ratio, along with no significant change in the activation energy. Electron microscopic studies are required for each of these systems to investigate the influence of the electrolyte content of the cathode on the microstructure, and hence gain more detained information on these composite cathode systems.

8.5 Conclusions

It has been demonstrated that the electrode and electrolyte materials studied here show some inter-reactivity although the changes observed were generally small. The employment of these composite cathodes was shown to improve the ASR in the electrode-electrolyte interface. It has been also shown that in most cases there appears to be an optimum electrode/electrolyte material ratio for the composite electrode, which is most likely determined by the competition between the beneficial (e.g. the increase in porosity) and detrimental (e.g. isolation of electrode materials, formation of secondary phase) effects toward ASR. The LSCF(90%)-LSG(10%) composite cathode on a LSG electrolyte showed the best ASR value of 0.56 Ω cm^2 at 700 °C, which indicated the potential of this composite cathode coupled with a LSG electrolyte for fuel cell applications.

8.6 References

[1] Marrero-Lopez, D.; Martin-Sedeno, M. C.; Pena-Martinez, J.; Ruiz-Morales, J. C.; Nunez, P.; Aranda, M. A. G.; Ramos-Barrado, J. R. *J. Power Sources* **2010**, *195*, 2496.

[2] Yoshioka, H.; Mitsui, T.; Mineshige, A.; Yazawa, T. *Solid State Ionics.* **2010**, *181*, 1707.

[3] Fukuda, K.; Asaka, T.; Hamaguchi, R.; Suzuki, T.; Oka, H.; Berghout, A.; Bechade, E.; Masson, O.; Julien, I.; Champion, E.; Thomas, P. *Chem. Mat.* **2011**, *23*, 5474.

[4] Shi, Q. L.; Lu, L. H.; Jin, H. J.; Zhang, H.; Zeng, Y. W. *Mater. Res. Bull.* **2012**, *47*, 719.

[5] Yaremchenko, A. A.; Kharton, V. V.; Bannikov, D. O.; Znosak, D. V.; Frade, J. R.; Cherepanov, V. A. *Solid State Ionics.* **2009**, *180*, 878.

[6] Porras-Vazquez, J. M.; dos Santos-Gomez, L.; Santacruz, I.; Aranda, M. A. G.; Marrero-Lopez, D.; Losilla, E. R. *Ceram. Int.* **2012**, *38*, 3327.

[7] Tanner, C. W.; Fung, K. Z.; Virkar, A. V. *J. Electrochem. Soc.* **1997**, *144*, 21.

[8] Letilly, M.; Joubert, O.; La Salle, A. L. *J. Power Sources* **2012**, *212*, 161.

[9] Porras-Vazquez, J. M.; Kemp, T. F.; Hanna, J. V.; Slater, P. R. *J. Mater. Chem.* **2012**, *22*, 8287.

[10] Macdonald, J. R. *Impedance Spectroscopy*, 2nd Edition, John Wiley & Sons, **2005**

[11] Johnson, D. *ZView: a Software Program for IES Analysis, Version 3.1c*, Scribner Associates Inc., **2007**.

[12] Cesario, M. R.; Macedo, D. A.; Martinelli, A. E.; Nascimento, R. M.; Barros, B. S.; Melo, D. M. A. *Cryst. Res. Technol.* **2012**, *47*, 723.

[13] Angoua, B. F.; Slamovich, E. B. *Solid State Ionics.* **2012**, *212*, 10.

[14] Nielsen, J.; Jacobsen, T.; Wandel, M. *Electrochim. Acta* **2011**, *56*, 7963.

Chapter 9 Summary of Conclusions

9.1 $Ba_2In_2O_5$ systems

The successful incorporation of oxyanions (phosphate, sulphate and silicate) has been demonstrated in $Ba_2In_2O_5$, which led to a transition from a low symmetry orthorhombic cell to a high symmetry cubic cell. Due to the increased oxygen sublattice disorder, the oxide ion conductivity at low temperature was significantly enhanced, and measurement in wet atmospheres showed the presence of significant proton conductivity. Among the oxyanions, silicate incorporation appeared to be most beneficial, which is also in contrast to prior reports of a detrimental effect on the conductivity of fluorite based oxide ion conductors by the addition of silica. This can be explained by the accommodation of Si into the structure of the perovskite system rather than the accumulation at the grain boundary observed for the fluorite systems. The stability towards CO_2 was also improved by oxyanion doping, and there was a further improvement by co-doping with La/Zr on the Ba/In sites. In particular, the composition $Ba_2In_{1.8}Zr_{0.2}Si_{0.2}O_{5.2}$ displayed promising results, with a combination of high conductivity and high CO_2 stability.

35% Y, Yb were successfully incorporated into $Ba_2In_2O_5$, and higher levels of Y, Yb (50%) were achieved with co-doping with phosphate (25%). The 35% Y, Yb doped systems adopted a cubic lattice and showed an improved oxide ion conductivity at low temperature. However, in these cases, phosphate co-doping reduced the oxide ion conductivity, which can be attributed to the reduction in the level of oxide ion vacancies. Improved CO_2 stability was obtained with further co-doping with La, but this was also shown to be to the detriment of the conductivity.

A novel oxide fluoride, $BaInO_2F$ was successfully prepared by the fluorination of $Ba_2In_2O_5$ with PTFE. The same method applied to phosphate and silicate doped systems only led to partial fluorination which can be explained by the unwillingness of the P and Si of the phosphate and silicate groups to increase their coordination number.

9.2 $Ba_2Sc_2O_5$ systems

The oxyanion doping strategy was extended to the $Ba_2Sc_2O_5$ system, resulting in single phase phosphate and sulphate doped $Ba_2Sc_2O_5$ samples, with silicate doped samples showing small Ba_2SiO_4 impurities. In addition, the results suggested that "undoped" $Ba_2Sc_2O_5$ contains oxyanions, in this case carbonate, which explains the previously reported thermal instability of this phase. The phosphate doped samples exhibited good thermal stability, high oxide ion conductivity along with significant proton contribution in wet atmospheres and high CO_2 stability. The results thus emphasise the potential of the oxyanion doping strategy for the preparation of new perovskite related phases with excellent properties.

9.3 Al doped $Nd_{9.33}Si_6O_{26}$ single crystals

Al doping in neodymium silicate single crystals was examined, and the results showed a detrimental effect on the conductivity. Due to the presence of a second semicircle in the impedance plot of these single crystals, the effect of long term (1-3 months) heat treatment at 950 °C was examined for $Nd_{9.33}Si_6O_{26}$ and $Nd_{9.5}Si_{5.5}Al_{0.5}O_{26}$. It was postulated that this second semicircle may be due to stacking faults/dislocations/cation inhomogeneity in the single crystals. Some support for this was provided by the fact that the second semicircle disappeared on long term annealing. The bulk conductivity was shown to be decreased upon annealing, and a further semicircle at lower frequency appeared for $Nd_{9.5}Si_{5.5}Al_{0.5}O_{26}$ having

the capacitance value for a typical grain boundary response. Further systematic studies utilising other lower valent cation (i.e. Ga, B) doped single crystals in conjunction with polycrystalline samples are required to identify the origin of this semicircle, although it may be due to Al being "precipitated" as $NdAlO_3$.

9.4 Polycrystalline lanthanum silicates

A structural refinement from neutron diffraction data was performed for the sample $La_{9.6}Si_6O_{26.4}$, with the refinement indicating a slightly lower La content, i.e. $La_{9.5}Si_6O_{26.26}$. Hydration of this sample led to an increase in the total oxygen content to approximately 27, i.e. $La_{9.50}Si_6O_{25.61}$ $(OH)_{1.37}$, having approximately 0.69 H_2O per formula unit. Structural refinement showed the interstitial oxide ion to be located near the channel centre, (0.003, 0.019, 0.405) for the dry sample. The incorporation of water displaced this interstitial oxide ion from the channel centre to an average site at (0.133, 0.143, 0.419), which was accompanied by the channel expansion to accommodate the high level of interstitial oxide ion, evidenced by a cell parameter increase along a/b and the reduction in LaO_6 metaprism twist angle. The data showed high atomic displacement parameters for these interstitial oxide ions, consistent with a range of sites with different displacements from the channel centre. The presence of these interstitial oxide ions also appears to cause local displacement of the oxide ion in the conventional oxide ion sites (evidenced by the high thermal displacement parameters) in line with the conclusions by Bechade et al [1]. Moreover, the demonstration of the ability to alter the size of channel by the variation in the metaprism twist angle suggested that there may be the participation of dynamic structure relaxation (similar to peristalsis) to enhance oxide ion migration along the c-axis.

The effect of long term (1-3 months) heat treatment at 950 °C was also examined. There was a general decrease in the bulk conductivity without a large structural change in the powder diffraction data, although the data did suggest a small reduction in La content. While the bulk conductivity was decreased, it was shown that the long term thermal treatment was beneficial on the total conductivity of the polycrystalline silicates at the temperature lower than 400 °C, due to an improvement in grain boundary conductivity. Further work is required in this area to explain these observations, which are the first reported experiments of the effect of long term annealing at SOFC operating temperature of apatite electrolytes.

Studies were also begun to investigate composite materials that could be employed as cathodes in conjunction with an apatite electrolyte. The presence of an optimum electrode/electrolyte material ratio for the composite electrode was demonstrated, which is most likely determined by the competition between the beneficial (e.g. the increase in porosity) and detrimental (e.g. isolation of electrode materials or formation of secondary phase) effects toward ASR. The LSCF(90%)-LSG(10%) composite cathode on LSG electrolyte showed the best ASR value of 0.56 Ω cm^2 at 700 °C without a significant reactivity between the materials, which showed the potential of this composite cathode coupled with a LSG electrolyte for fuel cell applications. Further work is planned to take these studies further towards full cell testing.

9.5 List of publications resulting from this project

[I] Shin, J. F., L. Hussey, et al. (2010). "Enhancement of the conductivity of Ba2In2O5 through phosphate doping." Chemical Communications **46**(25): 4613-4615.

[II] Shin, J. F., D. C. Apperley, et al. (2010). "Silicon Doping in Ba2In2O5: Example of a Beneficial Effect of Silicon Incorporation on Oxide Ion/Proton Conductivity." Chemistry of Materials **22**(21): 5945-5948.

[III] Shin, J. F., A. Orera, et al. (2011). "Oxyanion doping strategies to enhance the ionic conductivity in Ba2In2O5." Journal of Materials Chemistry **21**(3): 874-879.

[IV] Shin, J. F. and P. R. Slater (2011). "Enhanced CO2 stability of oxyanion doped Ba2In2O5 systems co-doped with La, Zr." Journal of Power Sources **196**(20): 8539-8543.

[V] Mancini, A., J. F. Shin, et al. (2012). "Insight into the local structure of barium indate oxide-ion conductors: An X-ray total scattering study." Dalton Transactions **41**(1): 50-53.

[VI] Shin, J. F., K. Joubel, et al. (2012). "Synthesis and characterization of proton conducting oxyanion doped Ba(2)Sc(2)O(5)." Dalton Transactions **41**(1): 261-266.

[VII] Shin, J. F. and P. R. Slater. "Investigation into the effect of Y, Yb doping in $Ba_2In_2O_5$: determination of the solid solution range and co-doping with phosphate." Submitted to Materials Research Bulletin

9.6 References

[1] Bechade, E.; Masson, O.; Iwata, T.; Julien, I.; Fukuda, K.; Thomas, P.; Champion, E. *Chem. Mater.* **2009**, *21*, 2508.

Chapter 10 Further Work

10.1 Investigation into the improvement of ionic conductivity of $Ba_2In_2O_5$ systems through fluorination

Animitsa *et al*. reported the enhanced ionic conductivity for fluorinated $Ba_2In_2O_5$ system (best conductivity for $Ba_{1.95}In_2O_{4.9}F_{0.1}$) [1]. In this work, the total anion content was fixed at 5, and the F as replacement for O was accommodated by Ba vacancies. A similar study is warranted where the Ba content is fixed and the anion content varied, i.e. $Ba_2In_2O_{5-x}F_{2x}$. Thermal stability studies of the fluorinated undoped, and phosphate and silicate doped, $Ba_2In_2O_5$ are also warranted, to establish the possibility for technological applications.

10.2 Fuel cell tests for $Ba_2In_{1.6}Si_{0.2}Zr_{0.2}O_{5.2}$

As $Ba_2In_{1.6}Si_{0.2}Zr_{0.2}O_{5.2}$ showed excellent ionic conductivity and CO_2 stability, a fuel cell test with this composition is warranted. Firstly, suitable cathode/anode having appropriate thermal expansion coefficient, chemical compatibility, low ASR would be selected and the optimum ratio for composite electrode would be determined. The fuel cell fabrication method also needs to be optimised and followed by the fuel cell test.

10.3 Preparation of doped $Ba_2In_2O_5$ phases with high oxide ion/proton conductivity, CO_2 stability along with low In content

Due to the high cost of In, the In content has to be lowered for technological applications. Y/Yb and P co-doping achieved the preparation of phases with only 25% In present. However, these phases showed lower conductivity and CO_2 stability compared to the P, Si doped $Ba_2In_2O_5$ systems. Thus, further doping studies for the preparation of the phases with low In

content are required to prepare systems having high oxide ion/proton conductivity and CO_2 stability.

Further studies of oxyanion doping in perovskite systems are also warranted to explore the widespread viability of these doping strategies.

10.4 Further studies on doped neodymium silicate single crystals

As Al doping in neodymium silicates showed a detrimental effect on the conductivity, in contrast to the reported beneficial effect of such doping on polycrystalline lanthanum silicates, further doping studies using similar low valent cation (e.g. B, Ga) are warranted. Further studies are required on other apatite silicate single crystals, to gather more information regarding the origin of the additional semicircle observed in impedance studies.

10.5 Further annealing studies on polycrystalline lanthanum silicates

As there was shown to be a detrimental effect on the bulk conductivity of some apatite silicate electrolytes upon annealing at 950 °C, further studies in this area are warranted, including a series of related systems containing varying degrees of cation vacancies and oxygen excess. These samples should be annealed for an extended period of time to make any structural changes significant and those changes would be analysed to correlate with the conductivity change utilising a combination of techniques such as X-ray and neutron powder diffraction, ^{29}Si NMR, electron microscopy coupled with energy dispersive X-ray spectroscopy, Raman and IR spectroscopy. In particular total scattering studies are warranted to elucidate, if there are any key local structural changes. In addition, microscopy studies will also provide information about the origin of the improved grain boundary conductivity for

polycrystalline samples (e.g. possibility of gradual improved sintering upon annealing, redistribution of cations between bulk and grain boundary).

10.6 Fuel cell tests using a $La_{10}Si_5GaO_{26.5}$ electrolyte

In order to illustrate the potential of apatite silicates as fuel cell electrolytes, further studies are required utilising these electrolytes in complete cells. As the $La_{0.6}Sr_{0.4}Fe_{0.8}Co_{0.2}O_{3-\delta}$(90%)-$La_{10}Si_5GaO_{26.5}$(10%) composite cathode showed the best ASR on $La_{10}Si_5GaO_{26.5}$, the next step is to identify an optimum anode composite ratio which could be used in the fabrication of a full cell. Following optimisation of the fabrication method, the potential for the $La_{10}Si_5GaO_{26.5}$ as an electrolyte in a fuel cell application could be assessed.

10.7 References

[1] Animitsa, I.; Tarasova, N.; Filinkova, Y. *Solid State Ionics* **2012**, *207*, 29.